THE UNIVERSITY OF CHICAGO

ULTRAFAST DYNAMICS OF FUNCTIONAL LIGHT-HARVESTING MATERIALS PROBED WITH NONLINEAR SPECTROSCOPIES

A DISSERTATION SUBMITTED TO
THE FACULTY OF THE DIVISION OF THE PHYSICAL SCIENCES
IN CANDIDACY FOR THE DEGREE OF
DOCTOR OF PHILOSOPHY

DEPARTMENT OF CHEMISTRY

BY

LILI WANG

CHICAGO, ILLINOIS

JUNE 2017

To My Parents Zehui Wang and Lianping Li

TABLE OF CONTENTS

LIST OF FIGURES

LIST OF TABLES

ACKNOWLEDGEMENTS

The work presented in this dissertation was supported by research grants from the Defense Threat Reduction Agency, the Air Force Office of Scientific Research, the Defense Advanced Research Projects Agency QuBE, the National Science Foundation MRSEC Program, the Vannevar Bush Fellowship, the Alfred P. Sloan Foundation and the Camille and Henry Dreyfus Foundation.

Our collaborators were supported by research grants from the Computational Materials Sciences Program, Laboratory Directed Research and Development Program funding by Argonne National Laboratory.The synthetic compounds presented in this dissertation were characterized using the Nuclear Magnetic Resonance Facilities, the Mass Spectrometry Facilities and the X-ray Diffraction and Photoelectron Spectroscopy Facilities at Department of Chemistry, the University of Chicago as well as the National Science Foundation Materials Research Science & Engineering Center at the University of Chicago. The calculations presented in this dissertation were conducted with the resources of the National Energy Research Scientific Computing Center, a DOE Office of Science User Facility supported by the Office of Science of the U.S. Department of Energy.

I would like to acknowledge my collaborators Dr. Feng Zhai and Prof. Richard F. Jordan for their professional advice on the synthesis and Schlenk-line operation related to the work described in Chapter 3. The success of the synthesis enabled me to investigate the design principles of vibronic coherence in artificial systems with 2D spectroscopy.

I would like to acknowledge my collaborators at Stanford University, Dr. Igor Pochorovski, Dr. Melanie Chiu (now Assistant Professor at SUNY Stony Brook University) and Prof. Zhenan Bao, for graciously providing the sample of cavitand molecular switch described in Chapter 4. The synthesis of this molecular switch is time-consuming and requires great synthetic expertise.

I would like to acknowledge my collaborator Prof. David M. Tiede for giving me access to the nanosecond transient spectroscopy setup at the Argonne National Lab, which enable

the experimental work presented in Chapter 5. I would also like to acknowledge my collaborators Nicholas P. Brawand, Dr. Márton Vörös and Prof. Giulia Galli for conducting great calculations that facilitate the interpretation of our experimental results described in Chapter 5.

I would like to acknowledge my collaborators Dr. Edward W. Malachosky and Prof. Philippe Guyot-Sionnest for their expertise on the characterization of the nanocrystals and excellent suggestions on the interpretation of photophysical properties of the NCs.

I would also like to thank Drs. Qiti Guo, Justin Jureller, and Alexander Filatov for their assistance with various facilities and characterization. I would also like to thank Eric Janke, Vishwas Srivastava, Igor Fedin and Prof. Dmitri Talapin for useful discussions on various projects.

I would like to acknowledge Dr. Kelly Fransted, Dr. Justin Caram, Haibin Zheng and Dr. Peter Dahlberg for building the instruments with which I acquired the data presented in this dissertation. I would like to acknowledge John Otto and Nick Williams who worked tirelessly with me for the data acquisition. I would like to acknowledge Alice Zhang for assistance with synthesis. I would like to thank former Engel Group members Dr. Dugan Hayes and Dr. Graham Griffin (now Assistant Professor at DePaul University) for training me on laser tuning when I first joined Engel Group. I would also like to thank other members of the Engel Group for their advice, discussions and support throughout my time at the University of Chicago. Importantly, I would like to thank Prof. Gregory S. Engel for giving me the opportunities to conduct the work described in this dissertation. Greg was always willing to consider and discuss any far-fetched ideas. Greg encouraged me to extend our current 2D technique to new areas and allowed me to explore synthesis and characterization of various samples. With his constant support, I was able to collaborate with other great scientists answering important questions that have not been explored before.

I would also like to thank the other three members of my thesis committee, Profs. Andrei Tokmakoff, Dmitri Talapin and Philippe Guyot-Sionnest. Last but not the least, I would

like to thank my family for their love and support throughout my life. I would like to thank my friends for their friendship during these years that make my life at University of Chicago great and memorable.

ABSTRACT

The photophysical dynamics of functional materials adopted in photosynthesis and photovoltaics are important for solar light harvesting. Observations of long-lived quantum coherences in photosynthetic complexes have spawned numerous research efforts on the microscopic origins, the design principles and the biological significance of these observed beating signals. The remarkable device performance demonstrated by perovskite photovoltaics have also drawn broad scientific interest to the fundamental photophysical properties of these perovskite materials in both bulk single crystals and nanocrystals. In this dissertation, I provide interesting observations and interpretations regarding the ultrafast dynamics of light-harvesting materials. By performing two-dimensional electronic spectroscopy (2DES) on a series of structurally flexible heterodimers with varied electronic transitions both in dilute solution or packed on single-walled carbon nanotubes, we have discovered two prerequisites to the observed vibronic coherences: one is a resonant vibrational mode with the electronic energy gap; the other is limiting the relative orientation between different chromophores. 2DES on a pair of BODIPY dyes attached to a cavitand molecular switch demonstrates the effects of nonradiative transitions on Förster resonance energy transfer. Transient absorption spectroscopy on $CH_3NH_3PbBr_3$ perovskite single-domain single crystals and related theoretical calculations show that free carriers and localized carriers coexist due to polaron formation in bulk perovskite. Transient absorption spectroscopy on $CH_3NH_3PbBr_3$ perovskite nanocrystals synthesized by a ligand-mediated method demonstrates radiation-fluence independent photoluminescence decay, indicating these nanocrystals are quantum confined. 2DES on perovskite nanocrystals reveals ultrafast dynamics (sub 50-fs exciton relaxation and coherences) and different spectral features that reflect the electronic structure of the NCs. The observations described in this dissertation will be important for understanding the fundamental photophysical properties of these functional light-harvesting materials and guide future material designs used in devices.

CHAPTER 1

INTRODUCTION TO LIGHT HARVESTING

1.1 Overview of light harvesting

Global energy consumption grew rapidly during the twentieth century. This trend still continues now with fossil fuels still used as the primary power source. Fossil fuels (oils, coal and natural gas) supplied 81.4 % of the world energy consumption in 2013, while renewable energy (solar, wind *et al*) only supplied 1.2% [1]. The demand for clean and renewable energy surges due to both the risk of depleting fossil fuels in the foreseeable future and the concern on air pollution caused by combustion of fossil fuels.

Solar energy is a promising source of renewable energy due to its abundance and sustainability. The solar power incident upon the Earth's surface is about 120,000 TW, exceeding human power consumption (15 TW) by four orders of magnitude [2]. Hence, approaches for efficient harvesting and utilization of solar energy become an important branch of current research. Solar energy can be harvested either in a biological manner by photosynthesis, in which biomass is stored as the final product, or in a chemical manner by photovoltaic devices to generate electric current, which can be readily utilized.

Photosynthetic organisms, including bacteria, algae and plants, collectively harvest about 100 TW of solar energy every year [3]. Although the overall thermodynamic efficiency of photosynthesis is quite low, the quantum efficiency of the energy transfer process from the location of photon absorption (photosynthetic antennae) to the location of charge separation (reaction centers) is near perfect [4, 5]. Such light-induced dynamics (called "light reactions" in photosynthesis) is also involved in photovoltaic devices. Photons are absorbed by the active layer and then separated into electrons and holes, prior to the migration toward different electrodes. Investigations on the design principles and the energy transfer mechanism of these photosynthetic organisms that exhibit near-perfect transfer quantum efficiency will provide insight to biomimetic strategies for artificial materials incorporated into

photovoltaic devices. In the mean time, investigations on light-induced dynamics of various active-layer materials of photovoltaic devices will improve the knowledge of their inherent photophysical properties. Such knowledge is crucial for understanding the photovoltaic device performance (either good or poor performance), and would in return guide the device design. Both routes lead to the same ultimate end, that is, harvesting solar energy efficiently to support human.

As a physical chemist, I seek to contribute to both of the aforementioned routes by interrogating the light-induced dynamics of several materials related to photosynthesis or photovoltaics, using ultrafast spectroscopic techniques, including two-dimensional electronic spectroscopy and transient absorption spectroscopy. The projects described in Chapter 3 and Chapter 4 are devoted to using synthetic small molecules as models to understand the design principles of vibronic coherences, the existence of which may account for the near-perfect quantum efficiency in photosynthetic energy transfer processes, and the effects of nonradiative relaxation on the overall Föster Resonance Energy transfer. The projects described in Chapter 5 and Chapter 6 are devoted to understanding the inherent photophysical properties of perovskites, which have been recently viewed as promising materials for light-harvesting [6–8] and light-emitting devices [9–11]. The general backgrounds and motivations of the projects regarding each route are described individually in Sections 1.2 and Section 1.3. Physicial and theoretical backgrounds that are necessary for interpreting the experimental results in the dissertation are included in Section 1.4 and Section 1.5, respectively.

1.2 Photosynthetic antennae and synthetic model systems

Photosynthetic organisms are equipped with pigment-protein complexes called antennae, which harvest solar light with near-perfect quantum efficiency. These photosynthetic antennae contain three-dimensional arrays of densely packed chromophores embedded in the protein scaffold [12]. The light harvesting process begins with absorption of a photon by an antenna chromophore, followed by highly efficient transfer of excitation to the reaction

center. The reaction center is another pigment-protein complex that converts an excitation to a charge-separated state, which powers subsequent biochemistry of the organism.

The energy transfer process within photosynthetic antennae was originally considered to follow an incoherent mechanism described by Förster theory (FRET). However, this simple model cannot explain the quantum efficiency of the transfer process. Observations of long-lived quantum coherences in Fenna–Matthews–Olson (FMO) antenna from the green sulfur bacterium *Chlorobaculum tepidum* [13] and other photosynthetic complexes [14–16] with two-dimensional electronic spectroscopy have suggested that coherences between different excited states may play an important role in the energy transfer process of photosynthetic antennae. That is, excitations may migrate through a wave-like quantum mechanism [17–19] and improve the transport efficiency by sampling the rugged energy landscape and avoiding classical "trapping" in local minima. The biological significance of these observed coherences depends on their microscopic origins; purely vibrational coherences on the electronic ground state cannot impact the energy transfer while coherences between electronic excited states can. Unfortunately, the signal observed in two-dimensional electronic spectroscopy is the summed signal from all accessible pathways and these photosynthetic antenna studied to date always contain vibrational modes coincident with the energy difference between electronic excited states [20–24]. Both facts frustrate the assignment of these observed coherences. Recently, vibronic coupling has also been proposed as a possible mechanism for the generation and survival of these coherences [21, 25–28], which further complicates the assignment.

Therefore, systems that can dissect contributions from vibrational, electronic and vibronic pathways would be ideal to unveil the design principles and biological significance of these coherences. However, photosynthetic antennae are not such systems due to their complex structures. Proteins hold chromophores in fixed spatial relationships and finely tunes the excitation energy gaps of the individual chromophores [12, 29], posing difficulties on mutations to detune the electronic energy gap away from vibrational modes without losing structural integrity.

Synthetic model systems can be used instead to investigate the design principles for the quantum coherences observed in photosynthetic systems due to their rich chemical variability, in which electronic transitions of the chromophores can be easily tuned to match or deviate from certain vibrational modes. Through molecular design, synthetic model systems can also be used to examine the effects on the coherences of either electronic energy gap or rigid structural support between the two functionalities separately. While in photosynthetic complexes, these functionalities are provided simultaneously by proteins and are difficult to disentangle. Such studies are presented in Chapter 3. By creating a series of structurally flexible fluorescein dimers and employing single-walled carbon nanotube packing strategy, we decipher the aspects of molecular design for controlling the presence of vibronic coherences in artificial systems, which would be informative for further investigations on coherent energy transport and biomimetic artificial materials that could exploit coherent transport in photovoltaics. The synthetic molecular switch described in Chapter 4 failed to meet the design requirements for vibronic coherences. However, 2DES on both *vase* and *kite* conformations of this molecular switch demonstrate the effect of nonradiative relaxation on the overall FRET efficiency, providing general insight to understanding of FRET mechanism.

1.3 Promising light-harvesting and light-emitting materials: perovskites

Perovskites have a crystal unit cell defined by the formula ABX_3, in which a cation B and an anion X form an octahedron. These octahedra share vertices with their neighbors to generate three-dimensional $[BX_3]^-$ frameworks that are stabilized by another type of cation A. Recently, lead halide perovskites have emerged as the promising materials for the next generation of optoelectronics, ranging from photovoltaics to light-emitting applications. In particular, perovskites are attractive due to their device performances that are competitive with established commercial technologies, as well as their solution processability with low

cost [30].

The renaissance of perovskite materials as light absorber in photovoltaics started in 2009 when organic-inorganic perovskite $CH_3NH_3PbI_3$ was demonstrated as a photosensitizer in a dye-sensitized solar cell with 3.8% power conversion efficiency by Miyasaka *et al* [31]. Within five years, the power conversion efficiencies have skyrocketed to over 20% [6–8, 32] with the highest efficiency to date as 21% [33], superior to similar technologies that have matured over more than a decade yet still failed to reach the efficiencies presented by perovskite materials, such as organic photovoltaics [34]. These impressive performances of lead halide perovskites in photovoltaic applications stem from their fundamental optical and electronic properties, attracting extensive research attentions. Recent studies have suggested that perovskite microcrystalline thin films and bulk single crystals exhibit characteristics including large absorption coefficients [35], small exciton binding energies [36], efficient photogeneration of free carriers [37, 38], high charge carrier mobility [39, 40], and bimolecular charge recombination dynamics [41, 42]. This collection of photophysical properties is more akin to crystalline inorganic semiconductors instead of molecular crystals, which defines perovskites as a new class of semiconductors that may potentially rival the current photovoltaic technologies heavily based on silicon and GaAs [43]. Although there are numerous reports on the photophysical properties of perovskite materials, the issue of which type of photo-generated species (exciton, free carriers or polaron) exists in these organic-inorganic hybrid perovskites is still under debate. In these organic-inorganic hybrid perovskites, methylammonium cations may solvate the electrons within the perovskites and play a crucial role in their optoelectronic properties [44, 45]. Therefore, we attempted to answer this question by probing the photophysical dynamics of perovskite bulk single-domain single crystals with nanosecond transient absorption spectroscopy. We observed that free carriers and localized carriers coexist due to polaron formation in organic-inorganic hybrid perovskites. These experimental results and related theoretical calculations are included In Chapter 5.

As mentioned above in this section, applications of perovskite materials can also be ex-

tended to light-emitting devices. The development on perovskite light-emitting diodes and electrochemical cells has achieved internal quantum efficiencies over 15% with tunable emission spectra across the visible range [46–49]. While the small exciton binding energy of bulk perovskites enable spontaneously dissociation of excitons into free carriers, which is beneficial for solar cell devices, nonradiative recombination of these carriers could limit the light-emitting performance of perovskites [50]. Compared to bulk perovskites, nanostructured perovskites exhibit increased photoluminescence quantum yield due to quantum confinement. Despite some pioneering synthetic efforts devoted to perovskite nanocrystals [50–55], methods to obtain quantum-confined perovskite nanocrystals still require delicate experimental controls. Meanwhile, some fundamental properties of these nanocrystals, such as detailed electronic structures, are still unrevealed. We have developed a scalable ligand-mediated transport synthesis of organic-inorganic hybrid perovskite nanocrystals that operates at ambient conditions and produces quantum-confined nanocrystals with PL quantum yield up to 97%. This synthetic method is presented in Chapter 6. We have also performed femtosecond two-dimensional electronic spectroscopy along with nanosecond transient absorption spectroscopy on these nanocrystals for the purpose of providing valuable information that facilitates the depiction of their detailed electronic structure.

Perovskites serve as both promising opportunities for the next generation of optoelectronic devices and intriguing materials that bridge solution processabilities of molecular systems with some photophysical properties of inorganic semiconductors. Several future projects in which other members of the Engel Group may contribute to the perovskite community are included in Chapter 7.

1.4 Energy transfer dynamics

For multi-chromophoric systems such as natural photosynthetic complexes and artificial molecular systems, energy usually migrates from the location of photon absorption to other locations before the energy can be dissipated radiatively through fluorescence or nonra-

diatively through subsequent charge separation. The energy transfer mechanism varies for different systems, depending on the electronic coupling between chromophores, the strength of system-bath coupling as well as the presence of coherences during the energy transfer process. In this section, we discuss several energy transfer mechanisms that are crucial for understanding the experimental results in the succeeding chapters.

1.4.1 Förster resonant energy transfer

Förster resonant energy transfer mechanism (FRET) has been extensively applied to systems within the weak electronic coupling regime, describing the incoherent transfer of an electronic excitation from a donor chromophore to a nearby acceptor. This theoretical description of the energy transfer between a electronically coupled pair of chromophores is first raised by Perrin in 1932 and extended by Förster [56] in 1948. FRET assumes that the molecules in the condensed matter are weakly coupled and the Coulombic coupling between the chromophores can be described with point dipole-dipole approximation, following equation 3.7.3.

$$V = \frac{1}{\vec{R}^3}[\vec{\mu}_D \cdot \vec{\mu} - 3(\vec{\mu}_D \cdot \vec{R})(\vec{\mu}_A \cdot \vec{R})] \tag{1.1}$$

$\vec{\mu}_D$ and $\vec{\mu}_A$ are the transition dipoles of the donor and acceptor chromophores, and $\vec{R}$ is the intermolecular distance. This dipole-dipole coupling is weak at a large distance and the energy transfer rate is moderately slow, usually at nanosecond time scale. Hence, the donor chromophore is assumed to relax to thermal vibrational equilibrium and the coherences are often assumed to dephase completely before energy transfer can occur. FRET describes an incoherent energy transfer mechanism where excitation is initially localized on individual donor chromophore and migrates in a hopping manner to the acceptor. The excitation wave function involves the excited state of only one chromophore between the donor-acceptor pair and the other one is in the ground state [57]. The FRET rate can be calculated from Fermi's golden rule, as shown in equation 1.2.

$$k_{D\to A} = \frac{2\pi}{h}|\langle\psi_D^*\psi_A|V|\psi_D\psi_A^*\rangle|^2\delta(E_D - E_A) \tag{1.2}$$

The delta function in equation 1.2 implies that the electronic transitions of the donor and the accepter need to be identical to observe this energy transfer. In general, the probability of the donor and the acceptor to simultaneously locate at the same transition energy within their corresponding spectral width is quite small, resulting in slow energy transfer rate, which can also be dictated by the weak coupling between the chromophores.

FRET is remarkably suitable for systems with intermolecular distance greater than 1 nm and can interpret energy transfer within these systems in terms of experimental accessible parameters [58], spawning extensive researches in chemistry [59–67] and biology [59, 60, 68–81]. The simplified formulation for FRET rate can be described by equation 1.3

$$k_e = k_f(\frac{R_0}{R})^6 \tag{1.3}$$

k_e is the energy transfer rate from the donor to the acceptor. k_f is the donor fluorescence rate. R is the intermolecular distance. R_0 is the distance at which the energy transfer efficiency is 50%, which can be calculated from equation 1.4.

$$R_0^6 = 8.79 \times 10^{-5} J\kappa^2 n^{-4} \tag{1.4}$$

n is the refractive index of the medium and κ^2 is the orientation factor that results from the dipole-dipole coupling, as shown in equation 1.5.

$$\kappa^2 = (\cos(\alpha) - 3\cos(\beta_1)\cos(\beta_2))^2 \tag{1.5}$$

where α is the angle between the transition dipoles of the donor and acceptor, β_1 and β_2 are the angles between the intermolecular displacement vector and the dipole of the donor or acceptor, respectively. For systems in which both the donor and the acceptor can be assumed

to orient isotropically, κ^2 can be estimated as 2/3. For systems in which the donor/acceptor cannot rotate freely or cannot reorient reasonably fast compared to fluorescence [82], κ^2 will take a value between 0 and 4.

The parameter J in equation 1.4 is the spectral overlap integral of the donor fluorescence and the acceptor absorbance. This parameter reflects the energy conservation requested by the δ function in equation 1.2. J can be calculated as

$$J(\lambda) = \int \epsilon_A(\lambda)\lambda^4 F_D(\lambda)d\lambda \tag{1.6}$$

where λ is wavelength, ϵ_A is the extinction coefficient of the acceptor and F_D is the normalized donor emission spectrum. Both ϵ_A and F_D are wavelength-dependent.

The aforementioned experimentally accessible parameters and the steep R^{-6} distance dependence of FRET rate enable FRET to be used as a sensitive probe for the local environment of the chromophores. However, the stochastic diffusion-like hopping manner of the excitation described by FRET may lead to energy loss within each transition and low overall transfer quantum efficiency, especially for large multichromophoric systems. The excitation may be trapped at certain local minima and then dissipates through fluorescence of the donor or other nonradiative relaxations before transfer to the acceptor occurs. In Chapter 4, we will discuss the effect of nonradiative transition on the donor to the overall FRET efficiency in a molecular cavitand switch.

1.4.2 Redfield theory

For systems such as photosynthetic antenna complexes, in which the chromophores can be strongly coupled to each other and the interchromophore distance is comparable to the size of molecular dipoles, FRET cannot accurately describe the energy transfer process due to the break down of dipole approximation. For systems with strong electronic couplings between chromophores and weak coupling to a phonon bath, the energy transfer is described

by Redfield theory [83] with a density matrix treatment of the exciton relaxation between electronic delocalized states. Modified Redfield theory has also been developed by Mukamel and coworkers [84] and Fleming and coworkers [85] to describe systems with both strong electronic coupling and strong system-bath couplings.

In Redfield theory, excitonic states and their corresponding energies can be expressed with eigenvectors and eigenvalues obtained by diagonalization of the system Hamiltonian at site basis. The system-bath coupling depends on available vibrational modes of the bath and drives the energy transfer between these excitonic states. Spectral density describes the weighted density of bath modes coupled to local transitions of the chromophores. The strength of system-bath coupling is then given by Huang-Rhys factor, which is an integral over the spectral density. The energy transfer rate from one excitonic state to another can be calculated from the correlation function and the spectral overlap of the two excitonic states.

The detailed equations describing Redfield energy transfer rate are not listed in this section due to the fact that none of these equations are used for the specific experimental results in the succeeding chapters. However, understanding the energy transfer mechanisms for various systems with different coupling is useful in general for analyzing the ultrafast dynamics of these systems.

1.4.3 Quantum coherences and coherent energy transfer

The two mechanisms in section 1.4.1 and 1.4.2 describe energy transfer in an incoherent manner. The coherent nature of the excitation needs to be taken into account if the system still has the memory of its initially prepared states and the coherences do not dephase completely before energy transfer occurs.

The studies on coherent energy transfer are inspired by the observation of long-lived quantum coherences in Fenna–Matthews–Olson (FMO) antenna from the green sulfur bacterium *Chlorobaculum tepidum* [13] as well as other photosynthetic complexes [14–16] with two-dimensionally electronic spectroscopy. These coherences are observed to be at similar

timescales with the energy transfer processes, yet FRET failed to explain the near-perfect transfer quantum efficiencies of these photosynthetic complexes. Recent studies have suggested that the energy transfer may proceed through a wave-like quantum mechanism [17–19], in which the excitation can move among superpositions of excitons as a quantum mechanical wave packet keeping its phase coherence. Interferences among coherences may help enhance transport efficiency by sampling the rugged energy landscape and avoiding classical "trapping" in local minima.

However, in two-dimensional electronic spectroscopy, any non-degenerate pair of states can generate quantum-beating signals in the waiting time domain. The microscopic states involved in these coherences may be vibrations on the ground electronic state, vibrations on the excited electronic state, between electronic states or between vibronic states of mixed character (states of mixed vibrational-electronic character arising from non-Born-Oppenheimer coupling). The exact microscopic origins of these coherences are extremely crucial for understanding their roles in energy transport. Purely vibrational coherences that locate on states of a single chromophore are less likely to contribute to the overall energy transfer efficiencies. Whereas, coherences involving different electronic excited states (purely electronic coherences or vibronic coherences due to the non-adiabatic coupling on the excited state surfaces) are more likely to impact the energy transport because the energy can readily migrate from one site to another through wave-like motions.

There is a debate over the exact nature of the observed coherences in the photosynthetic complexes and over their biological significance to the energy transport [20–24] due to multiple vibrational modes associating with these complex that frustrate definitive assignments of their microscopic origin. In Chapter 3, I show a series of structurally flexible fluorescein dimers, both in dilute solution and packed on single-walled carbon nanotubes, that provide clear distinction between vibrational and vibronic coherences, and offer the control on the presence of vibronic coherences between electronic excited states. Hopefully, the work in Chapter 3 can serve as a platform for further studies on the coherent energy transfer in

artificial systems.

1.5 Theory of two-dimensional electronic spectroscopy

Ultrafast two-dimensional electronic spectroscopy (2DES) has provided opportunities for the investigation on the coherences mentioned in the previous section [15, 20, 86–89]. This technique is sensitive to the coupling between different states and has the temporal resolution to capture these coherences before they diphase. In this section, we discuss some theoretical aspects for 2DES that are important for interpreting the experimental results in the succeeding chapters. Much of the description below is based on the theoretical work provided by Mukamel in reference [90].

Spectroscopy measures the polarization response of a material with one or more radiation fields. This light-matter induced time-dependent macroscopic polarization equals to the expectation value of the dipole operator and can be written as trace over the dipole operator μ acting on the density matrix ρ. A perturbative expansion on this polarization with the order of light-matter interaction gives equation 1.7.

$$P(t) = Tr[\mu\rho(t)] = Tr[\mu\rho^{(0)}] + Tr[\mu\rho^{(1)}(t)] + Tr[\mu\rho^{(2)}(t)] + Tr[\mu\rho^{(3)}(t)] + ... \qquad (1.7)$$

Two-dimensional electronic spectroscopy is a third-order nonlinear spectroscopy probing the third-order polarization $P^{(3)}(t)$ of the system, which is the last term listed in equation 1.7. Note that $P^{(3)}(t)$ contains a third-order expansion of the density matrix that requires time-dependent evolution of the density operator for calculation. Similar to the dynamics of a wave function described by time-dependent Schrödinger equation, the time evolution of a density operator can be described by Liouville-Von Neumann equation, as shown in equation 1.8.

$$\frac{\partial \rho}{\partial t} = -\frac{i}{\hbar}[H(t), \rho(t)] \tag{1.8}$$

The time-dependent Hamiltonian can be separated to two components in the interaction picture shown in equation 1.9; a time-independent system Hamiltonian H_0 and a time-dependent perturbative interaction with radiation fields $H_{int}(t)$. $H_{int}(t)$ can be described using equation 1.10.

$$H(t) = H_0 + H_{int}(t) \tag{1.9}$$

$$H_{int}(t) = -\mu \cdot E(t) \tag{1.10}$$

Hence, the expression for $P^{(3)}(t)$ can be obtained by using equations 1.8, 1.9 and 1.10 together and can be written as equation 1.11.

$$P^{(3)}(t) = \int_0^\infty dt_3 \int_0^\infty dt_2 \int_0^\infty dt_1 R^{(3)}(t_3, t_2, t_1) E(t - t_3) E(t - t_3 - t_2) E(t - t_3 - t_2 - t_1) \tag{1.11}$$

t_1, t_2 and t_3 are the times of interaction with the radiation fields respectively. $R^{(3)}$ is the third-order response function of the system that contains the density matrix and dipole operator term, shown in the following equation 1.12.

$$R^{(3)}(t_3, t_2, t_1) = (\frac{i}{\hbar})^3 \theta(t_1)\theta(t_2)\theta(t_3) Tr\{[[[\mu(t_3 + t_2 + t_1), \mu(t_2 + t_1)], \mu(t_1)]\mu(0)]\rho_{gg}\} \tag{1.12}$$

$\theta(t_1)$, $\theta(t_2)$, $\theta(t_3)$ are Heaviside step functions for causality, ensuring no light-matter interaction happens before the corresponding radiation field. The commutators in Equation 1.12 indicate that four dipole operators will either on the *bra* or *ket* side of the density matrix element. Complete expansion of $R^{(3)}$ could be trivial and is not listed here for simplicity. Instead, double-sided Feynman diagrams are more often used as graphic representations of

these interactions in various pathways.

A representative double-sided Feynman diagram is shown in the left of Fig. 1.1 with a figure that help interpret this Feynman diagram attached on the right. In a Feynman diagram, the two vertical lines represent the *ket* and *bra* sides of the density operator. The arrows indicate interaction with radiation fields on the density operator. Arrows pointing toward the double vertical lines represent absorption, while arrows pointing away from the double vertical lines represent emission. Time progresses vertically upward. The interactions induce transitions in the density matrix that evolve with time, and the density matrix elements for each time segment are written in the double-sided diagram. The time delays between the transitions are coherence time (τ), waiting time (T) and rephasing times (t), shown in the right of Fig 1.1, which can be experimentally controlled by the apparatus described in Chapter 2. By convention, the system starts from ground state, and the final state must be a population state with the last arrow pointing outward. The last interaction is the emitting signal from the macroscopic polarization of the system induced by the first three interactions. Thus, the direction of the emitting signal can be dictated by the first three interactions due to conservation of momentum. In a Feynman diagram, the arrow pointing to the right associates with a positive wave vector, whereas the arrow pointing to the left associates with a negative wave vector. Signals from all of the pathways in equation 1.12 may end up in different directions. In our two-dimensional experiment, we selectively measure the signals in the $k_s = -k_1 + k_2 + k_3$ phase-matched direction.

The Feynman diagrams can be categorized into rephasing pathways and nonrephasing pathways. If the phase evolutions in the coherence time and the rephasing time are in opposite directions, the signal is defined as rephasing signal. Otherwise, the signal is defined as nonrephasing signal. Our 2DES experiment setup can measure signals from both the rephasing and nonrephasing pathways without varying signal detection position. The detailed experiment designs are described in Chapter 2.

For a system with three electronic states, ground state given by g, the first excited state

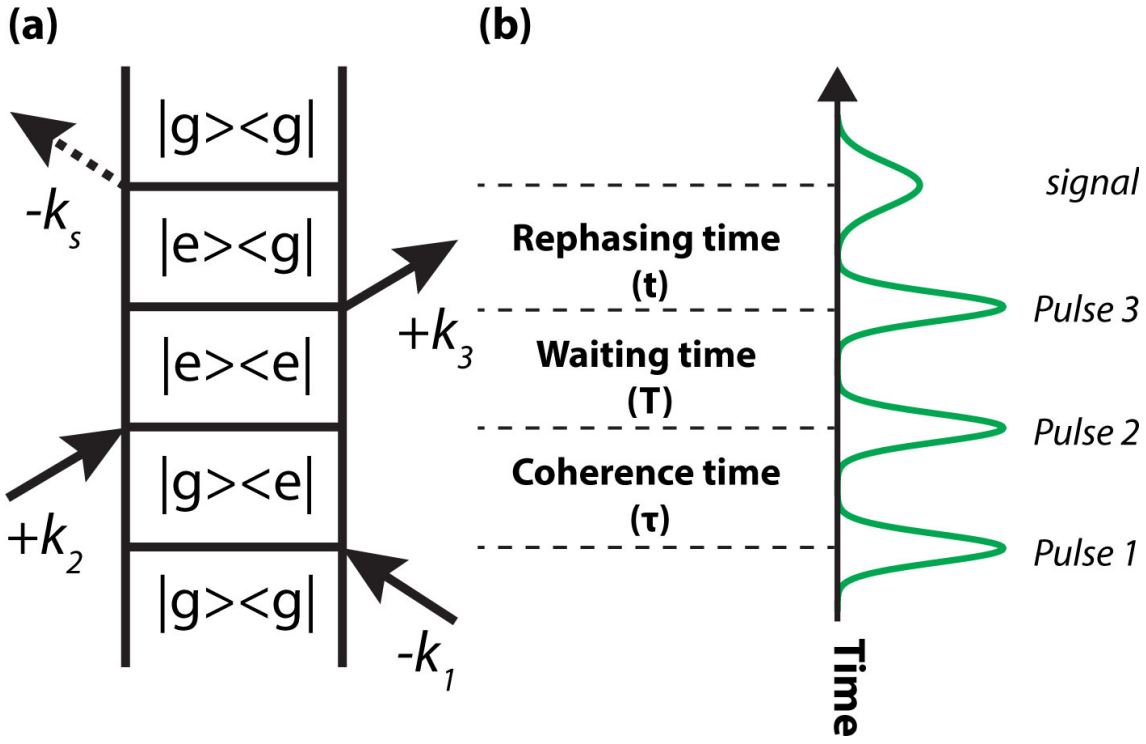

Figure 1.1: A representative Feynman diagram as a graphic representation of the interaction pathway in the third-order spectroscopy. (a) A representative Feynman diagram. The arrows represent interactions with radiation fields. The double-sided column represents the time evolution of the density operator with time progressing vertically upward. (b) Pulse sequences for interpreting the Feynman diagram. The time delay between the first two interactions is coherence time τ. The time delay between the second and the third interactions is waiting time T. The time delay between the third interaction and the emitting signal is rephasing time t.

given by e and the second excited state f, the Feynman diagrams that contribute to the signals in our detection direction are shown in Fig. 1.2

Signals from these Feynman diagrams can be further separated into ground state bleach, stimulated emission and excited state absorption. If the system is on the ground state surface during the waiting time, the signal is defined as ground state bleach. If the system is on the excited state surface during the waiting time and the third interaction represents emission, the signal is defined as stimulated emission. If the system is on the excited state surface during the waiting time but the third interaction represents absorption, the signal is then defined as excited state absorption. For a 2D spectrum plotted in the convention of transmitted light ΔT, ground state bleach and stimulate emission signals will appear as positive spectral features while the excited state absorption signals will appear as negative.

Feynman diagrams are especially useful for analyzing different spectral features and their corresponding waiting time dynamics in 2DES measurements. However, this type of the analysis could be rather complicated as the number of states involved increases (for example, multichromophoric systems with electronic and vibrational states considered). For a typical 2DES measurement, the coherence time and rephasing time are at tens to hundreds of femtosecond timescale but the waiting time can range from femtoseconds to hundreds of picoseconds. Therefore, pathways that represent energy transfer/relaxation dynamics during the waiting time need to be considered. For a two-chromophoric model system with ground electronic state g, excited electronic states e_B (higher in energy) and e_R (lower in energy), a Feynman diagram representing population transfer from e_B to e_R is shown in Fig 1.3.

In 2DES, it is also possible to observe beating signals during the waiting time due to excitation of superpositions of quantum states in the system [90] that oscillate at the frequency corresponding to the energy difference between these states. As mentioned in Section 1.4.3 of this chapter, the microscopic origins of these beating signals (coherences) could be purely vibrational, purely electronic or vibronic with mixed character arising from non-Born-Oppenheimer coupling. Here, we show representative Feynman diagrams for each type of

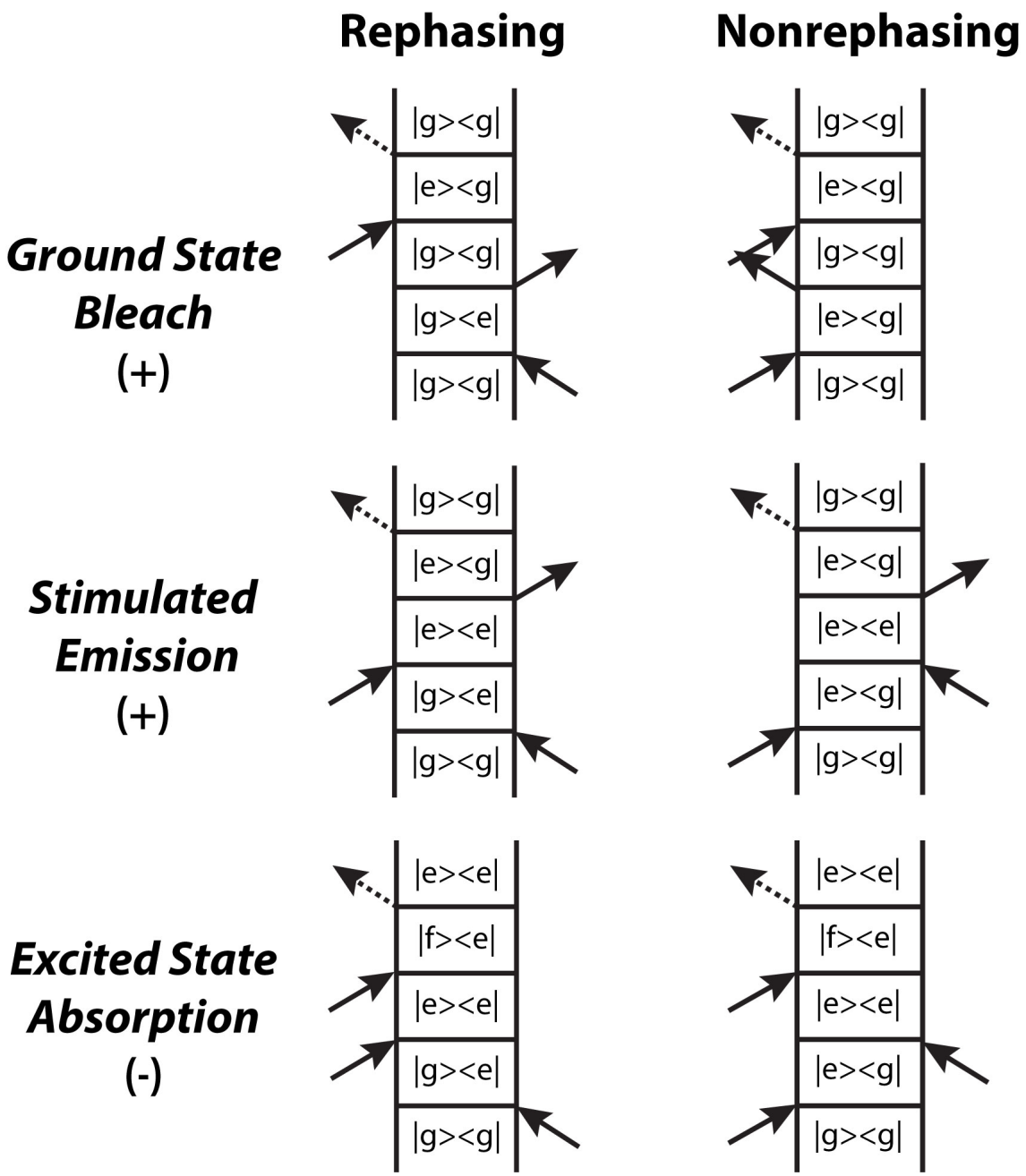

Figure 1.2: Feynman diagram in a certain detection direction for a system with three electronic states. Signals from these Feynman diagrams can be further separated into ground state bleach, excited emission and excited absorption. When plotting a 2D spectrum in the convention of transmitted light, ground state bleach and excited emission signals will show up as positive while the excited state absorption signals will show up as negative.

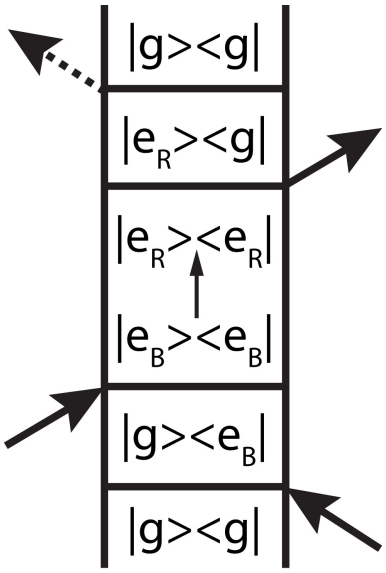

Figure 1.3: A Feynman diagram describing the energy transfer of a two-chromophoric model system with ground electronic state g and electronic excited states e_B and e_R during the waiting time.

these coherences using a two-chromophoric model system with vibrational modes on both ground- and excited-state surfaces as an example. These representative Feynman diagrams are listed in Fig. 1.4 and are drawn in the site basis not the exciton basis.

Purely vibrational coherences can be generated on both the ground- and the excited-state surface of a single chromophore. They have no knowledge of excitation on the other chromophore. Purely electronic coherences are due to excitation of superpositions between the two excited electronic states of the system and can exist with or without the presence of vibrational states on each of the chromophores. If, however, the vibrational state on the excited state surface of the chromophore with lower electronic transition happens to couple to the excited electronic state of the other chromophore, the third interaction can access both chromophores due to this non-adiabatic coupling. Therefore, a number of new pathways will be generated. These new pathways can be on the ground- or excited-state surface during waiting time but report on the vibronic coupling on the excited-state surfaces of the two chromophores, as shown in the last row of Fig. 1.4. These different pathways can give rise to beating signals at different spectral positions of the 2D spectra, as suggested by the color

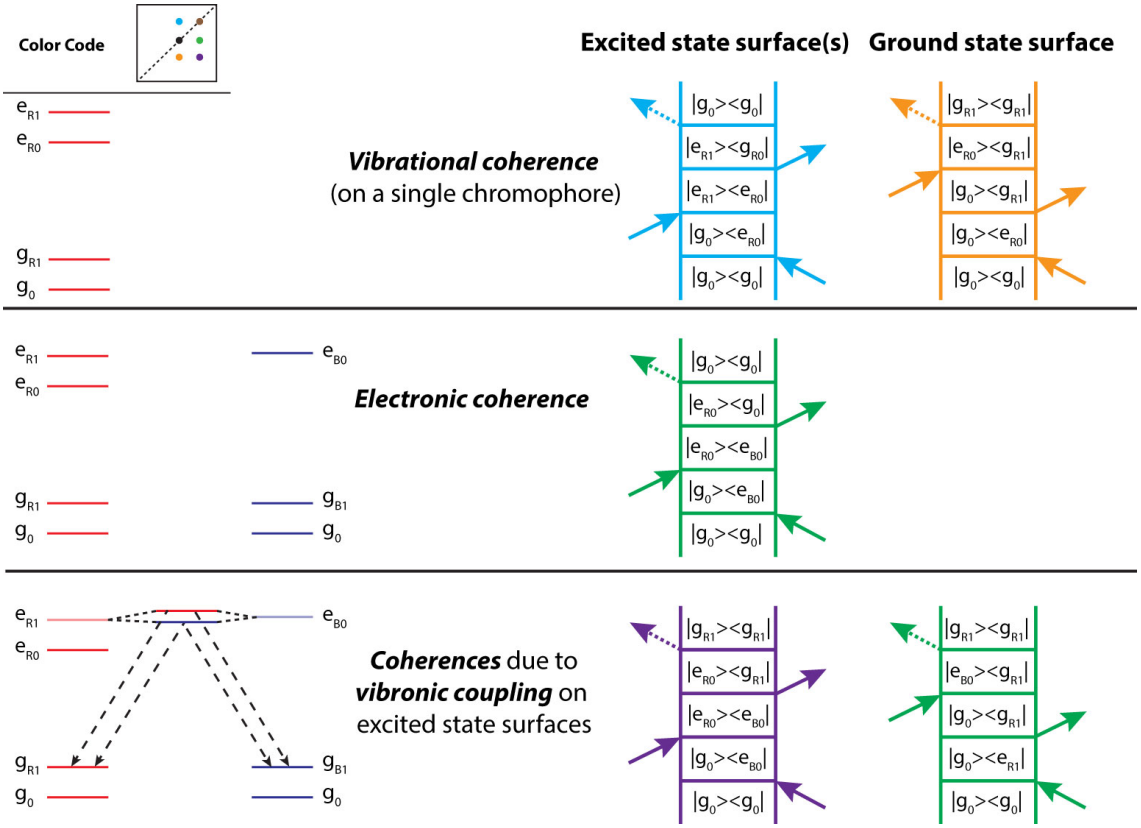

Figure 1.4: Feynman diagrams describing vibrational, electronic and vibronic coherences. The two-chromophoric model system with vibrational modes on both ground- and excited-state surfaces is used as an example. This figure is reproduced from Fig 3.55 in Chapter 3, showing only a few pathways as example.

code.

The spectral positions for coherences can be created as beating maps for detailed analysis of the coherences observed in 2DES measurements, as described in Chapter 3. Note that the signals from 2DES are always summed signals from various pathways. Therefore, detailed analysis and control experiments that differentiate signals from various pathways will be helpful for the assignment of 2D spectral features.

1.6 Outline of dissertation

The outline of this dissertation is as follows. Chapter 2 describes 2DES experimental details, including the optical layouts and data analysis methods applied in the following chapters. In Chapter 3, we create a series of structurally flexible fluorescein heterodimers and demonstrate that the presence of quantum beating signals (vibronic coherences) can be controlled by packing these heterodimers on single-walled carbon nanotubes. There are two prerequisites for observing the enhanced quantum beating signals: limiting the relative rotation of chromophores and tuning the electronic transition energy difference between the constituent monomers to match a vibrational mode on the lower energy monomer. Chapter 4 studies the effects of nonradiative relaxation on the FRET efficiencies by preforming 2D spectra of a molecular switch, which contains a pair of functionalized borondipyrromethine (BODIPY) dyes attached on the opposite arms of a resorcin[4]arene cavitand backbone and exhibits temperature-induced conformational switch between *vase* and *kite* forms. We observe significant changes of the nonradiative relaxation between the two conformations, suggesting that competing nonradiative processes must be taken into account when highly accurate measurements of FRET efficiency are desired. In Chapter 5, we move away from synthetic molecular systems and investigate the carrier dynamics of organo-halide perovskite bulk crystals with nanosecond transient absorption spectroscopy, observing coexistence of free carriers and localized carrier due to polaron formation. In Chapter 6, we develop the ligand-mediated transport synthesis of organic-inorganic hybrid perovskite nanocrystals under ambient con-

ditions and present some interesting ultrafast dynamics of these nanocrystals probed with 2DES. Finally, we discuss the future directions for more complex artificial systems such as heterotrimers and for perovskite materials as the form of colloidal nanocrystals, thin films and bulk crystals in Chapter 7.

REFERENCES

[1] IEA. Energy statistics 2015. *www.iea.org.*, 2015.

[2] Robert E. Blankenship, David M. Tiede, James Barber, Gary W. Brudvig, Graham Fleming, Maria Ghirardi, M. R. Gunner, Wolfgang Junge, David M. Kramer, Anastasios Melis, Thomas A. Moore, Christopher C. Moser, Daniel G. Nocera, Arthur J. Nozik, Donald R. Ort, William W. Parson, Roger C. Prince, and Richard T. Sayre. Comparing photosynthetic and photovoltaic efficiencies and recognizing the potential for improvement. *Science*, 332(6031):805, 2011.

[3] O. S. Ksenzhek. *Plant energetics*. Academic Press, San Diego, 1998.

[4] Jian Wang, Daniel C. Brune, and Robert E. Blankenship. Effects of oxidants and reductants on the efficiency of excitation transfer in green photosynthetic bacteria. *Biochimica et Biophysica Acta (BBA) - Bioenergetics*, 1015(3):457–463, 1990.

[5] R. J. van Dorssen, H. Vasmel, and J. Amesz. *Pigment organization and energy transfer in the green photosynthetic bacterium Chloroflexus aurantiacus*, pages 31–43. Springer Netherlands, Dordrecht, 1986.

[6] Huanping Zhou, Qi Chen, Gang Li, Song Luo, Tze-bing Song, Hsin-Sheng Duan, Ziruo Hong, Jingbi You, Yongsheng Liu, and Yang Yang. Interface engineering of highly efficient perovskite solar cells. *Science*, 345(6196):542, 2014.

[7] Woon Seok Yang, Jun Hong Noh, Nam Joong Jeon, Young Chan Kim, Seungchan Ryu, Jangwon Seo, and Sang Il Seok. High-performance photovoltaic perovskite layers fabricated through intramolecular exchange. *Science*, 348(6240):1234, 2015.

[8] Wanyi Nie, Hsinhan Tsai, Reza Asadpour, Jean-Christophe Blancon, Amanda J. Neukirch, Gautam Gupta, Jared J. Crochet, Manish Chhowalla, Sergei Tretiak, Muhammad A. Alam, Hsing-Lin Wang, and Aditya D. Mohite. High-efficiency solution-

processed perovskite solar cells with millimeter-scale grains. *Science*, 347(6221):522, 2015.

[9] Guichuan Xing, Nripan Mathews, Swee Sien Lim, Natalia Yantara, Xinfeng Liu, Dharani Sabba, Michael Grätzel, Subodh Mhaisalkar, and Tze Chien Sum. Low-temperature solution-processed wavelength-tunable perovskites for lasing. *Nat Mater*, 13(5):476–480, 2014.

[10] Haiming Zhu, Yongping Fu, Fei Meng, Xiaoxi Wu, Zizhou Gong, Qi Ding, Martin V. Gustafsson, M. Tuan Trinh, Song Jin, and X-Y. Zhu. Lead halide perovskite nanowire lasers with low lasing thresholds and high quality factors. *Nat Mater*, 14(6):636–642, 2015.

[11] Brandon R. Sutherland, Sjoerd Hoogland, Michael M. Adachi, Chris T. O. Wong, and Edward H. Sargent. Conformal organohalide perovskites enable lasing on spherical resonators. *ACS Nano*, 8(10):10947–10952, 2014.

[12] Robert E. Blankenship. Molecular mechanisms of photosynthesis, 2002.

[13] Gregory S. Engel, Tessa R. Calhoun, Elizabeth L. Read, Tae-Kyu Ahn, Tomas Mancal, Yuan-Chung Cheng, Robert E. Blankenship, and Graham R. Fleming. Evidence for wavelike energy transfer through quantum coherence in photosynthetic systems. *Nature*, 446(7137):782–786, 2007.

[14] Hohjai Lee, Yuan-Chung Cheng, and Graham R. Fleming. Coherence dynamics in photosynthesis: Protein protection of excitonic coherence. *Science*, 316(5830):1462, 2007.

[15] Elisabetta Collini, Cathy Y. Wong, Krystyna E. Wilk, Paul M. G. Curmi, Paul Brumer, and Gregory D. Scholes. Coherently wired light-harvesting in photosynthetic marine algae at ambient temperature. *Nature*, 463(7281):644–647, 2010.

[16] Gabriela S. Schlau-Cohen, Akihito Ishizaki, Tessa R. Calhoun, Naomi S. Ginsberg, Matteo Ballottari, Roberto Bassi, and Graham R. Fleming. Elucidation of the timescales and origins of quantum electronic coherence in lhcii. *Nat Chem*, 4(5):389–395, 2012.

[17] Masoud Mohseni, Patrick Rebentrost, Seth Lloyd, and Alán Aspuru-Guzik. Environment-assisted quantum walks in photosynthetic energy transfer. *The Journal of Chemical Physics*, 129(17):174106, 2008.

[18] Patrick Rebentrost, Masoud Mohseni, and Alán Aspuru-Guzik. Role of quantum coherence and environmental fluctuations in chromophoric energy transport. *The Journal of Physical Chemistry B*, 113(29):9942–9947, 2009.

[19] Gabriela S. Schlau-Cohen, Akihito Ishizaki, and Graham R. Fleming. Two-dimensional electronic spectroscopy and photosynthesis: Fundamentals and applications to photosynthetic light-harvesting. *Chemical Physics*, 386(1–3):1–22, 2011.

[20] Vivek Tiwari, William K. Peters, and David M. Jonas. Electronic resonance with anticorrelated pigment vibrations drives photosynthetic energy transfer outside the adiabatic framework. *Proceedings of the National Academy of Sciences*, 110(4):1203–1208, 2013.

[21] A. W. Chin, J. Prior, R. Rosenbach, F. Caycedo-Soler, S. F. Huelga, and M. B. Plenio. The role of non-equilibrium vibrational structures in electronic coherence and recoherence in pigment-protein complexes. *Nat Phys*, 9(2):113–118, 2013.

[22] N. Christensson, F. Milota, J. Hauer, J. Sperling, O. Bixner, A. Nemeth, and H. F. Kauffmann. High frequency vibrational modulations in two-dimensional electronic spectra and their resemblance to electronic coherence signatures. *The Journal of Physical Chemistry B*, 115(18):5383–5391, 2011.

[23] Daniel B. Turner, Krystyna E. Wilk, Paul M. G. Curmi, and Gregory D. Scholes. Comparison of electronic and vibrational coherence measured by two-dimensional electronic spectroscopy. *The Journal of Physical Chemistry Letters*, 2(15):1904–1911, 2011.

[24] Vytautas Butkus, Donatas Zigmantas, Leonas Valkunas, and Darius Abramavicius. Vibrational vs. electronic coherences in 2d spectrum of molecular systems. *Chemical Physics Letters*, 545:40–43, 2012.

[25] Franz Milota, Valentyn I. Prokhorenko, Tomas Mancal, Hans von Berlepsch, Oliver Bixner, Harald F. Kauffmann, and Jürgen Hauer. Vibronic and vibrational coherences in two-dimensional electronic spectra of supramolecular j-aggregates. *The Journal of Physical Chemistry A*, 117(29):6007–6014, 2013.

[26] A. W. Chin, S. F. Huelga, and M. B. Plenio. Coherence and decoherence in biological systems: principles of noise-assisted transport and the origin of long-lived coherences. *Philosophical Transactions of the Royal Society A: Mathematical, Physical and Engineering Sciences*, 370(1972):3638, 2012.

[27] Vivek Tiwari, William K. Peters, and David M. Jonas. Energy transfer: Vibronic coherence unveiled. *Nat Chem*, 6(3):173–175, 2014.

[28] Aurélia Chenu, Niklas Christensson, Harald F. Kauffmann, and Tomáš Mančal. Enhancement of vibronic and ground-state vibrational coherences in 2d spectra of photosynthetic complexes. *Scientific Reports*, 3:2029 EP –, 2013.

[29] Herbert van Amerongen. Photosynthetic excitons, 2000.

[30] Pablo Docampo and Thomas Bein. A long-term view on perovskite optoelectronics. *Accounts of Chemical Research*, 49(2):339–346, 2016.

[31] Akihiro Kojima, Kenjiro Teshima, Yasuo Shirai, and Tsutomu Miyasaka. Organometal halide perovskites as visible-light sensitizers for photovoltaic cells. *Journal of the American Chemical Society*, 131(17):6050–6051, 2009.

[32] Nam Joong Jeon, Jun Hong Noh, Woon Seok Yang, Young Chan Kim, Seungchan Ryu, Jangwon Seo, and Sang Il Seok. Compositional engineering of perovskite materials for high-performance solar cells. *Nature*, 517(7535):476–480, 2015.

[33] Dongqin Bi, Chenyi Yi, Jingshan Luo, Jean-David Décoppet, Fei Zhang, Shaik Mohammed Zakeeruddin, Xiong Li, Anders Hagfeldt, and Michael Grätzel. Polymer-templated nucleation and crystal growth of perovskite films for solar cells with efficiency greater than 21%. *Nature Energy*, 1:16142 EP –, 2016.

[34] Qianqian Lin, Ardalan Armin, Paul L. Burn, and Paul Meredith. Organohalide perovskites for solar energy conversion. *Accounts of Chemical Research*, 49(3):545–553, 2016.

[35] Martin A. Green, Anita Ho-Baillie, and Henry J. Snaith. The emergence of perovskite solar cells. *Nat Photon*, 8(7):506–514, 2014.

[36] Valerio D'Innocenzo, Giulia Grancini, Marcelo J. P. Alcocer, Ajay Ram Srimath Kandada, Samuel D. Stranks, Michael M. Lee, Guglielmo Lanzani, Henry J. Snaith, and Annamaria Petrozza. Excitons versus free charges in organo-lead tri-halide perovskites. *Nature Communications*, 5:3586 EP –, 2014.

[37] Arianna Marchioro, Joel Teuscher, Dennis Friedrich, Marinus Kunst, Roel van de Krol, Thomas Moehl, Michael Gratzel, and Jacques-E. Moser. Unravelling the mechanism of photoinduced charge transfer processes in lead iodide perovskite solar cells. *Nat Photon*, 8(3):250–255, 2014.

[38] Carlito S. Ponseca, Tom J. Savenije, Mohamed Abdellah, Kaibo Zheng, Arkady Yartsev, Tobjörn Pascher, Tobias Harlang, Pavel Chabera, Tonu Pullerits, Andrey Stepanov,

Jean-Pierre Wolf, and Villy Sundström. Organometal halide perovskite solar cell materials rationalized: Ultrafast charge generation, high and microsecond-long balanced mobilities, and slow recombination. *Journal of the American Chemical Society*, 136(14):5189–5192, 2014.

[39] Guichuan Xing, Nripan Mathews, Shuangyong Sun, Swee Sien Lim, Yeng Ming Lam, Michael Grätzel, Subodh Mhaisalkar, and Tze Chien Sum. Long-range balanced electron- and hole-transport lengths in organic-inorganic $CH_3NH_3PbI_3$. *Science*, 342(6156):344, 2013.

[40] Samuel D. Stranks, Giles E. Eperon, Giulia Grancini, Christopher Menelaou, Marcelo J. P. Alcocer, Tomas Leijtens, Laura M. Herz, Annamaria Petrozza, and Henry J. Snaith. Electron-hole diffusion lengths exceeding 1 micrometer in an organometal trihalide perovskite absorber. *Science*, 342(6156):341, 2013.

[41] Felix Deschler, Michael Price, Sandeep Pathak, Lina E. Klintberg, David-Dominik Jarausch, Ruben Higler, Sven Hüttner, Tomas Leijtens, Samuel D. Stranks, Henry J. Snaith, Mete Atatüre, Richard T. Phillips, and Richard H. Friend. High photoluminescence efficiency and optically pumped lasing in solution-processed mixed halide perovskite semiconductors. *The Journal of Physical Chemistry Letters*, 5(8):1421–1426, 2014.

[42] Joseph S. Manser and Prashant V. Kamat. Band filling with free charge carriers in organometal halide perovskites. *Nat Photon*, 8(9):737–743, 2014.

[43] Constantinos C. Stoumpos and Mercouri G. Kanatzidis. The renaissance of halide perovskites and their evolution as emerging semiconductors. *Accounts of Chemical Research*, 48(10):2791–2802, 2015.

[44] Haiming Zhu, Kiyoshi Miyata, Yongping Fu, Jue Wang, Prakriti P. Joshi, Daniel Niesner, Kristopher W. Williams, Song Jin, and X. Y. Zhu. Screening in crystalline liquids protects energetic carriers in hybrid perovskites. *Science*, 353(6306):1409, 2016.

[45] Jarvist M. Frost and Aron Walsh. What is moving in hybrid halide perovskite solar cells? *Accounts of Chemical Research*, 49(3):528–535, 2016.

[46] Zhi-Kuang Tan, Reza Saberi Moghaddam, May Ling Lai, Pablo Docampo, Ruben Higler, Felix Deschler, Michael Price, Aditya Sadhanala, Luis M. Pazos, Dan Credgington, Fabian Hanusch, Thomas Bein, Henry J. Snaith, and Richard H. Friend. Bright light-emitting diodes based on organometal halide perovskite. *Nat Nano*, 9(9):687–692, 2014.

[47] Jianpu Wang, Nana Wang, Yizheng Jin, Junjie Si, Zhi-Kuang Tan, Hui Du, Lu Cheng, Xingliang Dai, Sai Bai, Haiping He, Zhizhen Ye, May Ling Lai, Richard H. Friend, and Wei Huang. Interfacial control toward efficient and low-voltage perovskite light-emitting diodes. *Advanced Materials*, 27(14):2311–2316, 2015.

[48] Aditya Sadhanala, Shahab Ahmad, Baodan Zhao, Nadja Giesbrecht, Phoebe M. Pearce, Felix Deschler, Robert L. Z. Hoye, Karl C. Gödel, Thomas Bein, Pablo Docampo, Siân E. Dutton, Michael F. L. De Volder, and Richard H. Friend. Blue-green color tunable solution processable organolead chloride–bromide mixed halide perovskites for optoelectronic applications. *Nano Letters*, 15(9):6095–6101, 2015.

[49] Meltem F. Aygüler, Michael D. Weber, Bianka M. D. Puscher, Dana D. Medina, Pablo Docampo, and Rubén D. Costa. Light-emitting electrochemical cells based on hybrid lead halide perovskite nanoparticles. *The Journal of Physical Chemistry C*, 119(21):12047–12054, 2015.

[50] Jun Xing, Fei Yan, Yawen Zhao, Shi Chen, Huakang Yu, Qing Zhang, Rongguang Zeng, Hilmi Volkan Demir, Xiaowei Sun, Alfred Huan, and Qihua Xiong. High-efficiency light-

emitting diodes of organometal halide perovskite amorphous nanoparticles. *ACS Nano*, 10(7):6623–6630, 2016.

[51] Loredana Protesescu, Sergii Yakunin, Maryna I. Bodnarchuk, Franziska Krieg, Riccarda Caputo, Christopher H. Hendon, Ruo Xi Yang, Aron Walsh, and Maksym V. Kovalenko. Nanocrystals of cesium lead halide perovskites (cspbx3, x = cl, br, and i): Novel optoelectronic materials showing bright emission with wide color gamut. *Nano Letters*, 15(6):3692–3696, 2015.

[52] Sergii Yakunin, Loredana Protesescu, Franziska Krieg, Maryna I. Bodnarchuk, Georgian Nedelcu, Markus Humer, Gabriele De Luca, Manfred Fiebig, Wolfgang Heiss, and Maksym V. Kovalenko. Low-threshold amplified spontaneous emission and lasing from colloidal nanocrystals of caesium lead halide perovskites. *Nature Communications*, 6:8056 EP –, 2015.

[53] Luciana C. Schmidt, Antonio Pertegás, Soranyel González-Carrero, Olga Malinkiewicz, Said Agouram, Guillermo Mínguez Espallargas, Henk J. Bolink, Raquel E. Galian, and Julia Pérez-Prieto. Nontemplate synthesis of ch3nh3pbbr3 perovskite nanoparticles. *Journal of the American Chemical Society*, 136(3):850–853, 2014.

[54] Feng Zhang, Haizheng Zhong, Cheng Chen, Xian-gang Wu, Xiangmin Hu, Hailong Huang, Junbo Han, Bingsuo Zou, and Yuping Dong. Brightly luminescent and color-tunable colloidal $CH_3NH_3PbX_3$ (X = Br, I, Cl) quantum dots: Potential alternatives for display technology. *ACS Nano*, 9(4):4533–4542, 2015.

[55] Shibin Sun, Dan Yuan, Yuan Xu, Aifei Wang, and Zhengtao Deng. Ligand-mediated synthesis of shape-controlled cesium lead halide perovskite nanocrystals via reprecipitation process at room temperature. *ACS Nano*, 10(3):3648–3657, 2016.

[56] Th. Förster. Zwischenmolekulare energiewanderung und fluoreszenz. *Annalen der Physik*, 437(1-2):55–75, 1948.

[57] R. M. Clegg, M. Sener, and Govindjee. From förster resonance energy transfer to coherent resonance energy transfer and back. In *Optical Biopsy VII*, volume 7561, page 12, 2010.

[58] Robert M Clegg. Fluorescence resonance energy transfer. *Current Opinion in Biotechnology*, 6(1):103–110, 1995.

[59] Ben N. G. Giepmans, Stephen R. Adams, Mark H. Ellisman, and Roger Y. Tsien. The fluorescent toolbox for assessing protein location and function. *Science*, 312(5771):217, 2006.

[60] A Hillisch, M Lorenz, and S Diekmann. Recent advances in fret: distance determination in protein-dna complexes. *Current opinion in structural biology*, 11(2):201–207, 2001.

[61] David W. Piston and Gert-Jan Kremers. Fluorescent protein fret: the good, the bad and the ugly. *Trends in Biochemical Sciences*, 32(9):407–414, 2007.

[62] A. Paul Alivisatos, Weiwei Gu, and Carolyn Larabell. Quantum dots as cellular probes. *Annual Review of Biomedical Engineering*, 7(1):55–76, 2005.

[63] Xiaoqin Chi, Dengtong Huang, Zhenghuan Zhao, Zijian Zhou, Zhenyu Yin, and Jinhao Gao. Nanoprobes for in vitro diagnostics of cancer and infectious diseases. *Biomaterials*, 33(1):189–206, 2012.

[64] Aaron R. Clapp, Igor L. Medintz, and Hedi Mattoussi. Förster resonance energy transfer investigations using quantum-dot fluorophores. *ChemPhysChem*, 7(1):47–57, 2006.

[65] Philip D. Howes, Rona Chandrawati, and Molly M. Stevens. Colloidal nanoparticles as advanced biological sensors. *Science*, 346(6205), 2014.

[66] Kim E. Sapsford, Lorenzo Berti, and Igor L. Medintz. Materials for fluorescence resonance energy transfer analysis: Beyond traditional donor–acceptor combinations. *Angewandte Chemie International Edition*, 45(28):4562–4589, 2006.

[67] Lin Yuan, Weiying Lin, Kaibo Zheng, and Sasa Zhu. Fret-based small-molecule fluorescent probes: Rational design and bioimaging applications. *Accounts of Chemical Research*, 46(7):1462–1473, 07 2013.

[68] Philippe I. H. Bastiaens and Anthony Squire. Fluorescence lifetime imaging microscopy: spatial resolution of biochemical processes in the cell. *Trends in Cell Biology*, 9(2):48–52, 1999.

[69] Rajesh Babu Sekar and Ammasi Periasamy. Fluorescence resonance energy transfer (fret) microscopy imaging of live cell protein localizations. *The Journal of Cell Biology*, 160(5):629, 2003.

[70] Kevin Truong and Mitsuhiko Ikura. The use of fret imaging microscopy to detect protein–protein interactions and protein conformational changes in vivo. *Current Opinion in Structural Biology*, 11(5):573–578, 2001.

[71] Horst Wallrabe and Ammasi Periasamy. Imaging protein molecules using fret and flim microscopy. *Current Opinion in Biotechnology*, 16(1):19–27, 2005.

[72] W. BECKER. Fluorescence lifetime imaging –techniques and applications. *Journal of Microscopy*, 247(2):119–136, 2012.

[73] Elizabeth A Jares-Erijman and Thomas M Jovin. Fret imaging. *Nat Biotech*, 21(11):1387–1395, 2003.

[74] Elizabeth A Jares-Erijman and Thomas M Jovin. Imaging molecular interactions in living cells by fret microscopy. *Current Opinion in Chemical Biology*, 10(5):409–416, 2006.

[75] Cristobal G. dos Remedios and Pierre D. J. Moens. Fluorescence resonance energy transfer spectroscopy is a reliable "ruler" for measuring structural changes in proteins. *Journal of Structural Biology*, 115(2):175–185, 1995.

[76] Richard N. Day, Ammasi Periasamy, and Fred Schaufele. Fluorescence resonance energy transfer microscopy of localized protein interactions in the living cell nucleus. *Methods*, 25(1):4–18, 2001.

[77] Marc Tramier, Isabelle Gautier, Tristan Piolot, Sylvie Ravalet, Klaus Kemnitz, Jacques Coppey, Christiane Durieux, Vincent Mignotte, and Maïté Coppey-Moisan. Picosecond-hetero-fret microscopy to probe protein-protein interactions in live cells. *Biophysical Journal*, 83(6):3570–3577, 2002.

[78] Steven S. Vogel, Christopher Thaler, and Srinagesh V. Koushik. Fanciful fret. *Science's STKE*, 2006(331):re2, 2006.

[79] Vladimir V Didenko. Dna probes using fluorescence resonance energy transfer (fret): Designs and applications. *BioTechniques*, 31(5):1106–1121, 2001.

[80] Chun-Yang Zhang, Hsin-Chih Yeh, Marcos T. Kuroki, and Tza-Huei Wang. Single-quantum-dot-based dna nanosensor. *Nat Mater*, 4(11):826–831, 2005.

[81] Sohila Zadran, Steve Standley, Kaylee Wong, Erick Otiniano, Arash Amighi, and Michel Baudry. Fluorescence resonance energy transfer (fret)-based biosensors: visualizing cellular dynamics and bioenergetics. *Applied Microbiology and Biotechnology*, 96(4):895–902, 2012.

[82] A. P. Demchenko. Introduction to fluorescence sensing, 2015.

[83] A.G. Redfield. On the theroy of relaxation processes. *IBM Journal of Research and Development*, 1:19, 1957.

[84] Wei Min Zhang, Torsten Meier, Vladimir Chernyak, and Shaul Mukamel. Exciton-migration and three-pulse femtosecond optical spectroscopies of photosynthetic antenna complexes. *The Journal of Chemical Physics*, 108(18):7763–7774, 1998.

[85] Mino Yang and Graham R. Fleming. Influence of phonons on exciton transfer dynamics: comparison of the redfield, förster, and modified redfield equations. *Chemical Physics*, 282(1):163–180, 2002.

[86] Tobias Brixner, Jens Stenger, Harsha M. Vaswani, Minhaeng Cho, Robert E. Blankenship, and Graham R. Fleming. Two-dimensional spectroscopy of electronic couplings in photosynthesis. *Nature*, 434(7033):625–628, 2005.

[87] Minhaeng Cho, Harsha M. Vaswani, Tobias Brixner, Jens Stenger, and Graham R. Fleming. Exciton analysis in 2d electronic spectroscopy. *The Journal of Physical Chemistry B*, 109(21):10542–10556, 2005.

[88] M. L. Cowan, J. P. Ogilvie, and R. J. D. Miller. Two-dimensional spectroscopy using diffractive optics based phased-locked photon echoes. *Chemical Physics Letters*, 386(1–3):184–189, 2004.

[89] Tobias Brixner, Tomáš Mančal, Igor V. Stiopkin, and Graham R. Fleming. Phase-stabilized two-dimensional electronic spectroscopy. *The Journal of Chemical Physics*, 121(9):4221–4236, 2004.

[90] S. Mukamel. *Principles of nonlinear optical spectroscopy*. Oxford University Press, New York ; Oxford, 1995.

CHAPTER 2

OPTICAL APPARATUS AND DATA ANALYSIS METHODS

This chapter provides an overview of the spectroscopic techniques and data analysis for the experiments described in the succeeding chapters. The first section is a general description of the apparatus that are used in the experiments presented in this thesis. Particular details to a certain experiment are included in the corresponding chapters due to the unique propose of each experiment. The second section in this chapter describes the data acquisition and analysis methods.

2.1 Optical apparatus

Much of the discussion on the transient absorption spectroscopy in this section is based on the work presented by Dahlberg [1]. Much of the discussion on the two-dimensional electronic spectroscopy in this section is based on the worked presented by Brixner *et al* [2] and Cowan *et al* [3]. The specific designs of the two-dimensional electronic spectrometer are given by Fransted *et al* [4] and Zheng *et al* [5] that are located in the Franck Lab and Redfield Lab of the Engel Group, respectively.

2.1.1 Nanosecond transient absorption apparatus

The nanosecond transient absorption apparatus is built by Dahlberg *et al* [1] and locates at Argonne National Lab. This apparatus can probe dynamics ranging from nanosecond to microsecond timescales. These timescales are relevant to various interesting dynamics, including singlet and triplet exciton recombination in molecular systems [6], and electron-hole and Auger recombination in bulk semiconductor [7, 8].

Two different laser sources are used to generate the pump and the probe beams, respectively, both of which then interact with the sample. A narrow band picosecond Nd:YAG laser (Ekspla Pl2210) is tripled and then pumps an OPO (Ekspla PG403) to produce ~ 50

ps pulses as the pump beam with the wavelength tunable throughout the visible spectrum range. The probe beam is generated by a broadband super-continuum fiber laser (Leukos STM) with spectrum from 350 to 800 nm and a pulse duration of $\sim$ 700 ps. Time delays were achieved using a delay generator (SRS DG535) externally synchronized to a 1 kHz master clock from the pump laser. The repetition rate for the pump is set to be 500 Hz, a half of the repetition rate of the probe laser (1 kHz). The transmitted signal was spectrally resolved via a spectrometer (Acton Research Corporation Spectra Pro 2150i) and recorded with a line scan camera (Teledyne Dalsa Spyder3 1k) at 1 kHz. The signal difference between the frame with only the probe beam and the frame with both the pump and the probe beam will yield a transient absorption spectrum at a certain waiting time. Due to the 1 kHz repetition, dynamics that exceeds 1 ms will appear at negative times and may complicate the analysis on the nanosecond dynamics. Laser repetition rates need to be decreased to probe the dynamics of such long-lived species.

2.1.2 Ultrafast transient absorption apparatus

The ultrafast transient absorption apparatus was designed to take spectra for the purpose of phase correction in the 2DES measurements [9–11]. Therefore, the laser sources of this apparatus are the same as the 2DES apparatus for a certain experiment. The entire setup is constructed on a breadboard for the purpose of convenient transitions between different two-dimensional electronic spectrometers within the Engel Group. The input beam is separated into two beams by a beam splitter, yielding the pump and the probe beams with identical spectrum. A compensating glass is also placed in the beam path to guarantee equal compression for the two beams. Different from the nanosecond transient absorption apparatus described in section 2.1.1, time delay between the pump and probe pulses here are controlled by a motorized translational stage (Aerotech) that adjusts the path-length of the pump to the sample position. The repetition rates are 5 kHz for the probe, which is synchronized to the regenerative amplifier of the 2DES apparatus and 2.5 kHz for the pump,

which is modulated by a chopper. The pump and the probe beams overlap at the sample position, generating a third-order signal that co-propagates with the probe beam. Scatter propagating in other directions are physically blocked by a series of irises. The signal is then spectrally resolved and recorded on a CCD camera.

2.1.3 Ultrafast two-dimensional electronic spectroscopy apparatus

The light source for the 2D electronic spectrometer is a Ti:Sapphire regenerative amplifier (Legend Elite, Coherent) that is seeded with the output of a self-mode locking Ti:Sapphire oscillator (Micra, Coherent). A diode-pumped Nd:YAG continuous wave laser is doubled and then used to pump the oscillator. Mode-locked oscillator gives pulses centered at 800 nm with a bandwidth of 60 - 80 nm (full width at half maximum, FWHM) and an average power of about 500 mW. A stretcher grating temporally chirps these pulses to duration of hundreds of picosecond. These pulses are then used to seed the regenerative amplifier cavity, which contains a Ti:Sapphire crystals that is pumped with a doubled diode-pumped Nd:YLF laser at an average power of 30 W. Two Pockels cells and a quarter waveplate are used in combination as polarization controls to trap or eject pulses in the amplifier. The number of the seed pulses inside the cavity is extremely sensitive for later white light generation. The seed pulses usually plateau at 15 round trips through the crystal and are ejected afterwards. The ejected pulses are then compressed by another grating to give pulses at $\sim$ 35 fs duration with an average power of 2.75 W and a bandwidth of 35 nm (FWHM) centered at around 800 nm.

The aforementioned specifics are from the oscillator and the amplifier in the Redfield Lab of the Engel Group and are used for broadband white light generation. The oscillator and the amplifier in the Franck Lab of the Engel Group are intentionally tuned to have narrower bandwidth for the noncollinear optical parametric amplifier (NOPA, Light Conversion TOPAS White), which requires 100 fs pulses as the seed pulses. Therefore, in the Franck Lab, the output of the oscillator is about 40 nm (FWHM). A pair of postal holder is

placed before the stretcher grating to physically limit the bandwidth of the seed pulses for the amplifier. The regenerative amplifier then gives 100 fs pulses centered at 805 nm with a bandwidth of 10 nm (FWHM) at a repetition rate of 5 kHz and with an average power of 2.2 W.

For the 2D spectrometer in the Franck Lab, the output from the regenerative amplifier seeds the NOPA, which can generate pulses with spectrum tunable from 520 to 700 nm (as the blue edge and the red edge). The bandwidth of the NOPA output is usually about 60 nm (FWHM). Multiphoton intrapulse interference phase scan method (MIIPS) [12] and a spatial light modulator (Biophotonic Solutions) are used to correct for dispersion. The design of the 2D spectrometer in the Franck Lab is based on phase-stabilized, heterodyne-detected, non-collinear femtosecond four-wave mixing demonstrated by Brixner *et al* [2]. The beam is split into two beams by a 50/50 beam splitter. The heights of the two beams are vertically offset by bouncing off different retroreflectors mounted on translation stages, which also introduce a time delay (population time T) due to the path length difference. These beams are then focused onto a transmissive grating by a spherical mirror. A physical mask is placed after the diffractive optic to block beams other than the first order diffractions, yielding four beams arranged in a boxcar geometry after the mask. The coherence time delay (between Beams 1 and 2) is controlled by propagating these two beams through different pairs of one-degree fused silica wedges mounted on separate computer-controlled transitional stages. This approach ensures attosecond accuracy of the timing without changing the pointing directions of the two beams. Another beam (Beam 4, as the local oscillator) is attenuated by three orders of magnitude to avoid contamination on the third-order response of the sample. A compensating glass for Beam 3 is also carefully adjusted in the beam path to ensure the same compression with Beams 1 and 2. A spherical mirror then focuses the four beams onto the sample, generating a third-order signal that co-propagates with the local oscillator and is then recorded by a back-illuminated CCD camera (Andor Newton). Scatter propagating in other directions are physically blocked by sets of irises before reaching the camera.

For the 2D spectrometer in the Redfield Lab, the output from the regenerative amplifier was directed to a tube filled with argon gas (length: 2 m, pressure: 15 psi) to generate broadband white light. The 2D spectrometer in the Redfield Lab is designed differently due to the broad bandwidth of the pulses [5]. Here, we only mention the important difference from the apparatus in the Franck Lab. The beam is split into four beams with a set of two beam splitters instead of diffractive optics to avoid color dispersion. The coherence time delay is controlled by bouncing off the beams on reflective optics mounted onto angled translational stages instead of passing through pairs of glass wedges. This all reflective geometry delay stage design is similar to the four quadrant mirror design demonstrated by Zhang *et al* [13]. A 15-degree off-axis parabolic silver mirror focuses the four beams to a 100 μ diameter spot on the sample. The signal and LO are re-collimated by another 15 degree off-axis parabolic mirror and directed to the camera. Note that no gold mirrors should be used in this broadband 2D apparatus due to its steep cut off for the spectrum bluer than 550 nm.

2.2 Data acquisition and analysis

The data acquisition for transient absorption is straightforward. The scatter subtraction in the ultrafast transient absorption is similar to the data analysis for 2D electronic spectra. Therefore, we focus on the data acquisition and analysis for 2DES in this section.

2.2.1 2DES Data acquisition

2DES measurements are based on precise control and determination of the relative time delays between the beams. Therefore, accurate calibration of the delay stage is necessary before any 2DES experiments.

Delay stages can be calibrated using spectral interferometry described by Lepetit *et al* [14]. For the calibration of coherence time delay stages, we typically place a scatter

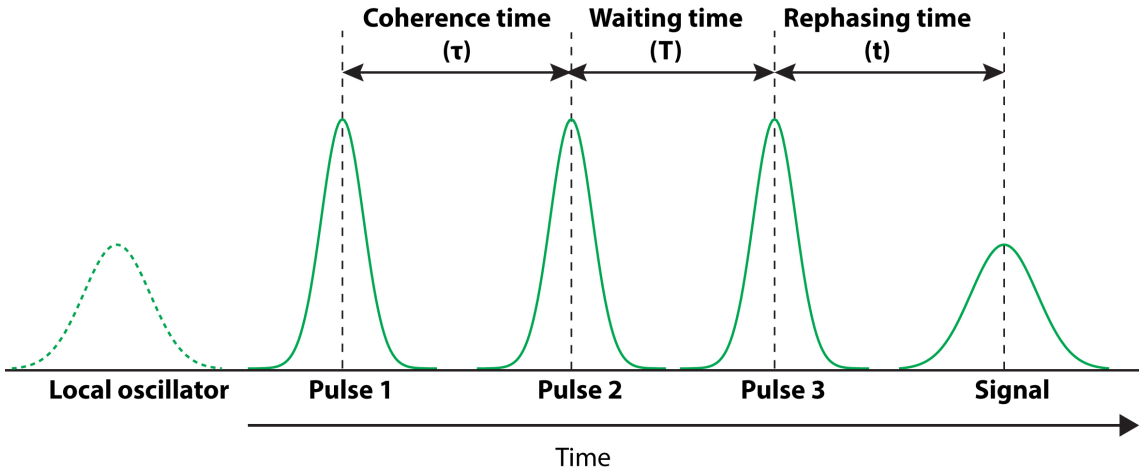

Figure 2.1: The pulse sequence for two-dimensional electronic spectroscopy. The local oscillator passes through the sample first. The time delay between pulses 1 and 2 is the coherence time τ. For negative coherence times, pulse 2 interacts with the sample before pulse 1. The time delay between the second pulse and pulse 3 is the waiting time T. The third-order signal is emitted after rephasing time t.

media (a thin glass slide with finger prints on) at the sample position. We then direct the local oscillator to the camera to obtain the interferogram between the local oscillator and scatter from the beam that needs calibration (Beam 1 or Beam 2). The counts of the local oscillator and the scatter need to be carefully balanced to afford nice interferograms with deep modulations. The delay stage can then be scanned from -600 to 100 fs with a stepsize of 0.4 fs. Fourier transforms of the series of interferograms yield the pulse timing between the beam and the LO. The slope of this timing relative to the translational distance of the stage gives the calibration constant. The delay stages also need to be recalibrated when the pulse bandwidth or the alignment changes.

The precise timing of each beam (Beams 1, 2 and 3) is adjusted by performing TG-FROG and measuring the non-resonant response of a blank solvent at the sample position [15]. The timing between Beam 3 and LO is set around 1 ps, with LO passing through the sample first to facilitate windowing in the rephasing time domain in the later data analysis while still providing resolvable fringes for the interferogram recorded on the camera. The pulse sequence for two-dimensional electronic spectroscopy is shown in Fig. 2.1.

2D spectra are usually acquired at a series of waiting times. At each waiting time, a 2D spectrum is obtained by evenly scanning the coherence time from the positive (rephasing) to the negative (nonrephasing) times to capture the signal until it completely decays. The signals at each coherence time is heterodyne-detected with the LO and spectrally resolved on the camera. Control frames with Beam 3 blocked at each coherence time record the scatter from Beams 1 and 2 in the detection direction. A control frame with the presence of Beam 3 and LO gives the scatter from Beam 3 while a control frame with LO only gives the beam profile of the oscillator. These control frames are used for the scatter subtraction in the later data analysis.

2.2.2 2DES Data analysis

The raw 2D data at each waiting time can be constructed as a 2D plot of signal wavelength *vs* coherence time via subtraction of the control frames [2], following equation 2.1 .

$$E_4^* E_{sig} = I_{1234} - I_{124} - I_{34} + I_4 \tag{2.1}$$

The raw 2D data can then be corrected by the beam profile of the local oscillator. The raw 2D data is linearly dispersed with wavelength. Fourier interpolation along rephasing wavelength dimension enables the signal to be linearly dispersed with frequency (energy). Then, Fourier transform over the rephasing frequency domain can yield a 2D rephasing time *vs* coherence time plot. The homodyne signals and residual scatter from other beams can be removed in the rephasing time domain via applying a window function to the signal. Fourier transforms over both dimensions of the windowed time-time plot give a 2D spectrum in frequency-frequency domain. Illustrative figures for each step of the 2DES data analysis is shown in Fig 2.2.

The phase of the 2D signals can be recovered by phasing the 2D spectra to transient absorption signals. According to the projection slice theorem, the real part of a phased

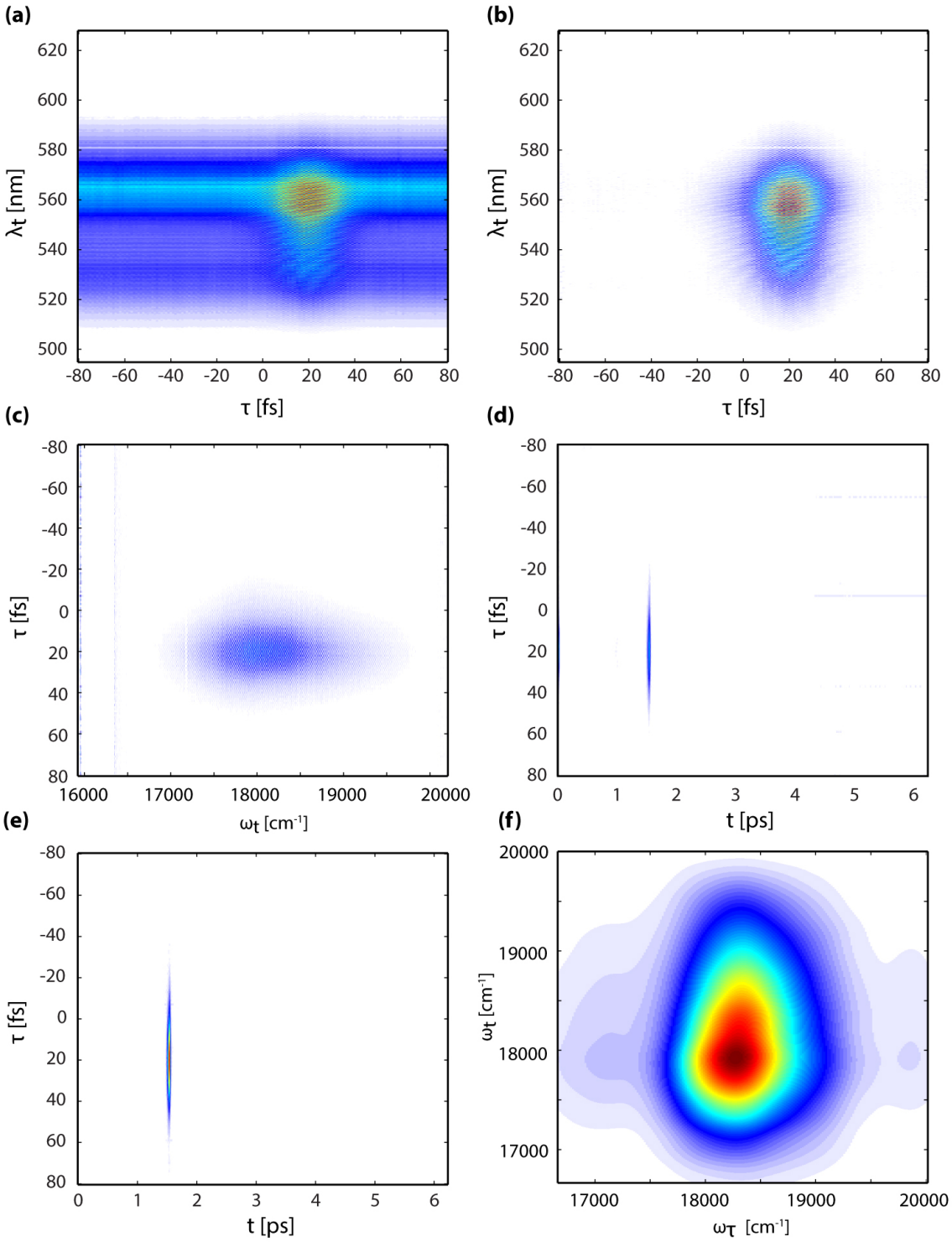

Figure 2.2: Illustrative figures for 2DES data analysis. The data shown corresponds to the 2D signal of fluorescein monomer M3 described in Chapter 3 at T=1000 fs and room temperature. (a) Raw signals recorded on the camera. (b) Signals after scatter subtraction. (c) Signals after Fourier interpolation. (d) 2D time-time plot. (e) 2D time-time plot with the applied window function. (f) 2D spectrum in frequency-frequency domain

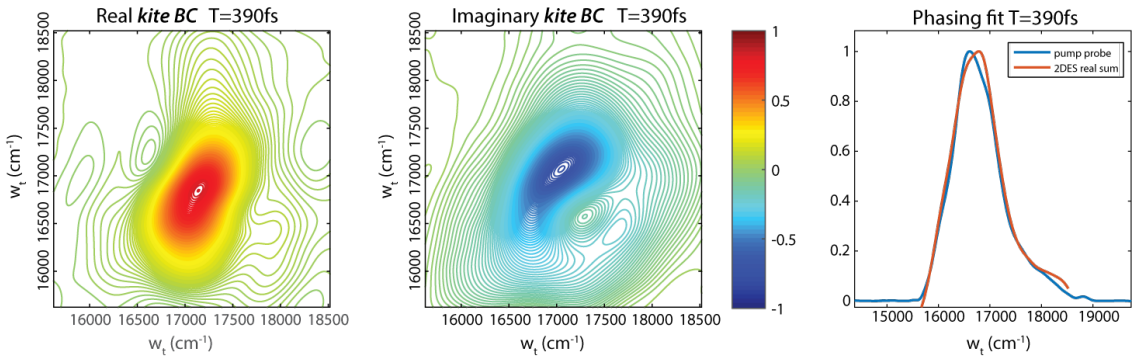

Figure 2.3: Representative phased data. The data shown here corresponds to the 2D signal of cavitand *kite* conformation described in Chapter 4 at T= 390 fs. (a) The real component of a phased 2D spectrum (Absorptive spectrum). (b) The imaginary component of a phased 2D spectrum (Dispersive spectrum). (c) Comparison between the transient absorption spectrum and the real part of the phased 2D spectrum projected along the coherence frequency dimension

2D spectrum projected along the coherence frequency dimension should match a symmetric transient absorption spectra acquired with the same pulses (both spectrum and compression) at the same waiting time. We obtain such transient absorption spectra for each waiting time using the apparatus described in Section 2.1.2 of this chapter. We then fit the 2D spectra with a phase correction term to the transient absorption spectra following equations 2.2 and 2.3, same as described in the literature [10, 11].

$$S_{2D}^{phased} = \alpha_1 S_{2D} e^{i[\alpha_2+\alpha_3(\omega_t-\omega_{t,0})+\alpha_4(\omega_t-\omega_{t,0})^2+\alpha_5(\omega_\tau-\omega_{\tau,0})+\alpha_6(\omega_\tau-\omega_{\tau,0})^2]} \tag{2.2}$$

$$S_{transient} = \int \Re[S_{2d}^{phased}] d\omega_\tau \tag{2.3}$$

After phasing, the real (absorptive) and imaginary (dispersive) components of the 2D signals can be separated. The same phase correction term is applied to the entire 2D data set to avoid possible phasing artifacts introduced to the waiting time dynamics. Representative spectra of the real and the imaginary components of a phased 2D data, as well as the fitting results compared to the transient absorption signal, is shown in Fig. 2.3

REFERENCES

[1] Peter D. Dahlberg. Energy transfer events in photosynthesis observed in vivo using nonlinear ultrafast spectroscopies. *ProQuest Dissertations and Theses, The University of Chicago*, 2016.

[2] Tobias Brixner, Tomáš Mančal, Igor V. Stiopkin, and Graham R. Fleming. Phase-stabilized two-dimensional electronic spectroscopy. *The Journal of Chemical Physics*, 121(9):4221–4236, 2004.

[3] M. L. Cowan, J. P. Ogilvie, and R. J. D. Miller. Two-dimensional spectroscopy using diffractive optics based phased-locked photon echoes. *Chemical Physics Letters*, 386(1–3):184–189, 3 2004.

[4] Kelly Fransted. Probing the origins of quantum beating signatures in two-dimensional spectroscopy. *ProQuest Dissertations and Theses, The University of Chicago*, 2012.

[5] Haibin Zheng, Justin R. Caram, Peter D. Dahlberg, Brian S. Rolczynski, Subha Viswanathan, Dmitriy S. Dolzhnikov, Amir Khadivi, Dmitri V. Talapin, and Gregory S. Engel. Dispersion-free continuum two-dimensional electronic spectrometer. *Applied Optics*, 53(9):1909–1917, 2014.

[6] Joseph R. Lakowicz. Principles of fluorescence spectroscopy, 1983.

[7] Qingfeng Dong, Yanjun Fang, Yuchuan Shao, Padhraic Mulligan, Jie Qiu, Lei Cao, and Jinsong Huang. Electron-hole diffusion lengths >175 m in solution-grown $CH_3NH_3PbI_3$ single crystals. *Science*, 347(6225):967, 02 2015.

[8] Dong Shi, Valerio Adinolfi, Riccardo Comin, Mingjian Yuan, Erkki Alarousu, Andrei Buin, Yin Chen, Sjoerd Hoogland, Alexander Rothenberger, Khabiboulakh Katsiev, Yaroslav Losovyj, Xin Zhang, Peter A. Dowben, Omar F. Mohammed, Edward H.

Sargent, and Osman M. Bakr. Low trap-state density and long carrier diffusion in organolead trihalide perovskite single crystals. *Science*, 347(6221):519, 01 2015.

[9] V. P. Singh, A. F. Fidler, B. S. Rolczynski, and G. S. Engel. Independent phasing of rephasing and non-rephasing 2d electronic spectra. *The Journal of Chemical Physics*, 139(8):084201, 2013.

[10] Moira L. Flanagan, Phillip D. Long, Peter D. Dahlberg, Brian S. Rolczynski, Sara C. Massey, and Gregory S. Engel. Mutations to r. sphaeroides reaction center perturb energy levels and vibronic coupling but not observed energy transfer rates. *The Journal of Physical Chemistry A*, 120(9):1479–1487, 03 2016.

[11] Justin R. Caram, Haibin Zheng, Peter D. Dahlberg, Brian S. Rolczynski, Graham B. Griffin, Dmitriy S. Dolzhnikov, Dmitri V. Talapin, and Gregory S. Engel. Exploring size and state dynamics in cdse quantum dots using two-dimensional electronic spectroscopy. *The Journal of Chemical Physics*, 140(8):084701, 2014.

[12] Vadim V. Lozovoy, Igor Pastirk, and Marcos Dantus. Multiphoton intrapulse interference. iv. ultrashort laser pulse spectral phase characterization and compensation. *Optics Letters*, 29(7):775–777, 2004.

[13] Yizhu Zhang, Kristina Meyer, Christian Ott, and Thomas Pfeifer. Passively phase-stable, monolithic, all-reflective two-dimensional electronic spectroscopy based on a four-quadrant mirror. *Optics Letters*, 38(3):356–358, 2013.

[14] L. Lepetit, G. Chériaux, and M. Joffre. Linear techniques of phase measurement by femtosecond spectral interferometry for applications in spectroscopy. *Journal of the Optical Society of America B*, 12(12):2467–2474, 1995.

[15] R. Trebino. Frequency-resolved optical gating : the measurement of ultrashort laser pulses, 2000.

CHAPTER 3

CONTROLLING QUANTUM-BEATING SIGNALS IN 2D ELECTRONIC SPECTRA BY PACKING SYNTHETIC HETERODIMERS ON SINGLE-WALLED CARBON NANOTUBES

In multidimensional spectroscopy, dynamics of coherences between excited states report on the interactions between electronic states and their environment. The prolonged coherence lifetimes observed in some systems may result from electronic-vibrational (vibronic) coupling between nearly degenerate states, and recent observations confirm the existence of vibronic coupling in both model systems and photosynthetic complexes. While understanding the origin of beating signals in photosynthetic complexes has been given considerable attention, strategies to generate beating signals in artificial systems that would allow us to test the hypotheses in detail are still lacking. In this chapter, we demonstrate that the presence of quantum beating signals can be controlled by packing a series of structurally flexible synthetic heterodimers on single-walled carbon nanotubes (SWNTs), thereby restricting the motions of chromophores. Using two-dimensional electronic spectroscopy (2DES), we find that both limiting the relative rotation of chromophores and tuning the energy difference between the two electronic transitions in the dimer to match a vibrational mode of the lower energy monomer are necessary to enhance the observed quantum beating signals.

The research described in this Chapter has been published in: L. Wang, G.B. Griffin, A. Zhang, F. Zhai, N.E. Williams, R.F. Jordan, and G.S. Engel. Controlling quantum-beating signals in 2D electronic spectra by packing synthetic heterodimers on single-walled carbon nanotubes. *Nat Chem* 9, 219–225 2017.

3.1 The debate over the observed quantum coherences in biological and artificial systems

Ultrafast two-dimensional electronic spectroscopy has afforded opportunities for detailed studies of energy transfer pathways and coupling between chromophores [1–6]. Using this femtosecond spectroscopy, we observe oscillations appearing in the spectra upon excitation of superpositions of quantum states in the system [7].Any nondegenerate pair of states can generate such oscillating signals; the microscopic states involved in these oscillating signals may be vibrational, electronic, or vibronic (states of mixed vibrational-electronic character arising from non-Born-Oppenheimer coupling). Coherences observed in the 2DES data persist longer than the measured dephasing time between the ground state and the excited state in several photosynthetic complexes [3, 8–10]as well as artificial systems, including synthetic small molecules [11, 12], polymers [13], and J-aggregates [14]. Despite the generality of these prolonged coherences, assignment of their microscopic origin is still in question. These coherences were originally assigned as purely electronic [15]. However, the systems studied to date have vibrational modes coincident with the energy differences between the electronic transitions of the constituent chromophores, frustrating the assignment of the observed signals [2, 16–19]. Recently, vibronic coupling has been proposed as a possible mechanism for the generation and survival of these coherences [14, 16, 20–22]. Coupling between the electronic excited state and an underdamped vibrational mode can enhance the lifetime of observed coherences [23]. Theoretical models for this coupling have approached this problem in different ways but rely on the same underlying physics: some express the electrodynamic coupling between chromophores using localized modes [22], while others invoke delocalized modes similar to those used to describe non-adiabatic effects near conical intersections [2, 24].

3.2 Molecular design and rationale

We vary the electronic transitions of a chemical series of heterodimers to identify the aspects of molecular design that affect quantum beating signals similar to those observed in photosynthetic systems. We investigate two important questions: what is the physical origin of the observed coherences, and how can we control the appearance of these coherences in artificial systems? In contrast to biological systems whose structures have evolved over a billion years to perform a specific function, and that are challenging to manipulate without loss of function, our samples afford more exogenous control over chromophores and their relative orientation. We use these synthetic degrees of freedom to disentangle electronic transitions from vibrational motion and to further understand the origins of the observed coherences. In particular, varying electronic energy levels in different heterodimers facilitates assignment of signals that would not be possible from spectroscopic analysis of a single system. We have designed a series of singly linked synthetic fluorescein heterodimers with tunable energy gaps. Because of the single linkage, the two fluorescein chromophores can rotate and therefore have no fixed relative orientation in solution. By packing these structurally flexible heterodimers on single-walled carbon nanotubes (SWNTs) using non-covalent π-π interactions, we can strongly hinder many degrees of freedom involving the relative rotation of the chromophores. We also force them to share the same local chemical environment, in crude analogy to conditions that the chromophores experience in photosynthetic complexes. Combining synthetic control of the monomers with our SWNT packing strategy, we disentangle the two functionalities that proteins provide in natural light-harvesting systems: tuned energy gaps, and rigid structural support that defines spatial relationships between chromophores. Using ultrafast 2DES measurements, we investigate the effect of these two functionalities on the observed beating signals.

Proteins in photosynthetic complexes hold chromophores in fixed spatial relationships via non-covalent interactions, which finely tunes the excitation energy gaps of the individual chromophores [25, 26]. Synthetic two-chromophore model systems have been used

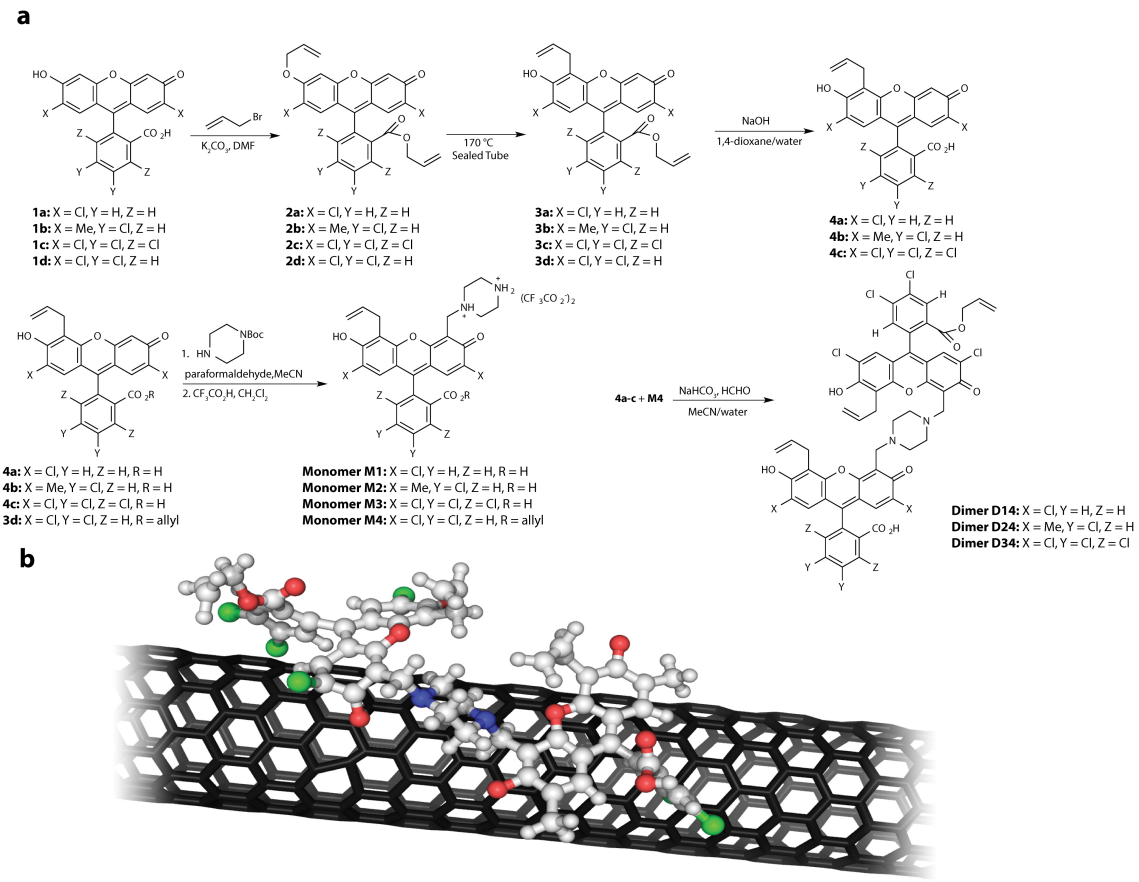

Figure 3.1: Synthetic routes and molecular structures of fluorescein heterodimers. (a) Synthetic scheme of singly linked fluorescein heterodimers D14, D24, and D34, and their corresponding monomers M1-4. (Boc = t-butyloxycarbonyl). (b) Conceptual structure of a heterodimer packed on the SWNT surface.

to reproduce this natural molecular design and to investigate the design principles for the quantum coherences observed in photosynthetic systems [11–13, 27–29]. However, previous attempts to create fixed spatial relationships in synthetic two-chromophore model systems for coherences have used relatively rigid linkers between chromophores, including metal-bridges [27, 28] and conjugated organic linkers [29]. In systems with metal-bridge linkers, the interpretation of the observed ultrafast dynamics was complicated by the presence of charge-transfer states [30]. In systems with conjugated organic linkers, chromophores were strongly coupled with each other and non-radiative transitions dominated population transfer rates, eliminating prolonged coherences [29]. Here, we introduce a new strategy to limit the relative orientation between chromophores. We use SWNTs as packing substrates via non-covalent π-π interactions for structurally flexible fluorescein heterodimers, as shown in Figure 3.1.b. This strategy is potentially applicable to all chromophores with strong π-stacking properties. Moreover, this approach tests the impact of spatial relationships on coherences, which we cannot test conveniently in natural systems.

We selected a series of substituted fluorescein dyes (1a-d) as starting materials because of their rich synthetic variability and tunable optical resonances. S_N2 allylation and successive Claisen rearrangement were conducted to install an allyl group *ortho* to the hydroxyl group [31], leaving the α-keto position as the single activated site on the xanthene ring. A single non-conjugated linker was then attached between monomers through stepwise Mannich condensations, creating singly linked heterodimers with structural flexibility, as shown in Figure 3.1.a. By employing an identical monomer unit (M4) in all three of the dimers (D14, D24, and D34), we hold one of the two electronic excitation energies constant, varying the other. As a result, we are able to vary the energy difference between the two electronic transitions of the heterodimers.

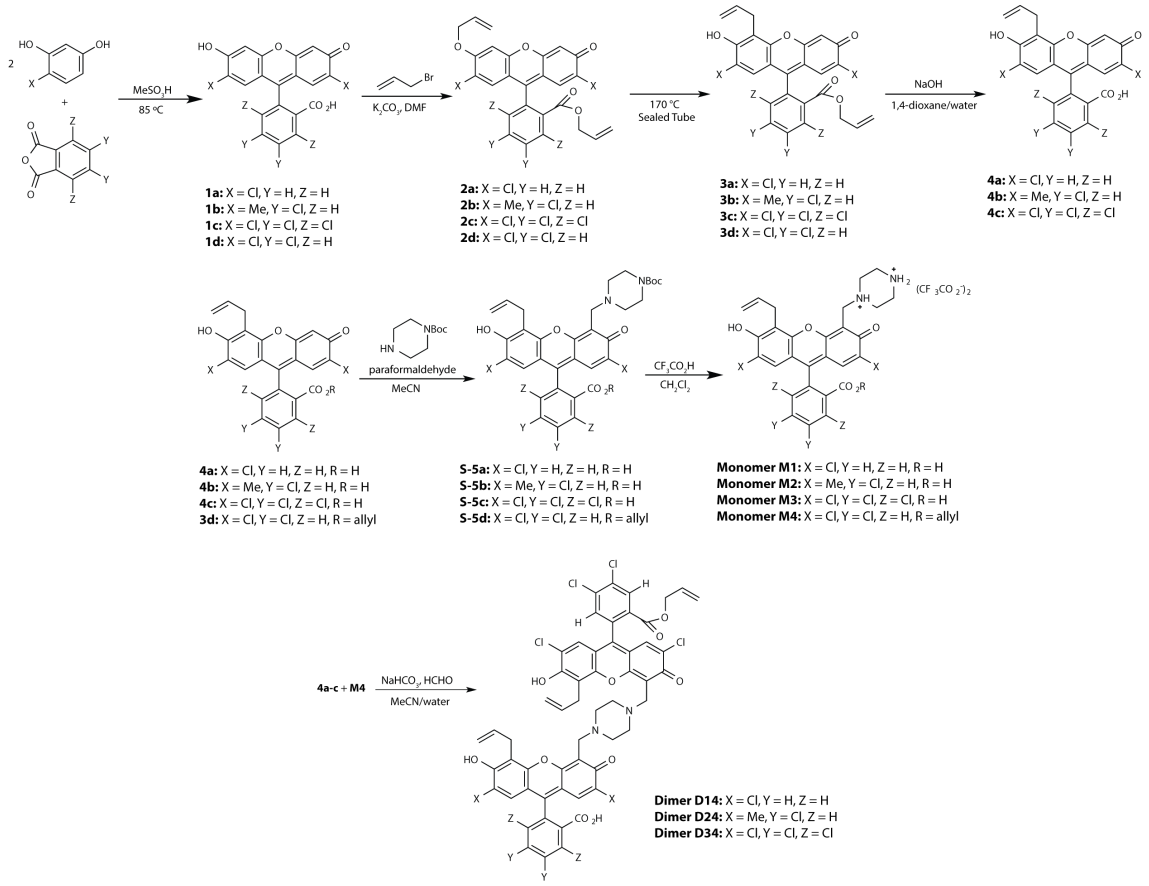

Figure 3.2: Synthetic scheme of fluorescein heterodimers.

3.3 Synthesis and characterization

All reagents were purchased from Aldrich and used without further purification. 4-Methylresorcinol was synthesized according to the procedure described in Elliger [32]. NMR spectra were recorded on a Bruker DMX-500 spectrometer. ^{1}H and ^{13}C chemical shifts are reported relative to $SiMe_4$ and were determined by reference to the residual ^{1}H and ^{13}C solvent resonances. When a $CD_3OD/CDCl_3$ mixture was used as an NMR solvent, the ^{1}H chemical shifts were referenced to the residual ^{1}H resonance of CD_3OD (δ 3.31). Coupling constants are given in hertz (Hz). High-resolution mass spectrometry was performed on an Agilent 6224 TOF mass spectrometer.

2′,7′-Dichlorofluorescein (1a) [33]. 4-Chlororesorcinol (10.6 g, 60 mmol) and phthalic anhydride (4.4 g, 30 mmol) were dissolved in methanesulfonic acid (150 mL) and stirred in the dark at 85 °C for 12 h. The mixture was cooled to room temperature, poured over ice, diluted to 600 mL with distilled water, and stirred vigorously for 1 h. The dark yellow precipitate, the crude product, was collected by using vacuum filtration. Recrystallization from EtOH/water yielded pure 1a as a light yellow powder (11.0 g, 73%). ^{1}H NMR (500 MHz, CD_3OD) is shown in Figure 3.3: δ 8.06 (dt, J = 7.7, 0.8, 1H), 7.83 (td, J = 7.5, 1.2, 1H), 7.76 (td, J = 7.5, 0.9, 1H), 7.26 (dt, J = 7.7, 0.8, 1H), 6.84 (s, 2H), 6.62 (br s, 2H).

5,6-Dichloro-2′,7′-dimethylfluorescein (1b) [11]. Prepared from 4-methylresorcinol and 4,5-dichlorophthalic anhydride following the procedure for 1a as a yellow solid. Yield: 81%. ^{1}H NMR (500 MHz, DMSO-d6) is shown in Figure 3.4: δ 10.16 (br s, 2H), 8.26 (s, 1H), 7.66 (s, 1H), 6.68 (s, 2H), 6.55 (s, 2H), 1.97 (s, 6H).

4,5,6,7,2′,7′-Hexachlorofluorescein (1c) [11]. Prepared from 4-chlororesorcinol and tetrachlorophthalic anhydride following the procedure for 1a as a pale yellow solid. Yield: 58%. ^{1}H NMR (500 MHz, CD_3OD) is shown in Figure 3.5: δ 6.92 (s, 2H), 6.82 (s, 2H).

5,6,2′,7′-Tetrachlorofluorescein (1d) [34]. Prepared from 4-chlororesorcinol and 4,5-dichlorophthalic anhydride following the procedure for 1a as a yellow solid. Yield: 87%. ^{1}H NMR (500 MHz, CD_3OD)is shown in Figure 3.6: δ 8.20 (d, J = 1.3, 1H), 7.52 (d, J = 0.8, 1H),

6.84 (s, 2H), 6.78 (br s, 2H).

2′,7′-Dichlorofluorescein diallyl ether ester (2a) [31, 35]. 1a (8.0 g, 20 mmol) was dissolved in DMF (40 mL), and K_2CO_3 (11.0 g, 80 mmol) and allyl bromide (6.9 mL, 80 mmol) were added. The mixture was stirred overnight at room temperature. The reaction mixture was diluted with CH_2Cl_2 (200 mL) and washed with water (400 mL x 3). The organic layer was dried over $MgSO_4$, filtered, and concentrated to yield an orange solid, the crude product. Recrystallization in EtOAc afforded pure 2a as bright orange crystals (5.6 g, 58%). ^{1}H NMR (500 MHz, $CDCl_3$) is shown in Figure 3.7: δ 8.33 (ddd, J = 7.8, 1.4, 0.4, 1H), 7.80 (td, J = 7.5, 1.4, 1H), 7.74 (td, J = 7.7, 1.4, 1H), 7.30 (ddd, J = 7.5, 1.4, 0.4, 1H), 7.03 (s, 1H), 7.02 (br s, 1H), 6.96 (s, 1H), 6.58 (s, 1H), 6.08 (ddt, J = 17.2, 10.5, 5.2, 1H), 5.69 (ddt, J = 17.2, 10.4, 5.6, 1H), 5.54 (dq, J = 17.2, 1.3, 1H), 5.42 (dq, J = 10.6, 1.3, 1H), 5.20-5.14 (m, 2H), 4.75 (dt, J = 5.1, 1.5, 2H), 4.57-4.49 (m, 2H).

5,6-Dichloro-2′,7′-dimethylfluorescein diallyl ether ester (2b). Prepared from 1b following the procedure for 2a as bright orange crystals. Yield: 85%. ^{1}H NMR (500 MHz, $CDCl_3$) is shown in Figure 3.8: δ 8.37 (s, 1H), 7.42 (s, 1H), 6.92 (s, 1H), 6.70-6.67 (br m, 2H), 6.62 (br s, 1H), 6.08 (ddt, J = 17.2, 10.5, 5.2, 1H), 5.56 (ddt, J = 16.9, 10.6, 6.1, 1H), 5.48 (dq, J = 17.3, 1.5, 1H), 5.37 (dq, J = 10.6, 1.3, 1H), 5.12-5.06 (m, 2H), 4.69 (dt, J = 5.0, 1.4, 2H), 4.51-4.42 (m, 2H), 2.17 (d, J = 0.4, 3H), 2.07 (d, J = 1.1, 3H). ^{13}C{^{1}H} NMR (126 MHz, $CDCl_3$) is shown in Figure 3.9: δ 184.3, 163.4, 161.6, 158.5, 152.9, 146.3, 138.4, 137.8, 134.6, 134.4, 133.2, 132.3, 132.0, 130.7, 130.2, 127.7, 126.6, 125.5, 119.8, 118.5, 118.0, 114.0, 104.9, 99.3, 69.6, 66.6, 17.0, 16.2. HRMS (ESI-TOF, positive ion, m/z): Calc. 509.0923 ($[M+H]^+$), found 509.0919.

4,5,6,7,2′,7′-Hexachlorofluorescein diallyl ether ester (2c). Prepared from 1c following the procedure for 2a as bright orange crystals. Yield: 64%. ^{1}H NMR (500 MHz, $CDCl_3$) is shown in Figure 3.10: δ 7.06 (s, 1H), 7.02 (s, 1H), 7.01 (br s, 1H), 6.59 (s, 1H), 6.08 (ddt, J = 17.2, 10.5, 5.2, 1H), 5.54 (dq, J = 17.3, 1.4, 1H), 5.46-5.38 (m, 2H), 5.10-5.05 (m, 2H), 4.77 (dt, J = 5.1, 1.5, 2H), 4.43 (dt, J = 6.4, 1.0, 2H). ^{13}C{^{1}H} NMR (126 MHz, $CDCl_3$)

is shown in Figure 3.11: δ 177.7, 162.9, 159.0, 157.3, 152.6, 140.7, 136.7, 136.4, 136.2, 134.2, 132.3, 131.0, 130.9, 129.7, 129.2, 127.6, 126.6, 121.4, 121.3, 119.5, 119.2, 113.1, 106.4, 101.4, 70.7, 67.4. HRMS (ESI-TOF, positive ion, *m/z*): Calc. 618.9022 ($[M+H]^+$), found 618.9018.

5,6,2′,7′-Tetrachlorofluorescein diallyl ether ester (2d). Prepared from 1d following the procedure for 2a as bright orange crystals. Yield: 71%. 1H NMR (500 MHz, $CDCl_3$) is shown in Figure 3.12: δ 8.40 (s, 1H), 7.43 (s, 1H), 7.03 (br s, 1H), 7.01 (s, 1H), 6.94 (s, 1H), 6.62 (br s, 1H), 6.08 (ddt, J = 17.2, 10.5, 5.2, 1H), 5.68 (ddt, J = 17.4, 10.1, 6.1, 1H), 5.53 (dq, J = 17.3, 1.4, 1H), 5.42 (dq, J = 10.6, 1.3, 1H), 5.21-5.16 (m, 2H), 4.76 (dt, J = 5.1, 1.5, 2H), 4.57-4.50 (m, 2H). $^{13}C\{^1H\}$ NMR (126 MHz, $CDCl_3$) is shown in Figure 3.13: δ 177.5, 162.9, 158.7, 157.6, 152.5, 146.8, 138.4, 135.8, 135.3, 133.6, 133.1, 132.1, 131.1, 130.7, 129.7, 127.7, 126.9, 121.0, 120.1, 119.4, 118.0, 114.6, 106.1, 101.4, 70.6, 66.8. HRMS (ESI-TOF, positive ion, *m/z*): Calc. 550.9801 ($[M+H]^+$), found 550.9793.

4′-Allyl-2′,7′-dichlorofluorescein allyl ester (3a) [31, 35]. 2a (500 mg, 1.04 mmol) in diphenyl ether (5 mL) was heated in sealed tube at 170 °C under N_2 overnight. The solution was then cooled to room temperature and transferred to a scintillation vial. The solution was diluted with $CHCl_3$ (5 mL). Crystals of 3a formed slowly from the mixture. Pure 3a was collected using vacuum filtration, resulting in dark orange crystals (325 mg, 65%). ^1H NMR (500 MHz, CD_3OD) is shown in Figure 3.14: δ 8.33 (ddd, J = 7.8, 1.4, 0.4, 1H), 7.89 (td, J = 7.5, 1.4, 1H), 7.83 (td, J = 7.7, 1.4, 1H), 7.47 (ddd, J = 7.5, 1.3, 0.3, 1H), 7.06 (br s, 1H), 7.05 (s, 1H), 6.99 (s, 1H), 5.98 (ddt, J = 16.9, 10.4, 6.2, 1H), 5.60 (ddt, J = 17.2, 10.2, 6.0, 1H), 5.17 (dq, J = 16.9, 1.5, 1H), 5.11-5.02 (m, 3H), 4.53-4.44 (m, 2H), 3.62 (dt, J = 6.0, 1.4, 2H).

4′-Allyl-5,6-dichloro-2′,7′-dimethylfluorescein allyl ester (3b). Prepared from 2b following the procedure for 3a as dark orange crystals. Yield: 70%. ^1H NMR (500 MHz, CD_3OD) is shown in Figure 3.15: δ 8.38 (q, J = 0.3, 1H), 7.68 (q, J = 0.3, 1H), 6.91 (br s, 1H), 6.81 (q, J = 1.2, 1H), 6.79 (q, J = 0.9, 1H), 5.98 (ddt, J = 16.9, 10.2, 6.5, 1H), 5.48 (ddt, J = 17.5, 10.0, 6.0, 1H), 5.14 (dq, J = 17.1, 1.8, 1H), 5.03-4.97 (m, 3H), 4.47-4.37 (m, 2H),

3.57 (dt, J = 6.3, 1.2, 2H), 2.12 (d, J = 0.9, 3H), 2.04 (d, J = 1.2, 3H). $^{13}C\{^{1}H\}$ NMR (126 MHz, CD_3OD) is shown in Figure 3.16: δ 164.9, 149.2, 138.4, 136.9, 135.9, 135.1, 134.0, 133.7, 132.2, 132.1, 130.8, 129.5, 127.5, 124.3, 119.8, 119.6, 117.7, 115.20, 115.16, 102.4, 67.4, 28.1, 17.2, 16.0. HRMS (ESI-TOF, positive ion, *m/z*): Calc. 509.0923 ($[M+H]^+$), found 509.0919.

4′-Allyl-4,5,6,7,2′,7′-hexachlorofluorescein allyl ester (3c). Prepared from 2c following the procedure for 3a as dark orange crystals. Yield: 52%. ^{1}H NMR (500 MHz, CD_3OD) is shown in Figure 3.17: δ 7.25 (s, 1H), 7.20 (s, 1H), 7.03 (br s, 1H), 5.96 (ddt, J = 16.9, 10.2, 6.5, 1H), 5.32 (ddt, J = 17.0, 10.4, 6.5, 1H), 5.17 (dq, J = 17.1, 1.7, 1H), 5.06-4.95 (m, 3H), 4.45-4.41 (m, 2H), 3.58 (dt, J = 6.4, 1.3, 2H). 3c was not characterized by $^{13}C\{^{1}H\}$ NMR because of low solubility. HRMS (ESI-TOF, positive ion, *m/z*): Calc. 618.9022 ($[M+H]^+$), found 618.9015.

4′-Allyl-5,6,2′,7′-tetrachlorofluorescein allyl ester (3d). Prepared from 2d following the procedure for 3d as dark orange crystals. Yield: 71%. ^{1}H NMR (500 MHz, CD_3OD) is shown in Figure 3.18: δ 8.42 (d, J = 0.3, 1H), 7.74 (d, J = 0.2, 1H), 7.10 (s, 1H), 7.04 (s, 1H), 6.97 (s, 1H), 5.98 (ddt, J = 16.9, 10.2, 6.5, 1H), 5.57 (ddt, J = 17.2, 10.4, 6.1, 1H), 5.17 (dq, J = 17.1, 1.8 Hz, 1H), 5.10-5.05 (m, 2H), 5.03 (dq, J = 10.0, 1.6, 1H), 4.53-4.44 (m, 2H), 3.61 (dt, J = 6.4, 1.5, 2H). $^{13}C\{^{1}H\}$ NMR (126 MHz, CD_3OD) is shown in Figure 3.19: δ 164.5, 150.4, 138.8, 136.1, 135.9, 134.5, 134.3, 133.6, 132.2, 131.7, 129.3, 127.8, 119.9, 116.9, 115.8, 104.5, 67.6, 28.5. HRMS (ESI-TOF, positive ion, *m/z*): Calc. 550.9801 ($[M+H]^+$), found 550.9801.

4′-Allyl-2′,7′-dichlorofluorescein (4a) [31, 35]. 3a (1.5 g, 3.13 mmol) and NaOH (625 mg, 15.6 mmol) were added in a mixture of 1,4-dioxane (37.5 mL) and water (11.5 mL). The resulting solution was refluxed for 2 h. The organic volatiles were removed under vacuum. The aqueous residue was neutralized with 1 N HCl and extracted with EtOAc (20 mL x 3). The combined organic phase was dried over $MgSO_4$, filtered, and concentrated under vacuum. The solid residue was further purified by recrystallization in EtOAc/hexanes to

afford pure 4a, resulting in a bright orange solid (1.0 g, 73%). ^{1}H NMR (500 MHz, CD_3OD) is shown in Figure 3.20: δ 8.05 (br s, 1H), 7.83 (td, J = 7.5, 1.0, 1H), 7.76 (td, J = 7.5, 0.6, 1H), 7.27 (br d, J = 6.4, 1H), 6.88 (br s, 1H), 6.62 (br s, 1H), 6.53 (br s, 1H), 6.01 (ddt, J = 16.9, 10.4, 6.3, 1H), 5.12 (dq, J = 17.2, 1.3, 1H), 5.04 (dq, J = 10.0, 1.3, 1H), 3.70-3.65 (br m, 2H).

4′-Allyl-5,6-dichloro-2′,7′-dimethylfluorescein (4b). Prepared from 3b following the procedure for 4a as a bright orange powder. Yield: 87%. ^{1}H NMR (500 MHz, CD_3OD) is shown in Figure 3.21: δ 8.33 (s, 1H), 7.55 (s, 1H), 6.85 (s, 1H), 6.71 (br q, J = 0.4, 1H), 6.70 (br q, J = 0.6, 1H), 5.98 (ddt, J = 16.9, 10.2, 6.5, 1H), 5.12 (dq, J = 17.1, 1.8, 1H), 4.98 (dq, J = 10.0, 1.7, 1H), 3.59 (dt, J = 6.3, 1.4, 2H), 2.10 (d, J = 0.6, 3H), 2.06 (d, J = 1.1, 3H). ^{13}C{^{1}H} NMR (126 MHz, CD_3OD) is shown in Figure 3.22: δ 167.4, 163.6, 154.6, 154.3, 138.8, 136.9, 135.1, 132.2, 131.8, 129.7, 127.6, 125.8, 119.6, 115.2, 115.0, 113.4, 102.4, 28.2, 17.0, 15.9. HRMS (ESI-TOF, positive ion, m/z): Calc. 469.0610 ($[M+H]^+$), found 469.0610.

4′-Allyl-4,5,6,7,2′,7′-hexachlorofluorescein (4c). Prepared from 3c following the procedure for 4a as a bright orange powder. Yield: 80%. ^{1}H NMR (500 MHz, CD_3OD) is shown in Figure 3.23: δ 6.91 (s, 1H), 6.84 (s, 1H), 6.83 (s, 1H), 6.02 (ddt, J = 17.1, 10.1, 6.1, 1H), 5.09-5.01 (m, 2H), 3.67 (dt, J = 6.1, 1.5, 2H). ^{13}C{^{1}H} NMR (126 MHz, CD_3OD) is shown in Figure 3.24: δ 165.2, 157.0, 154.2, 152.3, 150.2, 149.9, 141.4, 137.4, 136.3, 132.4, 129.2, 128.8, 126.0, 124.8, 118.6, 118.2, 117.5, 115.7, 109.6, 109.0, 104.8, 28.9. HRMS (ESI-TOF, positive ion, m/z): Calc. 578.8708 ($[M+H]^+$), found 578.8706.

Compound S-5a. 1-Boc-piperazine (141 mg, 0.75 mmol) and paraformaldehyde (47 mg, 1.6 mmol) were dissolved in MeCN (10 mL), and the mixture was refluxed for 0.5 h. Then, 4a (220 mg, 0.5 mmol) was dissolved in MeCN (15 mL) and added to the previous mixture. The mixture was refluxed overnight. The organic volatiles were removed under vacuum. The residue was subjected to flash column chromatography (silica, EtOAc) to afford the crude product. Recrystallization with EtOAc/hexanes resulted in pure S-5a as a pink orange solid

(270 mg, 85%). ^{1}H NMR (500 MHz, CD_3OD) is shown in Figure 3.25: δ 8.15 (d, J = 7.5, 1H), 7.82 (td, J = 7.5, 1.3, 1H), 7.77 (td, J = 7.6, 1.2, 1H), 7.30 (ddd, J = 7.5, 1.1, 0.7, 1H), 6.77 (br s, 1H), 6.73 (br s, 1H), 6.05 (ddt, J = 17.1, 10.2, 5.8, 1H), 5.06 (dq, J = 17.1, 1.8, 1H), 5.04 (dq, J = 10.2, 1.8, 1H), 4.32 (s, 2H), 3.71 (dt, J = 6.0, 1.6, 2H), 3.62 (s, 4H), 2.93 (s, 4H), 1.48 (s, 9H). HRMS (ESI-TOF, positive ion, *m/z*): Calc. 639.1665 ($[M+H]^+$), found 639.1665.

Compound S-5b. Prepared from 4b following the procedure for S-5a as a pink orange solid. Yield: 89%. ^{1}H NMR (500 MHz, CD_3OD) is shown in Figure 3.26: δ 8.23 (s, 1H), 7.47 (s, 1H), 6.87 (q, J = 1.0, 1H), 6.85 (q, J = 1.1, 1H), 6.03 (ddt, J = 17.1, 10.1, 5.8, 1H), 5.08 (dq, J = 17.2, 1.9, 1H), 5.03 (dq, J = 10.1, 1.7, 1H), 4.33 (s, 2H), 3.70-3.68 (m, 2H), 3.65-3.54 (br m, 4H), 3.01-2.84 (br m, 4H), 2.11 (d, J = 1.0, 3H), 2.10 (d, J = 1.0, 3H), 1.48 (s, 9H). HRMS (ESI-TOF, positive ion, *m/z*): Calc. 667.1978 ($[M+H]^+$), found 667.1981.

Compound S-5c. Prepared from 4c following the procedure for S-5a as a pink solid. Yield: 90%. ^{1}H NMR (500 MHz, CD_3OD) is shown in Figure 3.27: δ 6.99 (s, 1H), 6.94 (s, 1H), 6.06 (ddt, J = 17.1, 10.2, 5.6, 1H), 5.07-5.01 (m, 2H), 4.28 (s, 2H), 3.73-3.69 (m, 2H), 3.62-3.53 (br m, 4H), 2.93-2.83 (br m, 4H), 1.48 (s, 9H). HRMS (ESI-TOF, positive ion, *m/z*): Calc. 777.0077 ($[M+H]^+$), found 777.0090.

Compound S-5d. Prepared from 3d following the procedure for S-5a as a pink orange solid. Yield: 83%. ^{1}H NMR (500 MHz, CD_3OD) is shown in Figure 3.28: δ 8.40 (s, 1H), 7.63 (s, 1H), 7.02 (s, 1H), 6.99 (s, 1H), 6.04 (ddt, J = 17.1, 10.3, 5.5, 1H), 5.62 (ddt, J= 17.2, 10.4, 5.9, 1H), 5.12-5.02 (m, 4H), 4.54-4.47 (m, 4H), 3.83-3.63 (br m, 6H), 3.33-3.22 (br m, 4H), 1.49 (s, 9H). HRMS (ESI-TOF, positive ion, *m/z*): Calc. 749.1169 ($[M+H]^+$), found 749.1190.

Monomer M1. S-5a (200 mg, 0.31 mmol) was dissolved in a mixture of CH_2Cl_2 (2 mL) and CF_3CO_2H (1 mL), and was then stirred vigorously at room temperature for 0.5 h. Et_2O/hexanes (1/5, by volume) was added to the mixture to precipitate the product. Pure monomer M1 as a yellow solid was collected using vacuum filtration (210 mg, 88%). ^{1}H

NMR (500 MHz, CD_3OD) is shown in Figure 3.29: δ 8.10 (d, J = 7.7, 1H), 7.84 (td, J = 7.5, 1.2, 1H), 7.77 (td, J = 7.5, 0.9, 1H), 7.31 (d, J = 7.6, 1H), 6.75 (s, 1H), 6.63 (s, 1H), 6.11 (ddt, J = 17.1, 10.3, 5.6, 1H), 5.09 (dq, J = 10.2, 1.6, 1H), 5.05 (dq, J = 17.2, 1.7, 1H), 4.33 (s, 2H), 3.76 (d, J = 5.6, 2H), 3.47-3.40 (br m, 4H), 3.25-3.15 (br m, 4H). $^{13}C\{^1H\}$ NMR (126 MHz, CD_3OD) is shown in Figure 3.30: δ 170.3, 162.9 (q, J_{CF} = 35), 156.0, 151.6, 150.5, 136.6, 136.4, 131.8, 129.3, 128.5, 127.3, 126.8, 126.3, 119.5, 117.9 (q, J_{CF} = 292), 117.5, 115.9, 113.3, 110.3, 52.8, 50.6, 43.8, 41.7, 29.0. HRMS (ESI-TOF, positive ion, *m/z*): Calc. 539.1141 ([M-H-2CF_3CO_2]$^+$), found 539.1135.

Monomer M2. Prepared from S-5b (100 mg, 0.15 mmol) following the procedure for monomer M1 as a yellow solid. Yield: 109 mg (91%). ^1H NMR (500 MHz, CD_3OD) is shown in Figure 3.31: δ 8.41 (s, 1H), 7.59 (s, 1H), 6.94 (q, J = 1.2, 1H), 6.83 (q, J = 0.9, 1H), 6.14 (ddt, J = 17.2, 10.3, 5.2, 1H), 5.08 (dq, J = 10.2, 1.7, 1H), 4.98 (dq, J = 17.2, 1.7, 1H), 4.55 (s, 2H), 3.81 (dt, J = 5.2, 1.6, 2H), 3.63-3.48 (m, 8H), 2.19 (d, J = 0.9, 3H), 2.09 (d, J = 1.1, 3H). $^{13}C\{^1H\}$ NMR (126 MHz, CD_3OD) is shown in Figure 3.32: δ 166.7, 164.6, 162.2 (q, J_{CF} = 36), 157.2, 152.6, 138.8, 138.7, 136.6, 135.4, 133.4, 132.5, 131.6, 129.9, 128.3, 127.7, 117.6 (q, J_{CF} = 291), 115.6, 115.5, 114.9, 114.5, 105.3, 52.4, 50.3, 42.6, 41.7, 28.1, 16.9, 16.6. HRMS (ESI-TOF, positive ion, *m/z*): Calc. 567.1454 ([M-H-2CF_3CO_2]$^+$), found 567.1449.

Monomer M3. Prepared from S-5c (100 mg, 0.13 mmol) following the procedure for monomer M1 as a yellow orange solid. Yield: 96 mg (82%). ^1H NMR (500 MHz, CD_3OD) is shown in Figure 3.33: δ 6.99 (s, 1H), 6.88 (s, 1H), 6.10 (ddt, J = 17.1, 10.2, 5.6, 1H), 5.07 (dq, J = 10.2, 1.6, 1H), 5.01 (dq, J = 17.1, 1.7, 1H), 4.23 (s, 2H), 3.75-3.72 (m, 2H), 3.39-3.34 (br m, 4H), 3.10-2.97 (br m, 4H). $^{13}C\{^1H\}$ NMR (126 MHz, CD_3OD) is shown in Figure 3.34: δ 165.1, 162.5 (q, J_{CF} = 36), 156.6, 154.5, 150.3, 149.9, 149.7, 141.4, 137.5, 136.4, 132.6, 129.1, 128.5, 126.1, 124.8, 118.6, 118.5, 117.8 (q, J_{CF} = 291), 117.4, 115.7, 111.0, 109.5, 109.4, 53.0, 50.6, 44.3, 41.7, 29.0. HRMS (ESI-TOF, positive ion, *m/z*): Calc. 676.9552 ([M-H-2CF_3CO_2]$^+$), found 676.9551.

Monomer M4. Prepared from S-5d (310 mg, 0.41 mmol) following the procedure for monomer M1 as a yellow solid. Yield: 340 mg (95%). ^{1}H NMR (500 MHz, CD_3OD) is shown in Figure 3.35: δ 8.44 (s, 1H), 7.70 (s, 1H), 7.22 (s, 1H), 7.10 (s, 1H), 6.11 (ddt, J = 17.1, 10.4, 5.6, 1H), 5.66 (ddt, J = 17.1, 10.4, 6.0, 1H), 5.15-5.04 (m, 4H), 4.52 (dt, J = 5.9, 1.2, 2H), 4.30-4.24 (m, 2H), 3.85-3.76 (m, 2H), 3.52-3.46 (br m, 4H), 3.43-3.35 (br m, 4H). ^{13}C{^{1}H} NMR (126 MHz, CD_3OD) is shown in Figure 3.36: δ 173.1, 164.8, 164.4, 162.3 (q, J_{CF} = 36), 157.2, 153.1, 152.2, 139.0, 136.1, 135.9, 134.37, 134.35, 133.5, 132.4, 131.5, 130.7, 129.3, 127.5, 125.6, 119.7, 117.7 (q, J_{CF} = 292), 117.2, 116.6, 116.3, 116.1, 108.8, 67.6, 51.9, 50.6, 43.2, 41.7, 28.6. HRMS (ESI-TOF, positive ion, *m/z*): Calc. 649.0645 ([M-H-2CF_3CO_2]$^+$), found 649.0648.

Dimer D14. Monomer M1 (88 mg, 0.1 mmol) and $NaHCO_3$ (17 mg, 0.2 mmol) were mixed in water (1 mL) and sonicated until a precipitate formed. The mixture was diluted with MeCN (2 mL). Aqueous formaldehyde solution (37%, 25 μL, 0.3 mmol) and 4d (35 mg, 0.08 mmol) were added, and the resulting mixture was refluxed for 4 h. The hot mixture was filtered and washed with MeOH. The solid residue was recrystallized with $CHCl_3$ to afford pure dimer D14 as a red orange solid (47 mg, 53%). ^{1}H NMR (500 MHz, $CD_3OD/CDCl_3$, 1/1, by volume) is shown in Figure 3.37: δ 8.38 (s, 1H), 8.09 (br d, J = 7.2, 1H), 7.78 (td, J = 7.4, 1.0, 1H), 7.72 (td, J = 7.6, 1.0, 1H), 7.47 (d, J = 0.4, 1H), 7.24 (br d, J = 7.6, 1H), 6.98 (s, 1H), 6.96 (s, 1H), 6.69 (br s, 1H), 6.63 (br s, 1H), 6.05-5.94 (m, 2H), 5.69-5.61 (m, 1H), 5.14-5.01 (m, 6H), 4.56-4.49 (m, 2H), 4.34 (s, 2H), 4.21-4.15 (m, 2H), 3.70-3.65 (m, 2H), 3.64-3.59 (m, 2H), 3.23-2.82 (br m, 8H). D14 was not characterized using ^{13}C{^{1}H} NMR because of low solubility. HRMS (ESI-TOF, positive ion, *m/z*): Calc. 1101.0864 ([M+H]$^+$), found 1101.0871.

Dimer D24. Prepared from monomer M2 (88 mg, 0.1 mmol) and 4d (47 mg, 0.1 mmol) following the procedure for dimer D14 as a red orange solid. Yield: 85 mg (75%). ^{1}H NMR (500 MHz, $CD_3OD/CDCl_3$, 1/1, by volume) is shown in Figure 3.38: δ 8.39 (s, 1H), 8.30 (br s, 1H), 7.46 (s, 1H), 7.35 (s, 1H), 6.98 (q, J = 1.3, 1H), 6.97 (s, 1H), 6.66 (br s, 1H),

6.63 (br s, 1H), 6.02-5.94 (m, 2H), 5.66 (ddtd, J = 17.1, 10.4, 5.9, 0.7, 1H), 5.15-4.98 (m, 6H), 4.56-4.49 (m, 2H), 4.39 (s, 2H), 4.19 (s, 2H), 3.66-3.57 (m, 4H), 3.24-2.80 (br m, 8H), 2.11 (d, J = 0.6, 3H), 2.07 (d, J = 0.7, 3H). D24 was not characterized by $^{13}C\{^{1}H\}$ NMR because of low solubility. HRMS (ESI-TOF, positive ion, m/z): Calc. 1129.1176 ($[M+H]^+$), found 1129.1150.

Dimer D34. Prepared from monomer M3 (62 mg, 0.07 mmol) and 4d (36 mg, 0.06 mmol) following the procedure for dimer D14 as a red orange solid. Yield: 39 mg (50%). ^{1}H NMR (500 MHz, $CD_3OD/CDCl_3$, 1/1, by volume) is shown in Figure 3.39: δ 8.44 (s, 1H), 7.52 (s, 1H), 7.17 (br s, 1H), 7.01 (s, 1H), 6.84 (br s, 1H), 6.71 (s, 1H), 6.11-5.99 (m, 2H), 5.77-5.69 (m, 1H), 5.21-4.94 (m, 6H), 4.57-4.54 (m, 2H), 4.42 (br s, 2H), 4.23 (br s, 2H), 3.80 (br s, 2H), 3.73-3.64 (m, 2H), 3.57-2.77 (br m, 8H). D34 was not characterized using $^{13}C\{^{1}H\}$ NMR because of low solubility. HRMS (ESI-TOF, positive ion, m/z): Calc. 1238.9275 ($[M+H]^+$), found 1238.9301.

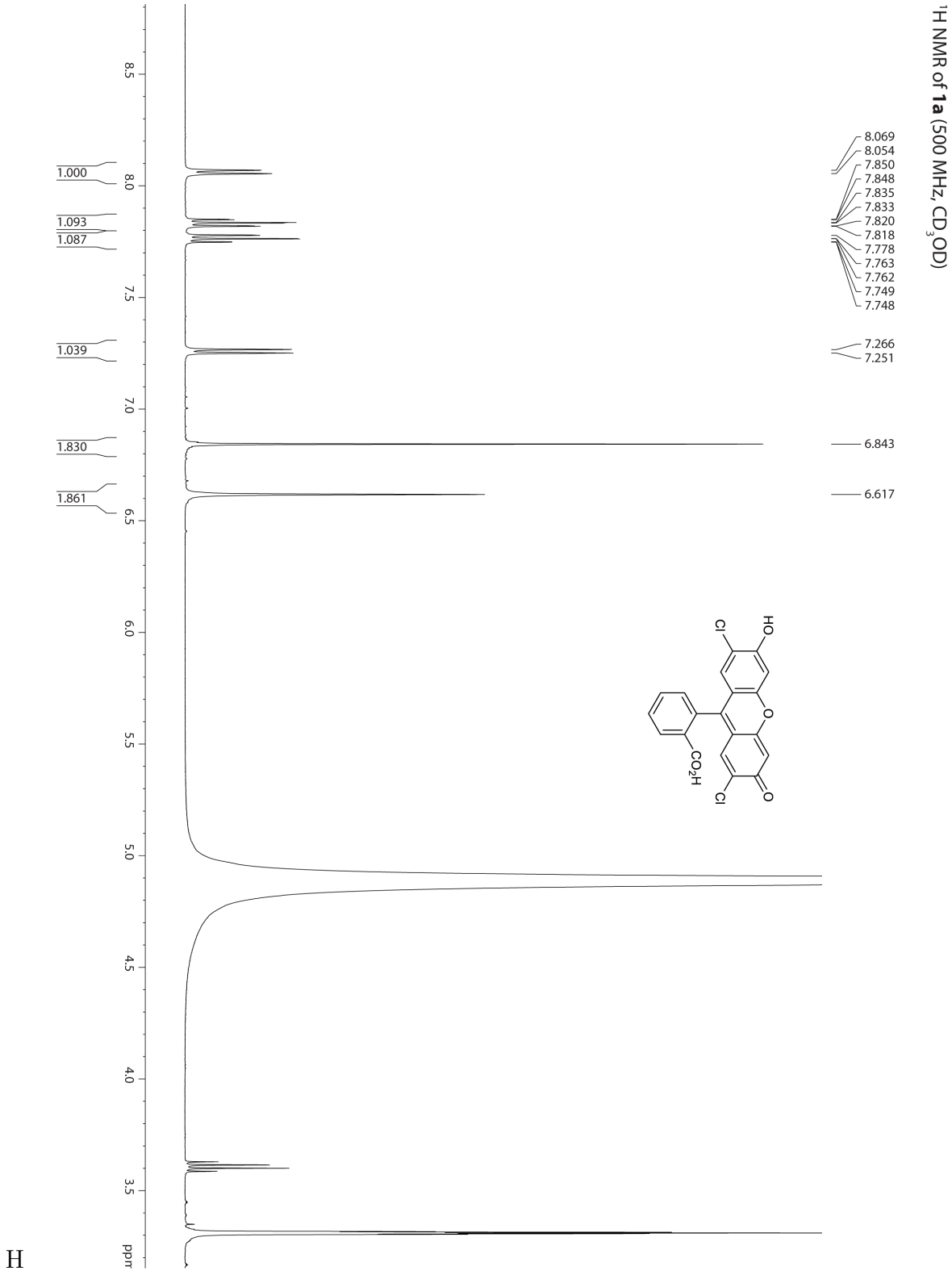

H

Figure 3.3: ^{1}H NMR spectrum of 1a

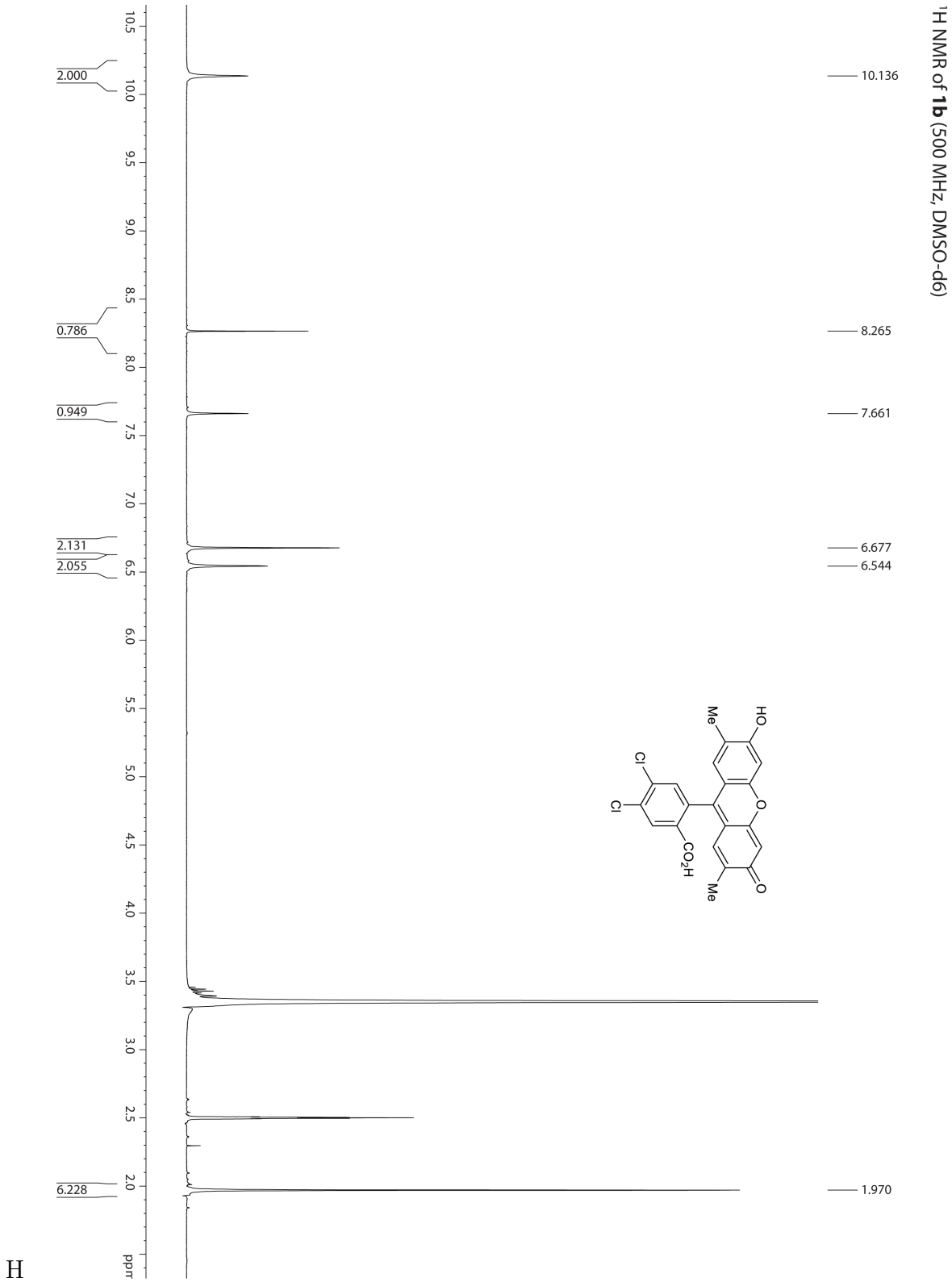

H

Figure 3.4: ^{1}H NMR spectrum of 1b

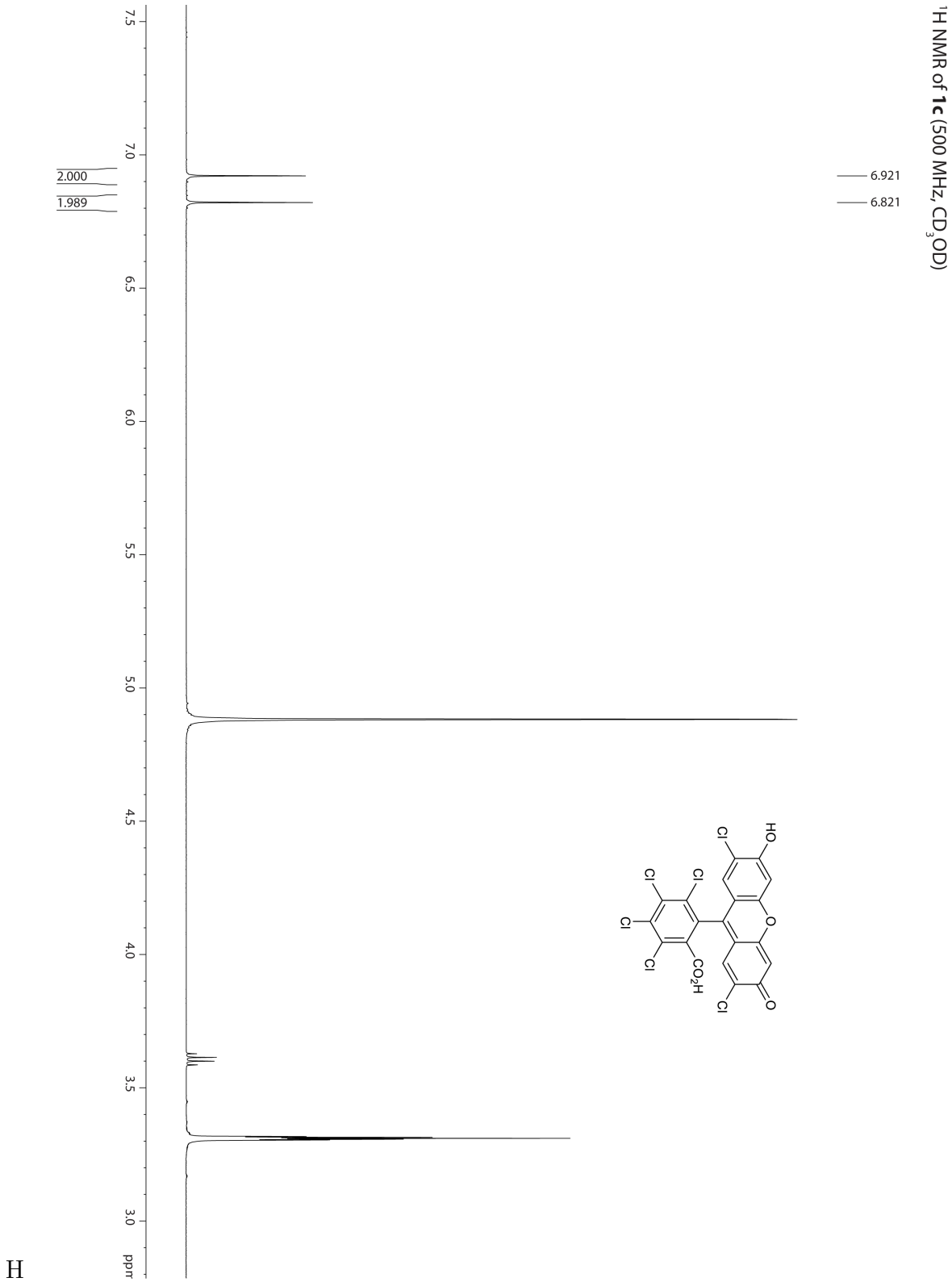

H

Figure 3.5: ^{1}H NMR spectrum of 1c

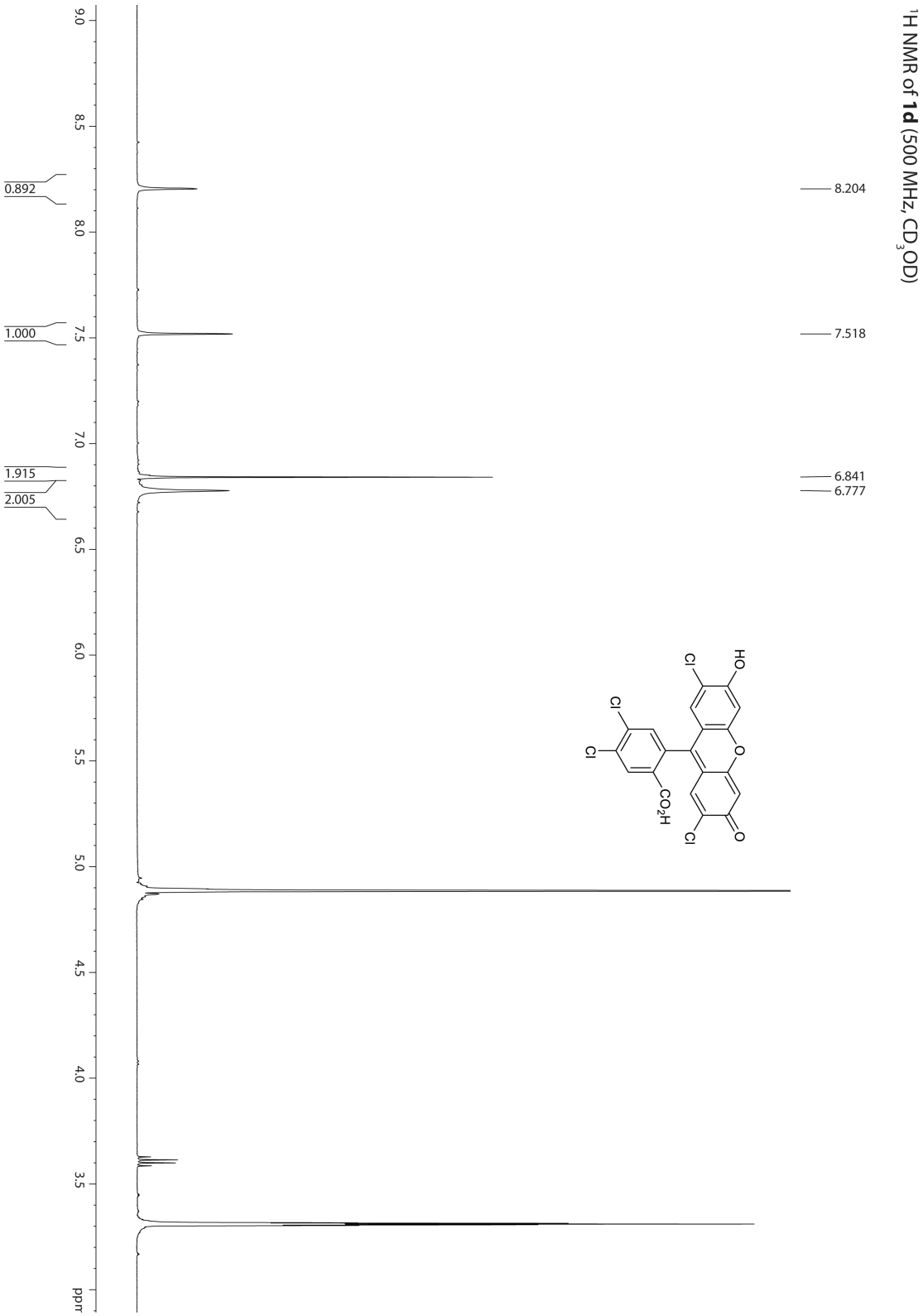

H

Figure 3.6: ^{1}H NMR spectrum of 1d

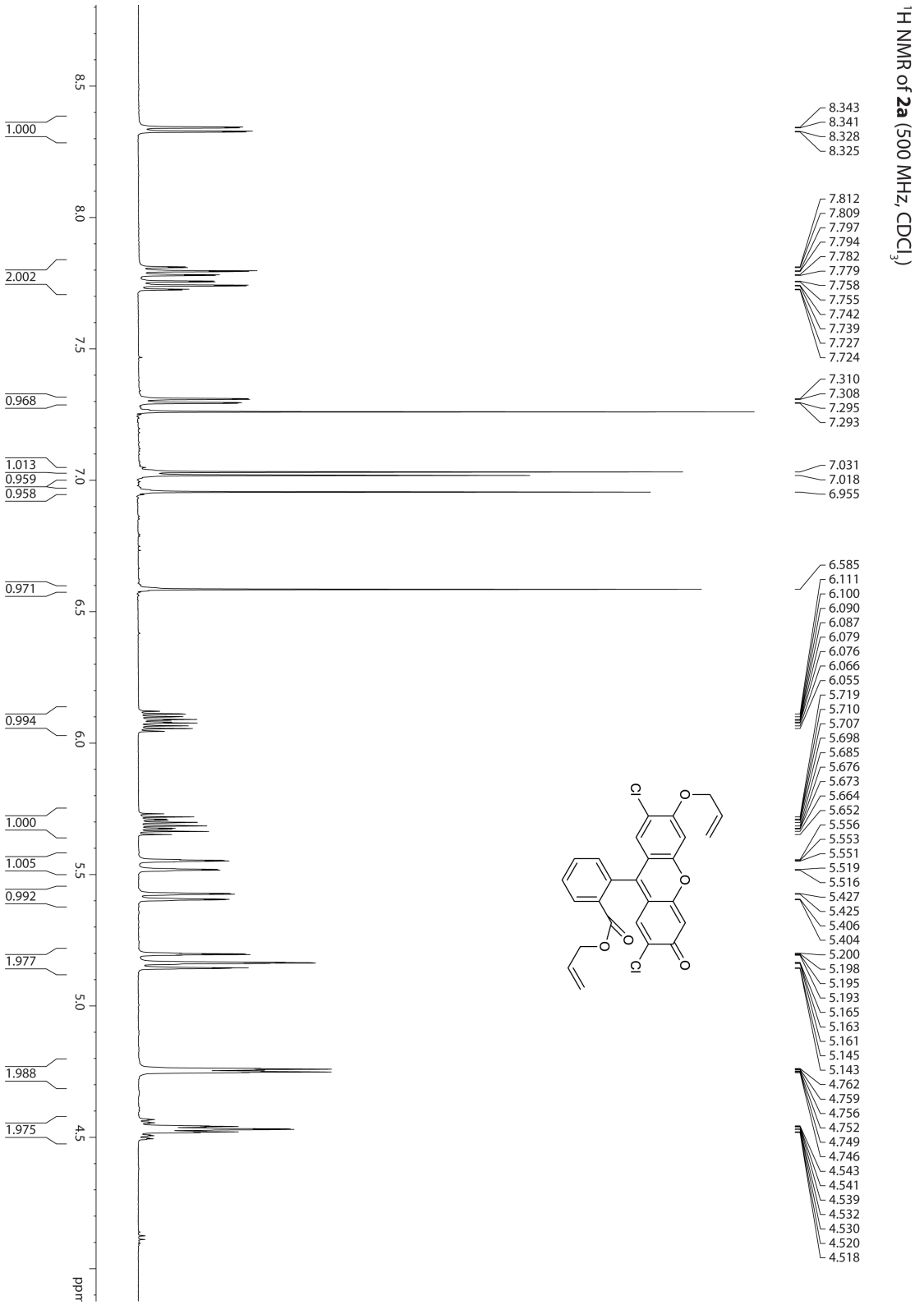

Figure 3.7: ^{1}H NMR spectrum of 2a

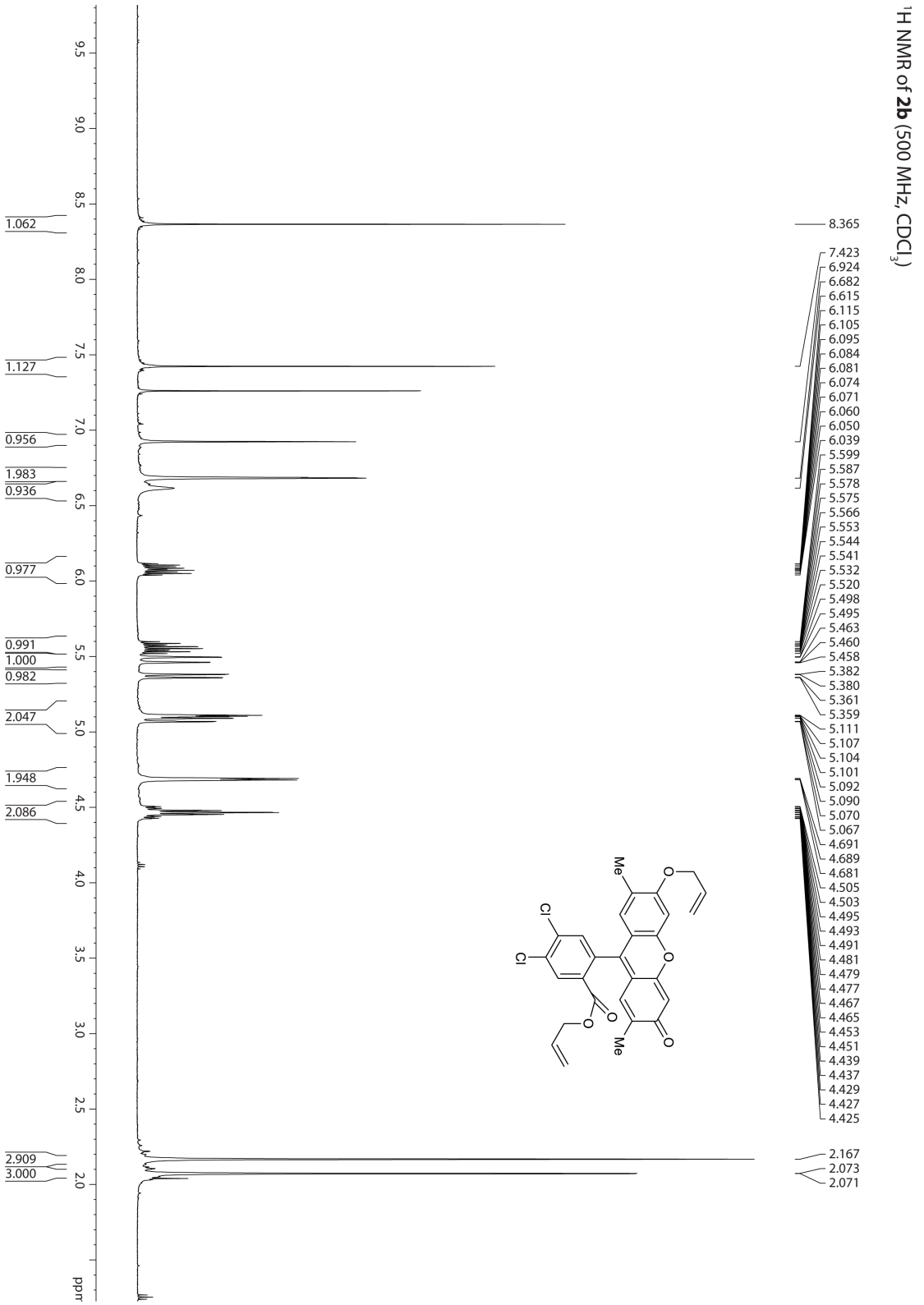

Figure 3.8: ^{1}H NMR spectrum of 2b

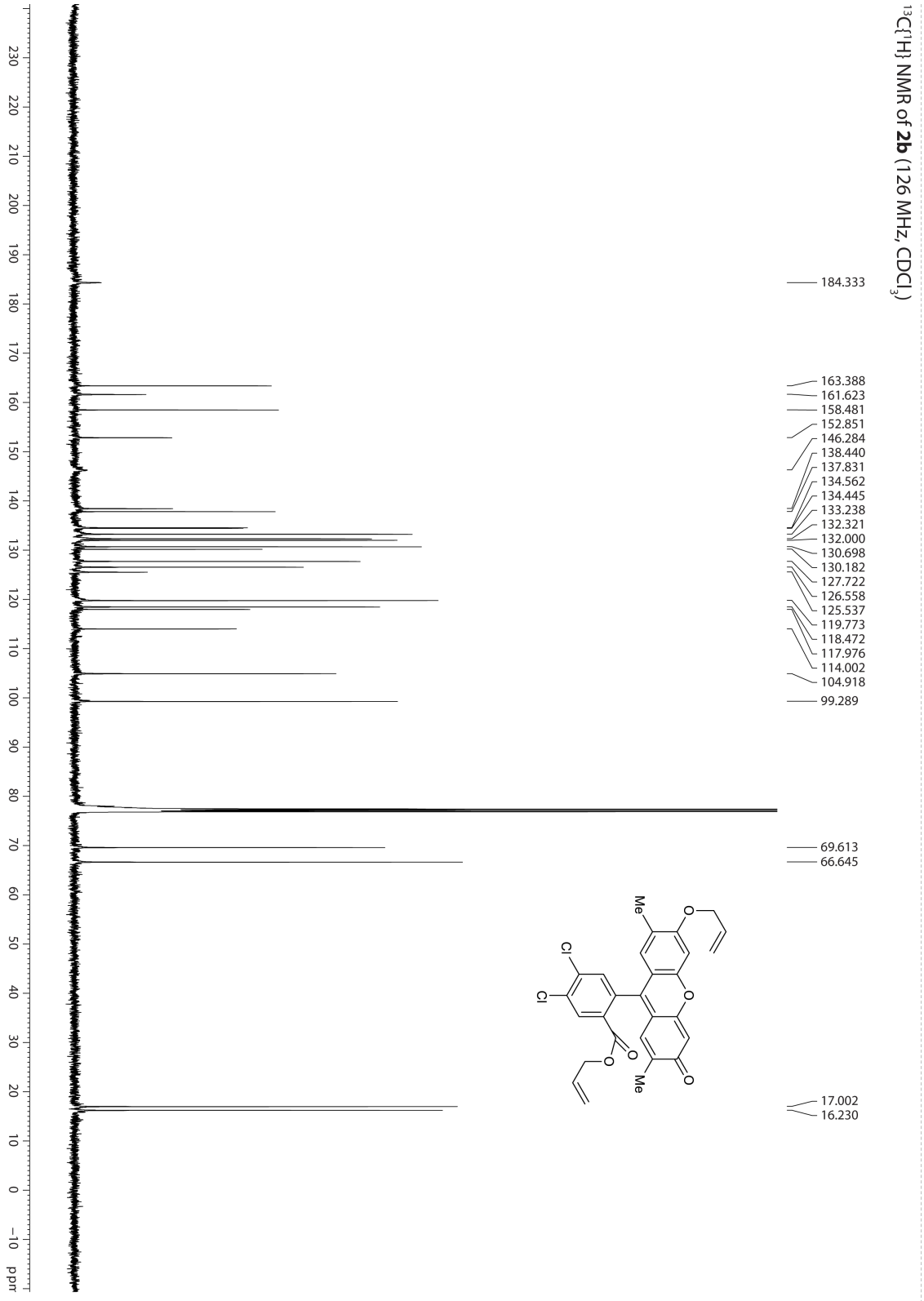

Figure 3.9: $^{13}C\{^1H\}$ NMR spectrum of 2b

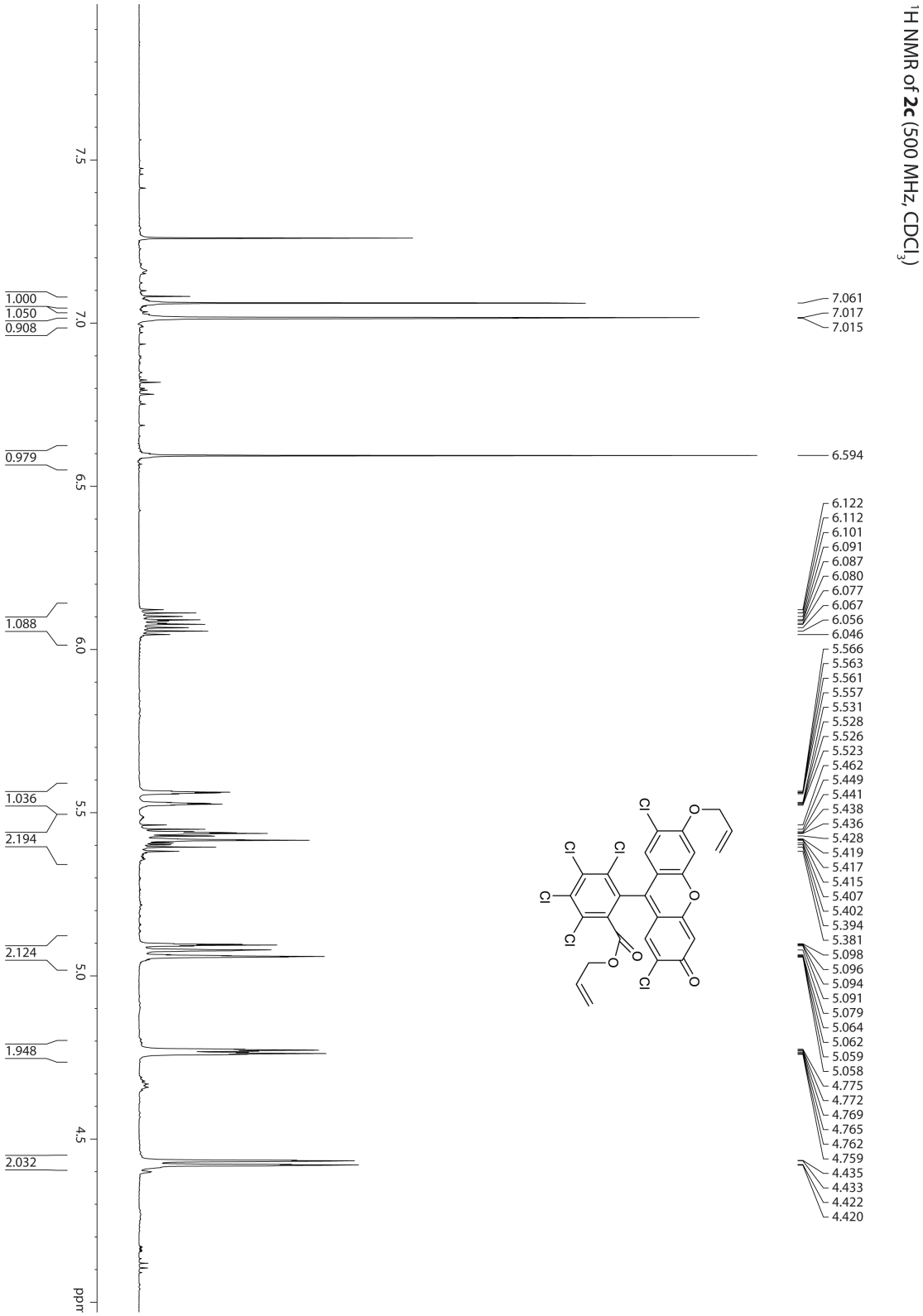

Figure 3.10: ^{1}H NMR spectrum of 2c

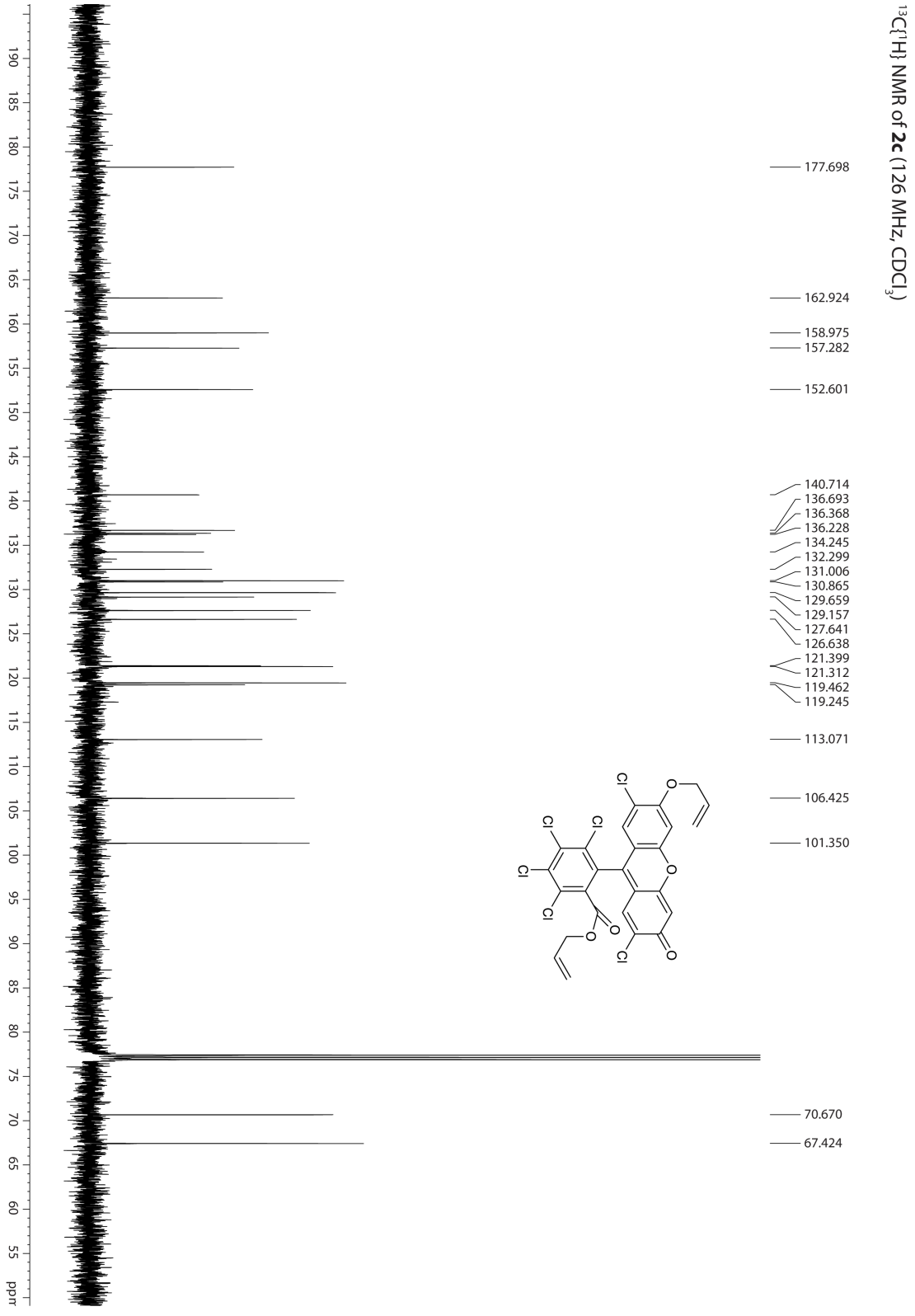

Figure 3.11: $^{13}C\{^1H\}$ NMR spectrum of 2c

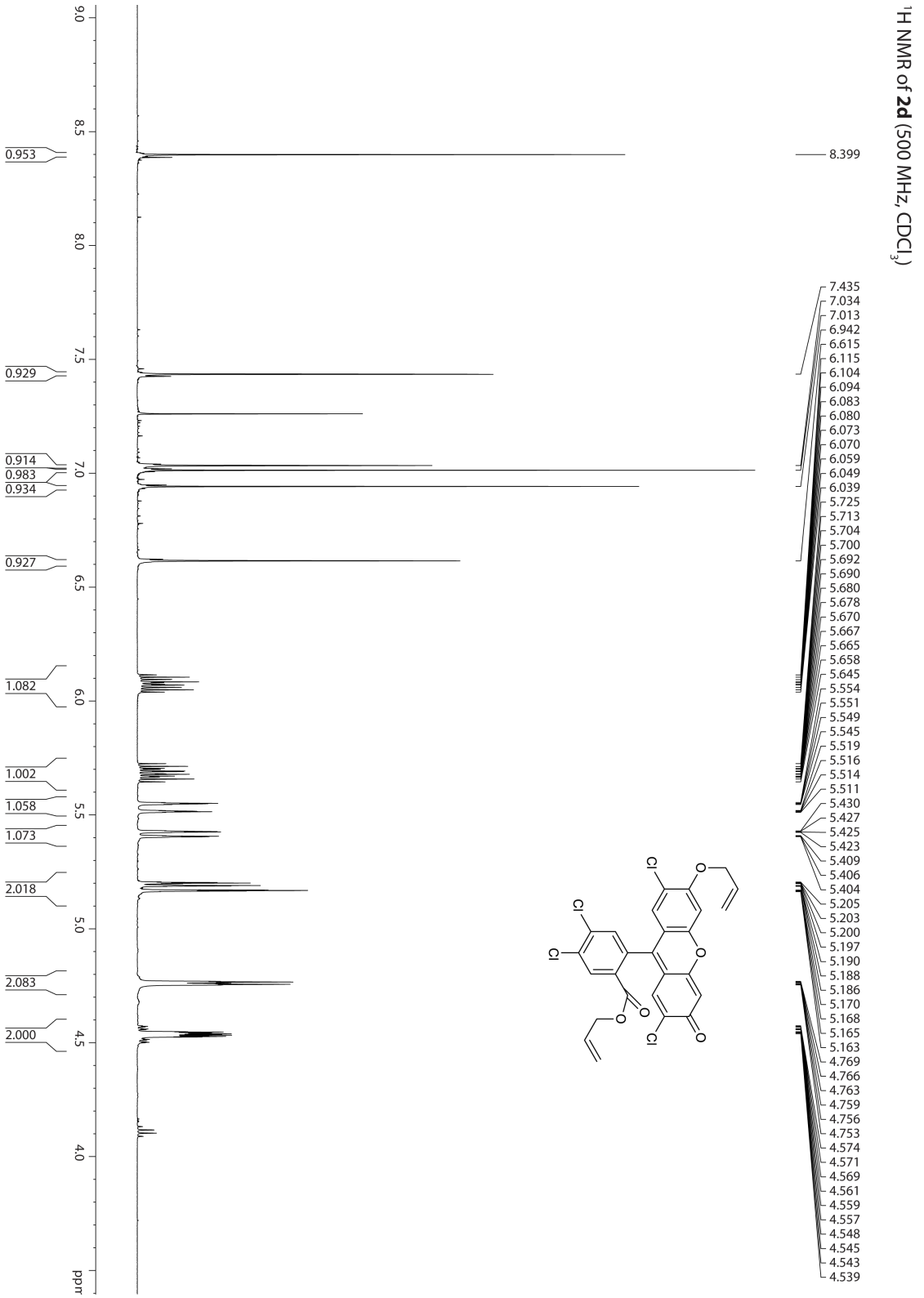

Figure 3.12: ^{1}H NMR spectrum of 2d

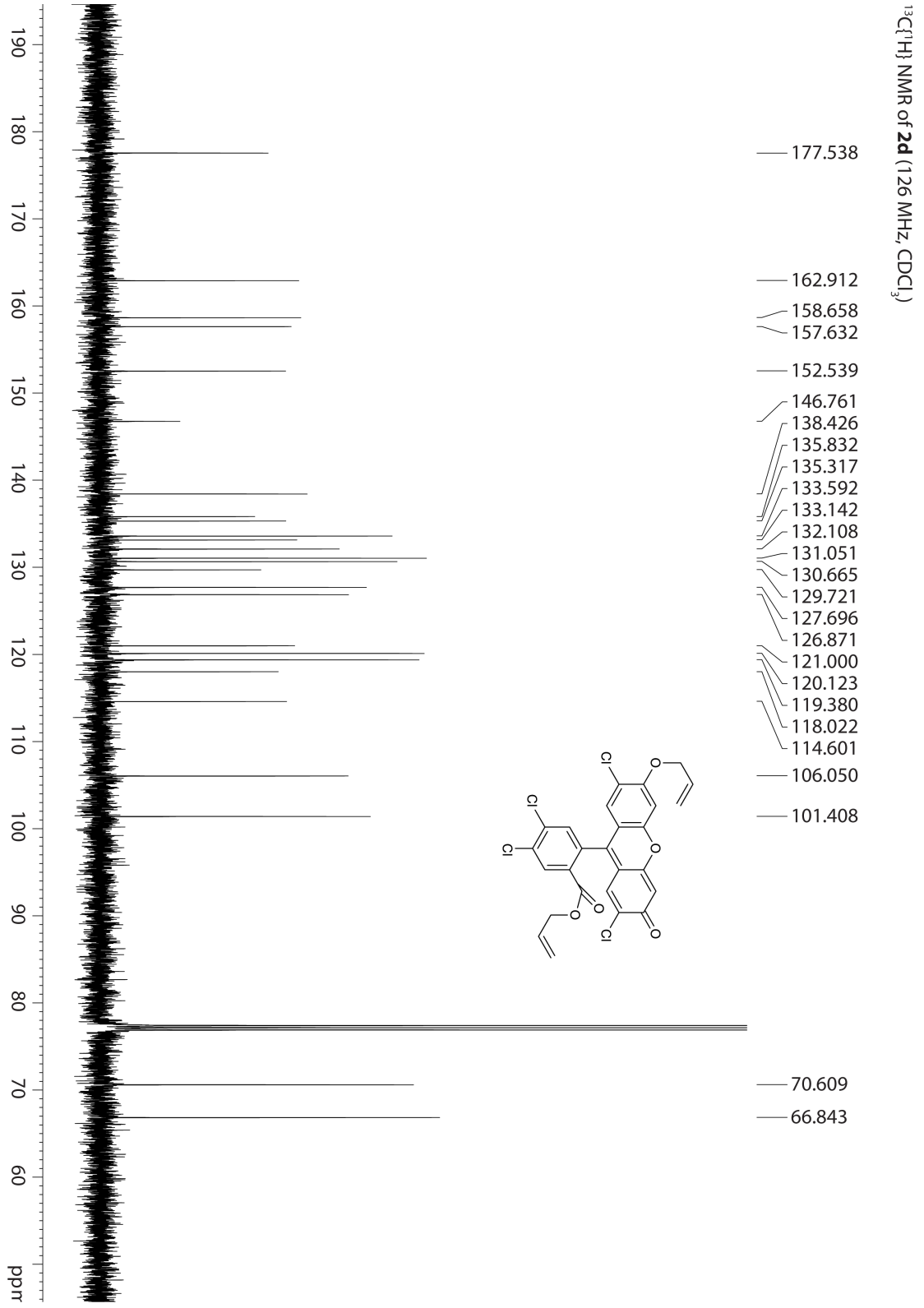

Figure 3.13: $^{13}C\{^1H\}$ NMR spectrum of 2d

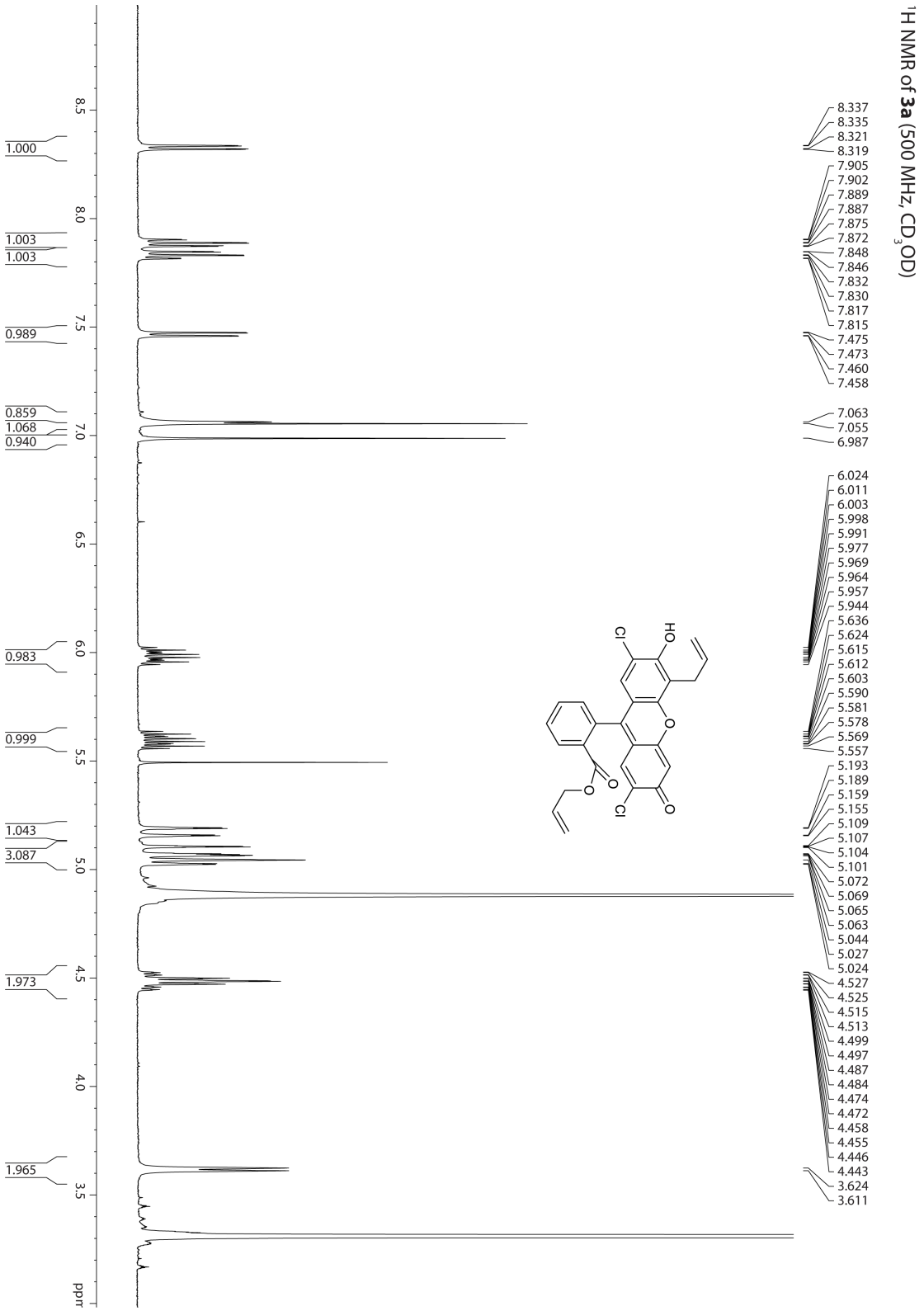

Figure 3.14: ^{1}H NMR spectrum of 3a

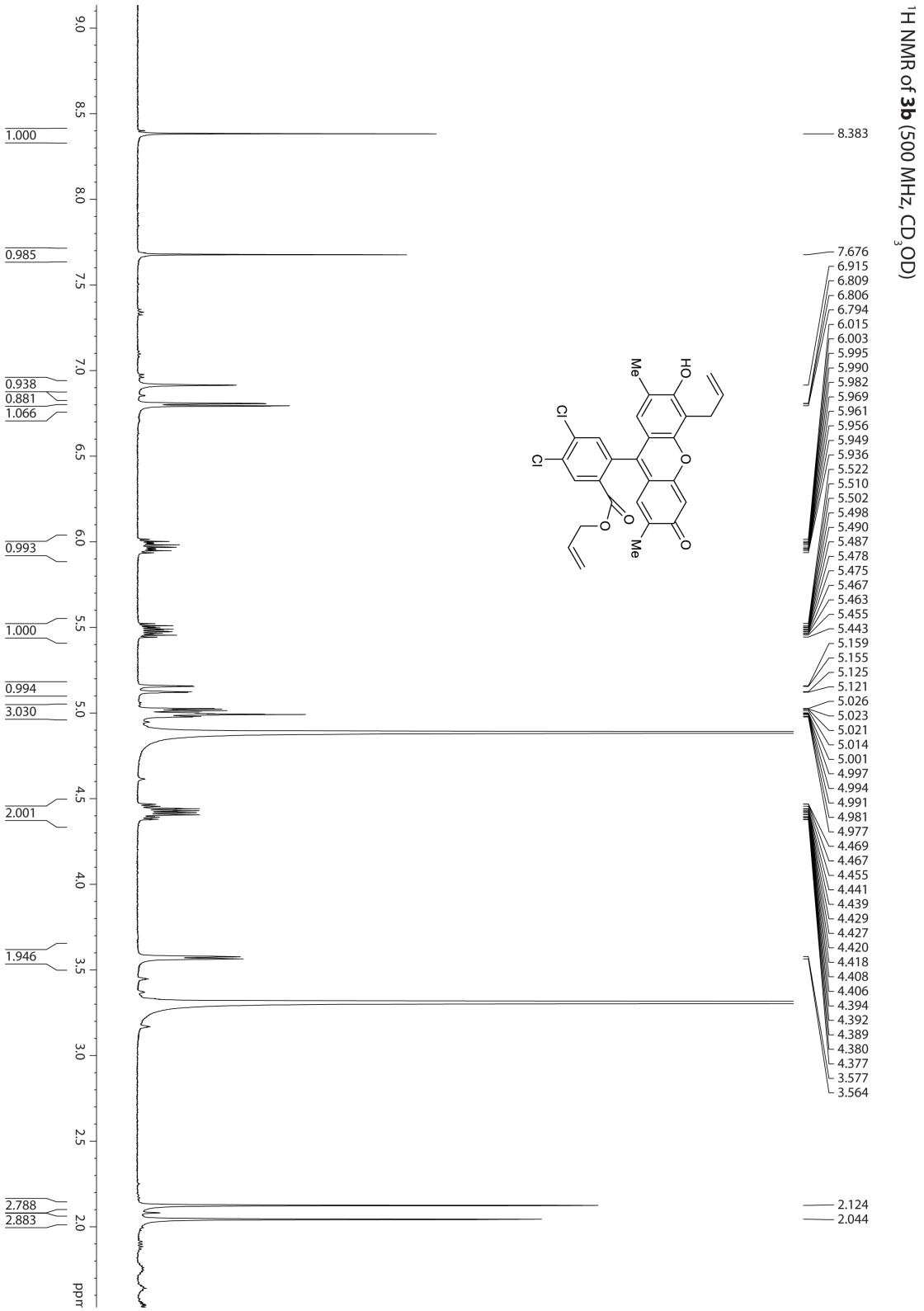

Figure 3.15: ^{1}H NMR spectrum of 3b

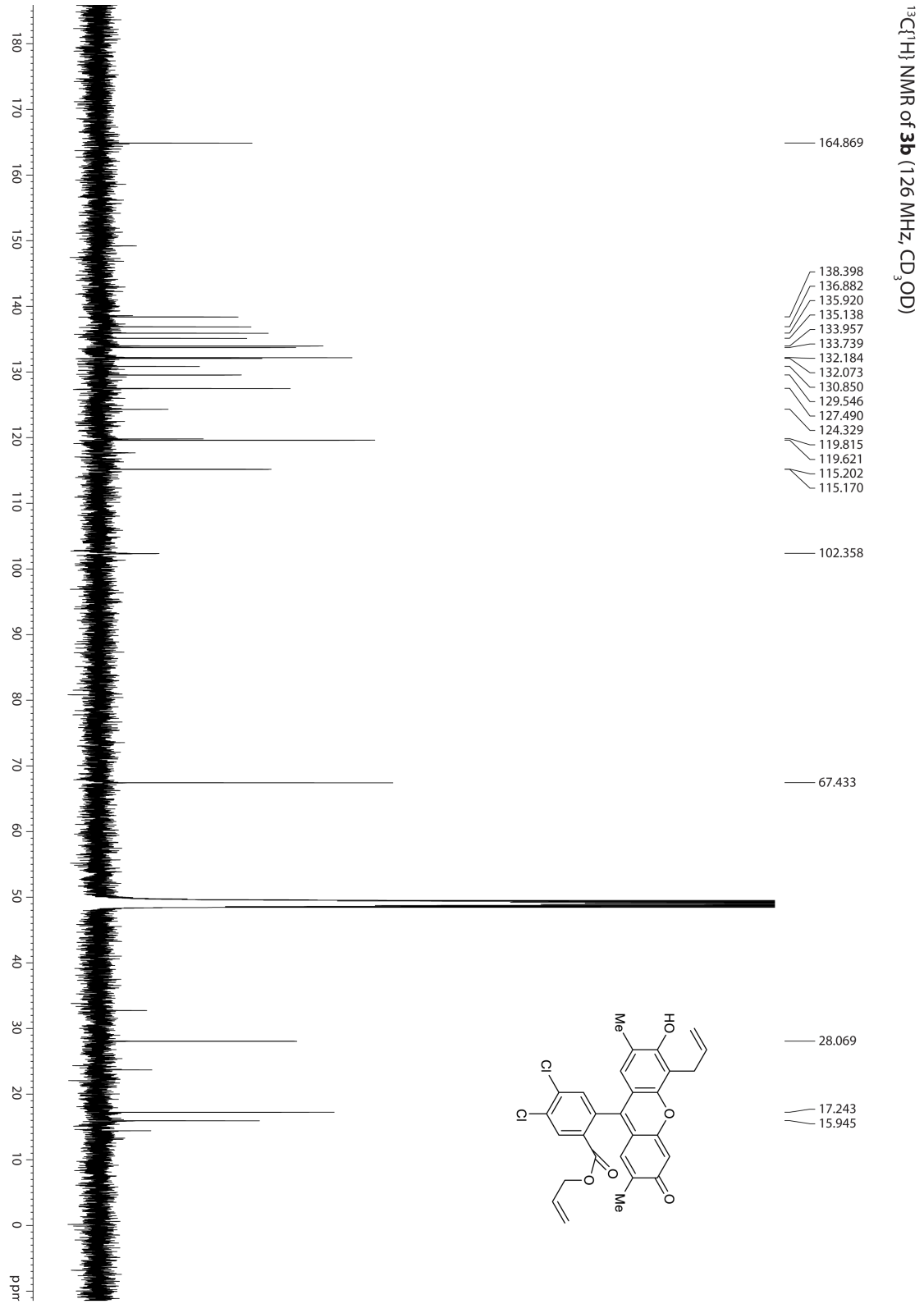

Figure 3.16: $^{13}C\{^1H\}$ NMR spectrum of 3b

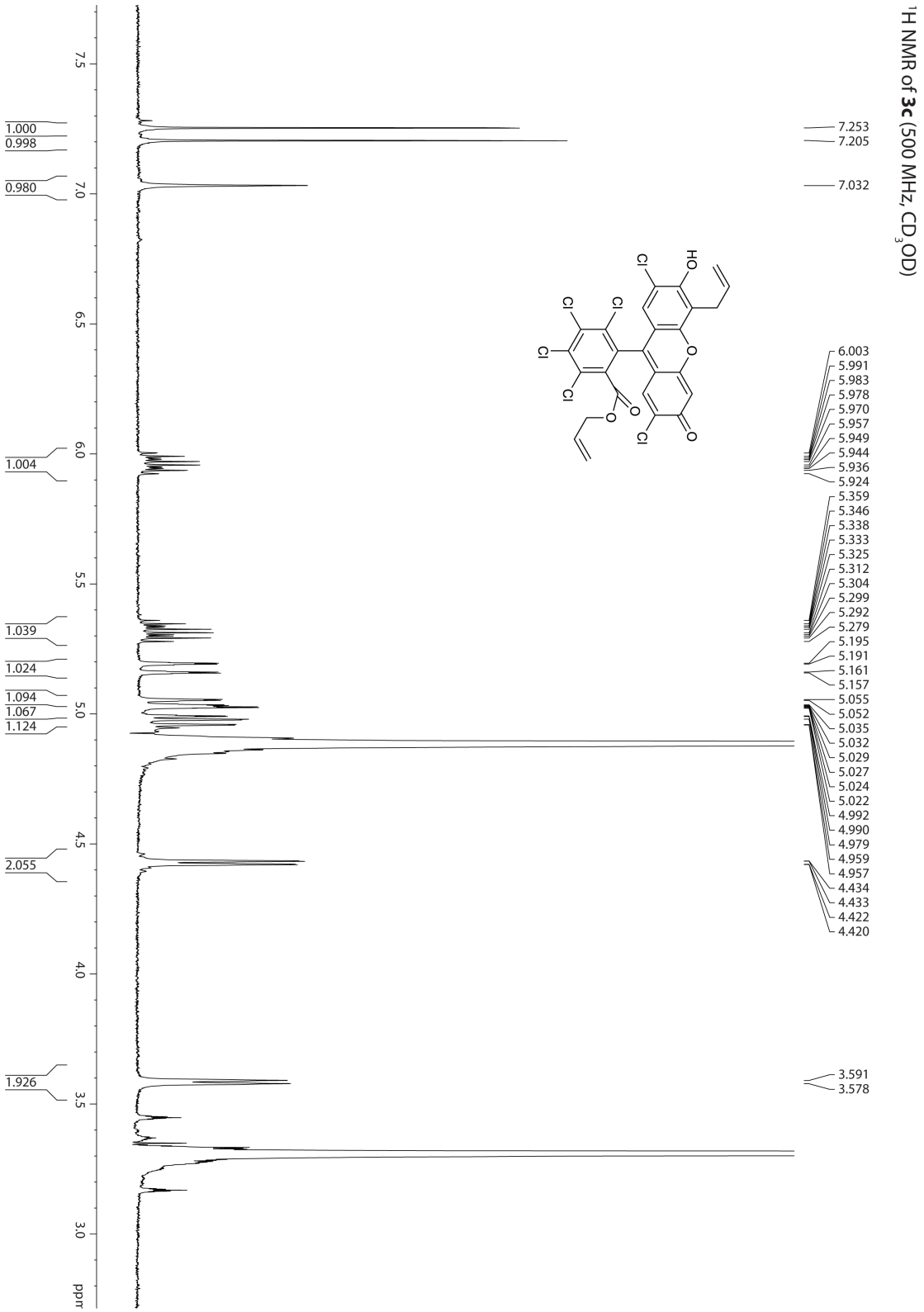

Figure 3.17: ^{1}H NMR spectrum of 3c

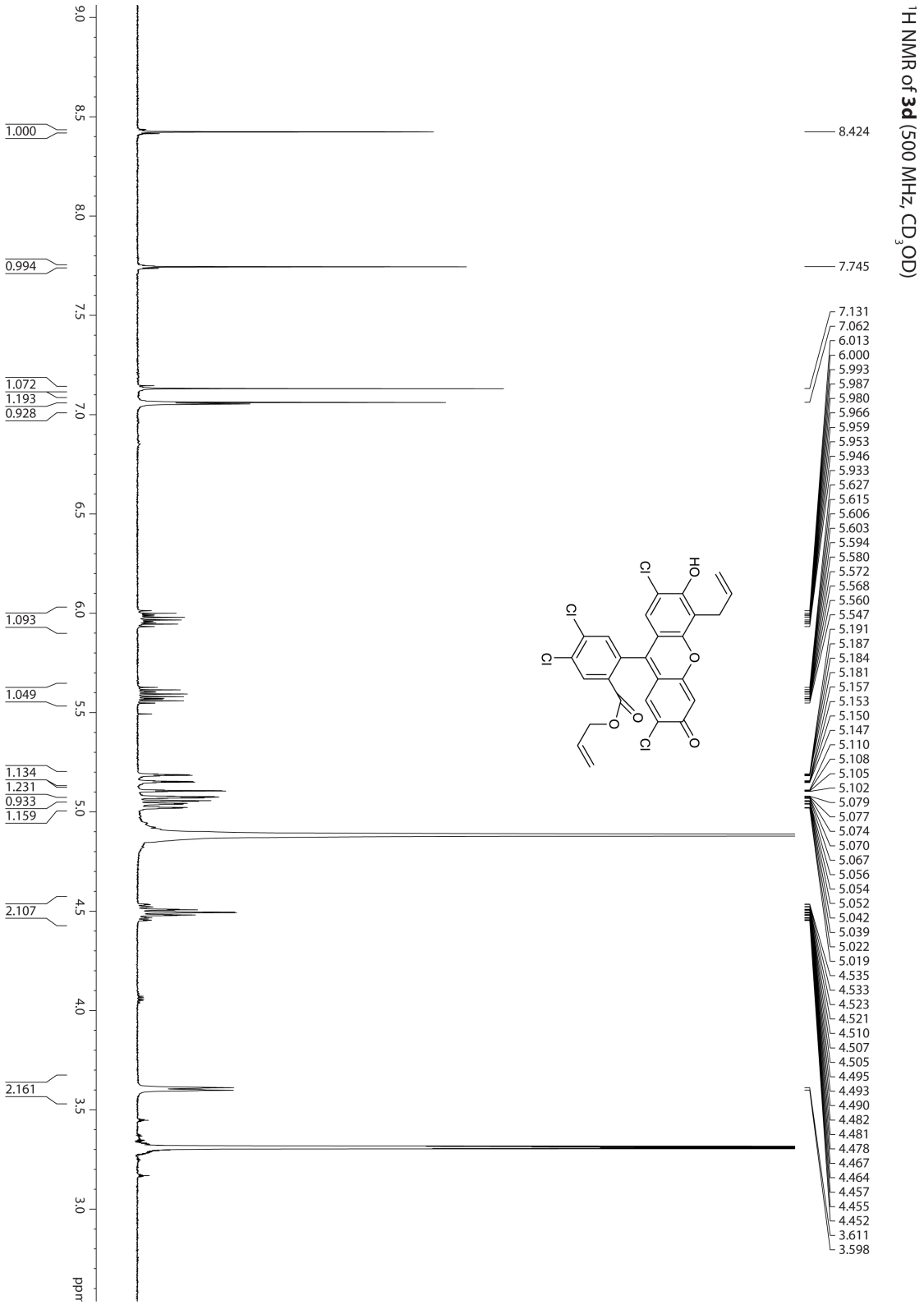

Figure 3.18: ^{1}H NMR spectrum of 3d

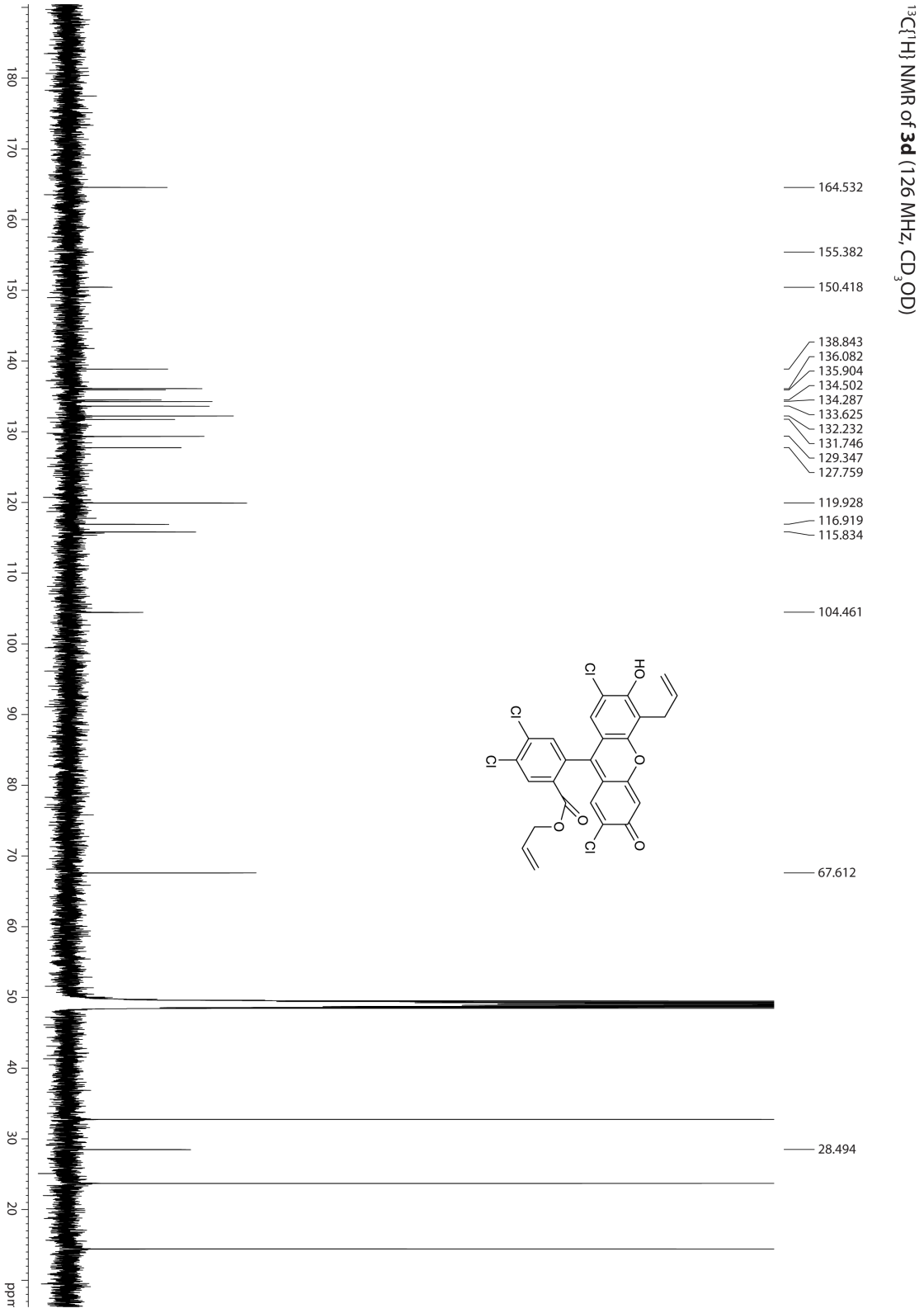

Figure 3.19: $^{13}C\{^1H\}$ NMR spectrum of 3d

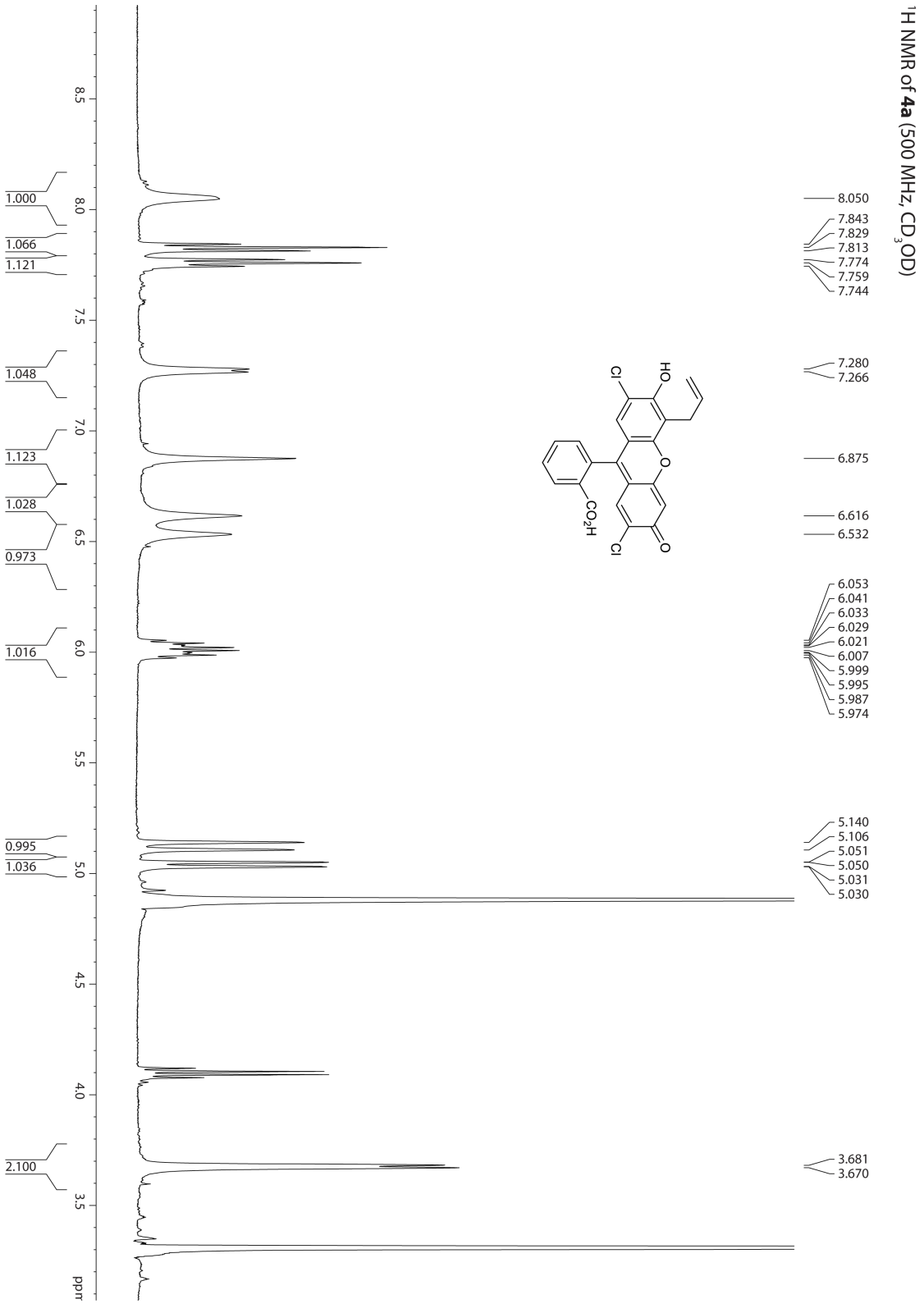

Figure 3.20: ^{1}H NMR spectrum of 4a

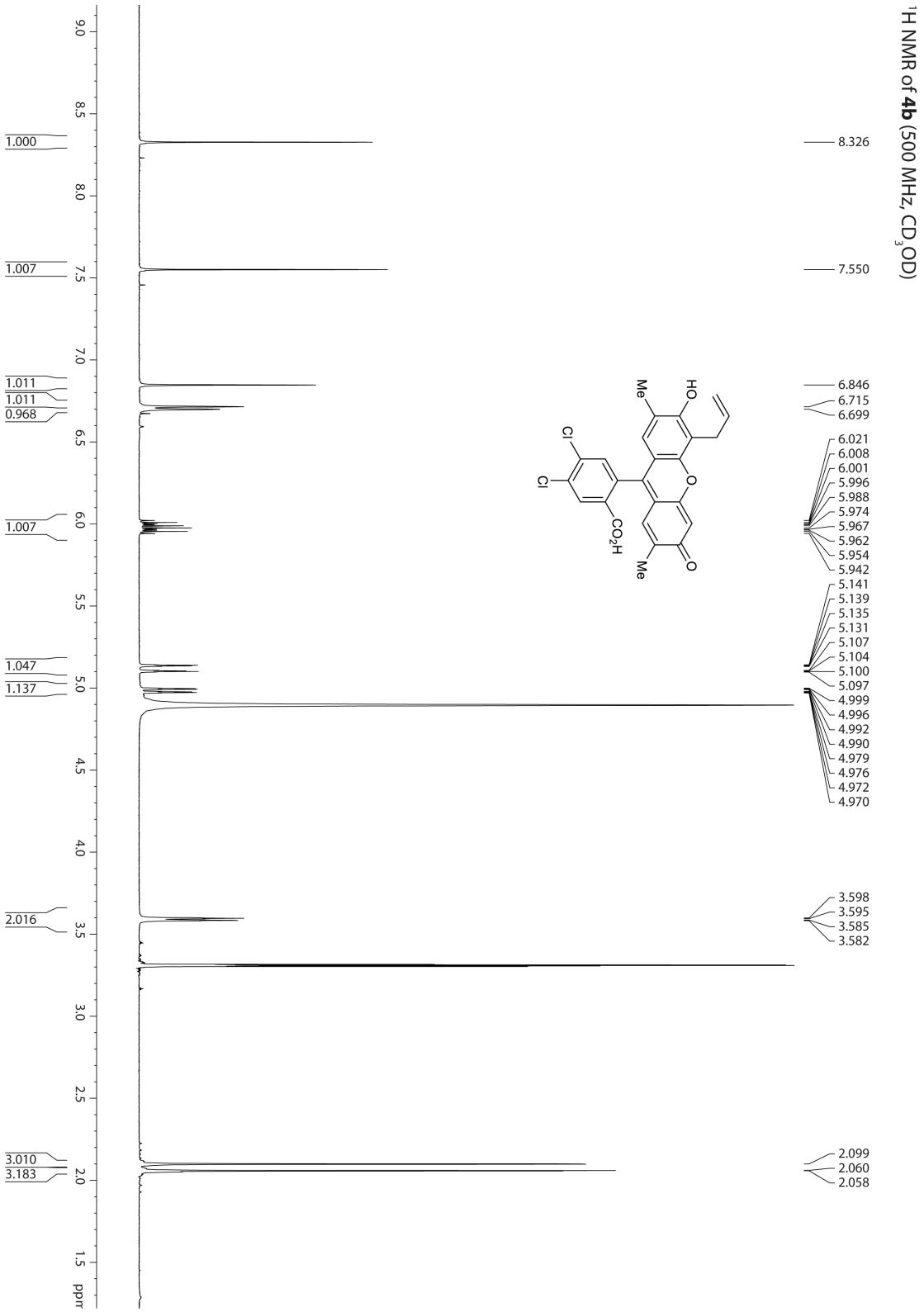

Figure 3.21: ^{1}H NMR spectrum of 4b

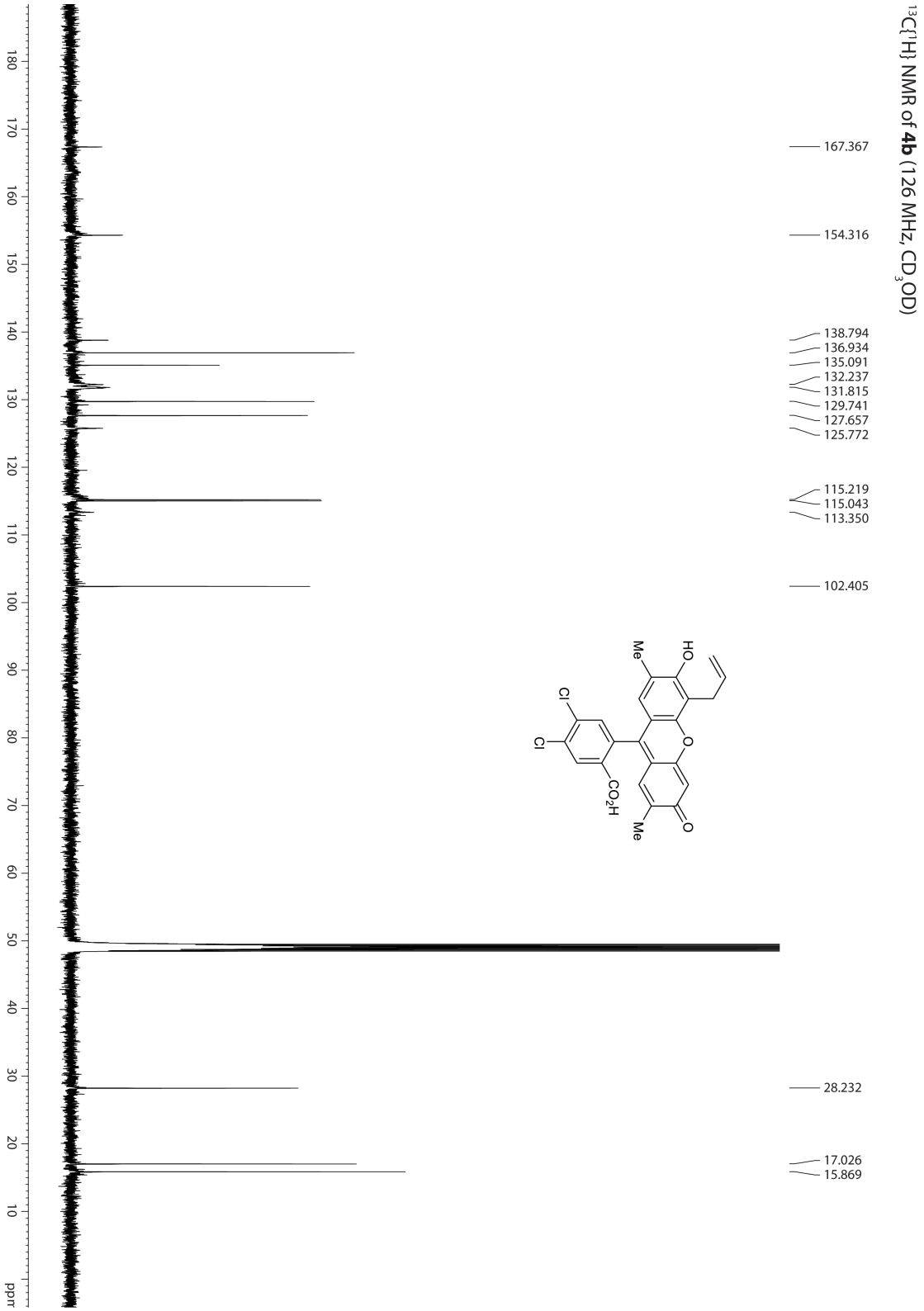

Figure 3.22: $^{13}C\{^1H\}$ NMR spectrum of 4b

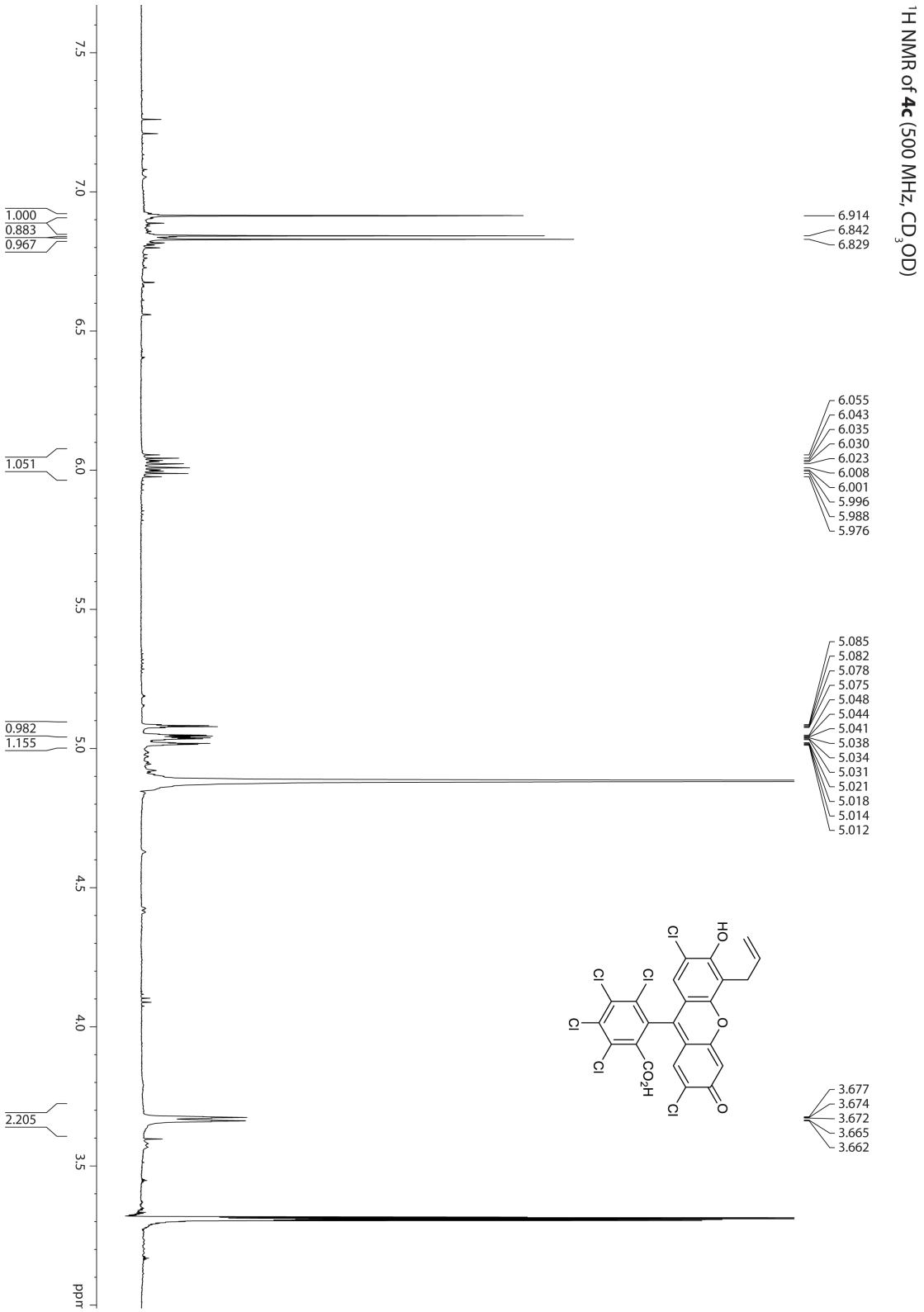

Figure 3.23: ^{1}H NMR spectrum of 4c

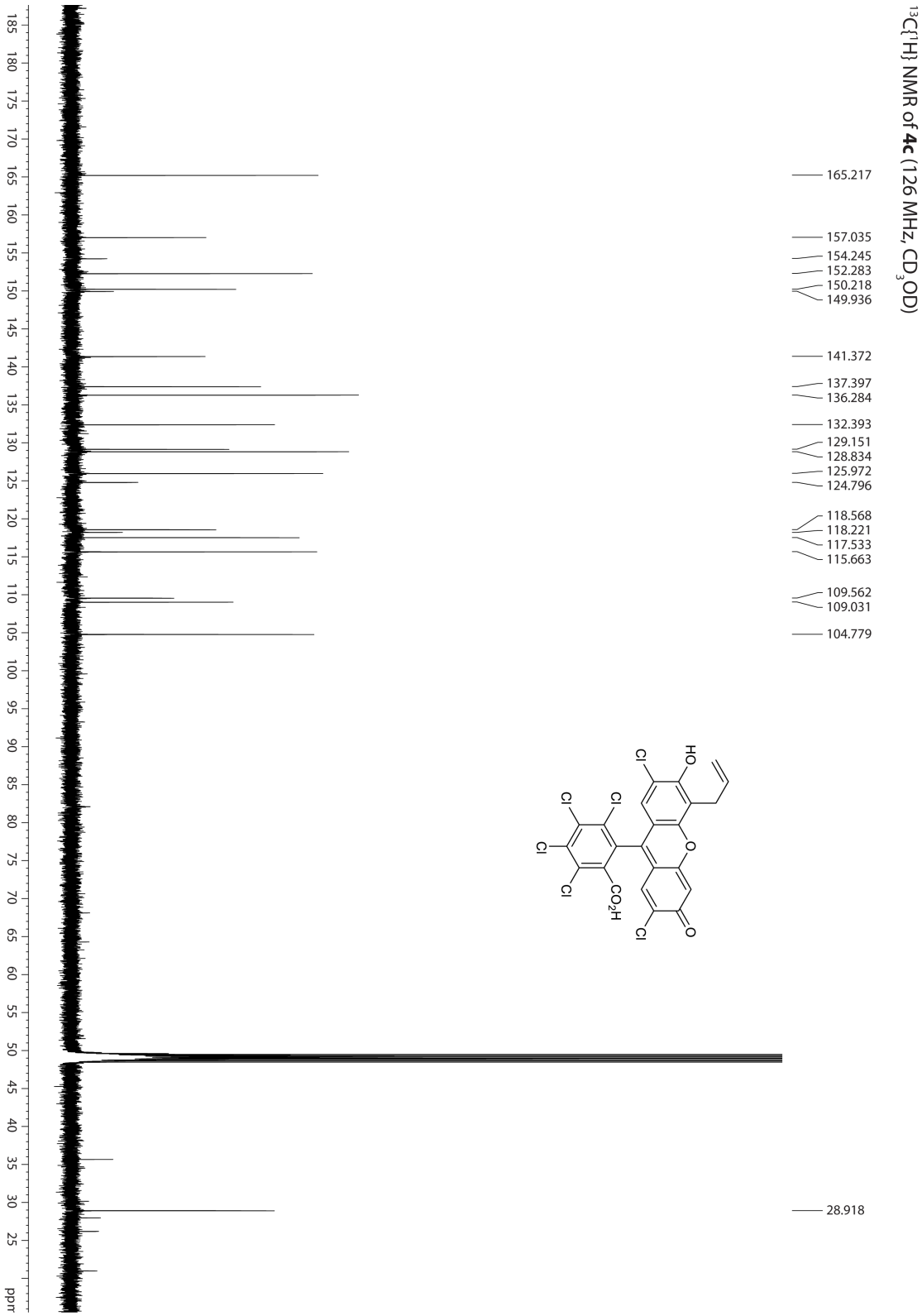

Figure 3.24: $^{13}C\{^1H\}$ NMR spectrum of 4c

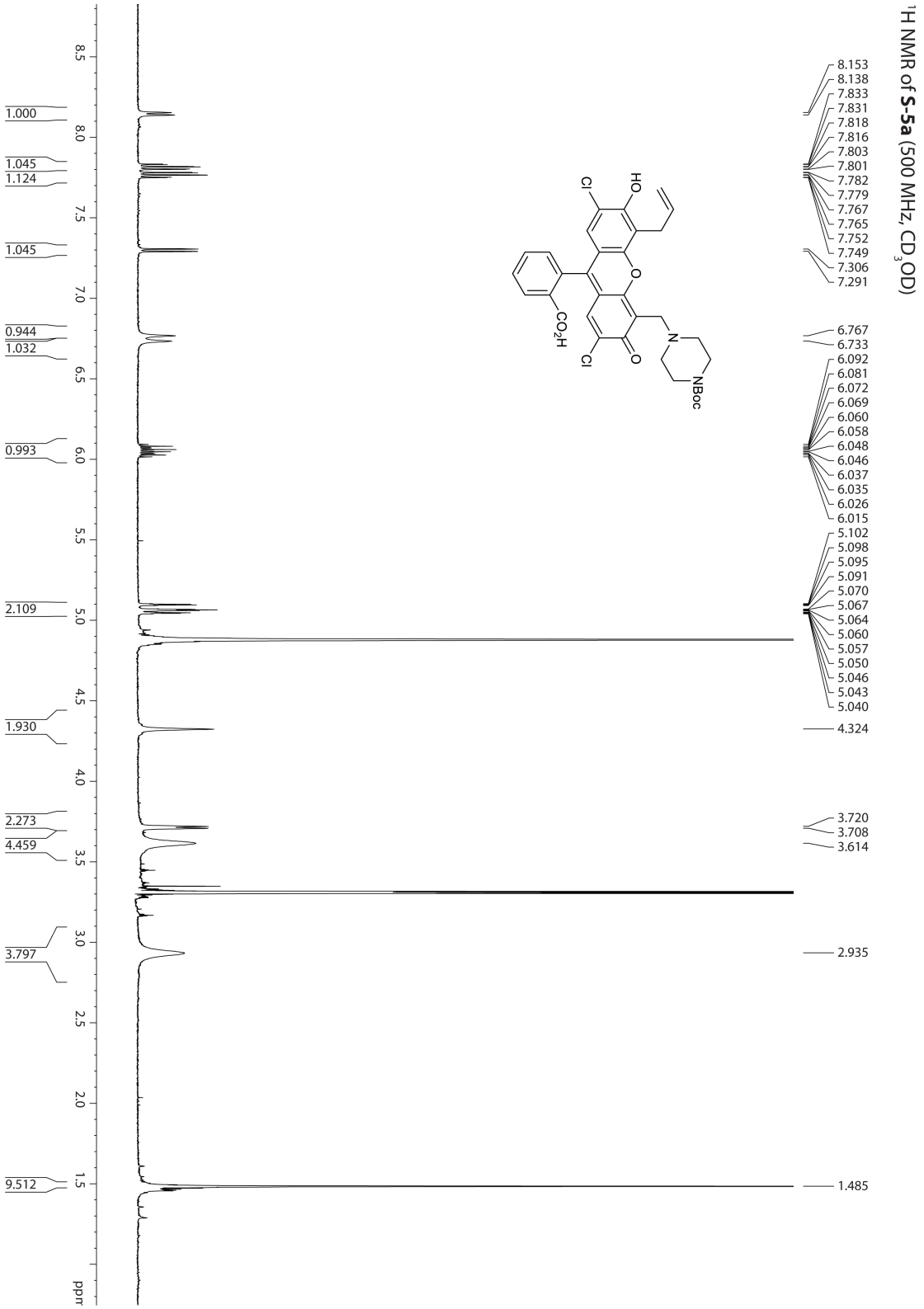

Figure 3.25: ^{1}H NMR spectrum of 5a

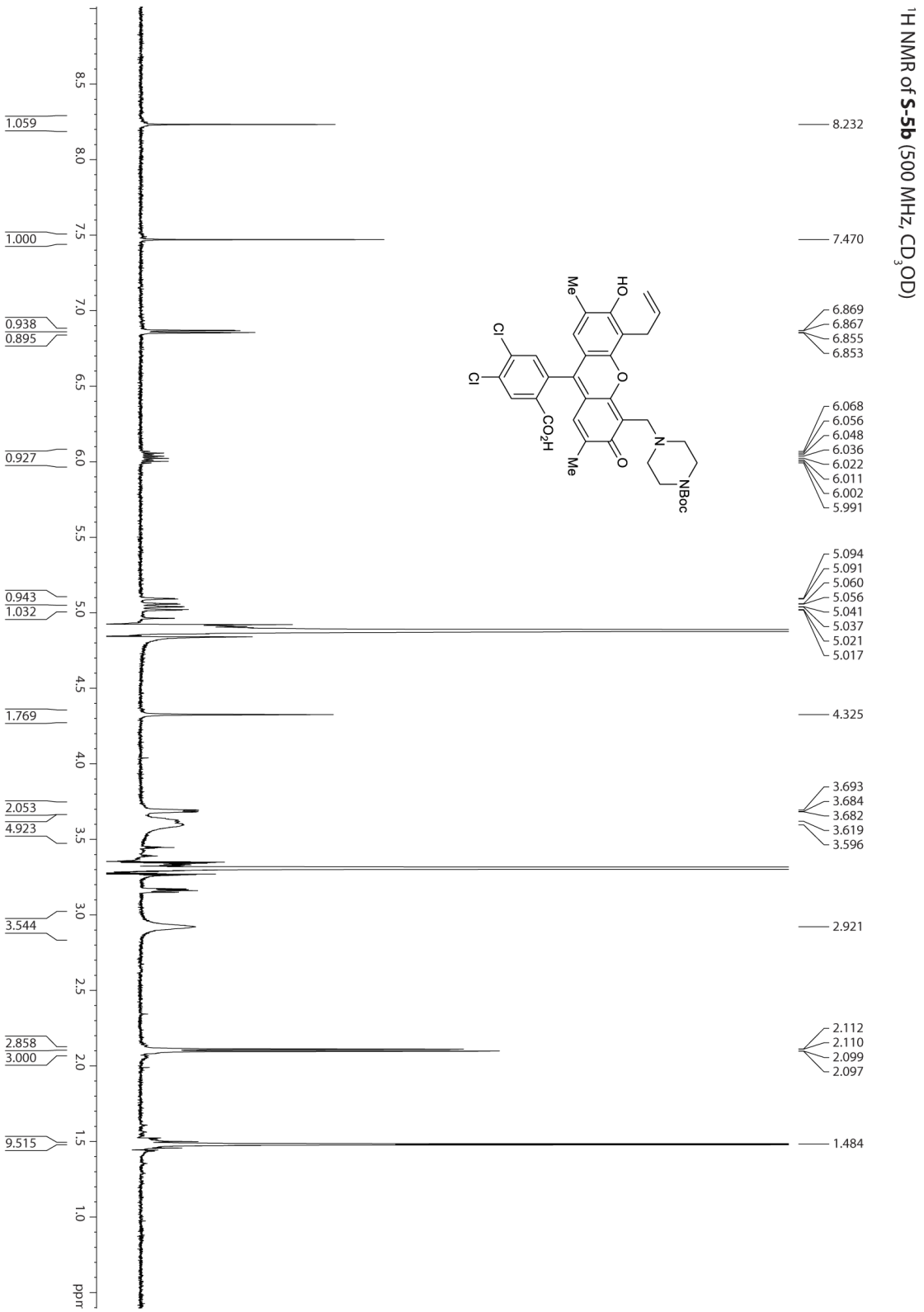

Figure 3.26: ^{1}H NMR spectrum of 5b

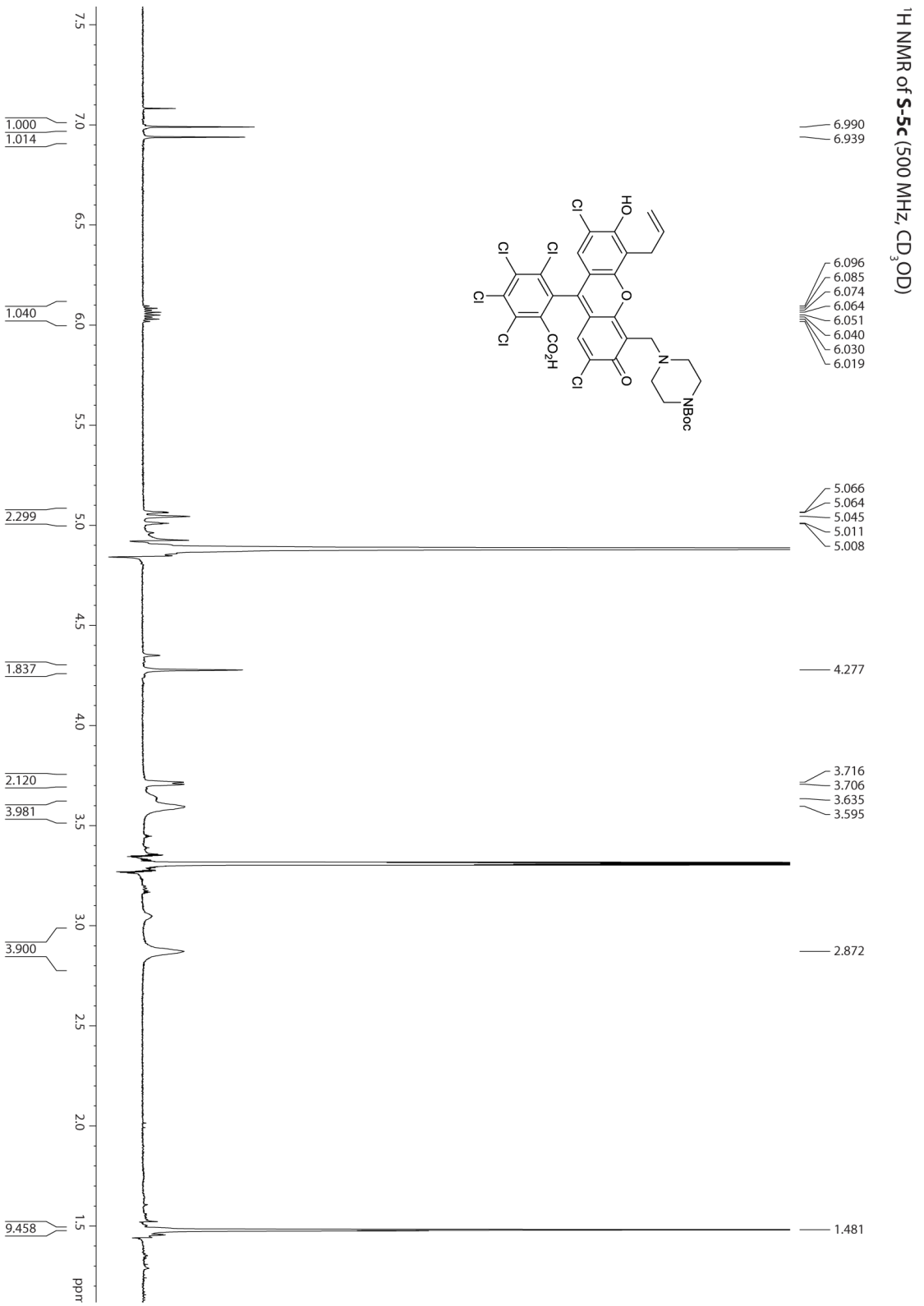

Figure 3.27: ^{1}H NMR spectrum of 5c

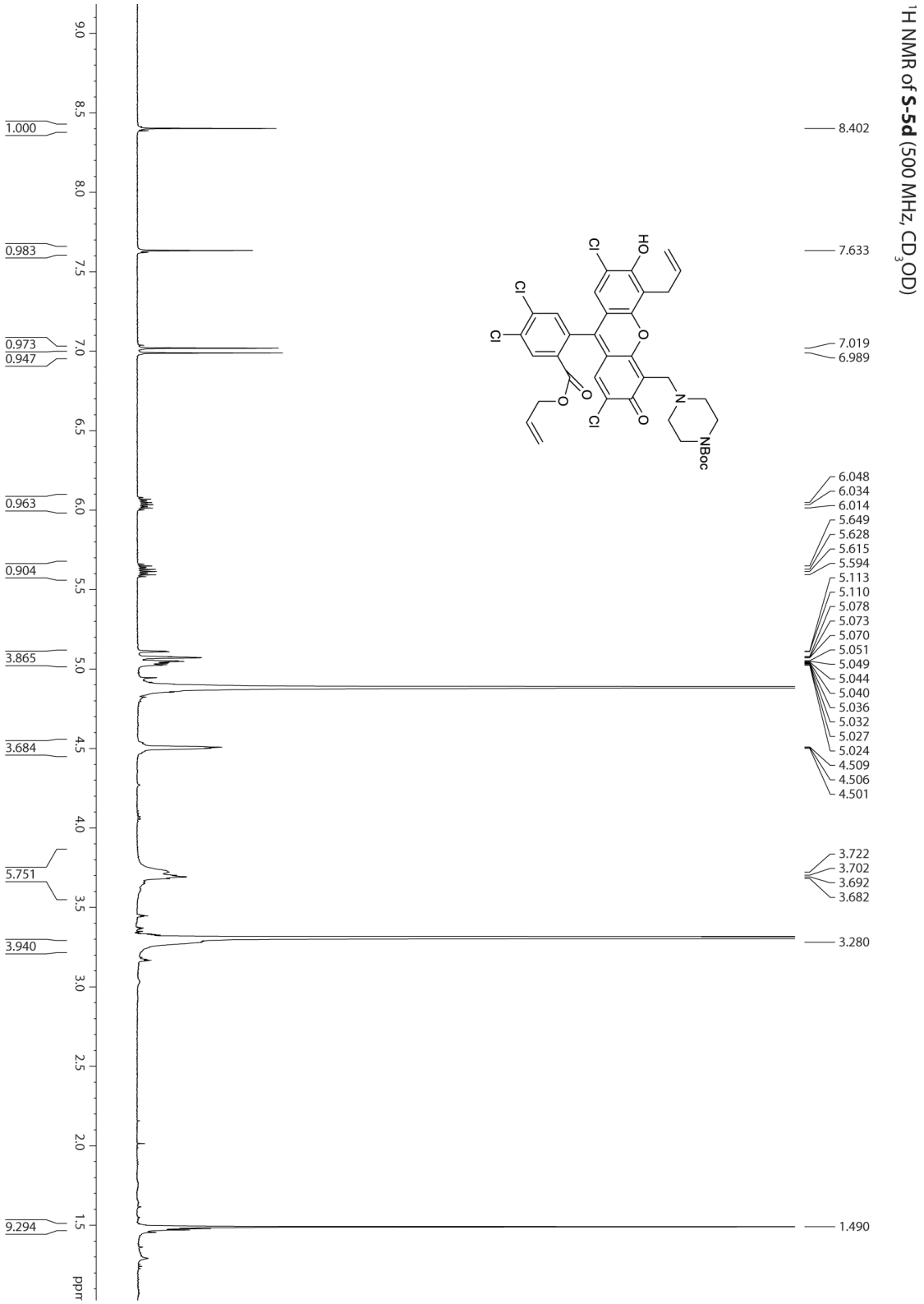

Figure 3.28: ^{1}H NMR spectrum of 5d

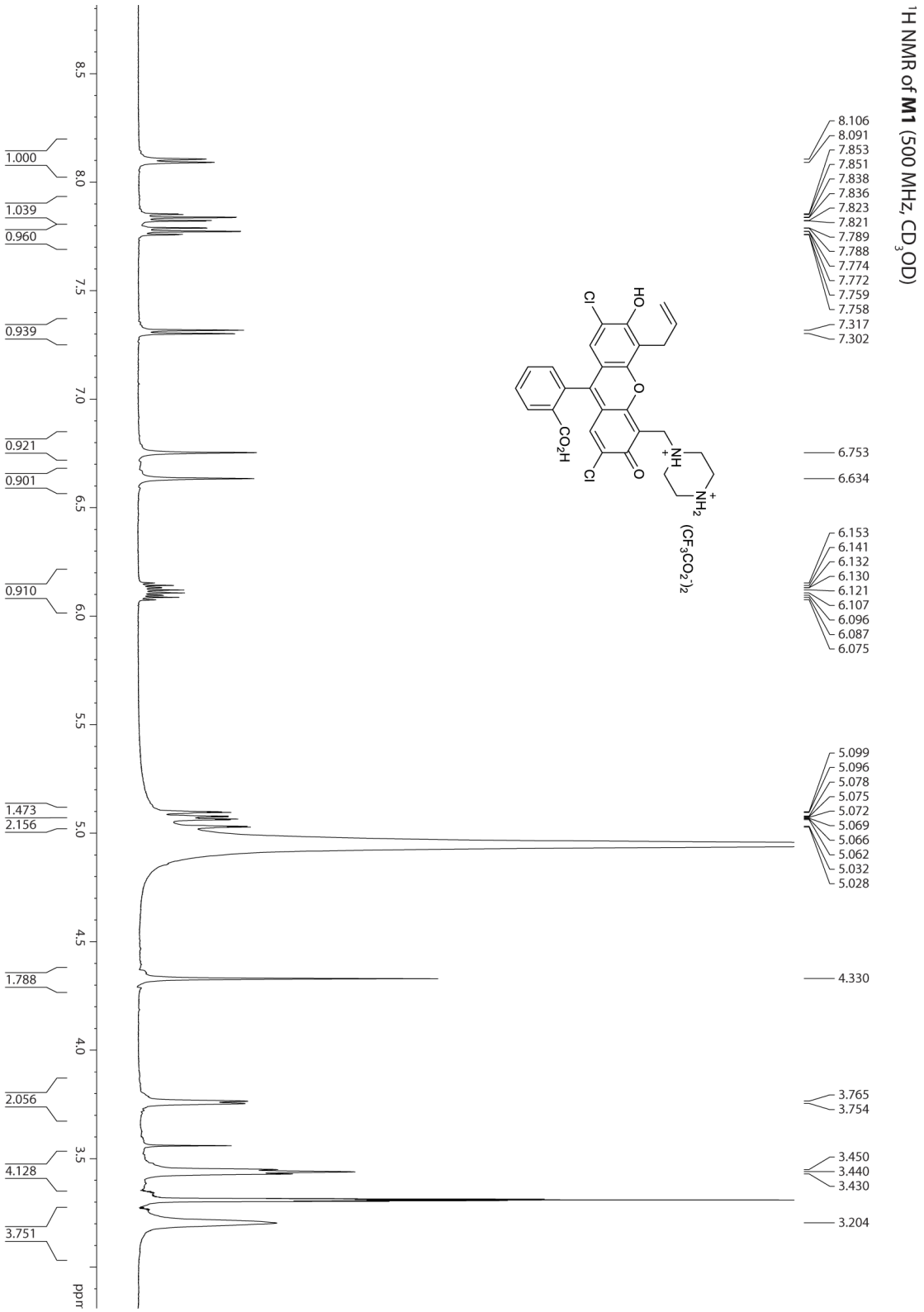

Figure 3.29: ^{1}H NMR spectrum of M1

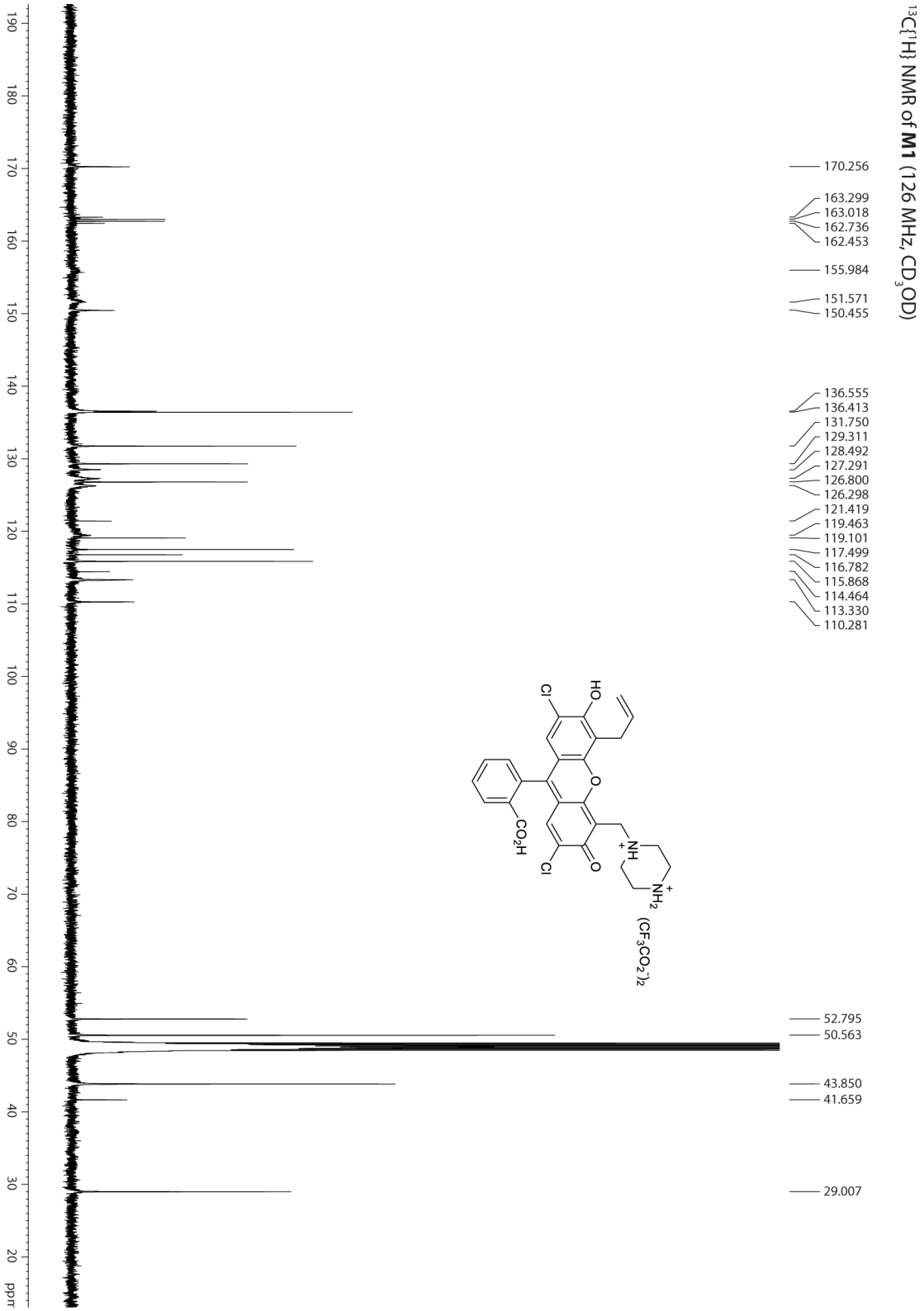

Figure 3.30: $^{13}C\{^1H\}$ NMR spectrum of M1

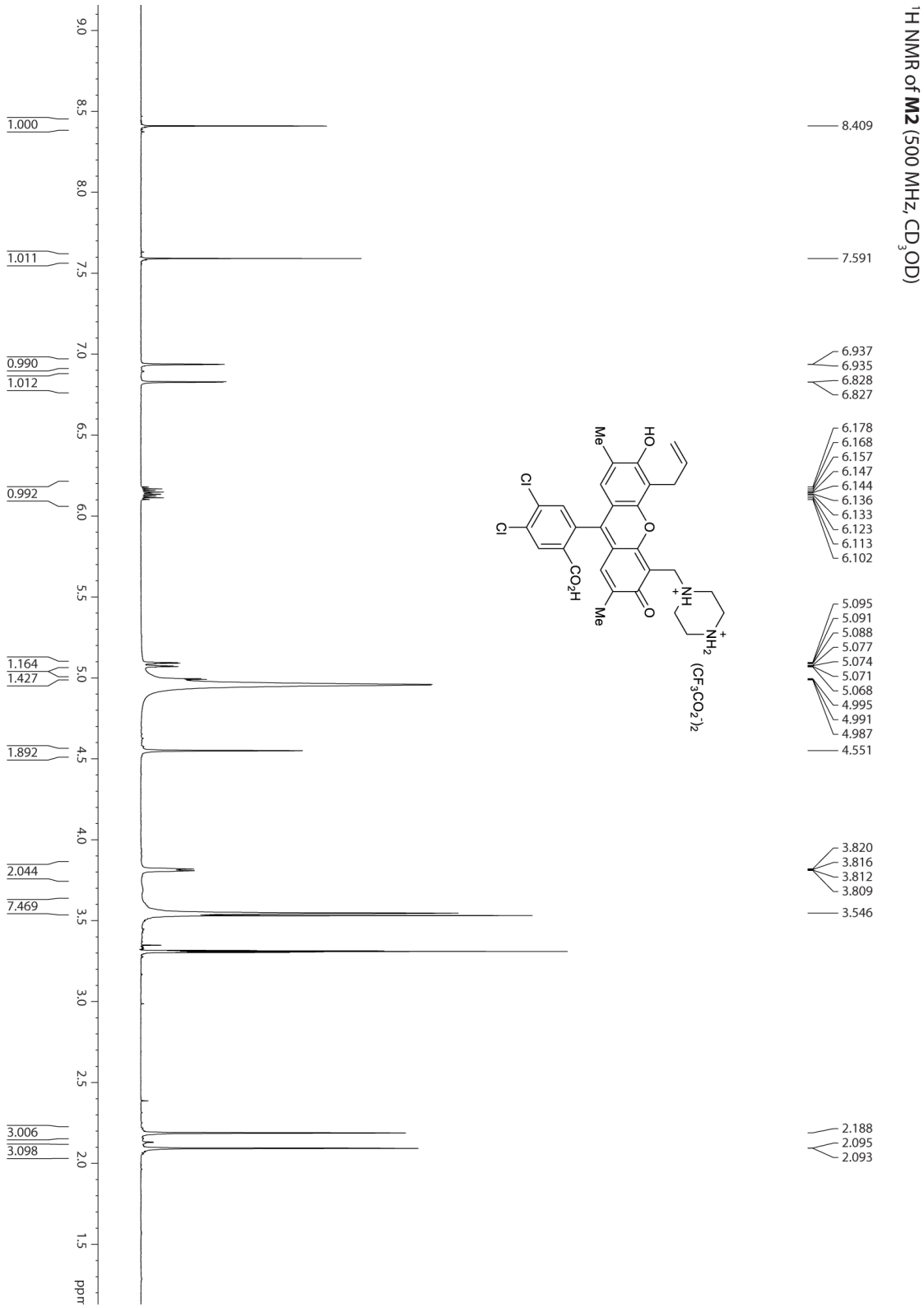

Figure 3.31: ^{1}H NMR spectrum of M2

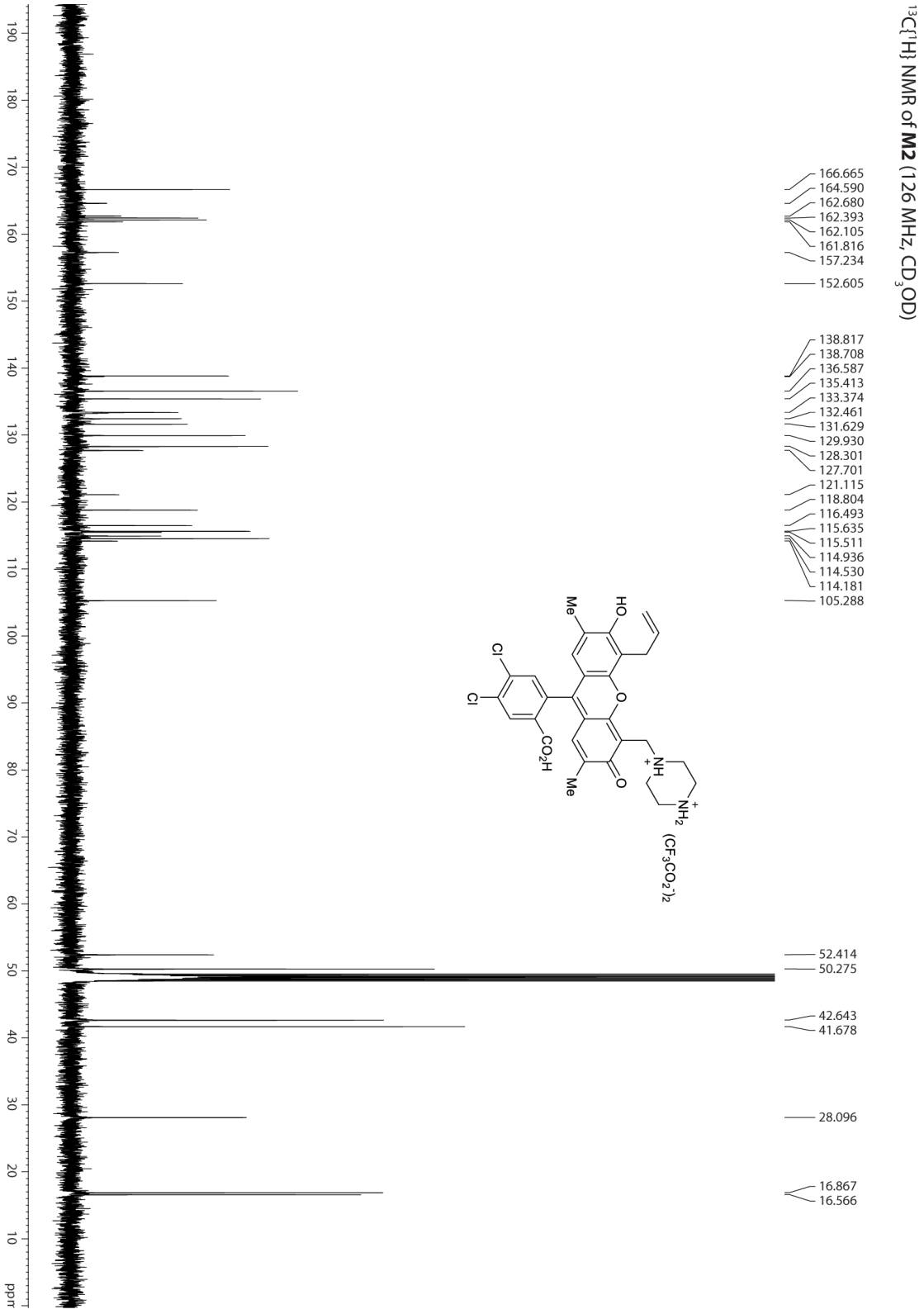

Figure 3.32: $^{13}C\{^1H\}$ NMR spectrum of M2

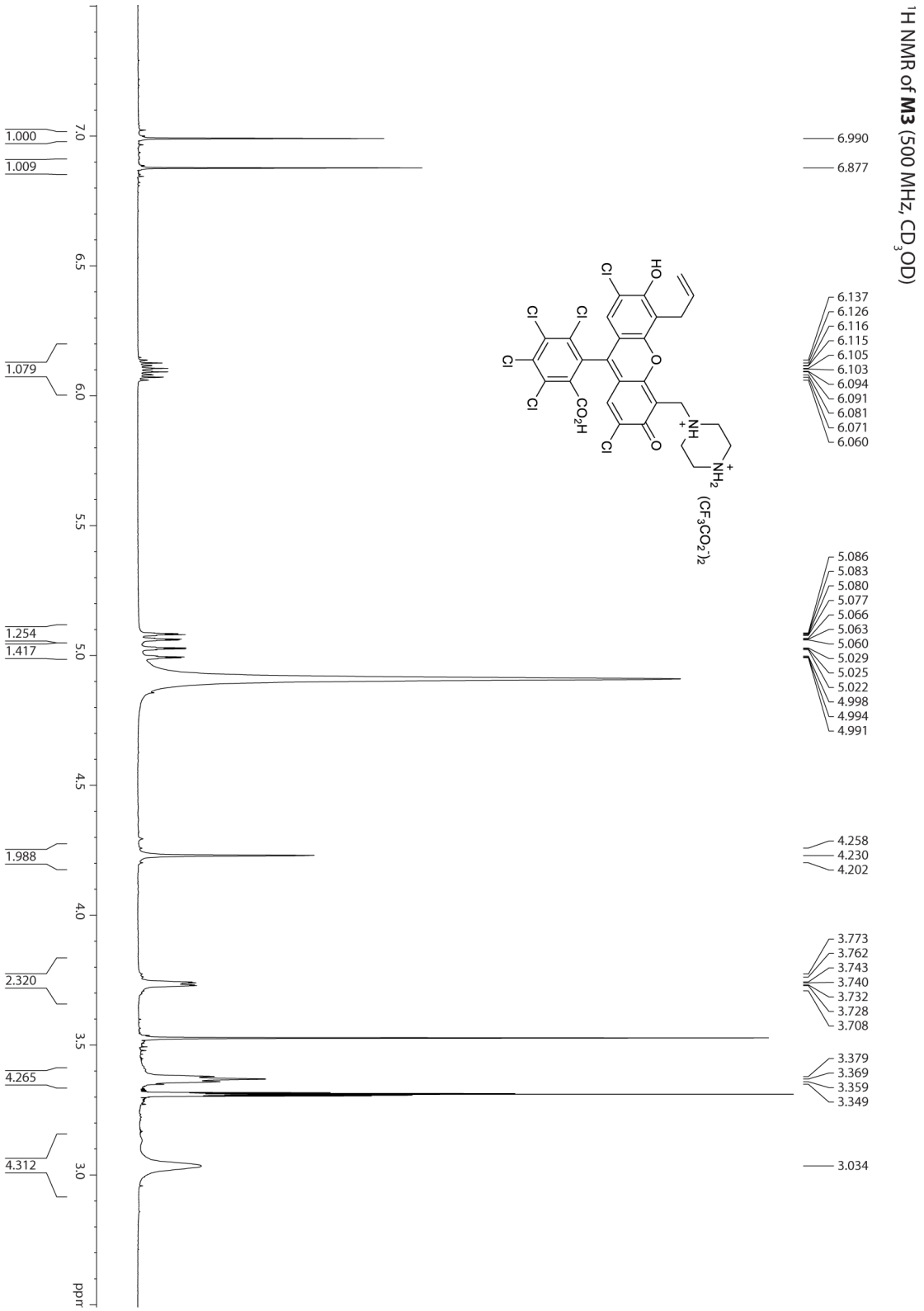

Figure 3.33: ^{1}H NMR spectrum of M3

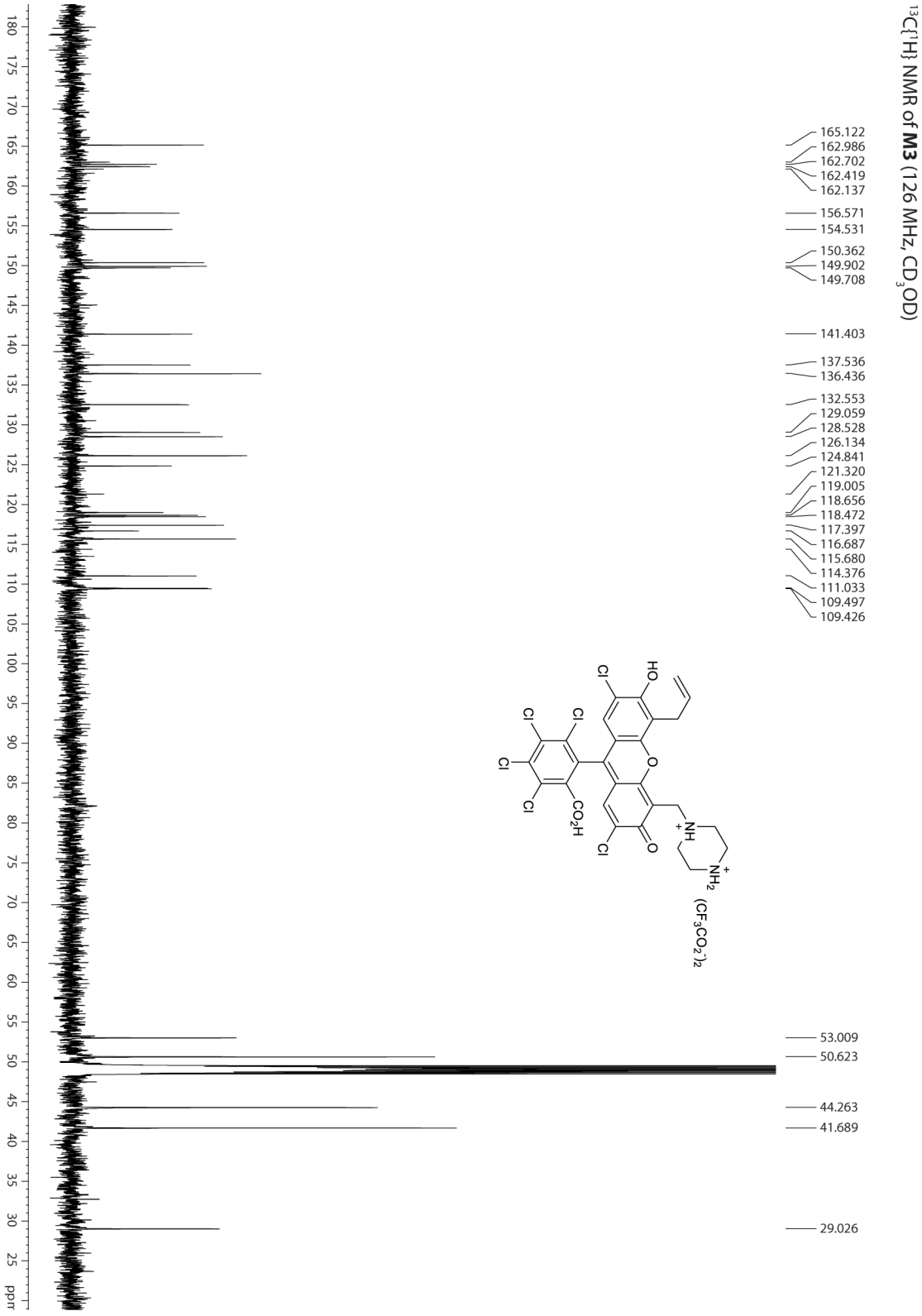

Figure 3.34: $^{13}C\{^1H\}$ NMR spectrum of M3

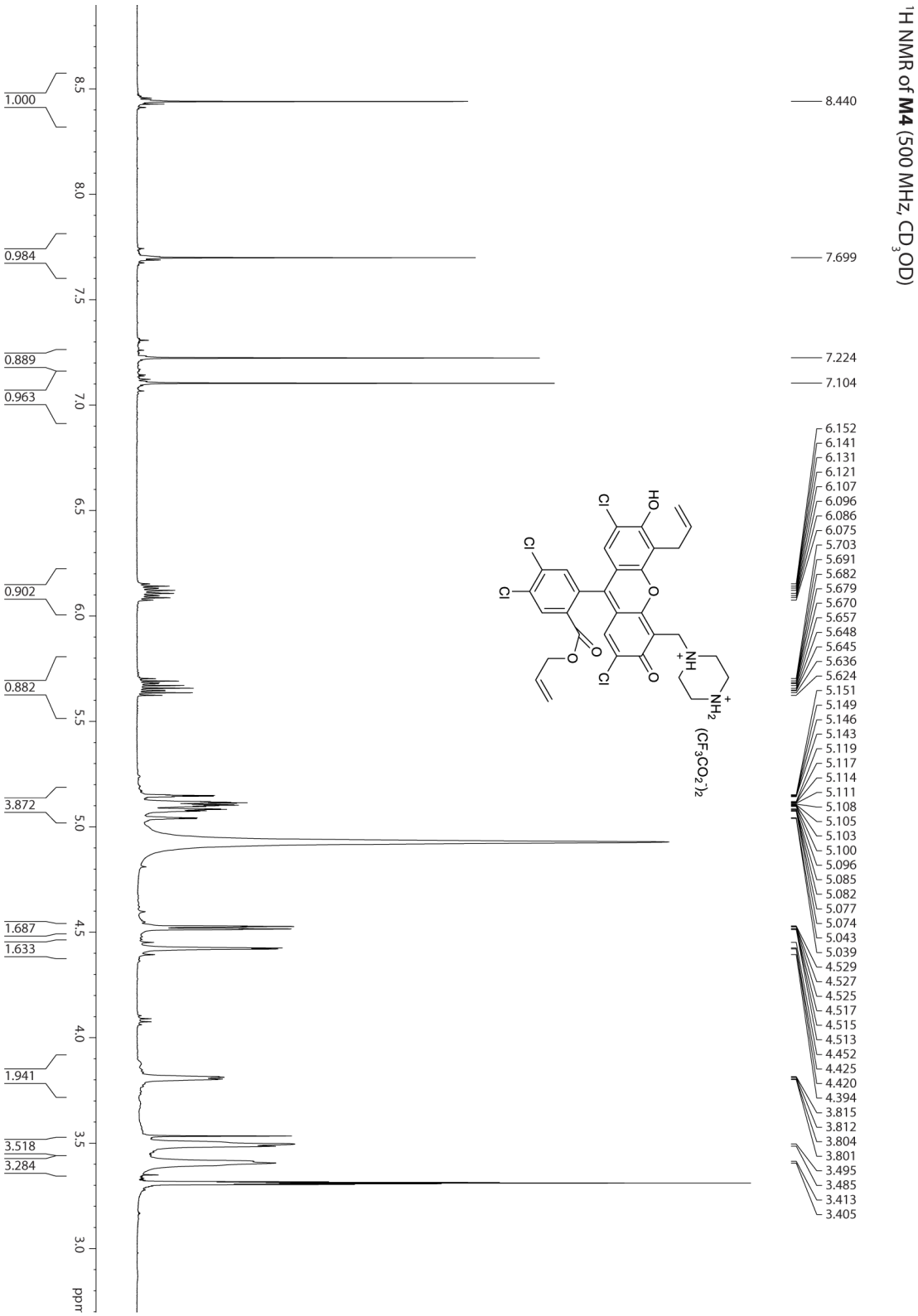

Figure 3.35: ^{1}H NMR spectrum of M4

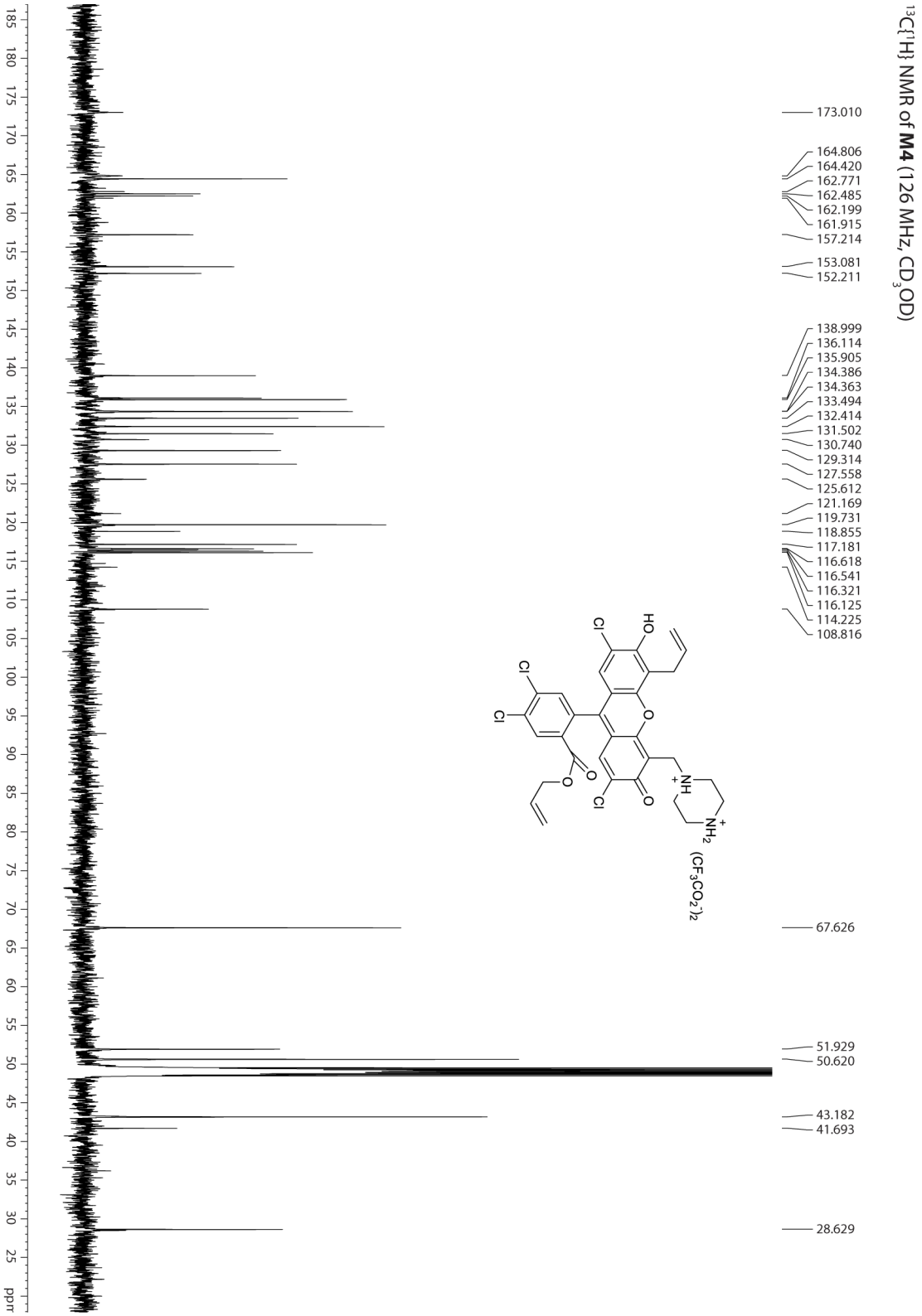

Figure 3.36: $^{13}C\{^1H\}$ NMR spectrum of M4

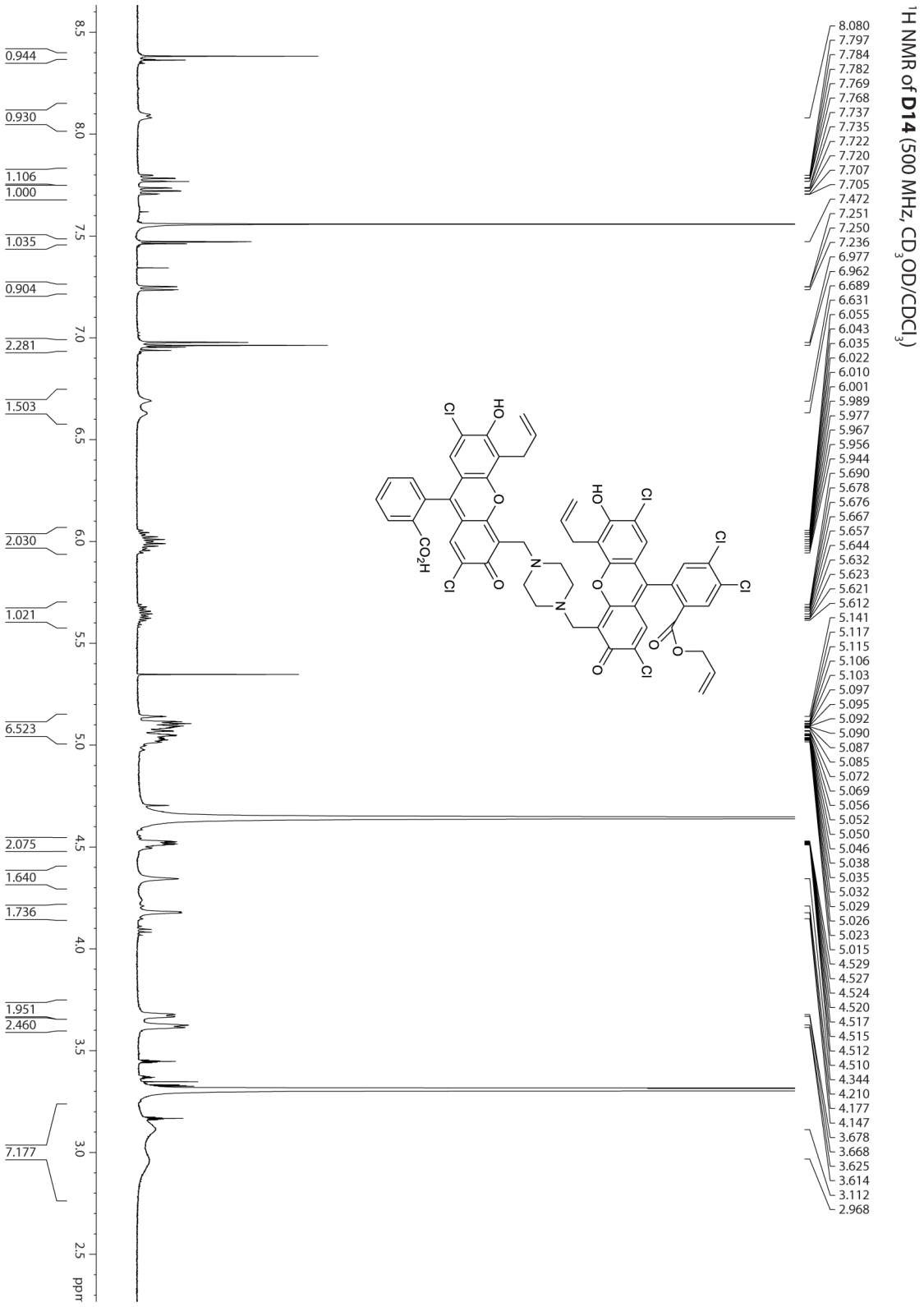

Figure 3.37: ^{1}H NMR spectrum of D14

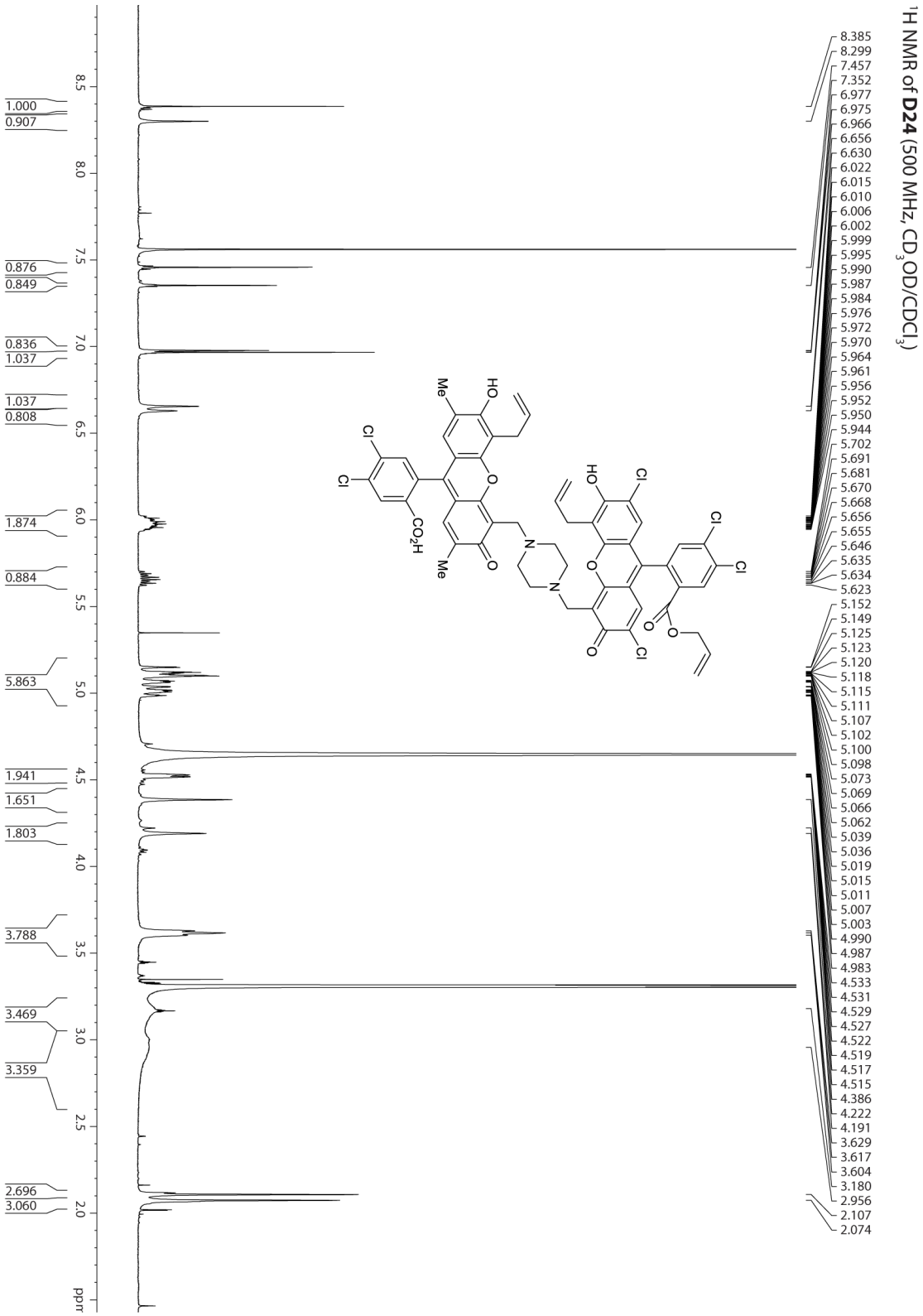

Figure 3.38: ^{1}H NMR spectrum of D24

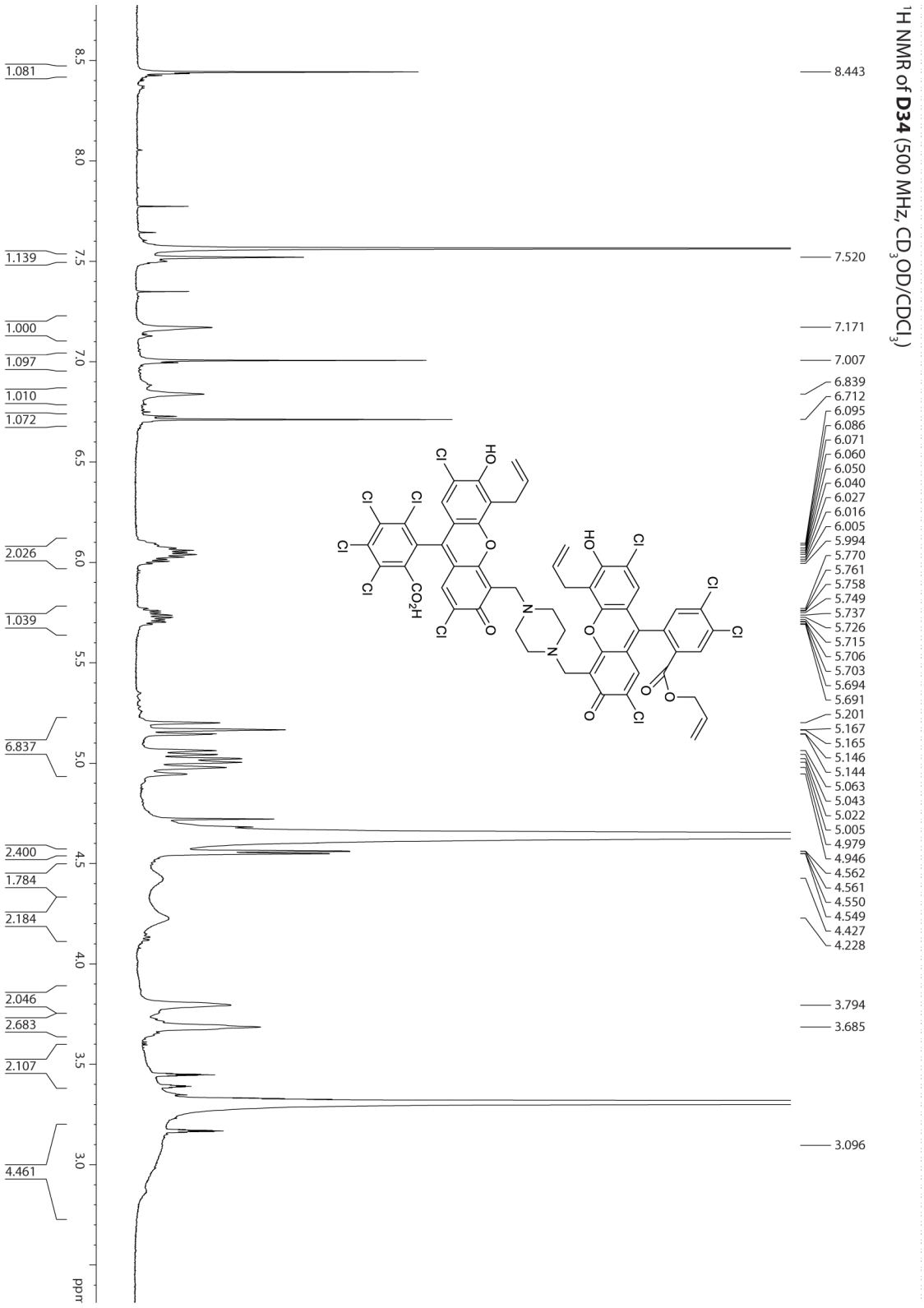

Figure 3.39: ^{1}H NMR spectrum of D34

3.4 Single-walled nanotube packing strategy and affinity tests

The strategy of using single-walled nanotubes (SWNTs) as substrates to restrict the distribution of relative orientations of the chromophores is potentially applicable to all chromophores with strong π-stacking properties. Here, we employ this approach to separately test energetic requirements and the impact of spatial relationships on coherences. Our goal is to test hypotheses and conditions that have given rise to long-lived quantum beating signals in photosynthetic systems. Unfortunately, such a test is impossible to realize in natural photosynthetic systems. The mutation of photosynthetic systems by deuteration or adjusting amino acids of proteins affects energy gaps but does not seem to change coherences in these mutants [24, 36, 37]. Photosynthetic protein-chromophore complexes cannot be engineered to provide the prescribed rotation of the chromophores. We therefore have designed the heterodimers described in section 3.3 to allow control over the energy gaps while simultaneously and separately allowing some control over the relative orientation between the chromophores.

3.4.1 Packing fluorescein heterodimers on single-walled nanotubes

A 20 mL scintillation vial was charged with 5.0 mg of SWNTs (carbon nanotube, single-walled, poly(ethylene glycol) functionalized, Aldrich) and 10.0 mL of EtOH (200 proof). The mixture was sonicated for 30 min in a water bath. The temperature of the water bath rose from room temperature to ca. 50 °C at the end. The SWNT suspension was kept still in a water bath at room temperature for 10 min. 4.0 mL of the SWNT suspension was pipetted out from the top of the 10.0 mL SWNT suspension. 4.0 mg of each heterodimer was dissolved separately in EtOAc (4.0 mL) and pipetted separately into the 4.0 mL SWNT suspension. The mixture was sonicated for 10 min in a water bath at room temperature and stirred overnight at room temperature to yield suspensions of fluffy fluorescein/SWNT aggregates. The suspension was centrifuged for 20 min (Spectrafuge 16M, Labnet), and the solid residues were washed twice with EtOAc and once with EtOH. The resulting aggregates

were dissolved in EtOH with 2 vol.% triethylamine and diluted to an optical density of approximately 0.2 for 200 μm path length. These samples were then measured by 2DES.

3.4.2 Packing fluorescein monomers on single-walled nanotubes

Because M1-4 are fluorescein TFA salts, the TFA content may vary between samples. To exclude the effects of TFA, we used 4a, 4b, 4c, and 3d for the affinity test. 8.0 mL of the SWNT suspension was pipetted out from the top of a freshly prepared 10.0 mL SWNT suspension and divided into four equal portions (2.0 mL each). Compounds 4a, 4b, 4c, and 3d (2.0 mg each) were dissolved separately in EtOH (2.0 mL, 200 proof) and pipetted separately into the SWNT suspensions (2.0 mL each). The four mixtures were sonicated for 10 min in a water bath at room temperature and stirred overnight at room temperature to yield suspensions of fluffy fluorescein/SWNT aggregates. The suspensions were centrifuged for 20 min, and the solid residues were washed three times with EtOH (200 proof). The resulting aggregates were dissolved in 1 mL of EtOH with 2 vol.% triethylamine and subjected to linear absorption measurements.

3.4.3 Packing affinity test

6.0 mL of the SWNT suspension was pipetted out from the top of a freshly prepared 10.0 mL SWNT suspension and divided into three portions of equal volume (2.0 mL each). Compounds 4c, 3d, and D34 (2.0 mg each) were dissolved separately in EtOAc (2.0 mL, 200 proof) and pipetted separately into the SWNT suspensions (2.0 mL each). The three mixtures were sonicated for 10 min in a water bath at room temperature and stirred overnight at room temperature to yield suspensions of fluffy fluorescein/SWNT aggregates. The suspensions were centrifuged for 20 min, and the solid residues were washed twice with EtOAc and once with EtOH (200 proof). The resulting aggregates were dissolved in 1 mL of EtOH with 2 vol.% triethylamine and subjected to linear absorption measurements. The resulting linear absorption spectra are shown in Figure 3.40.

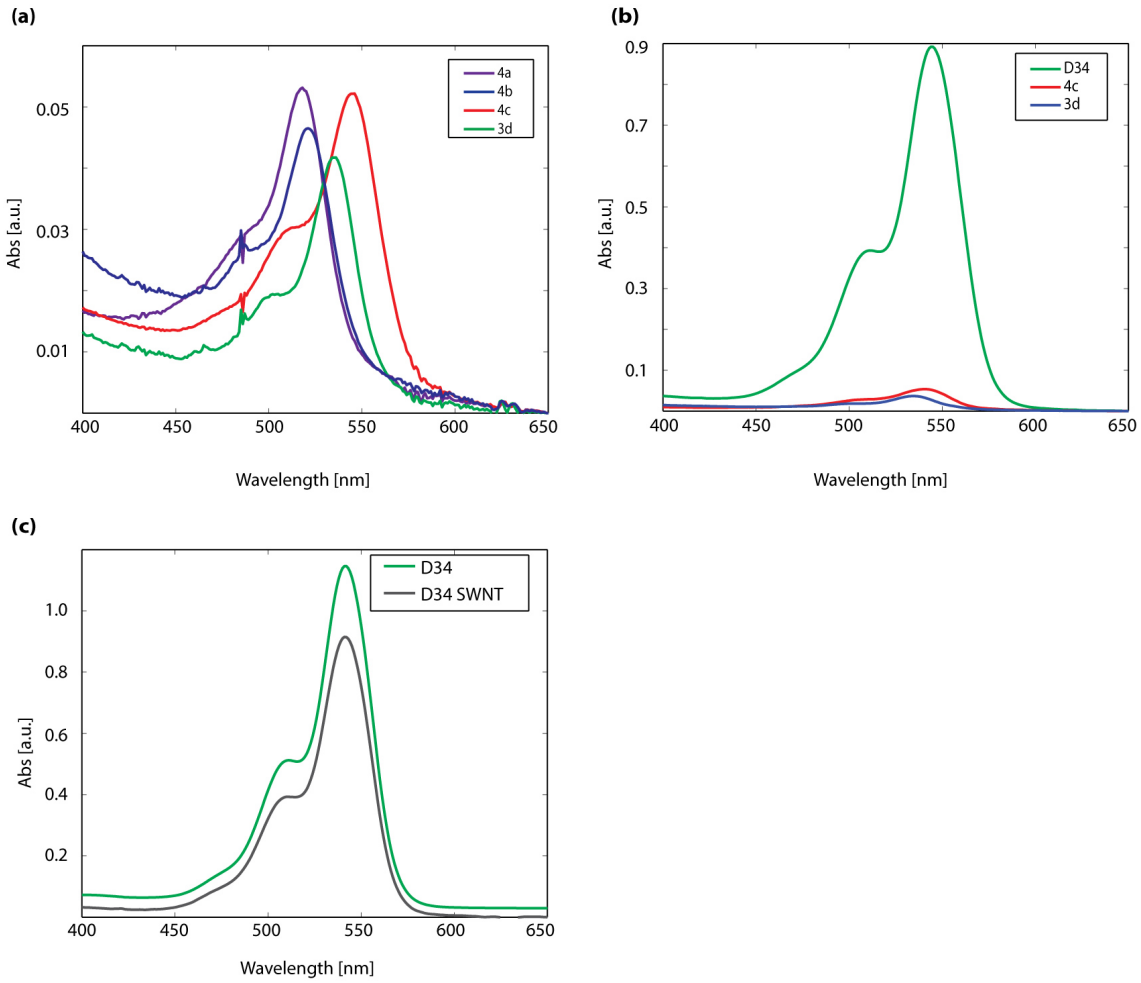

Figure 3.40: Packing affinity tests show the rigidity of heterodimers on SWNTs. (a) Packing affinity test of 4a, 4b, 4c, and 3d shows similar affinities for each monomer. (b) Packing affinity test of 4c, 3d, and D34. (c) Linear absorption spectra of D34 with and without SWNTs are almost identical, indicating that the energy gaps in dimers are reserved when packed on SWNTs.

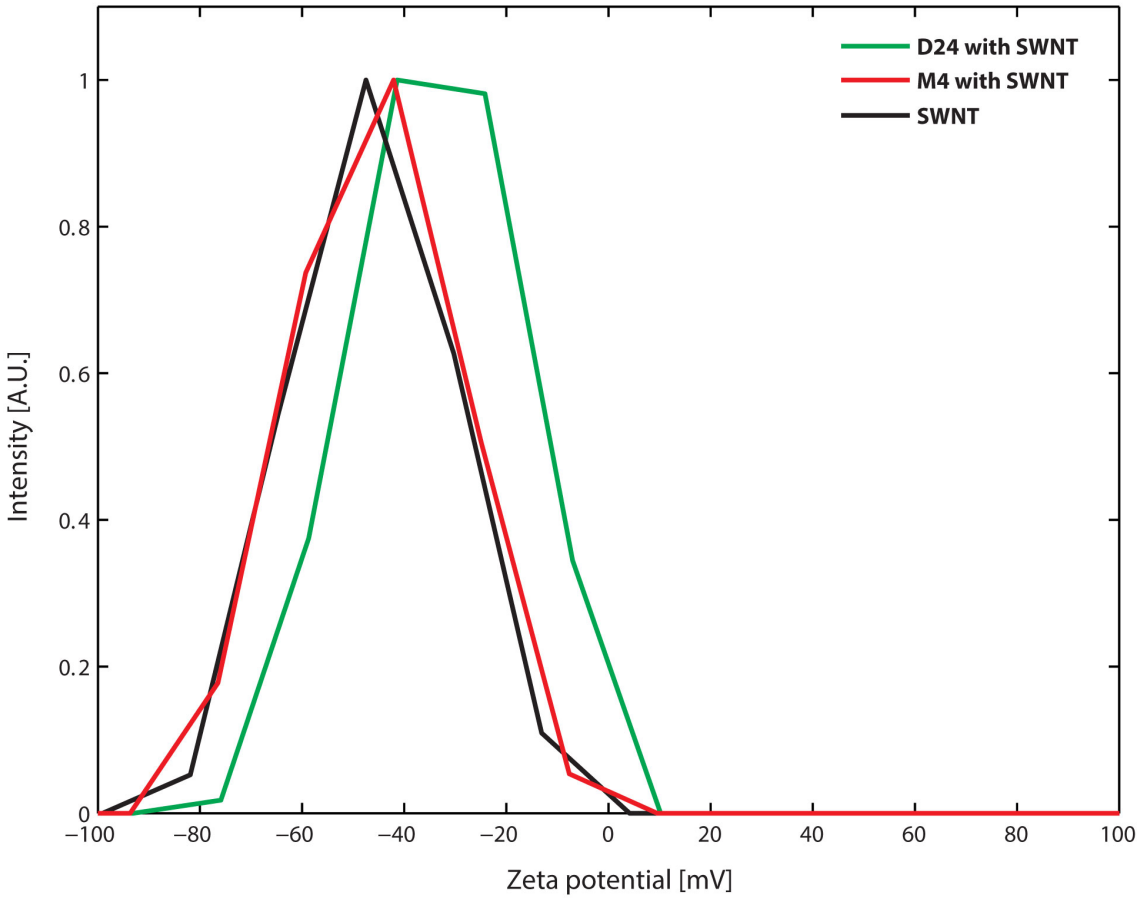

Figure 3.41: Zeta potential measurements of bare SWNTs, SWNTs packed with M4, and SWNTs packed with D24. The zeta potential data shows the high packing affinity of D24 on SWNTs, while M4 has a low affinity. These results are consistent with the packing affinity test shown in Figure 3.40

The linear absorption spectra of the monomers packed with SWNT indicate that the packing affinities of each monomer are close to each other, as shown in Figure 3.40.a. In a heterodimer, when one chromophore is packed on a SWNT, the other chromophore will come in close proximity to the SWNT. The short distance facilitates π-packing of the second chromophore, resulting in drastic packing affinity differences between dimers and monomers, shown in Figure 3.40.b. This difference in packing affinities confirms that both chromophores of each heterodimer were packed on the SWNT, holding the heterodimers in a structurally rigid conformation with the SWNT environment. Zeta potential measurements are also consistent with the packing affinity tests. The zeta potential mean value of the SWNT changed from -46 mV before packing to -34 mV after it was packed with D24 shown in Figure 3.41 , suggesting that the SWNT surface engaged in packing with D24 molecules.

3.5 Data acquisition

The specifics about the light source for the 2DES measurements are described in Chapter 2 Section 2.1.3. The output from a regenerative amplifier was used to seed a noncollinear optical parametric amplifier (NOPA, Light Conversion TOPAS White), generating pulses centered at 549 nm (520-570 nm FWHM). Multiphoton intrapulse interference phase scan method (MIIPS) [38] and a spatial light modulator (Biophotonic Solutions) were used to compress the pulses to 13 fs at the sample position. 2D electronic spectra were measured with a phase-stabilized four-wave mixing apparatus [6]. Three pulses with incident power of 3 nJ per pulse and a local oscillator attenuated by three orders of magnitude were focused on the sample to a spot size of approximately 70 μm. The coherence time was scanned from -60 to 60 fs with a step-size of 1 fs at room temperature, and the population time was scanned from 0 to 1000 fs with a step size of 10 fs. The third-order signal was heterodyne-detected with a local oscillator pulse and recorded on a 1600 x 5 pixel region of a CCD (Andor Newton) thermoelectrically cooled to -50 °C. 2D electronic spectra were obtained through scatter subtraction, windowing, and Fourier transform to the frequency-frequency

domain [6]. The samples were prepared by dissolving the compounds in ethanol with 2 vol.% triethylamine and diluting to a maximum optical density of approximately 0.2 for a 200 μm path length. For room temperature 2DES measurements, samples were pumped (Masterflex, Cole-Palmer) through a 200 μm flow cell (Starna). For cryogenic temperature 2DES measurements, the samples were cooled in a cryostat (Oxford Instruments) to 77 K.

3.6 Two-dimensional electronic spectra

2DES interrogates ultrafast coherent dynamics, energy transfer pathways, and electronic coupling between chromophores [1, 39, 40] by directly probing frequency-frequency correlations as a function of time in complex systems [41]. In this four-wave mixing technique [5, 6, 42], three ultrashort laser pulses interact with the sample generating a signal in the phase-matched direction [6]. The first two pulses, separated by a coherence time (τ), produce a population state, a coherence between excited states, or a vibrational coherence. After a waiting time (T), during which the system undergoes both incoherent relaxation and coherent oscillation, a third pulse interacts with the sample leading to emission of a third-order signal after a rephasing time (t), which is spectrally resolved using a spectrometer and CCD camera. Fourier transforms over both coherence time (τ) and rephasing time (t) domains yield two-dimensional electronic spectra in the frequency-frequency domain [6].

We used 2DES to examine all three heterodimers in dilute solution as well as packed on SWNTs. The 2D spectra of the heterodimers (Figure 3.42) show a strong crosspeak below the main diagonal. This crosspeak appears at a position corresponding to the absorption maximum of the monomer with the higher-energy electronic transition (energy donor) in the coherence dimension, and in the rephasing dimension, the position corresponds to the energy of the monomer with the lower-energy transition (energy acceptor) after ultrafast solvent reorganization. The decay of this crosspeak provides insight into the time evolution of the system. To separate coherences in the waiting time from relaxation dynamics, we fit time traces from these crosspeak positions to multi-exponential decays (shown in red in

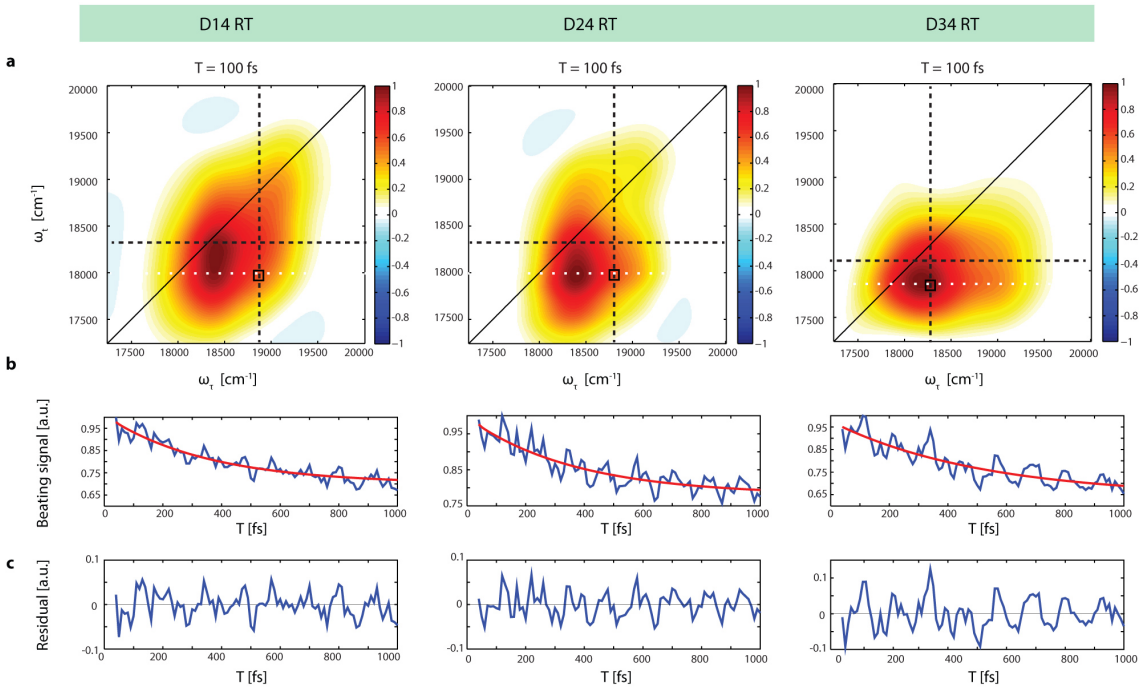

Figure 3.42: 2D electronic spectra showing coherent dynamics of fluorescein heterodimers in solution. (a) Real-valued 2D spectra of dimers D14, D24, and D34 at ambient temperature and a waiting time of 100 fs. The black dotted lines indicate the absorption maxima of the monomers. The white dotted lines indicate the electronic emission of the monomer with lower-energy electronic transition (acceptor), which red-shifts because of solvent reorganization during the waiting time. Boxes mark the lower diagonal crosspeak between maximum absorption of higher-energy monomers (donors) and solvent reorganized positions of lower-energy monomers (acceptors). (b) 2DES signals taken from the crosspeaks marked by the boxes in panel a are plotted in blue as a function of waiting time. Multi-exponential decays for waiting times later than 40 fs are fitted to the time traces and shown in red. (c) Residual beating signals remaining after subtraction of multi-exponential decay from the traces shown in panel b are plotted as a function of waiting time.

Figure 3.42.b) and subtracted these fits from the data. We fit the data after 40 fs to eliminate any possible artifacts from pulse-overlap effects. Residuals (Figure 3.42.c), as a function of waiting time (T), show oscillatory dynamics. These beating signals report on evolution of the coherences created by the first two laser pulses during the waiting time.

3.7 Beating frequency analysis of heterodimers and heterodimers packed on SWNTs

Quantum beating in 2D spectra can arise from any coherence between states including vibrations on the ground electronic state, vibrations on the excited electronic state, between electronic states, and between vibronic states of mixed character. Power spectra of the observed beating, generated by Fourier transforming along the waiting time (T), reveal the frequencies and relative intensities of oscillations. The power spectra of the solvent-reorganized crosspeak of the three heterodimers (Figure 3.43) appear nearly identical in the presence (gray panel) and absence (green panel) of the SWNT environment except for D24, which shows a marked change in the beating intensity at the crosspeak position and frequency of energy difference between the electronic transitions. To understand these oscillatory signals in the context of the vibrational modes of the molecule, we performed 2DES (Figure 3.49 and Figure 3.50) and Raman spectroscopy (Figure 3.51) on the monomers. We use these data to assign the ground-state vibrational frequencies of the heterodimers (dotted lines in Figure 3.43). To assign the electronic energy gaps (yellow/green lines in Figure 3.43), we use the linear absorption maxima of the monomers (Figure 3.48). The electronic transitions will shift after excitation because of ultrafast solvation of the excited state (a dynamic Stokes shift). These ultrafast dynamics are shown in Figure 3.44 for room-temperature and in Figure 3.45 for 77 K 2DES measurements. As seen in Figure 3.43, the energy difference between electronic transitions (not the ground-electronic gap) in heterodimer D24 appears at the same frequency as a ground-state vibrational mode on monomer M4, which has the lower-energy electronic transition. This frequency overlap implies that a vibrational level on the excited state of M4 is resonant with the electronic excitation of monomer M2. That is, the energy required for electronic excitation of monomer M2 is equivalent to the energy required for electronic excitation of M4 plus the energy of this resonant vibrational mode.

None of the structurally flexible heterodimers in solution (Figure 3.43, bottom) exhibit

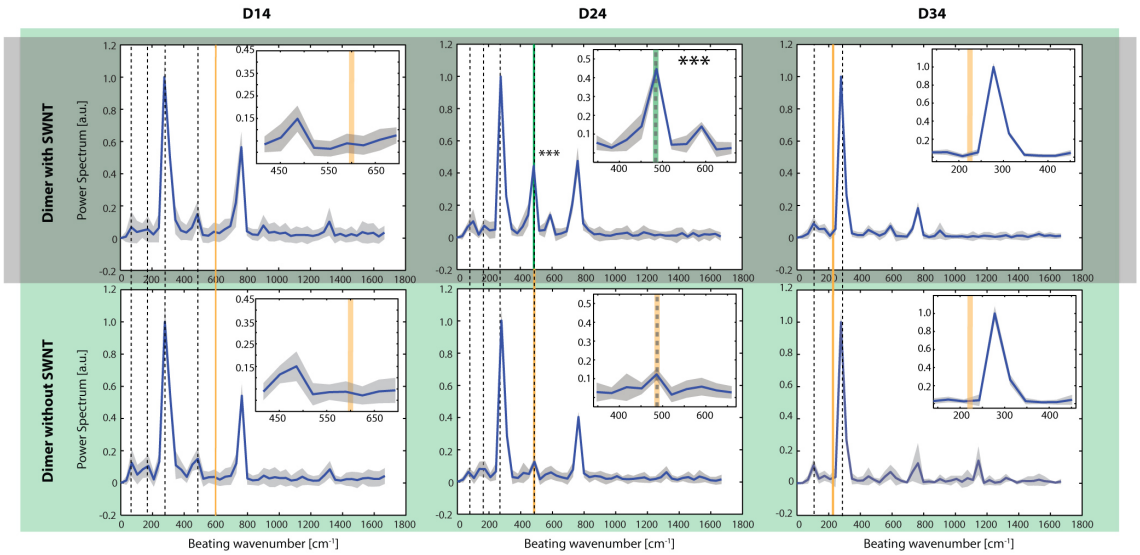

Figure 3.43: Power spectra of waiting time (T) dynamics of heterodimers in solution and on SWNTs. Fourier transforms of the residual beating signals at positions marked by boxes in Fig. 2a yield power spectra of quantum beating signals observed in heterodimers with SWNTs (gray panel) and without SWNTs (green panel). Black dashed lines indicate peaks assigned to vibrational coherences through control studies of monomers and Raman spectroscopy. Solid yellow and green lines show the electronic energy gaps of the dimers, calculated as the difference in peak absorption energies of the constituent monomers. Multiple datasets (5) were averaged to generate these beating power spectra, with the mean values shown in blue and 2 SDM (standard deviation of the mean) intervals shaded in gray. Inset spectra show detailed regions of interest. The data show no electronic coherences between excited states in solution, but when packed on SWNTs, D24 shows an enhanced beating signal coincident with the electronic energy gap.

strong peaks at the frequency corresponding to the energy difference between their respective electronic transitions, suggesting that conformational disorder in the Hamiltonian and/or system-bath coupling dwarf the off-diagonal coupling in the Hamiltonian that could lead to observable coherences between the constituent monomers. We also conducted the same experiments at 77 K on each of the heterodimers D24 and D34 and monomers M2, M3, and M4 in the absence of SWNTs (Figure 3.46). The power spectra in these cryogenic experiments reveal no new coherences, consistent with static conformational disorder rather than dynamic system-bath coupling obscuring the couplings that might give rise to observable coherences.

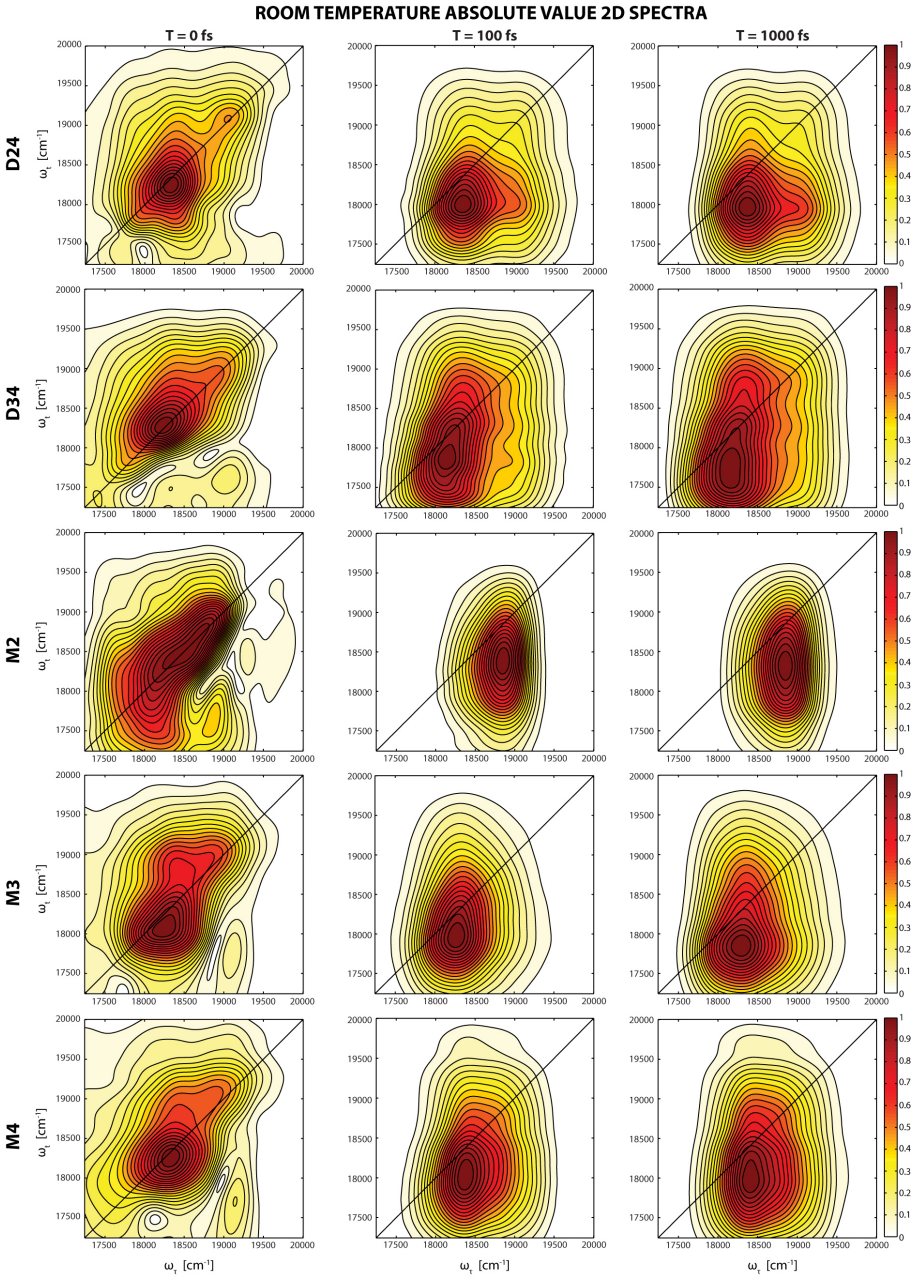

Figure 3.44: Stokes shifts during initial femtoseconds after excitation at room temperature. 2D absolute-value spectra of dimers D24 and D34, and monomers M2, M3, and M4 at 77 K and waiting times of 0 fs, 100 fs, and 1000 fs. All spectra are normalized. The line shapes at T = 0 fs are broader than at 77 K but remain elongated, consistent with inhomogeneous broadening, and again show little horizontal broadening indicative of relaxation or solvation during the initial coherence time.

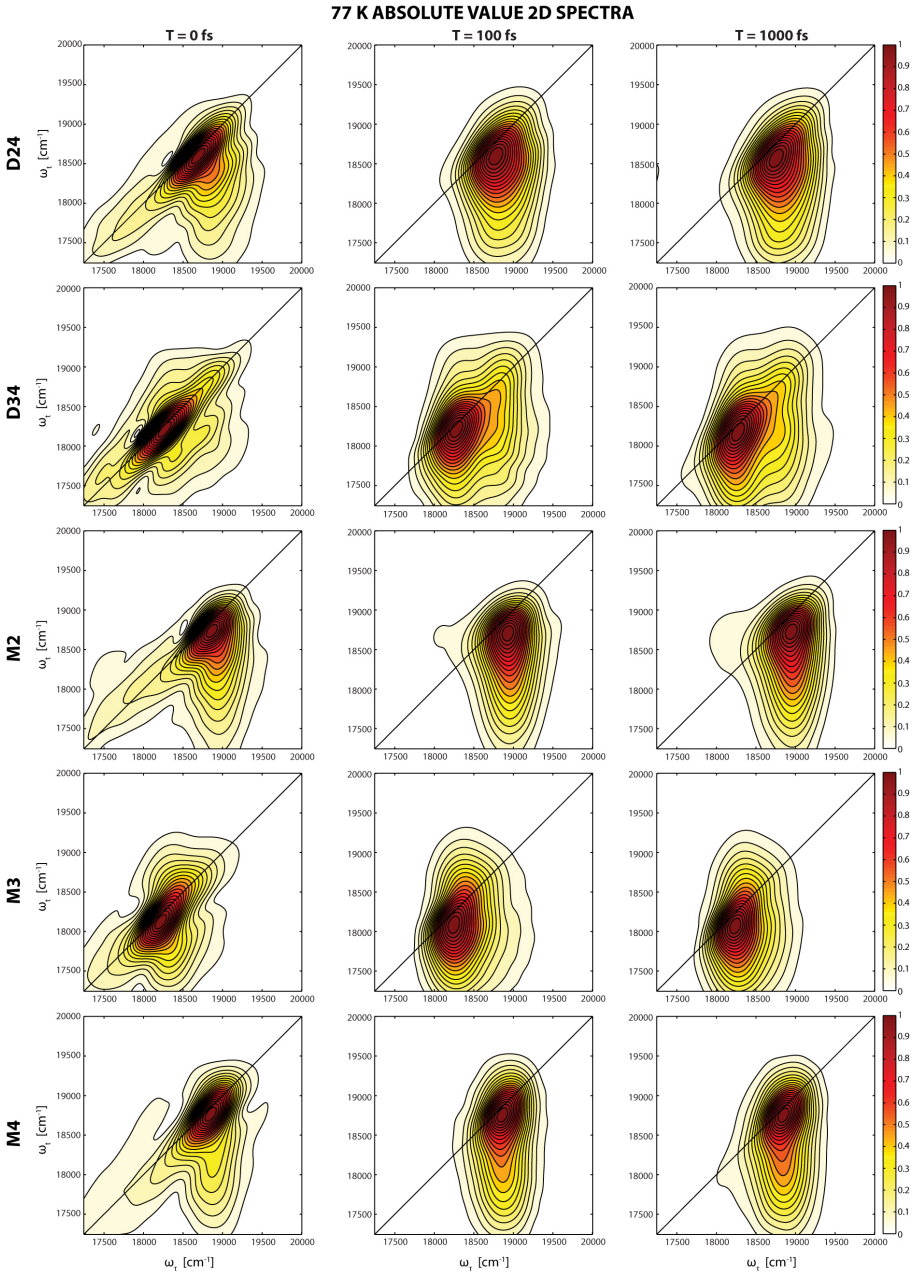

Figure 3.45: Stokes shifts during initial femtoseconds after excitation at 77 K. 2D absolute-value spectra of dimers D24 and D34, and monomers M2, M3, and M4 at 77 K and waiting times of 0 fs, 100 fs, and 1000 fs. All spectra are normalized. The line shapes at T = 0 fs are elongated, consistent with inhomogeneous broadening, and show little horizontal broadening that would be indicative of relaxation/solvation during the initial coherence time.

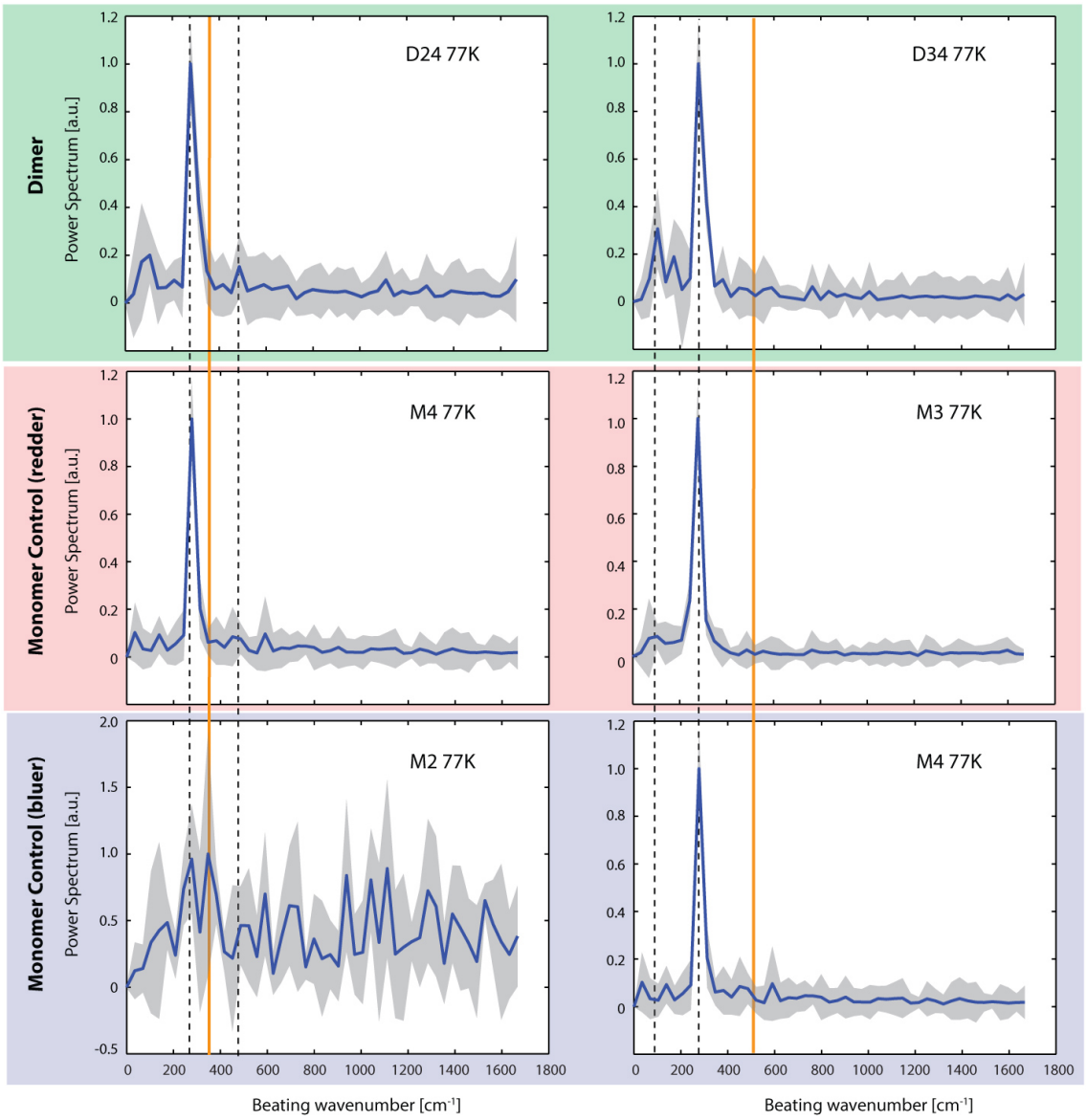

Figure 3.46: Power spectra of D24, D34, and their corresponding monomers at cryogenic temperature (77 K). Fourier transforms of the residual beating signal gave the power spectra of heterodimers (top green panel). Control experiments on corresponding monomers for D24 and D34 are shown in the lower two panels: lower-energy monomers (middle red panel) and higher-energy monomers (bottom blue panel). Black dashed lines indicate peaks assigned to vibrational coherences. Solid yellow lines show the electronic energy gaps. Temperature changes the corresponding energy gaps of each dimer at 77 K to 340 cm^{-1} for D24 and 530 cm^{-1} for D34. 2DES experiments for D14 and all three dimers on SWNTs at 77 K were not performed because of the blue-shifted absorption of D14 out of our laser bandwidth and the glass transition of SWNTs at low temperatures is difficult. Multiple datasets (3) were averaged where the mean values are shown in blue and 2 SDM intervals are shaded in gray.

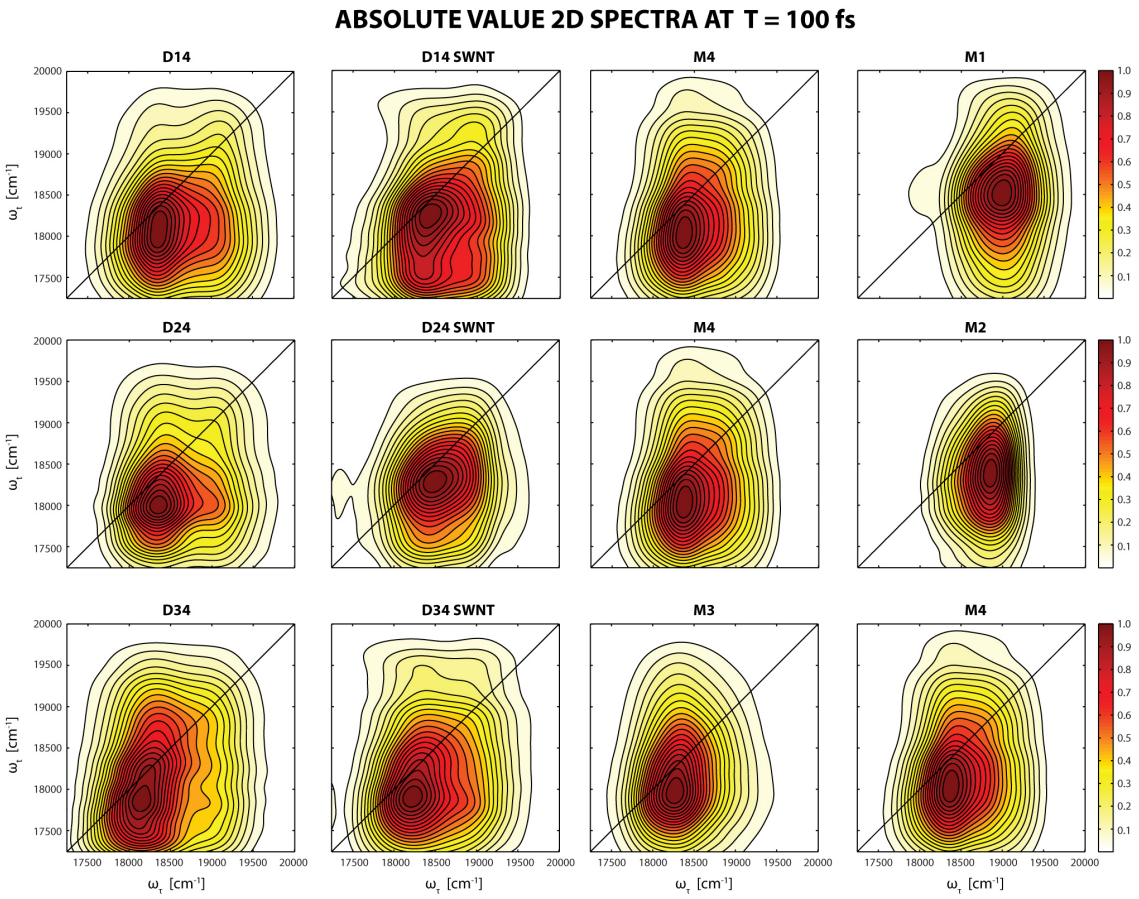

Figure 3.47: 2D absolute-value spectra of each dimer and monomer at ambient temperature and a waiting time of 100 fs.

3.7.1 Determination of the electronic energy gap for each dimer

The linear absorption spectra of the monomers are shown in Figure 3.48. The energy gaps in the heterodimers at ambient temperature are 600 cm^{-1} for D14, 490 cm^{-1} for D24, and 230 cm^{-1} for D34. From the 2D spectra of each monomer at a waiting time of 100 fs (Figure 3.47), the signal peak is shifted off-diagonal by roughly the same extent because of solvent reorganization. Because the four monomers have similar chemical structures and undergo similar solvent reorganization dynamics, it is appropriate to assume that the electronic energy gaps determined from linear absorption spectra of the monomers accurately represent the energy difference between excited states in the dimers.

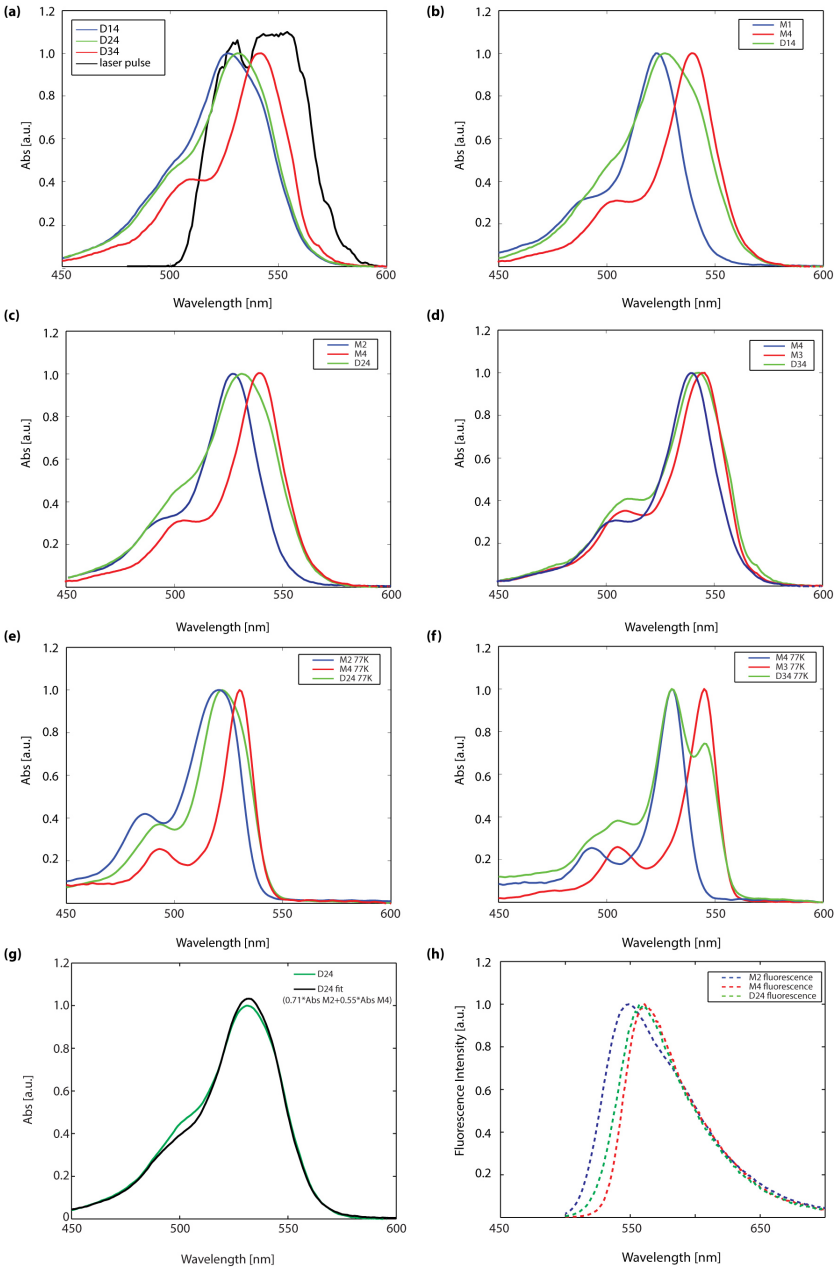

Figure 3.48: Linear spectra of fluorescein heterodimers and their corresponding monomers taken in EtOH with 2 vol.% triethylamine. (a) Absorption spectra of D14 (in blue), D24 (in green), and D34 (in red). The laser spectrum is shown as solid black line. (b) Absorption spectra of D14, M1, and M4 at an ambient temperature. (c) Absorption spectra of D24, M2, and M4 at an ambient temperature. (d) Absorption spectra of D34, M3, and M4 at an ambient temperature. (e) Absorption spectra of D24, M2, and M4 at a cryogenic temperature (77 K). (f) Absorption spectra of D34, M3, and M4 at a cryogenic temperature (77 K). (g) Simulation of D24 absorption spectrum from the sum of the monomer absorption spectra. (h) Fluorescence spectra of D24, M2, and M4.

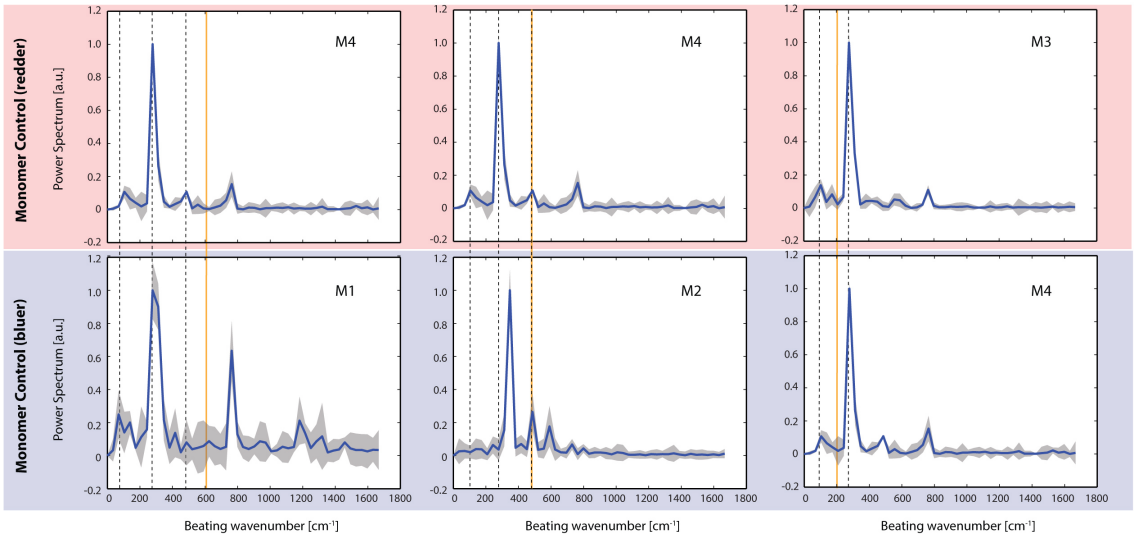

Figure 3.49: Power spectra of monomers compared to excitonic energy gaps. Control experiments on the corresponding monomers for each dimer are shown in two panels: lower-energy monomers (red panel) and higher-energy monomers (blue panel). Black dashed lines indicate peaks assigned to vibrational coherences. Yellow solid lines indicate the electronic energy gaps. Multiple datasets (5) were averaged where the mean values are shown in blue and 2 SDM (standard deviation of the mean) intervals are shaded in gray.

3.7.2 Assignment of vibrational modes of monomers

The same 2DES experiments and analyses in Figure 3.43 were applied to monomers M1-4, shown in Figure 3.49 and Figure 3.50. These control spectra, along with Raman spectra (Figure 3.51), were utilized to facilitate assignment of vibrational peaks in the power spectra. In the single-chromophore spectra, all peaks were assigned as vibrational because only one excited state is accessible within our laser bandwidth, preventing excitation of electronic or vibronic coherences. The observed vibrational frequencies are: 70 cm^{-1}, 139 cm^{-1}, 278 cm^{-1}, 764 cm^{-1} in M1; 347 cm^{-1}, 487 cm^{-1}, 590 cm^{-1} in M2; 104 cm^{-1}, 278 cm^{-1}, 590 cm^{-1}, 764 cm^{-1} in M3; and 104 cm^{-1} 278 cm^{-1}, 487 cm^{-1}, 764 cm^{-1} in M4.

3.7.3 Estimating the coupling between monomeric units within a dimer

We interpret our 2DES data of the synthesized heterodimers within a weak coupling regime. We have attempted to quantify the coupling between the constituent monomers within the

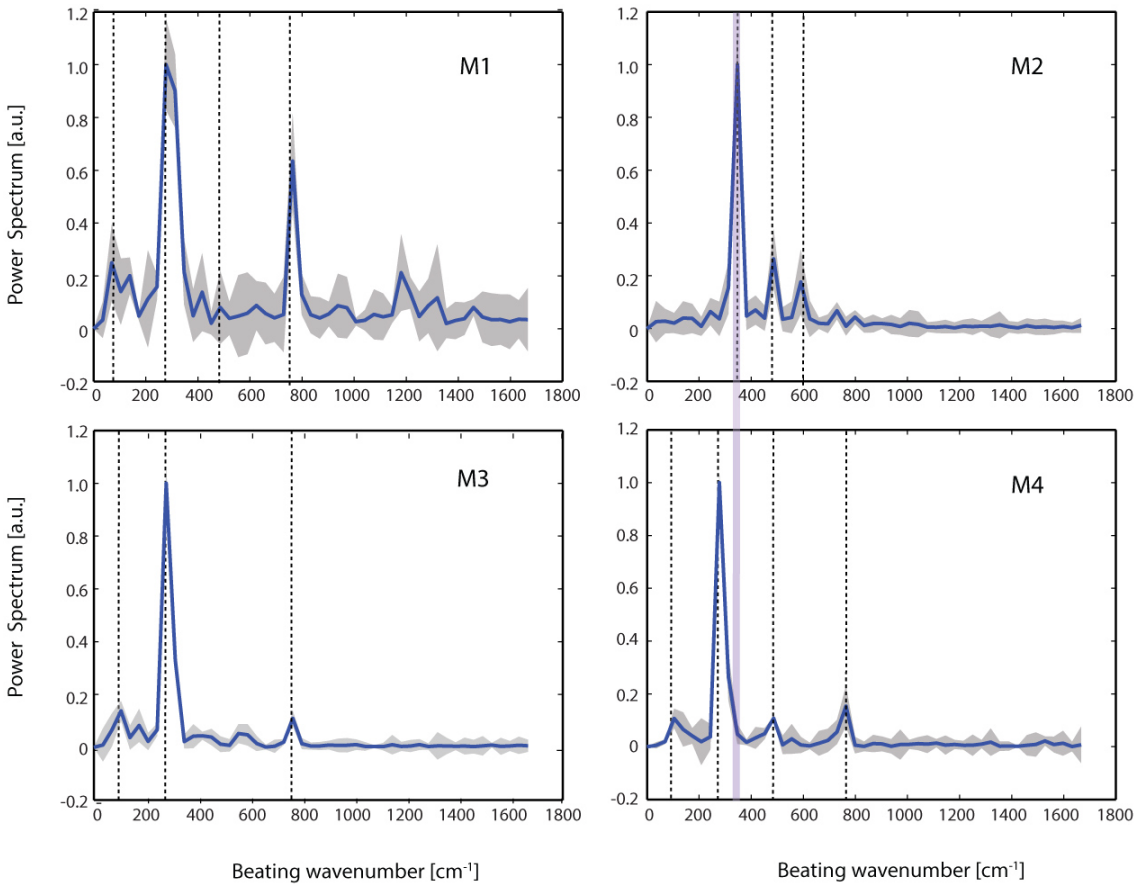

Figure 3.50: Power spectra of monomers taken from 2DES experiments at room temperature show that M2′s strongest vibrational mode differs from the others. Data identical to Figure 3.49. The purple solid line indicates that the strongest vibrational mode on M2 is offset from the common strongest vibrational mode of 278 cm^{-1} found in M1, M3, and M4. Black dashed lines indicate peaks assigned to vibrational coherences. Multiple datasets (5) were averaged where the mean values are shown in blue and 2 SDM intervals are shaded in gray.

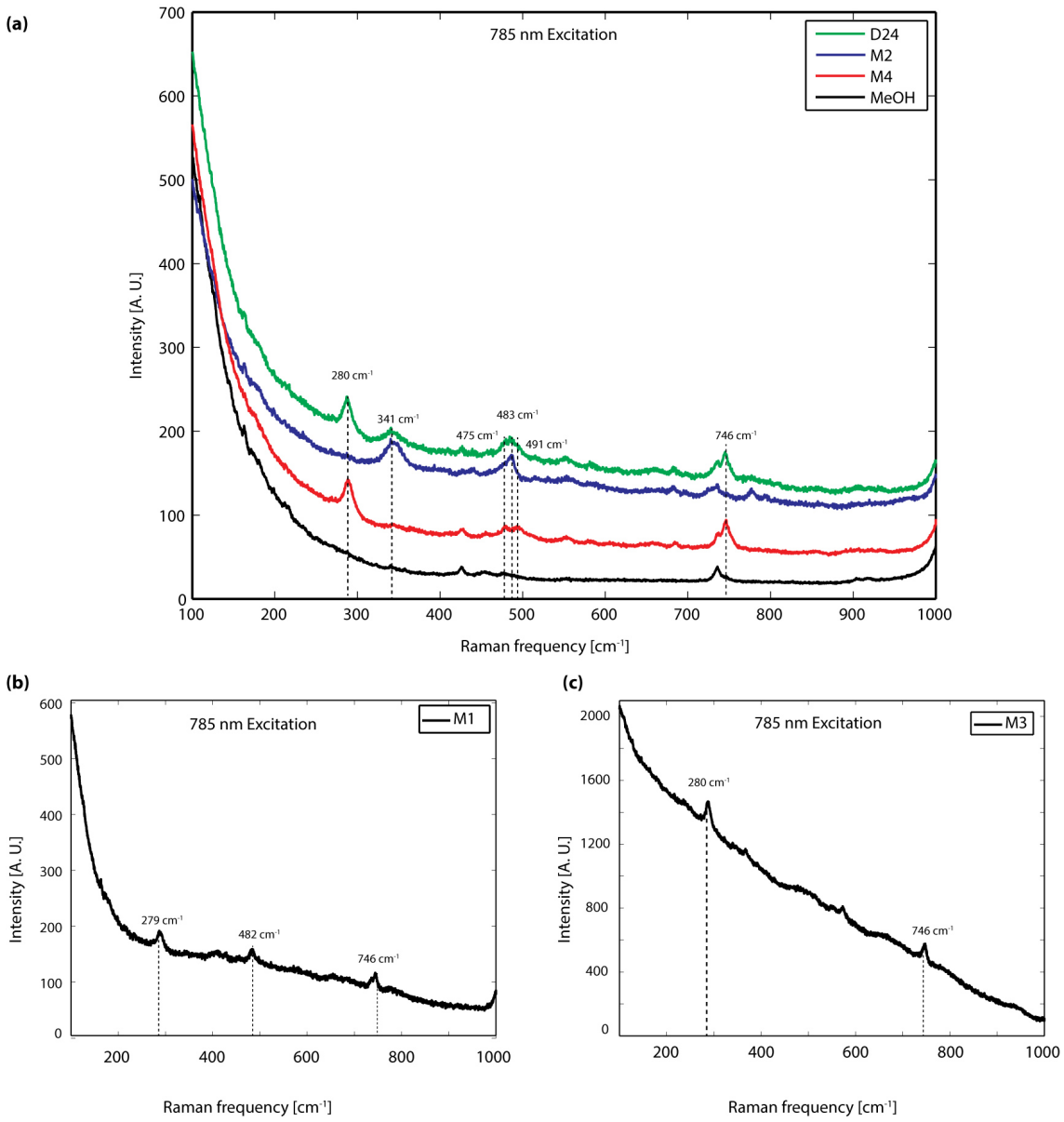

Figure 3.51: Raman spectra of fluorescein monomers and heterodimers. (a) Raman spectra of D24, M2, M4, and MeOH solvent. (b) Raman spectrum of M1. (c) Raman spectrum of M3.

heterodimers experimentally as well as theoretically. We first tried to quantify the coupling from the linear absorption data directly, but the linear absorption spectra for the dimer shown in Figure 3.48.g is well-approximated by a sum of the monomer spectra. The Raman spectra (Figure 3.51) show little vibrational coupling between the monomeric units, confirming that the ground-state vibrational structure of the monomers within the heterodimers is neither strongly coupled nor perturbed by the linkage. Similarly, packing on the SWNTs does not appear to affect the linear absorption spectrum significantly either by changing the coupling, intrinsically perturbing the electronic states, or by introducing stronger vibronic progressions into the spectra. Thus, we can confirm that we are in the weak coupling regime, but we are unable to quantify the coupling experimentally.

We therefore attempt to quantify the coupling using theoretical electronic structure calculations. We performed B3LYP calculations with a 6-311G(d,p) basis set on the dimer. The geometry was optimized for the dimer (Figure 3.52.a) and single point energy calculations were used to calculate the HOMO-LUMO transitions of each monomeric unit. Then, counterpoise calculations for each monomer were performed on the identical geometry to calculate the perturbation to the energy gap from the adjacent monomer. Qualitatively, we see that our eigenstates are located on the two monomers, as shown in Figure 3.52.b. More quantitatively, we calculate a coupling strength of 45 cm^{-1} between the constituent monomers.

Ultimately, the coupling between our dimers is very small compared to the difference in energy between the observed monomer transitions and compared to the system-bath coupling of the monomers. In any conventional sense, this is a weak coupling regime that is appropriate for Förster theory (which is exact in the system-bath coupling and a second order perturbation theory with regard to electronic coupling), as proved in Figure 3.48.h that the fluorescence is observed primarily from the lower energy monomer M4 in the heterodimer D24. However, in this dimer there is another energy scale against which this coupling should be compared: the differential system bath coupling between the two excited states.

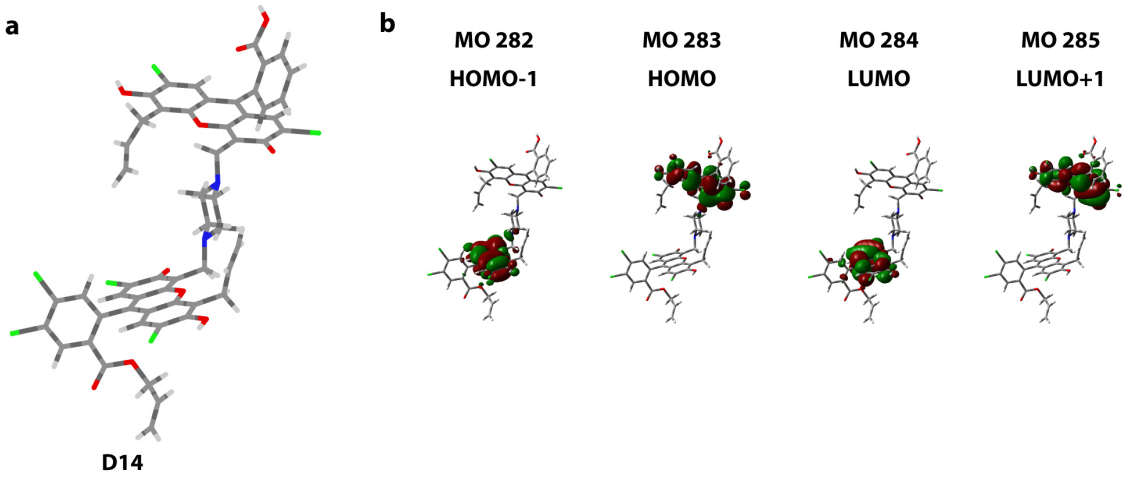

Figure 3.52: DFT calculations on the dimer demonstrate weak coupling between the two constituent monomers. (a) The optimized geometry of dimer D14 is obtained by using the B3LYP function with the 6-311G (d,p) basis set. (b) Frontier orbitals obtained from time-dependent DFT calculations.

The energy of one monomer is about equal to the energy of the other plus a vibration; further, the differential bath coupling is likely weaker than the overall system bath coupling implying some degree of correlated electrostatic fluctuations. (Even for a random matrix, half the power is in symmetric modes so this statement is not a strong claim, especially given the size of the system). The electronic coupling is weak by any conventional measurement (Raman, linear absorption, quantum chemistry *etc.*) but may not be strictly weak when it comes to vibronic coupling within the excited state manifold.

3.8 2D frequency beating maps

To place the beating signal at 487 cm^{-1} in the context of the entire 2D spectrum, we analyze 2D frequency beating maps of D24 both with and without SWNTs (Figure 3.53). We obtain 2D frequency beating maps by generating a power spectrum at each pixel in a 2D spectrum via a Fourier transform over the waiting time (T) domain [9]. These maps display the distributions of oscillation frequencies of the coherences. In the absence of SWNTs, beating at 487 cm^{-1} in D24 appears primarily on the diagonal position. When the D24 molecules

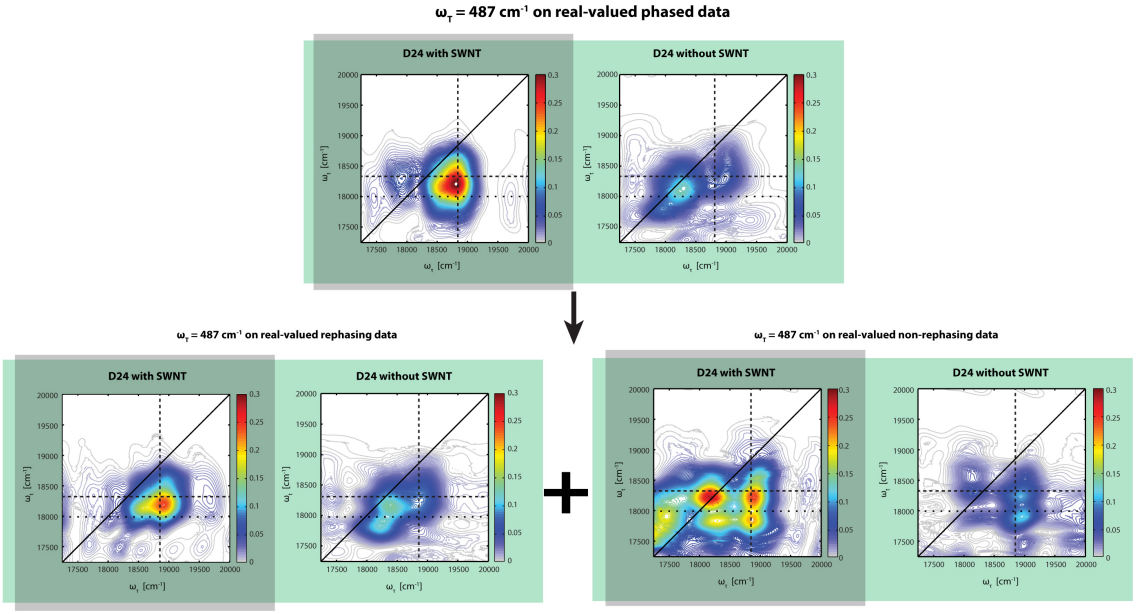

Figure 3.53: 2D frequency beating maps of D24 with (gray panel) and without (green panel) the SWNT environment at 487 cm^{-1} for real-valued phased data (top), real-valued rephasing data (bottom left) and real-valued non-rephasing data (bottom right).

are packed on SWNTs, the beating signal at 487 cm^{-1} shifts to a lower diagonal crosspeak position. In contrast, the beating signals at 104 $cm^{-1}$and 278 cm^{-1} appear primarily along the diagonal and remain unperturbed upon packing on SWNTs, as do all beating signals for dimers D14 and D34 (Figure 3.54).

The detailed patterns of the beating signals can be used, in the absence of solvent reorganization, to assign the origin of the signal [43]. Unfortunately, in our fluorescein heterodimers, the Stokes shift complicates the assignment of the beating signals using this method because ground-state signals will show minimal solvent reorganization, while excited-state signals will shift more. The separation is not enough to fully separate the excited- and ground-state signals, leading to vertically elongated beating patterns in the beating maps. We therefore performed separate beating map analyses for the rephasing and non-rephasing portions of the 2D spectra of D24 both with and without SWNTs to obtain a better understanding of the enhanced beating signal at 487 cm^{-1}. All the possible Feynman pathways within our laser bandwidth that could contribute to the 487 cm^{-1} beating signal are listed in Figure

3.55).

3.9 Control experiments on bare single-walled nanotubes

We performed control experiments on our SWNTs to verify that we did not observe excitonic coupling from the SWNTs in our spectral range. The linear absorption spectrum of SWNTs (Figure 3.56) indicates no exciton peaks in our laser spectral range (520 nm - 570 nm). 2D electronic spectra of SWNTs are shown in Figure 3.57. No signal above the noise floor are observed in the 2D spectra beyond 40 fs. No solvent signals are observed after 40 fs (Figure 3.58). Beating map analysis on the 2D spectra of SWNT demonstrates no coherences at 487 cm^{-1}, excluding vibrational modes on SWNTs as possible explanation for the enhanced beating signal we observed on D24 with SWNTs.

3.10 Discussion on the origin of enhanced signal in the power spectrum of D24 packed on single-walled nanotubes

Many models have been created to explain beating signals in 2DES data invoking physical mechanisms involving purely electronic coherence with correlated spectral motion [15], vibrational wavepackets on both the excited and ground states arising from vibronic coupling [22], and ground-state vibrational coherences arising from non-adiabatic coupling among excited states [2]. When packed on SWNTs, only D24 shows enhanced beating signals; the beating signals in D14 and D34 are almost unchanged. This observation allows us to rule out purely electronic origins for our signal because such a coherence should appear in all dimers at a frequency corresponding to the energy difference between electronic excited states. All dimers contain M4 as one of the constituents, yet we do not observe any enhancement in the beating signals from D14 and D34. The strongest vibrational mode of M2 is at 347 cm^{-1} (Figure 3.50). However, this 347 cm^{-1} vibrational mode is not captured in the power spectra of D24 either with or without SWNTs, probably due to the fact that our laser spectrum falls off

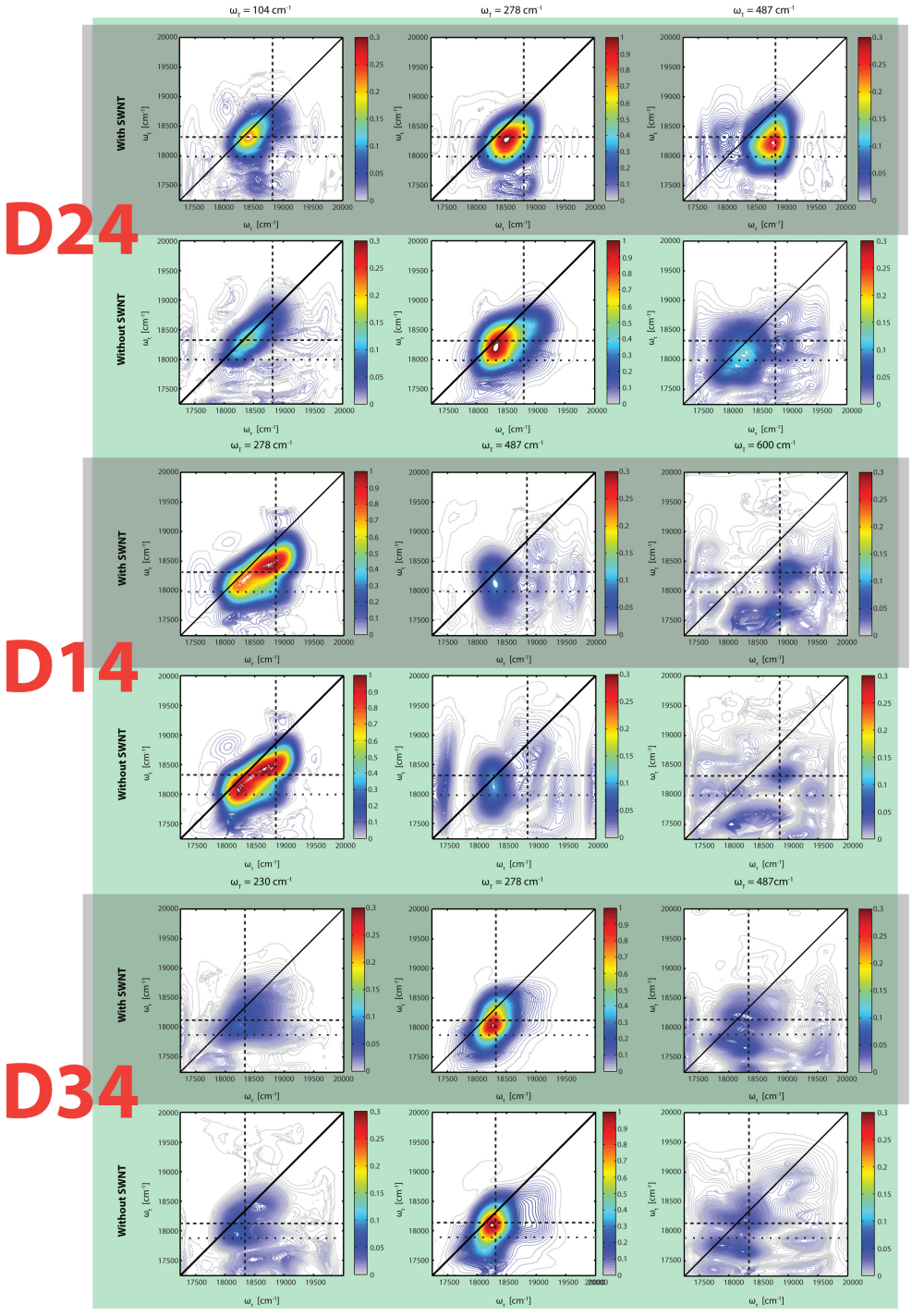

Figure 3.54: 2D frequency beating maps of D24, D14, and D34 with (gray panel) and without (green panel) SWNTs. The Fourier amplitudes are indicated by color bars.

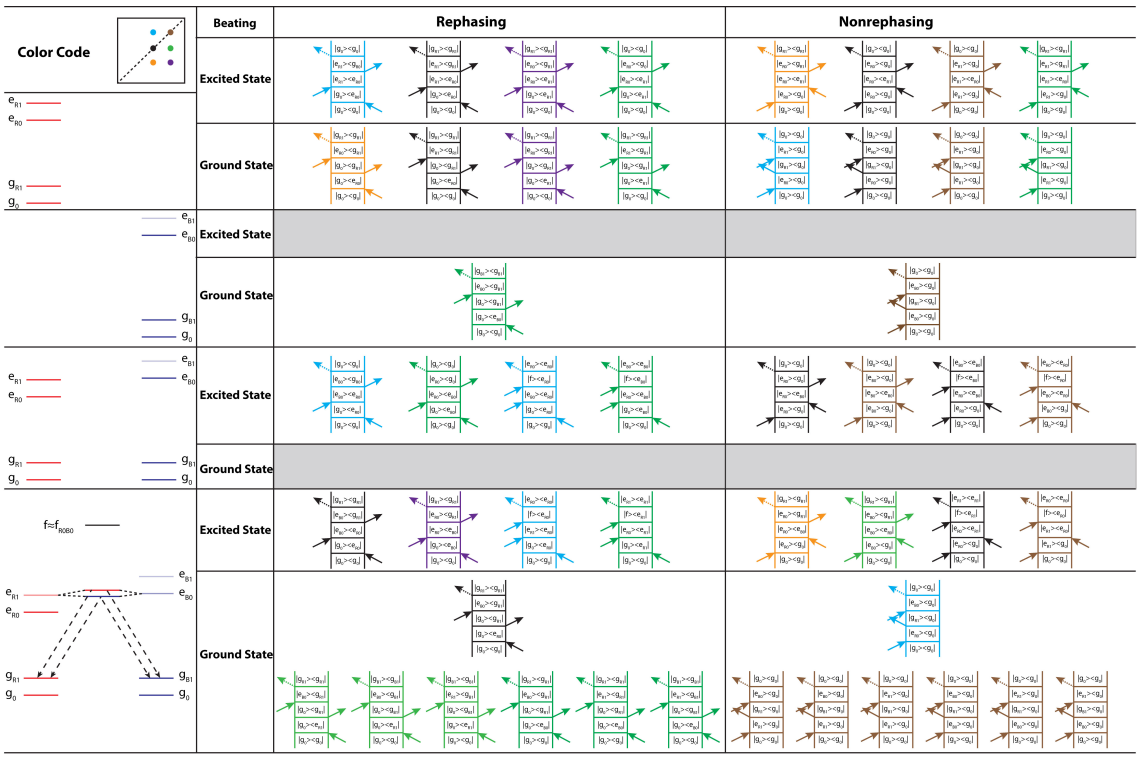

Figure 3.55: Feynman pathways accessible to our experimental laser bandwidth in a vibronically coupled dimer. Pathways involving out-of-band transitions are not listed above (e.g., $g_0 \rightarrow eB_1$ and ESA pathways involving similar transitions). Pathways involving each monomer arising from coupling between the electronic excited states and from vibronic mixing between the monomers are listed separately for clarity.

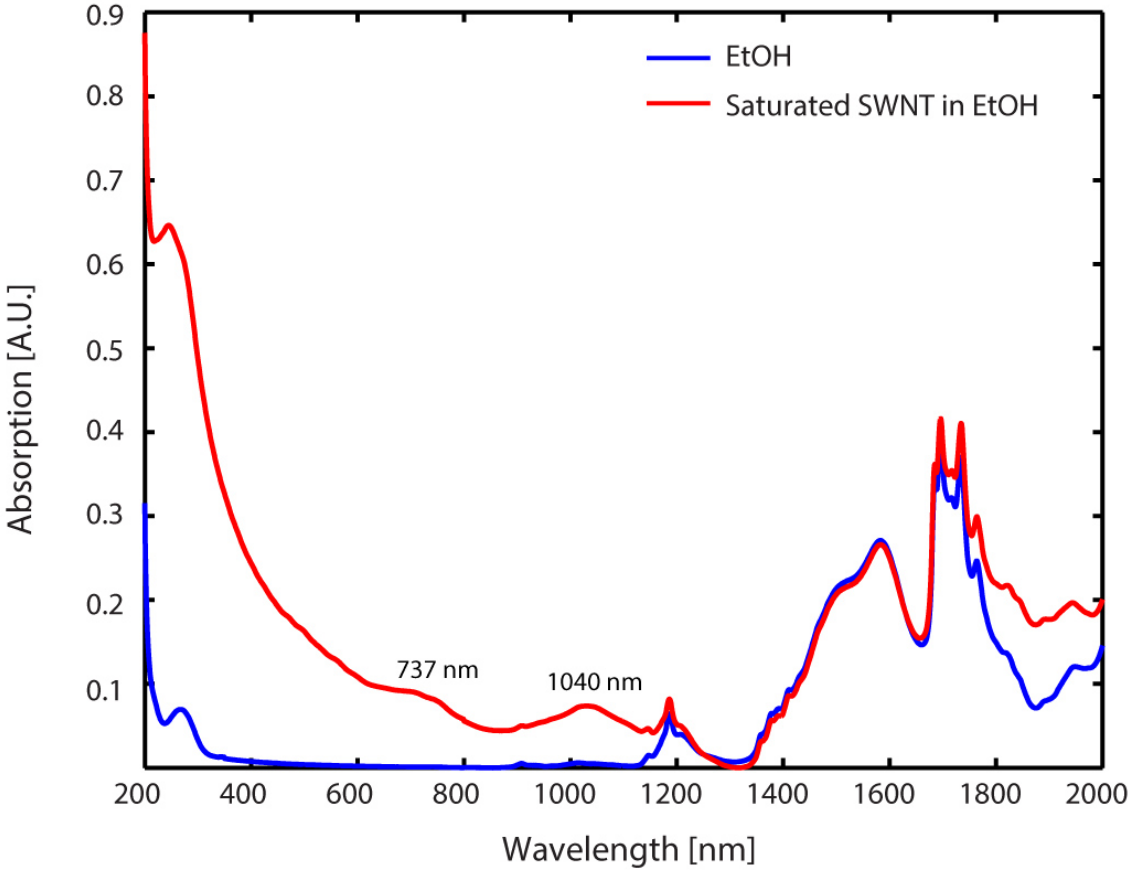

Figure 3.56: Linear absorption spectra of EtOH and saturated SWNT solution in EtOH show no excitonic peak in our laser spectral range (520 – 570 nm).

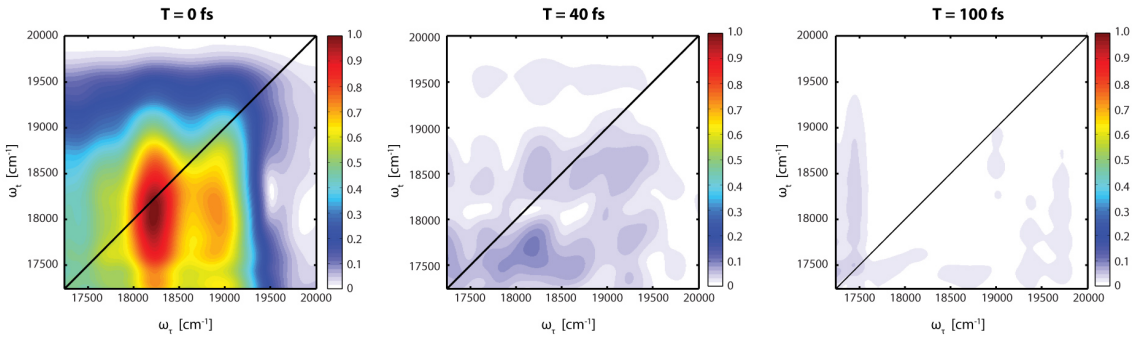

Figure 3.57: Absolute-valued 2D spectra of saturated SWNT solution in EtOH at 0 fs, 40 fs, and 100 fs demonstrate weak signal contribution from SWNTs in 2DES measurements.

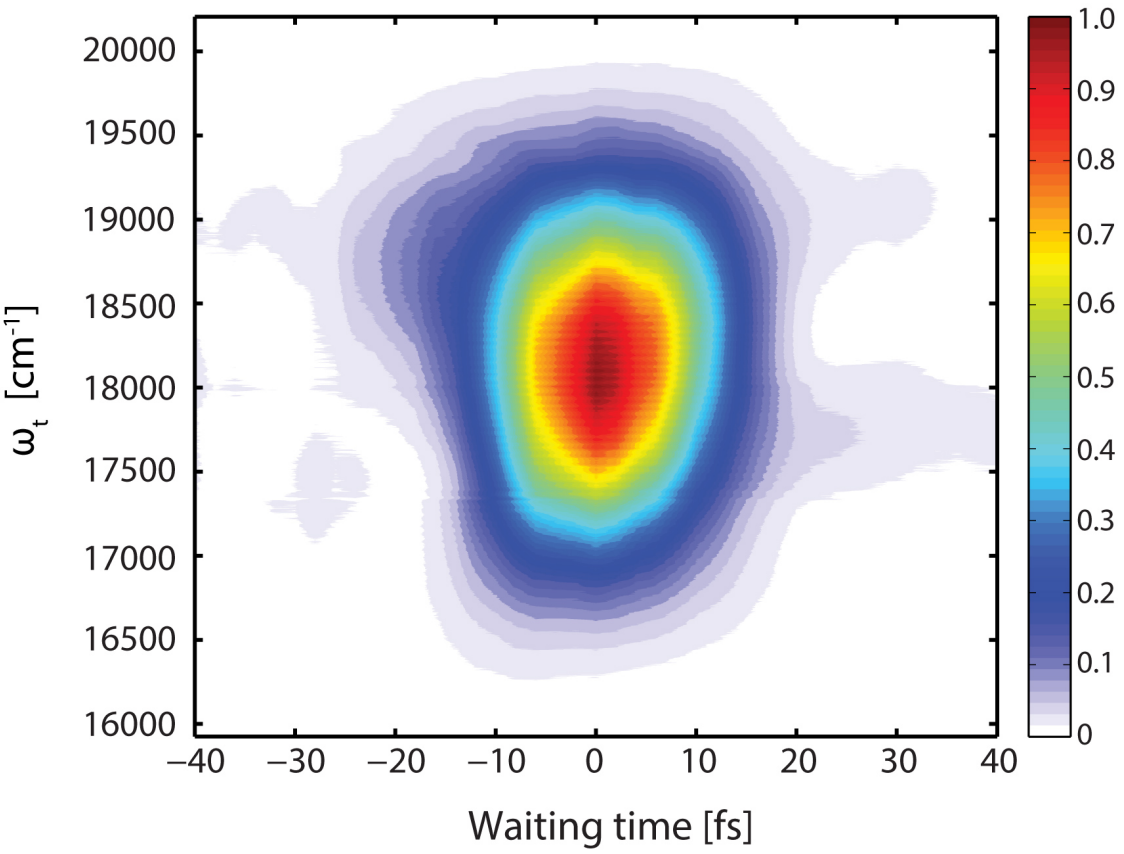

Figure 3.58: Spectrum of the solvent induced signal shows no solvent signal contribution after 40 fs.

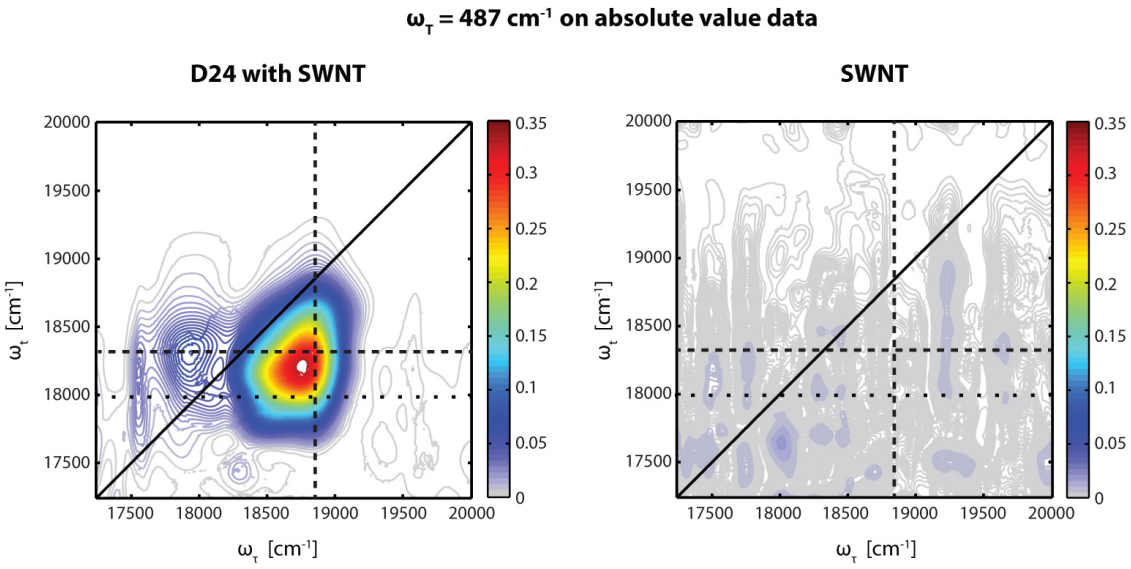

Figure 3.59: 2D frequency beating maps of D24 with SWNTs and saturated bare SWNT solution at 487 cm^{-1} show no beating contribution from SWNTs alone. The beating maps are generated from absolute-valued 2D data that are normalized to a 0 fs waiting time. Dotted lines from Figure 3.42 and Figure 3.53 for D24 are overlaid on the figure for reference purposes.

quickly at the blue edge. The vibrational modes of M2 are weak compared to M4, which is shown clearly in the Raman spectrum of D24 as green trace in Figure 3.51. Therefore, the amplified vibrational mode on M2 is also excluded as the origin of the significant signal amplification observed in the power spectra of D24 with a SWNT substrate. Two-dimensional frequency beating maps of vibrational modes on M2 and M4 are shown in Figure 3.60. The locations of the 487 cm^{-1} mode on M2 and M4 are different from what is observed in the frequency beating map of D24 packed on SWNTs and further validate our conclusion that the increased beating signal at 487 cm^{-1} does not arise from purely vibrational modes on monomers. A vibrational signal should not depend on the tuning of the excited-state transitions. That is, a purely vibrational mechanism is not likely to be the source of this enhanced beating signal in D24 with SWNTs. Another possible explanation could be that the SWNT displaces the M4 excited electronic state changing the Franck-Condon factors (formally, an increase in the Huang-Rhys factor). In this case, we would expect a stronger signal from the M4 vibration in all dimers because M4 is present in all dimers; we would further expect

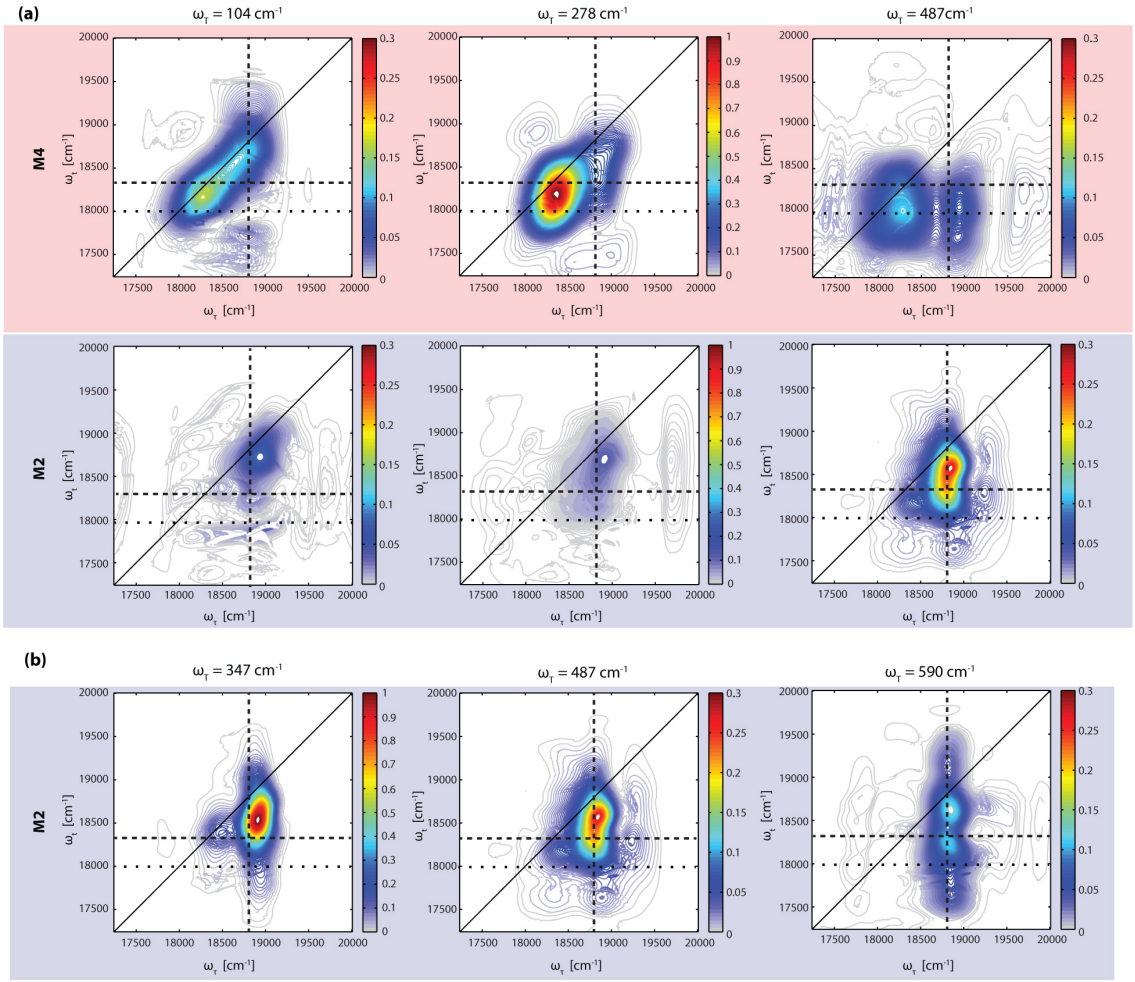

Figure 3.60: 2D frequency beating maps of M2 and M4. (a) 2D frequency maps of M2 (blue panel) and M4 (red panel) for 104 cm^{-1}, 278 cm^{-1}, and 487 cm^{-1}. (b) 2D frequency maps of M2 (blue panel) for 347 cm^{-1}, 487 cm^{-1}, and 590 cm^{-1}. The Fourier amplitudes are indicated by color bars. Dotted lines from Figure 3.42 and Figure 3.53 for D24 are overlaid on the figure for reference purposes.

that the beating pattern would remain the same. This hypothesis is inconsistent with our observation. For the same reason, we believe that this signal is inconsistent with a resonant Raman process.

We have attempted to analyze our data in the context of Feynman diagrams akin to those presented by Turner *et al* [43]. This analysis was frustrated by the Stokes shifts of our excited states, but we include some of our discussion and analysis here. For the Feynman pathways in Figure 3.55, all pathways involving vibrational beating on the ground states

go through two transitions that would be weighted by Franck–Condon factors (e.g., two vibrational |0> to |1> transitions). Thus, for any given vibrational mode, the beating would be enhanced by the same amount for all of the corresponding vibrational beating pathways. That is, if we observed increased signal from these pathways, the pattern would not change in a 2D frequency beating map. This is not what we observe in the experiment. Similarly, the differences in the pattern in the rephasing data (enhancement at the green point) as well as the changes in the non-rephasing data, in which the left-hand peaks (black and orange) are significantly more enhanced than the right (green and purple), are inconsistent with this "purely ground-state vibration" hypothesis. In fact, we observed strong enhancement at the green spot in the rephasing data, and strong enhancement at the black spot along with weaker enhancement at the green and orange spots in the non-rephasing data. These observations further support our assertion that we observe some beating on the excited-state surface because of vibronic mixing.

Non-adiabatic couplings between electronic transitions and vibrational motions can give rise to microscopic origins that are very hard to distinguish from one another. In one treatment, suggested by Jonas and coworkers [2] to explain signals in photosynthetic complexes, vibronic couplings in the excited-state manifold can give rise to ground-state vibrational wavepackets implying that the observed coherences are simply ground-state vibrations (but these ground-state vibrations do report on excited-state couplings). In the subsequent treatment suggested by Mancal and coworkers [22], the beating arises from wavepacket motion on both the excited- and ground-state surfaces when the electronic transition of one monomer is nearly resonant with a vibration on the excited state of the other monomer. Both approaches invoke the same underlying mechanism and require a vibrational energy gap to be resonant with the energy difference between the ground-to-excited-state transitions. Both treatments involve a non-Born-Oppenheimer coupling and can be operative with weak electronic coupling, as in this system. The treatment suggested by Jonas and coworkers [2] projects the nuclear motion onto a shared vibrational mode that couples to the two electronic states with

an opposite sign to drive dynamic changes in the character of the excited state. Such a mode is a normal mode and therefore a natural representation only in the presence of strong vibrational coupling. Our Raman spectra show little difference between the vibrational modes in the monomers and in the dimer, implying extremely weak vibrational mixing between the monomers. Rather, we think that our vibronic mixing is more readily expressed in the second treatment that is more akin to a Fermi resonance whereby the electronic state of M2 mixes with a vibrational mode on the excited state of M4. This non-adiabatic mixing gives rise to both ground- and excited-state wavepackets in our spectroscopy. The requirement for this type of mixing would be that the coupling between the excited states (likely dipolar in nature) must be greater than the differential noise induced by system?bath coupling. Consistent with this prediction, the patterns that we see in the beating maps (Figure 3.53 appear to contain contributions from both excited-state coherences as well as ground-state coherences generated by vibronic coupling between the excited states.

The beating maximum of 487 cm^{-1} in D24 with SWNTs along the ω_t axis appears about 150 cm^{-1} below the absorption maximum of M4. We attribute this shift to fast solvent reorganization around the nascent excited states. Because this solvent reorganization only happens for excited states and not for the ground state, this observation further supports our assertion that we detect some beating on the excited-state surface. That is, some portion of the amplified beating signal at 487 cm^{-1} is due to coherence involving excited electronic states.

Thus far, our discussion has focused primarily on the amplitudes and energies of the observed signals, as is natural in analyzing spectra. However, we believe that it is equally important to understand the role of the rigidity of the molecule as we analyze possible coupling mechanisms. In our 2DES data, we observe a dependence on the restricted distribution of orientations between chromophores – that is, our observation of enhanced vibronic coherence occurs only when we pack D24 on SWNTs not when D24 is in solution. Though existing vibronic models do not explicitly consider orientation, the models do not prevent inclusion

of this degree of freedom. For example, Mancal′s vibronic model [22] depends on Coulomb couplings between chromophores. These couplings are usually modeled as dipole-dipole couplings that necessarily involve orientational dependence. By restricting the distribution of relative orientations of chromophores within the heterodimer on the SWNT substrates, our approach narrows the distribution of off-diagonal Coulomb couplings between the chromophores. This more ordered Hamiltonian may help support vibronic mixing, leading to larger signals in an ensemble measurement.

3.11 Vibronic coherence and coherent energy transfer

The constructive role of vibronic coherence in energy transfer process has been suggested by theoretical calculations [44–48] and observed by Womick and Moran in one photosynthetic system [49]. We also observe some subtle changes in the decay dynamics of D24 packed with SWNTs that may be due to vibronic coherence as shown in Figure 3.61. However, our dimer system is simply not designed to optimize energy transfer. We specifically designed our system to explore design principles of vibronic coherence and therefore created weak coupling between the chromophores. That is, we wanted to measure the effects of orientation and shared environment on dynamics of an excited state resonant with another excited state plus a vibration. To observe our signal, we specifically worked in the weak coupling regime where energy transfer is rather slow compared to dephasing. As shown in Figure 3.62, the beating signal at 487 cm^{-1} dephases below the noise floor by 520 fs.

One could instead optimize energy transfer by creating stronger coupling between constituent monomers so that more energy transfer occurs before the vibronic coherence dephases. The corresponding experiment would, of course, presume that the vibronic coherence was generated but probably could not be measured directly. It is difficult to test this hypothesis in these samples because only an oscillation or two are visible. This is the same issue seen in photosynthetic systems at room temperature where the data provides little insight into the energy transfer mechanism [3, 50].We have provided the waiting time traces in the

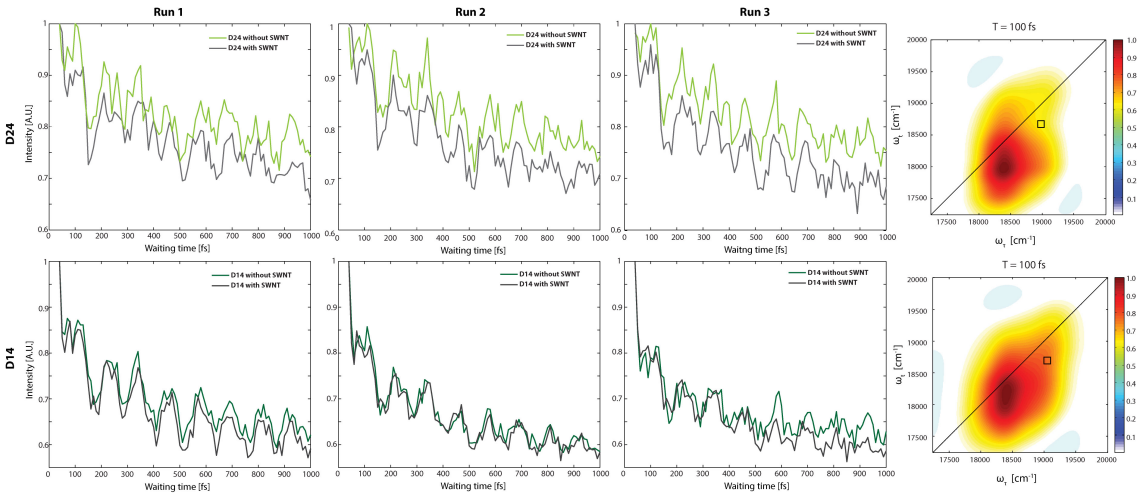

Figure 3.61: Time traces extracted from the 2D data for D24 and D14 both in solution and packed on SWNTs. Data are taken at a point below the diagonal (marked with a box on the 2D spectrum in the right column) that accounts for solvation of the excited state of the higher energy constituent monomer (donor). In dimer D14 (bottom row), the data traces fall nearly on top of one another, while in D24 (top row) slight separation occurs in the initial 100-200 fs. This timescale corresponds to the timescale of the vibronic coherence observed in our data. We cannot assign statistical significance to the separation observed above because of strong vibrational beating or definitively assign it to coherent energy transfer. However, we find it interesting that we observed this reproducible difference. Our dimer systems were designed to preserve vibronic coherence by exploiting weak coupling (slow transfer) between the constituent monomers, but we still see hints of dynamics consistent with accelerated energy transfer during the initial period following excitation.

2DES data of D24 and D14 both in solution and packed with SWNTs in Figure 3.61. The fitting process is the same as that of Figure 3.42.b. We observe faster dynamics when D24 is packed on SWNTs, while the decay dynamics in D14 show much less change regardless of the presence of SWNTs. This faster decay of D24 packed on SWNTs may suggest that vibronic coherence facilitates relaxation dynamics. However, we feel that we lack sufficient evidence to claim that this faster decay results exclusively from the vibronic coherence because of the changed chemical environment around the chromophores in our system.

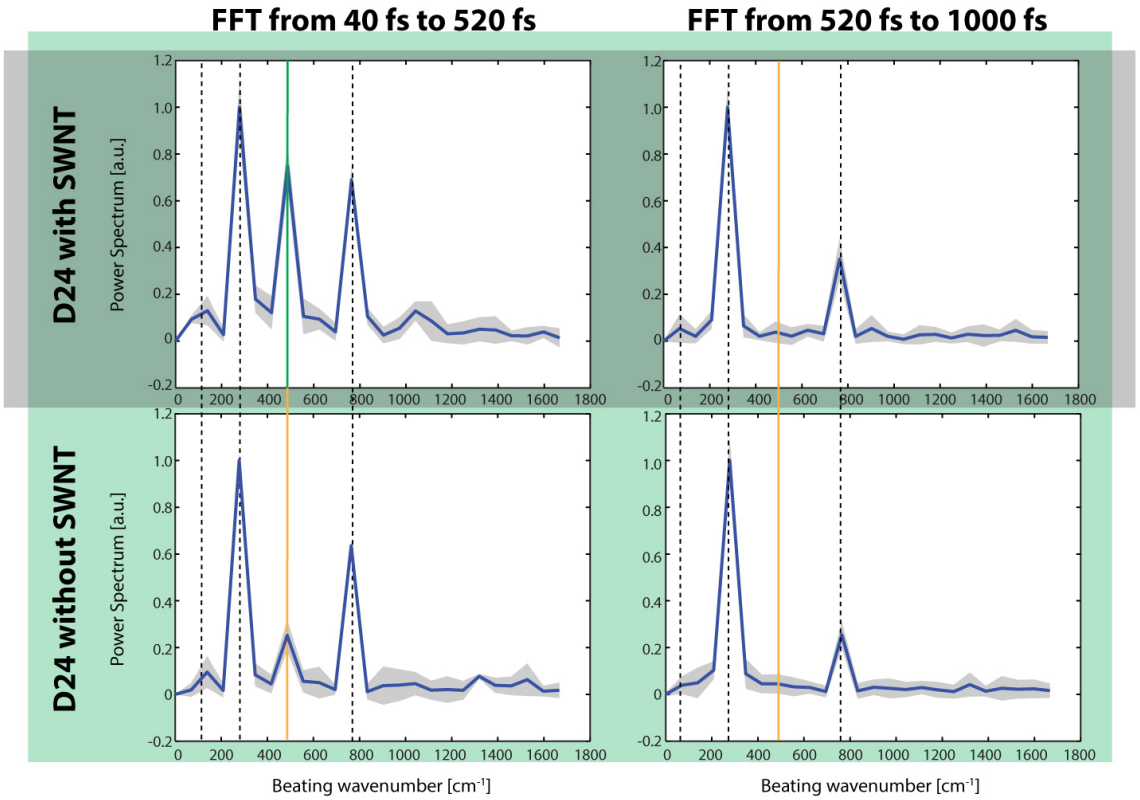

Figure 3.62: Power spectra of heterodimer D24 with and without SWNTs from 40 fs to 520 fs and from 520 fs to 1 ps. Fourier transforms of the residual beating signal are extracted at positions indicated by boxes in Figure 3.42. The beating signal at 487 cm^{-1} decays below the noise floor well before 1 ps, although some vibrational coherences are still visible in the dataset at 1 ps.

3.12 Conclusion

Synthetic control of electronic energy levels and two-dimensional electronic spectroscopy combine to provide a toolset to dissect contributions to coherent beating signals experimentally. Contrasting the beating power spectra of structurally flexible heterodimers with and without SWNT, we show that limiting the relative orientation of the chromophores by packing on SWNT can generate stronger vibronic coherences. The same data show that electronic coupling between the two proximal chromophores in our synthetic dimer alone is insufficient to create observable vibronic coherences. The controllable energy gap in the synthetic heterodimers enables us to explore the contribution of a resonant vibrational mode to observed coherences. If the physical origin of the observed coherences were purely electronic, peaks at corresponding energy gaps would emerge consistently in all three heterodimers. Similarly, if the origin were purely vibrational (Raman), we would expect to observe the signal in all heterodimers because they all include monomer M4. In conclusion, we report that we observe vibronic coherence in 2D spectra only when we both restrict the relative orientation between chromophores (transition dipoles) and ensure that a vibrational mode matches the energy difference between the two electronic transitions of the dimer. We speculate that this resonant vibrational mode may provide a mechanism for fast coherent relaxation within these molecular systems because the higher-lying excited state can readily dissipate energy by coupling to the lower state plus a single vibrational quantum of energy as has been observed in light-harvesting allophycocyanin dimers [49]. We believe that the general applicability of SWNTs as substrates for molecules with π-interaction properties may help guide future development of artificial energy-transfer devices that can exploit improved efficiency from vibronic coupling.

REFERENCES

[1] Tobias Brixner, Jens Stenger, Harsha M. Vaswani, Minhaeng Cho, Robert E. Blankenship, and Graham R. Fleming. Two-dimensional spectroscopy of electronic couplings in photosynthesis. *Nature*, 434(7033):625–628, 03 2005.

[2] Vivek Tiwari, William K. Peters, and David M. Jonas. Electronic resonance with anticorrelated pigment vibrations drives photosynthetic energy transfer outside the adiabatic framework. *Proceedings of the National Academy of Sciences*, 110(4):1203–1208, 01 2013.

[3] Elisabetta Collini, Cathy Y. Wong, Krystyna E. Wilk, Paul M. G. Curmi, Paul Brumer, and Gregory D. Scholes. Coherently wired light-harvesting in photosynthetic marine algae at ambient temperature. *Nature*, 463(7281):644–647, 02 2010.

[4] Minhaeng Cho, Harsha M. Vaswani, Tobias Brixner, Jens Stenger, and Graham R. Fleming. Exciton analysis in 2d electronic spectroscopy. *The Journal of Physical Chemistry B*, 109(21):10542–10556, 06 2005.

[5] M. L. Cowan, J. P. Ogilvie, and R. J. D. Miller. Two-dimensional spectroscopy using diffractive optics based phased-locked photon echoes. *Chemical Physics Letters*, 386(1–3):184–189, 3 2004.

[6] Tobias Brixner, Tomáš Mančal, Igor V. Stiopkin, and Graham R. Fleming. Phase-stabilized two-dimensional electronic spectroscopy. *The Journal of Chemical Physics*, 121(9):4221–4236, 2004.

[7] 1948 Mukamel, S. (Shaul). Principles of nonlinear optical spectroscopy, 1995.

[8] Gabriela S. Schlau-Cohen, Akihito Ishizaki, Tessa R. Calhoun, Naomi S. Ginsberg, Matteo Ballottari, Roberto Bassi, and Graham R. Fleming. Elucidation of the timescales and origins of quantum electronic coherence in lhcii. *Nat Chem*, 4(5):389–395, 05 2012.

[9] Franklin D. Fuller, Jie Pan, Andrius Gelzinis, Vytautas Butkus, S. Seckin Senlik, Daniel E. Wilcox, Charles F. Yocum, Leonas Valkunas, Darius Abramavicius, and Jennifer P. Ogilvie. Vibronic coherence in oxygenic photosynthesis. *Nat Chem*, 6(8):706–711, 08 2014.

[10] Elisabet Romero, Ramunas Augulis, Vladimir I. Novoderezhkin, Marco Ferretti, Jos Thieme, Donatas Zigmantas, and Rienk van Grondelle. Quantum coherence in photosynthesis for efficient solar-energy conversion. *Nat Phys*, 10(9):676–682, 09 2014.

[11] Dugan Hayes, Graham B. Griffin, and Gregory S. Engel. Engineering coherence among excited states in synthetic heterodimer systems. *Science*, 340(6139):1431, 06 2013.

[12] Alexei Halpin, JohnsonPhilip J. M., Roel Tempelaar, R. Scott Murphy, Jasper Knoester, JansenThomas L. C., and MillerR. J. Dwayne. Two-dimensional spectroscopy of a molecular dimer unveils the effects of vibronic coupling on exciton coherences. *Nat Chem*, 6(3):196–201, 03 2014.

[13] Elisabetta Collini and Gregory D. Scholes. Coherent intrachain energy migration in a conjugated polymer at room temperature. *Science*, 323(5912):369, 01 2009.

[14] Franz Milota, Valentyn I. Prokhorenko, Tomas Mancal, Hans von Berlepsch, Oliver Bixner, Harald F. Kauffmann, and Jürgen Hauer. Vibronic and vibrational coherences in two-dimensional electronic spectra of supramolecular j-aggregates. *The Journal of Physical Chemistry A*, 117(29):6007–6014, 07 2013.

[15] Gregory S. Engel, Tessa R. Calhoun, Elizabeth L. Read, Tae-Kyu Ahn, Tomas Mancal, Yuan-Chung Cheng, Robert E. Blankenship, and Graham R. Fleming. Evidence for wavelike energy transfer through quantum coherence in photosynthetic systems. *Nature*, 446(7137):782–786, 04 2007.

[16] A. W. Chin, J. Prior, R. Rosenbach, F. Caycedo-Soler, S. F. Huelga, and M. B. Plenio. The role of non-equilibrium vibrational structures in electronic coherence and recoherence in pigment-protein complexes. *Nat Phys*, 9(2):113–118, 02 2013.

[17] N. Christensson, F. Milota, J. Hauer, J. Sperling, O. Bixner, A. Nemeth, and H. F. Kauffmann. High frequency vibrational modulations in two-dimensional electronic spectra and their resemblance to electronic coherence signatures. *The Journal of Physical Chemistry B*, 115(18):5383–5391, 05 2011.

[18] Daniel B. Turner, Krystyna E. Wilk, Paul M. G. Curmi, and Gregory D. Scholes. Comparison of electronic and vibrational coherence measured by two-dimensional electronic spectroscopy. *The Journal of Physical Chemistry Letters*, 2(15):1904–1911, 08 2011.

[19] Vytautas Butkus, Donatas Zigmantas, Leonas Valkunas, and Darius Abramavicius. Vibrational vs. electronic coherences in 2d spectrum of molecular systems. *Chemical Physics Letters*, 545:40–43, 8 2012.

[20] A. W. Chin, S. F. Huelga, and M. B. Plenio. Coherence and decoherence in biological systems: principles of noise-assisted transport and the origin of long-lived coherences. *Philosophical Transactions of the Royal Society A: Mathematical, Physical and Engineering Sciences*, 370(1972):3638, 07 2012.

[21] Vivek Tiwari, William K. Peters, and David M. Jonas. Energy transfer: Vibronic coherence unveiled. *Nat Chem*, 6(3):173–175, 03 2014.

[22] Aurélia Chenu, Niklas Christensson, Harald F. Kauffmann, and Tomáš Mančal. Enhancement of vibronic and ground-state vibrational coherences in 2d spectra of photosynthetic complexes. *Scientific Reports*, 3:2029 EP –, 06 2013.

[23] James Lim, David Paleček, Felipe Caycedo-Soler, Craig N. Lincoln, Javier Prior, Hans von Berlepsch, Susana F. Huelga, Martin B. Plenio, Donatas Zigmantas, and Jürgen

Hauer. Vibronic origin of long-lived coherence in an artificial molecular light harvester. *Nature Communications*, 6:7755 EP –, 07 2015.

[24] V. P. Singh, M. Westberg, C. Wang, P. D. Dahlberg, T. Gellen, A. T. Gardiner, R. J. Cogdell, and G. S. Engel. Towards quantification of vibronic coupling in photosynthetic antenna complexes. *The Journal of Chemical Physics*, 142(21):212446, 2015.

[25] Robert E. Blankenship. Molecular mechanisms of photosynthesis, 2002.

[26] Herbert van Amerongen. Photosynthetic excitons, 2000.

[27] Oliver Bixner, Vladimír Lukeš, Tomáš Mančal, Jürgen Hauer, Franz Milota, Michael Fischer, Igor Pugliesi, Maximilian Bradler, Walther Schmid, Eberhard Riedle, Harald F. Kauffmann, and Niklas Christensson. Ultrafast photo-induced charge transfer unveiled by two-dimensional electronic spectroscopy. *The Journal of Chemical Physics*, 136(20):204503, 2012.

[28] Bradley S. Prall, Dilworth Y. Parkinson, Naoto Ishikawa, and Graham R. Fleming. Anticorrelated spectral motion in bisphthalocyanines: Evidence for vibrational modulation of electronic mixing. *The Journal of Physical Chemistry A*, 109(48):10870–10879, 12 2005.

[29] Chanelle C. Jumper, Jessica M. Anna, Anna Stradomska, Juleon Schins, Mykhaylo Myahkostupov, Valentina Prusakova, Daniel G. Oblinsky, Felix N. Castellano, Jasper Knoester, and Gregory D. Scholes. Intramolecular radiationless transitions dominate exciton relaxation dynamics. *Chemical Physics Letters*, 599:23–33, 4 2014.

[30] Sung Cho, Michael W. Mara, Xianghuai Wang, Jenny V. Lockard, Aaron A. Rachford, Felix N. Castellano, and Lin X. Chen. Coherence in metalmetal-to-ligand-charge-transfer excited states of a dimetallic complex investigated by ultrafast transient absorption anisotropy. *The Journal of Physical Chemistry A*, 115(16):3990–3996, 04 2011.

[31] Brian A. Sparano, Shatrughan P. Shahi, and Kazunori Koide. Effect of binding and conformation on fluorescence quenching in new 2‘,7‘-dichlorofluorescein derivatives. *Organic Letters*, 6(12):1947–1949, 06 2004.

[32] Carl A. Elliger. Deoxygenation of aldehydes and ketones with sodium cyanoborohydride. *Synthetic Communications*, 15(14):1315–1324, 12 1985.

[33] Michal Afri, Aryeh A Frimer, and Yael Cohen. Active oxygen chemistry within the liposomal bilayer. part iv: Locating 2',7'-dichlorofluorescein (dcf), 2',7'-dichlorodihydrofluorescein (dcfh) and 2',7'-dichlorodihydrofluorescein diacetate (dcfh-da) in the lipid bilayer. *Chemistry and physics of lipids*, 131(1):123–133, 2004.

[34] M. Reddington and M. Lyttle. Xanthene dyes, 2005.

[35] Shenyi Zhang, Chunmei Yang, Weiqiang Lu, Jin Huang, Weiping Zhu, Honglin Li, Yufang Xu, and Xuhong Qian. A highly selective space-folded photo-induced electron transfer fluorescent probe for carbonic anhydrase isozymes ix and its applications for biological imaging. *Chemical Communications*, 47(29):8301–8303, 2011.

[36] Moira L. Flanagan, Phillip D. Long, Peter D. Dahlberg, Brian S. Rolczynski, Sara C. Massey, and Gregory S. Engel. Mutations to r. sphaeroides reaction center perturb energy levels and vibronic coupling but not observed energy transfer rates. *The Journal of Physical Chemistry A*, 120(9):1479–1487, 03 2016.

[37] Dugan Hayes, Jianzhong Wen, Gitt Panitchayangkoon, Robert E. Blankenship, and Gregory S. Engel. Robustness of electronic coherence in the fenna-matthews-olson complex to vibronic and structural modifications. *Faraday Discussions*, 150(0):459–469, 2011.

[38] Vadim V. Lozovoy, Igor Pastirk, and Marcos Dantus. Multiphoton intrapulse interference. iv. ultrashort laser pulse spectral phase characterization and compensation. *Optics Letters*, 29(7):775–777, 2004.

[39] Yuan-Chung Cheng and Graham R. Fleming. Dynamics of light harvesting in photosynthesis. *Annual Review of Physical Chemistry*, 60(1):241–262, 2016/10/26 2009.

[40] Gregory D. Scholes, Graham R. Fleming, Alexandra Olaya-Castro, and Rienk van Grondelle. Lessons from nature about solar light harvesting. *Nat Chem*, 3(10):763–774, 10 2011.

[41] Yuan-Chung Cheng, Gregory S. Engel, and Graham R. Fleming. Elucidation of population and coherence dynamics using cross-peaks in two-dimensional electronic spectroscopy. *Chemical Physics*, 341(1–3):285–295, 11 2007.

[42] John D. Hybl, Allison Albrecht Ferro, and David M. Jonas. Two-dimensional fourier transform electronic spectroscopy. *The Journal of Chemical Physics*, 115(14):6606–6622, 2001.

[43] Daniel B. Turner, Rayomond Dinshaw, Kyung-Koo Lee, Michael S. Belsley, Krystyna E. Wilk, Paul M. G. Curmi, and Gregory D. Scholes. Quantitative investigations of quantum coherence for a light-harvesting protein at conditions simulating photosynthesis. *Physical Chemistry Chemical Physics*, 14(14):4857–4874, 2012.

[44] N. Killoran, S. F. Huelga, and M. B. Plenio. Enhancing light-harvesting power with coherent vibrational interactions: A quantum heat engine picture. *The Journal of Chemical Physics*, 143(15):155102, 2015.

[45] Jake Iles-Smith, Arend G. Dijkstra, Neill Lambert, and Ahsan Nazir. Energy transfer in structured and unstructured environments: Master equations beyond the born-markov approximations. *The Journal of Chemical Physics*, 144(4):044110, 2016.

[46] Akihito Ishizaki and Graham R. Fleming. Quantum coherence in photosynthetic light harvesting. *Annual Review of Condensed Matter Physics*, 3(1):333–361, 2016/11/01 2012.

[47] Darius Abramavicius and Leonas Valkunas. Role of coherent vibrations in energy transfer and conversion in photosynthetic pigment–protein complexes. *Photosynthesis Research*, 127(1):33–47, 2016.

[48] S. Oviedo-Casado, J. Prior, A. W. Chin, R. Rosenbach, S. F. Huelga, and M. B. Plenio. Phase-dependent exciton transport and energy harvesting from thermal environments. *Physical Review A*, 93(2):020102–, 02 2016.

[49] Jordan M. Womick and Andrew M. Moran. Exciton coherence and energy transport in the light-harvesting dimers of allophycocyanin. *The Journal of Physical Chemistry B*, 113(48):15747–15759, 12 2009.

[50] Gitt Panitchayangkoon, Dugan Hayes, Kelly A. Fransted, Justin R. Caram, Elad Harel, Jianzhong Wen, Robert E. Blankenship, and Gregory S. Engel. Long-lived quantum coherence in photosynthetic complexes at physiological temperature. *Proceedings of the National Academy of Sciences*, 107(29):12766–12770, 07 2010.

CHAPTER 4

TWO DIMENSIONAL ELECTRONIC SPECTROSCOPY OF CAVITAND MOLECULAR SWITCH REVEALS DYNAMICS THAT FRUSTRATE ACCURATE FRET MEASUREMENTS

Förster Resonance Energy Transfer (FRET) describes the incoherent transfer of an electronic excitation from a donor fluorophore to a nearby acceptor. FRET has been applied as a probe of local chromophore environments and distances on the nanoscale, taking advantage of the steep distance dependence of transfer efficiency and the ability to extract efficiencies from standard experimental values such as fluorescence intensities or lifetimes. Competition from nonradiative relaxation processes is often assumed to be constant, but as this competition depends on the donor environment, which may change substantially with conformational changes. In this chapter, we perform two dimensional electronic spectroscopy (2DES) on a pair of functionalized borondipyrromethine (BODIPY) dyes, that are attached on opposite arms of a resorcin[4]arene cavitand molecular switch, to study the effects of nonradiative relaxation on FRET dynamics. Temperature induced switching between two conformations (from *vase* to *kite*) increases the donor-acceptor distance from 0.5 to 3 nm, affecting both FRET efficiency and nonradiative relaxation. By disentangling different dynamics based on lifetimes in 2D spectra, we independently observe nonradiative relaxation, energy transfer (FRET), and residual fluorescence from the donor in both *vase* to *kite* conformations. We observe changes in both FRET rate and nonradiative relaxation when the molecule switches from *vase* to *kite*, and measure a 70% greater change in transfer efficiency with donor-acceptor distance than would be determined by standard lifetime-based measurements. These observations show that changes in competing nonradiative processes must be taken into account when highly accurate measurements of FRET efficiency are desired.

The work presented in this chapter has equal contributions from L. Wang and John. P. Otto.

4.1 Nonradiative processes contributions to FRET measurements in complex environments.

Förster Resonance Energy Transfer (FRET) is a mechanism that moves an excitation nonradiatively from a donor fluorophore to a nearby acceptor via transition dipole interactions [1]. FRET can be elegantly described by readily accessible experimental parameters such the distance between chromophores (R), the fluorescence spectrum of the donor, and the absorption spectrum of the acceptor [2]. The mechanism's well known R^{-6} distance dependence has led to widespread application [3, 4] of FRET as a spectroscopic measure of distances on the single nanometer scale [5, 6] particularly to probe interactions between biomolecules such as proteins [6–10] and DNA [11–14] and to image those interactions within cells [15–21] and an extensive array of donor-acceptor pairs have been developed for these purposes [8, 14, 22–28]. In Förster's model, the coupling between the donor and acceptor electronic states is treated as a second order perturbation allowing the interaction to be governed by the transition dipole moments of the excited electronic states. The coupling is sufficiently weak (and the transfer rate therefore sufficiently slow) that the donor relaxes to thermal vibrational equilibrium in its electronic excited state before transfer can occur. Although no absorption or emission occurs in the transfer itself (FRET is nonradiative), the same transition dipoles as donor emission and acceptor absorption drive the transfer, so resonance can be determined by absorption and emission spectra, and transfer competes with donor fluorescence (and, as we will show, non-radiative relaxation).

Experimentally, FRET efficiency can be determined by photon counts of donor or acceptor fluorescence, or by changes in the donor's decay lifetime [20, 29]. The latter approach is often preferred due to relative immunity to cross-talk and concentration artifacts [7, 19, 22] and is based on kinetic competition of decay processes, leading to equations for efficiency such as

$$E = 1 - \frac{\tau_{DA}}{\tau_D} = \frac{1}{1 + (R/R_0)^6} \tag{4.1}$$

where τ_D and τ_{DA} are measured lifetimes of the donor alone and in the presence of the acceptor, R is the donor-acceptor distance, and R_0 is the distance at which the transfer rate is equal to τ_D, corresponding to 50% transfer [9, 21]. The donor lifetime depends on the relative rates of competing processes as

$$\frac{1}{\tau_D} = k_D = k_{D,f} + k_{D,nr} \tag{4.2}$$

$$\frac{1}{\tau_{DA}} = k_{DA} = k_{D,f} + k_{D,nr} + k_{tr} \tag{4.3}$$

where $k_{D,f}$, $k_{D,nr}$, and k_{tr} correspond to fluorescence, nonradiative relaxation, and energy transfer. Lifetime based FRET determinations of this nature rely on assumptions that all processes involved are in kinetic competition, and that processes other than FRET, i.e. nonradiative relaxation, behave similarly for the donor regardless of the donor-acceptor distance [30]. However, local solvation conditions and system-bath coupling can change as molecular conformation changes. Such changes can break the assumptions above and frustrate accurate measurement of FRET efficiency. We demonstrate this scenario using 2D electronic spectroscopy and show how nonradiative processes affect FRET measurements.

To investigate the interactions between nonradiative relaxation and FRET, we synthesized a model dimer consisting of a pair of functionalized boron-dipyrromethine (BODIPY) dyes (donor and acceptor) attached to opposite walls of a resorcin[4]arene cavitand molecular switch. Derived from previous studies that established cavitands as a platform for FRET dynamics [31–33], this BODIPY-cavitand dimer switches via temperature change between two conformations, *vase* at room temperature (RT) and *kite* at -80°C. Short linkers on the cavitand base hold donor-acceptor distances at 0.5 nm in the *vase* conformation and at 3 nm for *kite*. The BODIPY derivatives used as donor and acceptor are chosen due to their known intrachromophore nonradiative relaxation pathways [34–36]. Observing interactions between nonradiative relaxation and FRET is made possible by resolving signals from these processes in energy and time. Two-dimensional electronic spectroscopy (2DES) has this

ability, and has previously given insight into ultrafast energy transfer and relaxation dynamics in both biological [37–39] and synthetic [40–42] systems. Here we use this technique to probe the energy transfer and relaxation dynamics in a model dimer in order to drive future improvements in FRET techniques.

By performing 2DES measurements on the BODIPY-cavitand dimer and separating the signal based on time dynamics, we disentangle three relaxation pathways (nonradiative relaxation, energy transfer, and residual fluorescence) and isolate their lineshapes from the donor in both conformations (*kite* at -80°C and *vase* at room temperature). Based on our signal isolation analysis, we observe that the contribution of nonradiative relaxation to the overall donor decay changes with conformation. We show that due to this change in nonradiative relaxation, lifetime measurements underreport the transfer efficiency difference between *kite* and *vase* conformations, highlighting the need to test assumptions about nonradiative processes when measuring FRET in complex environments.

4.2 The BODIPY-cavitand dimer system.

To understand the interactions between nonradiative relaxation and FRET, we developed a model dimer that undergoes both processes and gives us external control of the transfer dynamics. The chemical structure of the BODIPY-cavitand dimer is shown in Figure 4.1. Figure 4.2.a shows molecular geometries of the dimer in both conformations, calculated using the semi-empirical AM1 Hamiltonian in Gaussian 09 [43, 44]. The BODIPY-cavitand dimer adopts the *vase* conformation at room temperature (RT, 21°C), but switches to the *kite* conformation at low temperature due entropic interactions with the surrounding solvent [45]. Switching begins near -50°C, and by -80°C all molecules are in the *kite* conformation. The molecular switch design provides a direct handle on donor-acceptor distance and the vibrational bath that defines the local environments of the donor and acceptor. In the *vase* conformation, the donor and acceptor are sterically confined in an orientation that promotes dipole-dipole coupling, and the ∼0.5 nm donor-acceptor distance is too close to

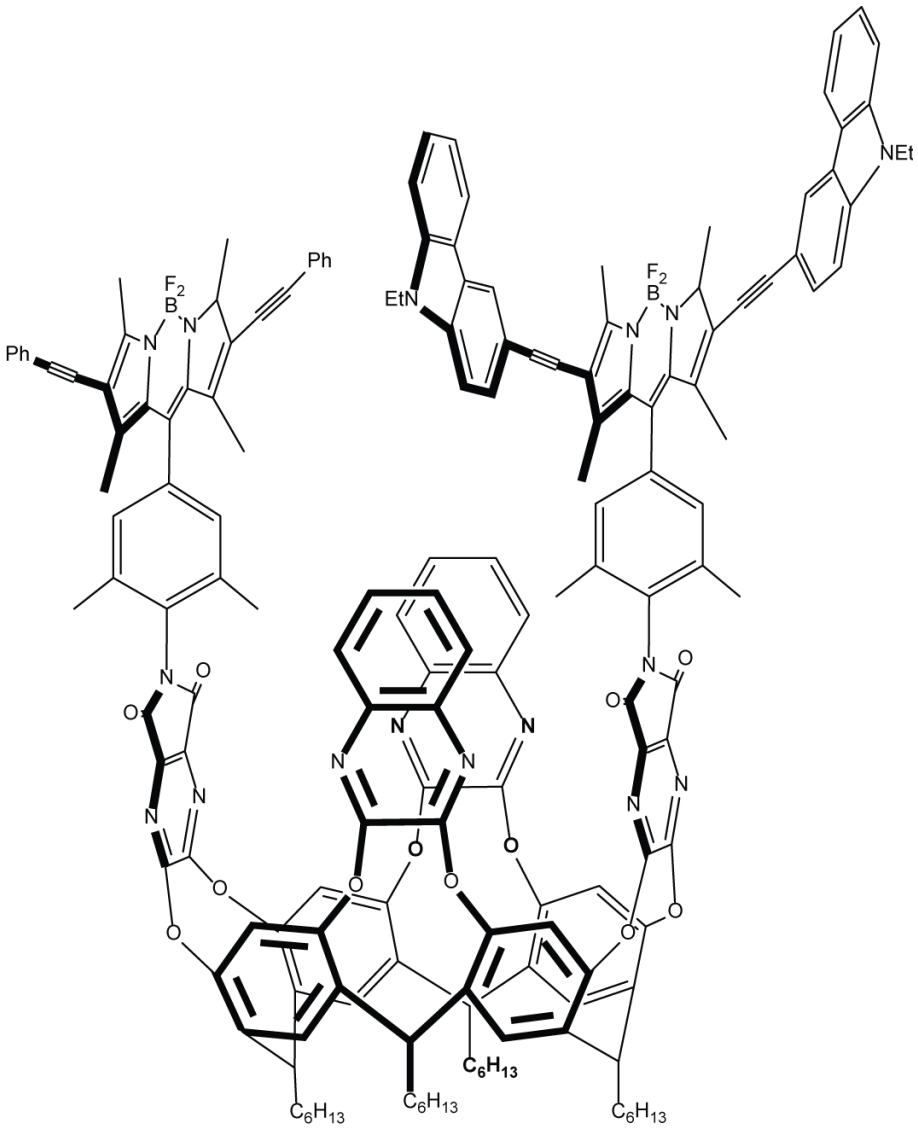

Figure 4.1: The chemical structure of the BODIPY-cavitand dimer. Donor (left) consists of an extended BODIPY core substituted with phenylacetylene groups, while the acceptor (right) is the same but with the phenyl groups replaced with N-ethyl carbazole

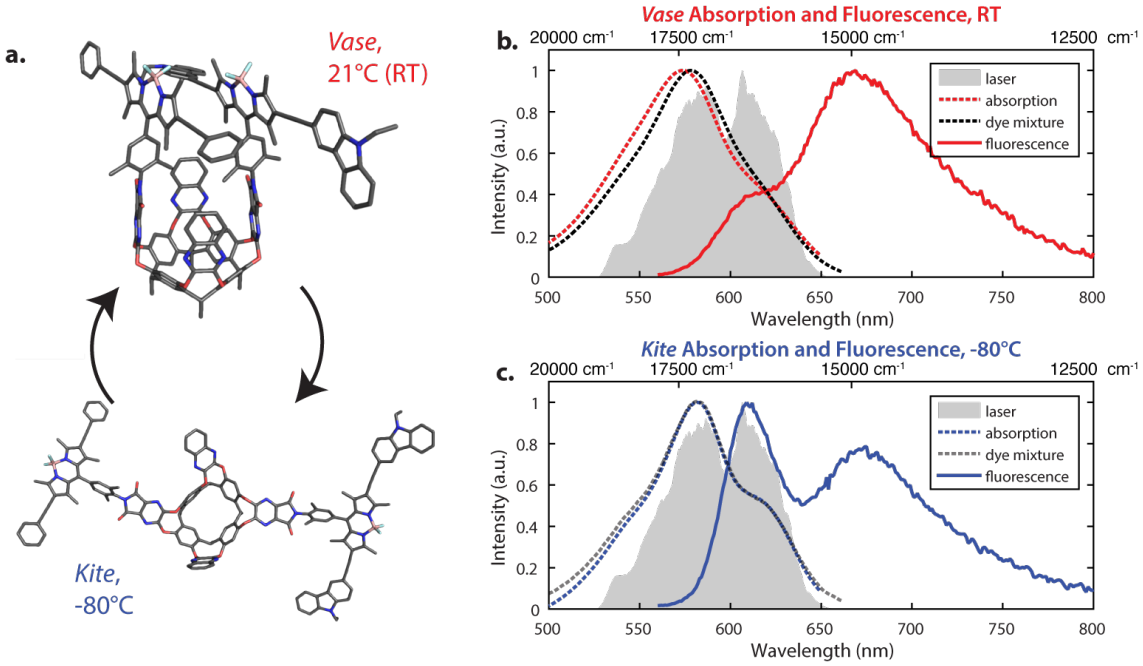

Figure 4.2: Calculated structures and corresponding optical properties of *vase*/*kite* conformations. (a) AM1 optimized geometries of the cavitand in *vase* (top left) and *kite* (bottom left) conformations, representative of the structure at 21°C and -80°C, respectively. (b) Absorption (red dashed line) and fluorescence (solid line) of the *vase* conformation. (c) Absorption (blue dashed line) and fluorescence (solid line) of the *kite* conformation. Laser spectrum is filled with grey area. Absorption of donor-acceptor mixture (1:1 molar ratio) at RT and -80°C are plotted with black dashed lines in panel b and dark grey dashed lines in panel c. The absorption mismatch between cavitand and dye mixture in the *vase* conformation indicates strong donor-acceptor interaction. The fluorescence spectra, excited at 525 nm for both conformations, show increased energy transfer in the *vase* conformation than in the *kite*, as evidenced by the intensity shift from donor emission at 610 nm to acceptor emission at 670 nm.

allow independent solvation of the two chromophores, suggesting that they must interact vibrationally as well. By comparison, the *kite* conformation provides relative orientational freedom to the donor and acceptor and a separation of ∼3 nm, and while they are separated by less than R_0, they interact weakly enough that the approximations made in FRET theory accurately describe their interaction. The large donor and acceptor dyes in the BODIPY-cavitand dimer were chosen both for their significant nonradiative relaxation (evident from fluorescence quantum yields) and for their large spectral overlap of donor emission with acceptor absorption, which promotes FRET.

Quantum Yield (%)	
Donor	30.6 ± 0.8
Acceptor	4.40 ± 0.02

Table 4.1: Fluorescence quantum yield of donor and acceptor.

The quantum yields of the donor and acceptor are shown in table 4.1 and Figure 4.3. All spectra for the quantum yield measurement were recorded using a Horiba Fluorolog 3 with the Quanta-Phi integrating sphere attachment. Actual calculation of quantum yields was performed via the software packaged with the instrument, and the values are recorded below in Table 4.1. Scatter-corrected absorption is determined by subtracting the scatter signal at from the fluorophore solution from that of a solvent blank, measured with the same excitation source. Scatter-corrected emission is similarly determined by subtracting solvent blank signal from the fluorophore emission spectrum. The ratio of integrated fluorophore emission counts to absorption counts defines the quantum yield. In this case, acceptor emission spectra are scaled by a factor of 1/100 to account for a 100x longer integration time due to weak signal.

UV/Vis absorption spectra of the BODIPY-cavitand dimer were recorded using a Cary 5000 dual-beam UV/VIS/NIR spectrophotometer and the steady state fluorescence spectra were measured via a Horiba Fluorolog 3. Absorption and fluorescence spectra of the *vase* conformation at room temperature and *kite* conformation at -80°C are shown in Figure 4.2.b

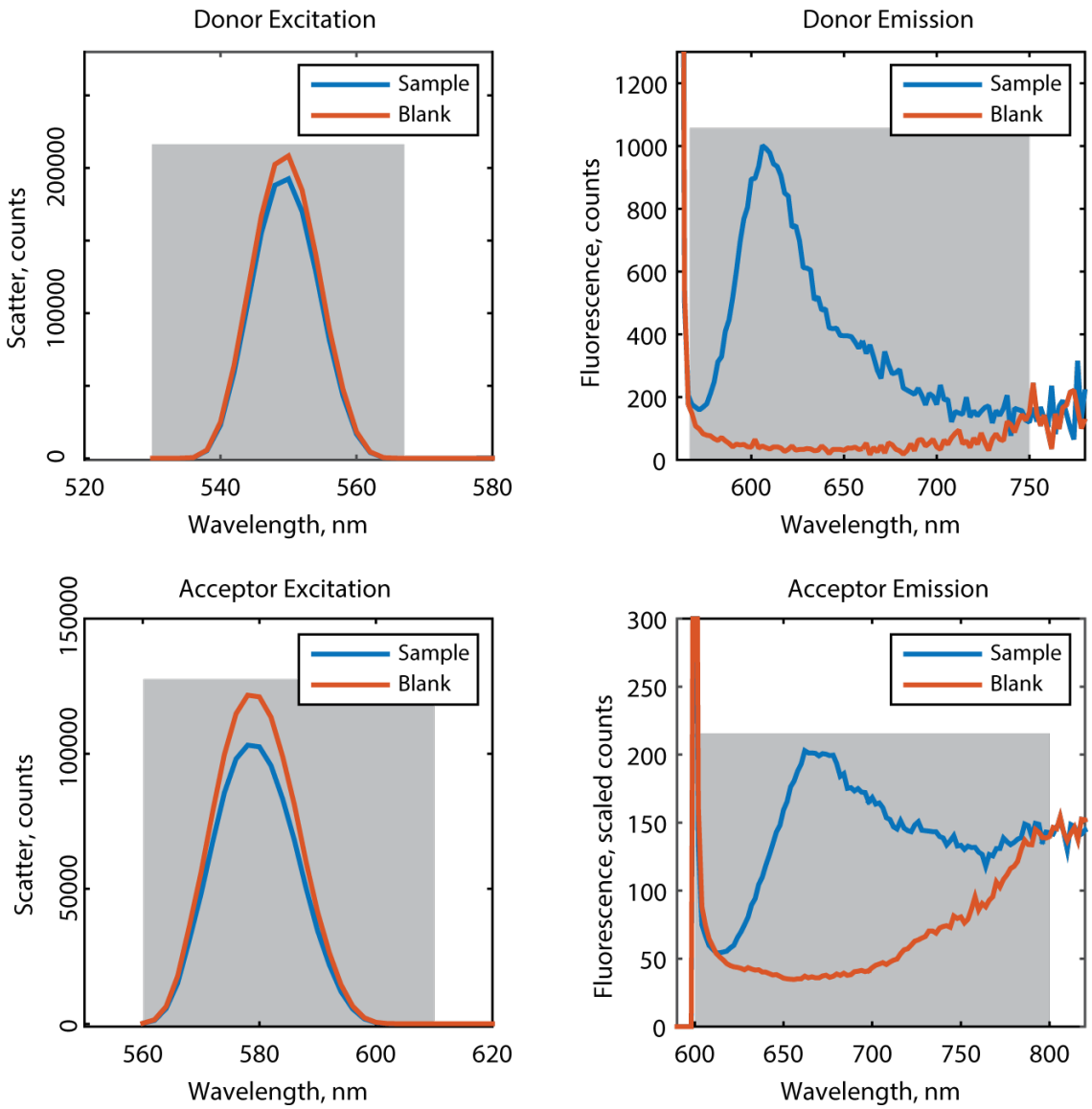

Figure 4.3: Excitation and emission spectra (with reference solvent blank) for fluorescence quantum yield calculation. Grey boxes indicate bounds of integration for quantum yield calculations.

and Figure 4.2.c. Comparison of the BODIPY-cavitand dimer absorption spectra (dashed red/blue lines) to that of a 1:1 mixture of donor and acceptor in solution at the two temperatures (dashed black/grey lines) highlights the change in electronic coupling that occurs with conformational switching. The *kite* spectra resembles that of the dye mixture, but the *vase* absorption blue-shifts relative to the dye mixture, indicating interactions between the donor and acceptor that shift their ground and excited state energies. Fluorescence spectra of *vase* (red solid line in Figure 4.2.b) and *kite* (blue solid line in Figure 4.2.c) dimers show a clear increase in donor emission and concurrent decrease in acceptor emission when the BODIPY-cavitand dimer switches from *kite* to *vase*. These fluorescence intensity changes suggest a decrease in FRET efficiency when the donor-acceptor distance increases, indicating that the BODIPY-cavitand dimer performs as designed.

4.3 2D electronic spectra of the BODIPY-cavitand dimer.

Two-dimensional electronic spectroscopy (2DES) is a four-wave mixing technique that uses three ultrafast pulses at controlled time delays to interact with a sample, generating a third order nonlinear signal. Two frequency axes, ω_τ and ω_t, are produced via Fourier transformation over the first and third time delays (coherence time, τ, and rephasing time, t). These axes represent the frequencies of excitation and detection, respectively, and correspond to the horizontal (ω_τ) and vertical (ω_t) axes on all 2D spectra shown in this paper. Shown as the change in transmitted light (ΔT), signal recorded at a series of waiting times (T) can reveal the time dynamics of the interrogated sample. Positive features can be attributed to stimulated emission (SE) or to ground state bleach (GSB, a decrease in absorption caused by depletion of the ground state population). Negative features are due to excited state absorption (ESA).

2D spectra are frequency-frequency correlation maps; describing the optical response of a system (recorded on ω_t axis) at a series of waiting time T after initial excitation at ω_τ. In contrast to typical fluorescence techniques, which only capture spontaneous emission

from excited states, 2DES captures dynamics on both the excited states (ESA and SE) and the ground states (GSB) of the chromophores. Signals due to excited state dynamics (e.g. energy transfer or Stokes shift within an individual chromophore) will lead to spectral position changes from diagonal to off diagonal in a 2D spectrum. By comparison, ground state bleach signals will stay on the diagonal, and can thus be separated from excited state dynamics. Separate observation of ground and excited state dynamics can be useful for de-convoluting complex energy transfer pathways.

Additionally, the lineshapes of 2D signals inform on the mechanisms that lead to broad spectral signals [46]. Inhomogeneous broadening (extension along the diagonal) gives insight into static variation in chemical environments, which perturb the excitation energies of individual chromophores [47]. Comparatively, homogeneous broadening (which determines antidiagonal linewidth) occurs when frequency fluctuations due to bath interactions occur quickly compared to the experimental timescale, such that an individual chromophore experiences all configurations of its local environment during a given measurement and thus represents the entire ensemble [48]. In the homogeneous limit, one can estimate the dephasing time of a transition by its homogeneous linewidth [49].

Two-dimensional electronic spectra of the BODIPY-cavitand dimer were acquired using a homebuilt instrument that has been described previously [40]. A Ti:Sapphire oscillator and regenerative amplifier (Micra and Legend Elite, Coherent) generate a 5kHz, 100fs pulse train that is directed into a noncollinear optical parametric amplifier (NOPA, TOPAS). The output of the NOPA is then compressed using a prism pair followed by a spatial light modulator array (FemtoJock, Biophotonics). The resulting pulse (12 fs, 530-650 nm FWHM) is then split into four via a beamsplitter and a transmissive grating. The four beams are directed to the sample with a boxcar geometry. The time delays are controlled by paired glass wedges (coherence time, τ) and a translational stage (waiting time, T). Beam 1, 2 and 3 interacts with sample to generate the third-order signal. Beam 4 is attenuated by three orders of magnitude and serves as local oscillator for heterodyne detection. Signal, along

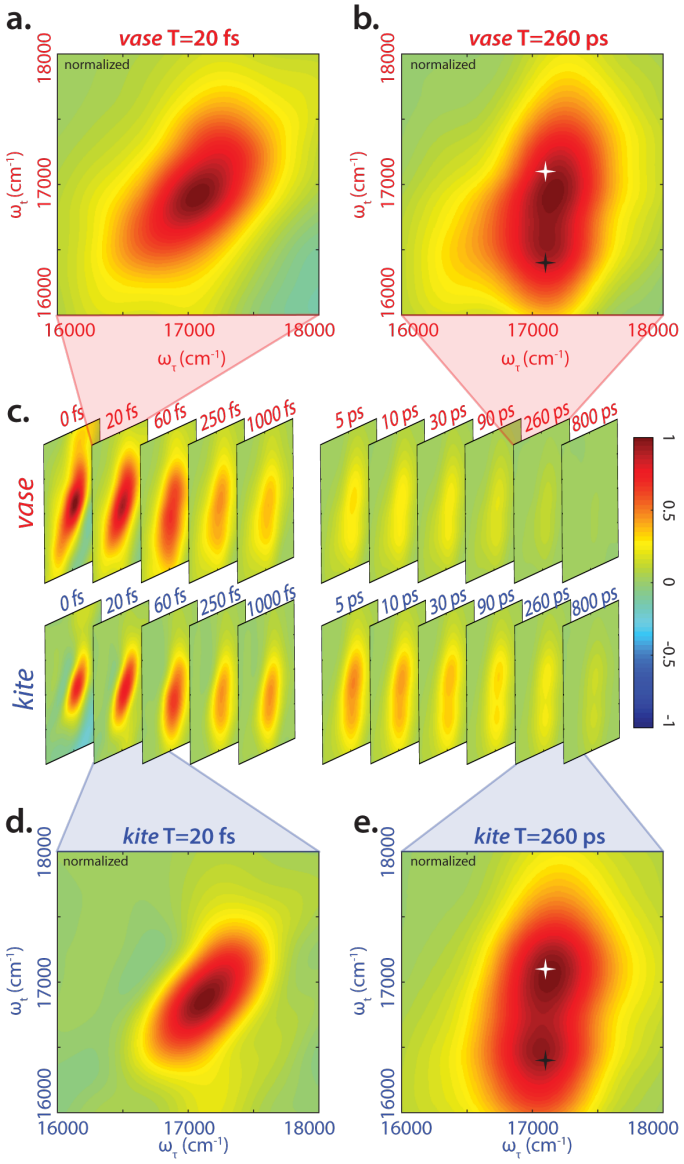

Figure 4.4: Representative real-valued phased 2DES spectra for *vase*/*kite* conformation. (a) 2DES spectra of *vase* at 20 fs waiting time. (b) 2DES spectra of *vase* at 260 ps waiting time. Highlighted points are 17100 cm^{-1} (585 nm) diagonal (white star) and crosspeak (black star) at the same ω_τ (17100 cm^{-1}, 585 nm) and ω_t of 16400 cm^{-1} (610 nm). (c) Time series of 2D spectra ranging 0-1000 fs and 5-800 ps for both *vase* and *kite*, normalized to T=0. (d) 2DES spectra of *kite* at 20 fs waiting time. (e) 2DES spectra of *kite* at 260 ps waiting time, with same highlights as in b. Spectra in a and d are normalized independently for the two conformations at 20 fs, while spectra b and e are normalized independently for the two conformations at 260 ps. The growth of the cross peak (black star, 17100 cm^{-1} in ω_τ and 16400 cm^{-1} in ω_t) corresponds to donor relaxation to donor fluorescence as well as FRET transfer to acceptor absorption during waiting time.

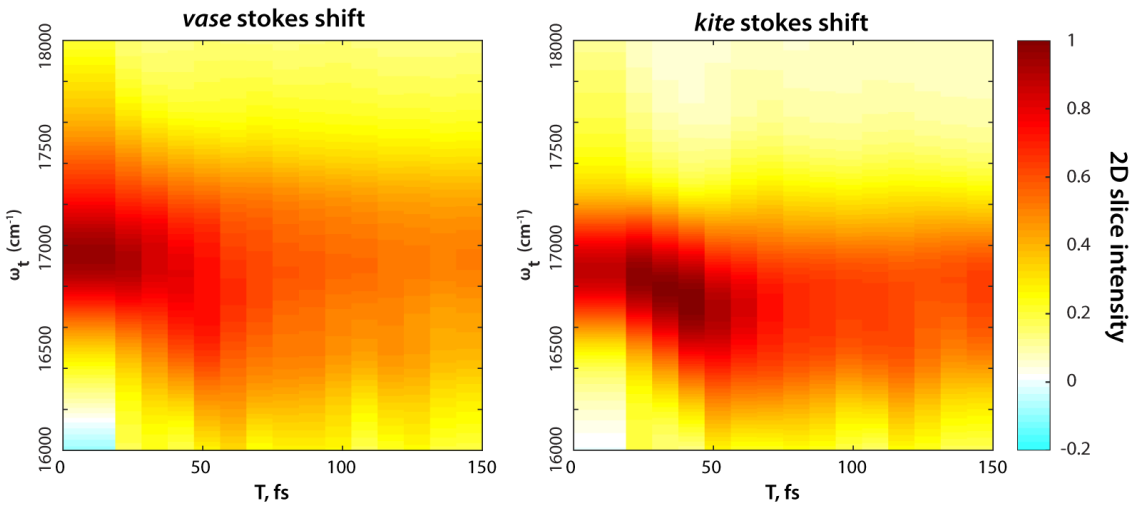

Figure 4.5: Stokes shift in *vase* and *kite* measured by ultrafast 2DES. A vertical slice of the 2D spectrum taken at ω_τ =17100 cm^{-1} from 0 to 150 fs waiting time is shown. Vertical axis ω_t is the same as in all other 2D spectra shown. Initial excitations relax on the order of 30-50 fs, consistent with dephasing lifetimes calculated from Figure 4.6.

with the local oscillator, is directed to a spectrometer and the resulting interferogram is recorded on a CCD array (Andor).

We performed 2DES measurements on the BODIPY-cavitand dimer at both room temperature and -80°C in two sets of waiting times: one from -20 to 1000 fs with a 10 fs stepsize, and the other from -5 to 800 ps with a 5 ps stepsize. Representative real-valued 2D spectra for the *kite* and *vase* conformations of the dimer are shown in Figure 4.4, which contains logarithmically spaced time series and highlights time points for comparison. The 2D spectra of each conformation in Figure 4.4.c are normalized to the maximum of 2D spectrum at T=0 fs in both datasets, and the frames in the highlighted spectra (Figure 4.4.a, Figure 4.4.b, Figure 4.4.d, and Figure 4.4.e) are normalized individually.

At T=20 fs, 2D spectra of both vase (Figure 4.4.a) and kite (Figure 4.4.d) show an inhomogeneously broadened peak along the diagonal at roughly 17100 cm^{-1}. This signal corresponds to the initial absorption of the donor, because at 20 fs the system has not yet relaxed past this starting point. Vibrational relaxation (aka Stokes shift) from this initial absorption occurs within the first 100 fs, leading to the below diagonal cross peak in all

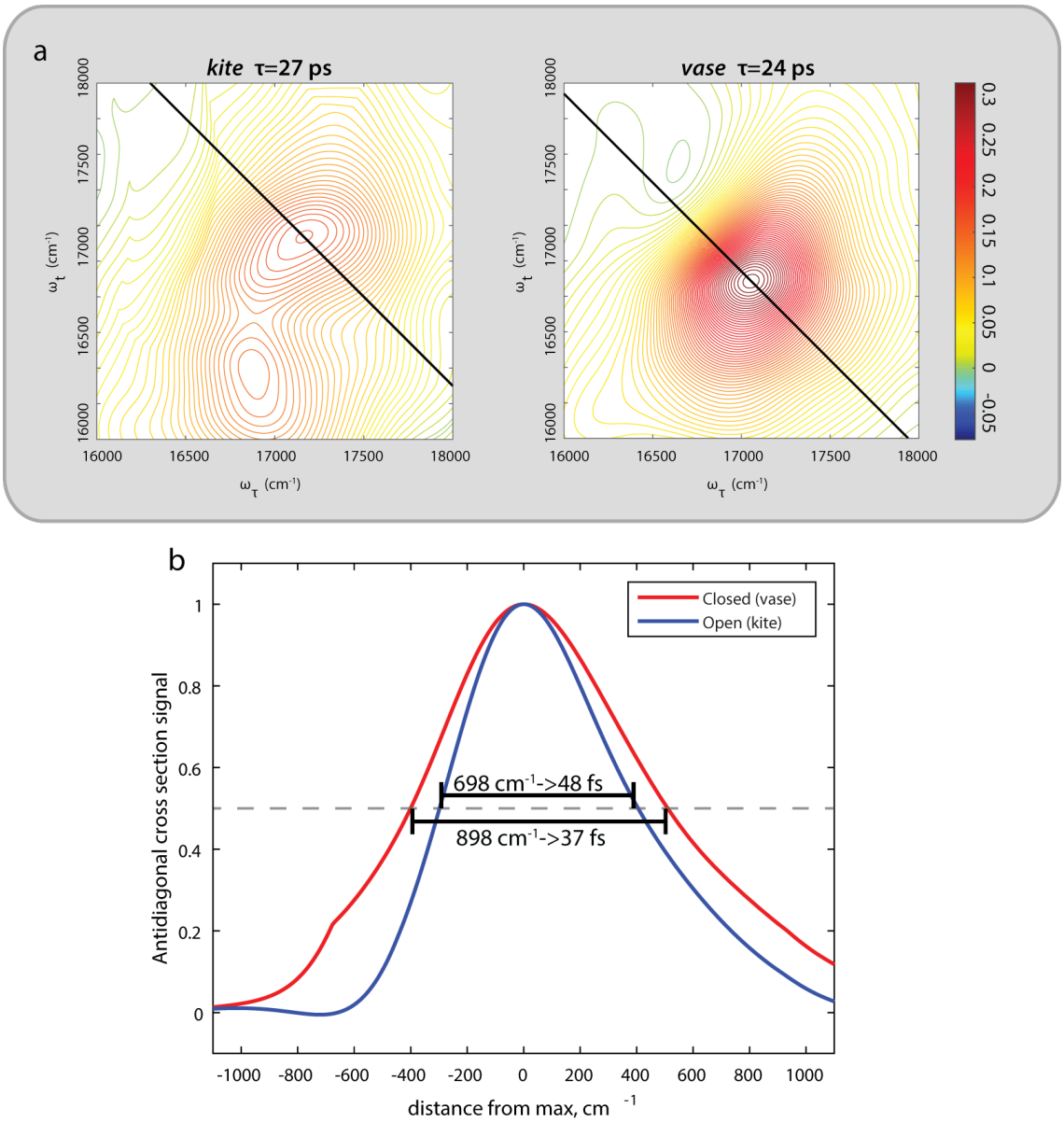

Figure 4.6: Dephasing lifetimes derived from nonradiative relaxation signals. (a) Nonradiative relaxation lifetime maps of *kite* and *vase* conformation. The figures are the same as Figure 4.8 in the main text, overlaid with location of antidiagonal cut, aligned with max signal. (b) Antidiagonal profile with inset FWHM and corresponding dephasing lifetimes, calculated as the inverse of the frequency FWHM [49].

subsequent spectra.

At T=260 ps (Figure 4.4.b and Figure 4.4.e), two dominant features are present in both 2D spectra —a diagonal peak at 17100 cm^{-1} (white star) and a crosspeak at 17100 cm $^{-1}$ (585 nm) in ω_τ and 16400 (610 nm) cm^{-1} in ω_t (black star). The diagonal feature at T=260 ps is due to ground state bleach on the donor, because Stokes shift from the initial excitation has completed by this time. The below diagonal crosspeak corresponds primarily to stimulated emission from the Stokes shifted excited state of the donor. Additionally, all features are very broad along the anti-diagonal direction, indicating the homogeneity of excited donor molecules. This homogeneity is caused by rapid dephasing on the scale of tens of fs, possibly driven by the same processes as the Stokes shift observed in femtosecond resolved 2D spectra (as shown in Figure 4.5), which occurs on the same timescale. The dephasing lifetimes are shown in Figure 4.6.

4.4 Lifetime specific 2D signal isolation.

Lifetime maps, generated from global fitting of the decay dynamics of each pixel in a 2D spectrum, quantify the contributions of various pathways to the overall signal. We performed this lifetime map analysis on the long waiting time (5 ps resolved) 2D data, specifically from 5 ps to 800 ps.

4.4.1 Fitting algorithm.

To obtain the lifetime maps shown in Figure 4.8, the following approach was taken: First, lifetimes were determined using a binned dataset (10x in both frequency dimensions) with waiting times from 5 ps to 800 ps. Time traces associated with each pixel in the 2D spectra were fit to a bi-exponential decay with an offset

$$S(T) = A_1 e^{-T/\tau_1} + A_2 e^{-T/\tau_2} + A_3 \tag{4.4}$$

where τ_1 and τ_2 are globally optimized decay constants for different transfer or relaxation processes. The A_i values correspond to the contribution of each process with A_3 corresponding to the contribution of signals with decay constant $\tau_3 \gg 800$ ps (our experimental timescale). Results of this fit were used to filter out points with less than 10% total signal from the first or second lifetime. The remaining signal was then least-squares fit to the same model, but with τ_1 and τ_2 constant across the dataset (to optimize those values, listed in Table 4.2). These lifetimes were then used to generate the maps shown in Figure 4.8 using an unbinned dataset. For this, each pixel in frequency space was normalized and least-squares fit to the same model with the global times. The resulting map of pre-exponentials (which summed to one in each pixel) was then weighted by the signal at T=5ps (the first nonzero waiting time) to give the plots in Figure 4.8.

	τ_1 (ps)	τ_2 (ps)
kite	24.3 ± 3.4	510.5 ± 41.4
vase	27.4 ± 5.2	271.4 ± 8.2

Table 4.2: Lifetimes used to generate lifetime maps.

Confidence bounds for the pre-exponentials are shown in Figure 4.7. To generate the maps shown in Figure 4.7, we scaled one side of the 95% confidence bound for the given parameter by the intensity of the starting value (same scaling as in Figure 4.8 in main text).

4.4.2 Lifetime maps of the BODIPY-cavitand dimer.

The lifetime maps generated by the algorithm described in Section 4.4.1 is shown in Figure 4.8.The left (grey) column in Figure 4.8 shows a fast ($\sim$ 25ps) decay for the BODIPY-cavitand dimer in the *vase* (RT, top) and *kite* (-80°C, bottom) conformations. These lifetimes are consistent with reports of a decay in the 15-30 ps range for meso-aryl substituted boron dipyrrin structures [34, 35] and in BODIPY. We assign this fast decay to a nonradiative, vibrationally driven relaxation via combination of flexing in the dipyrrin backbone and in rotation of the aryl group as suggested by references [34] and [35].This vibrational relax-

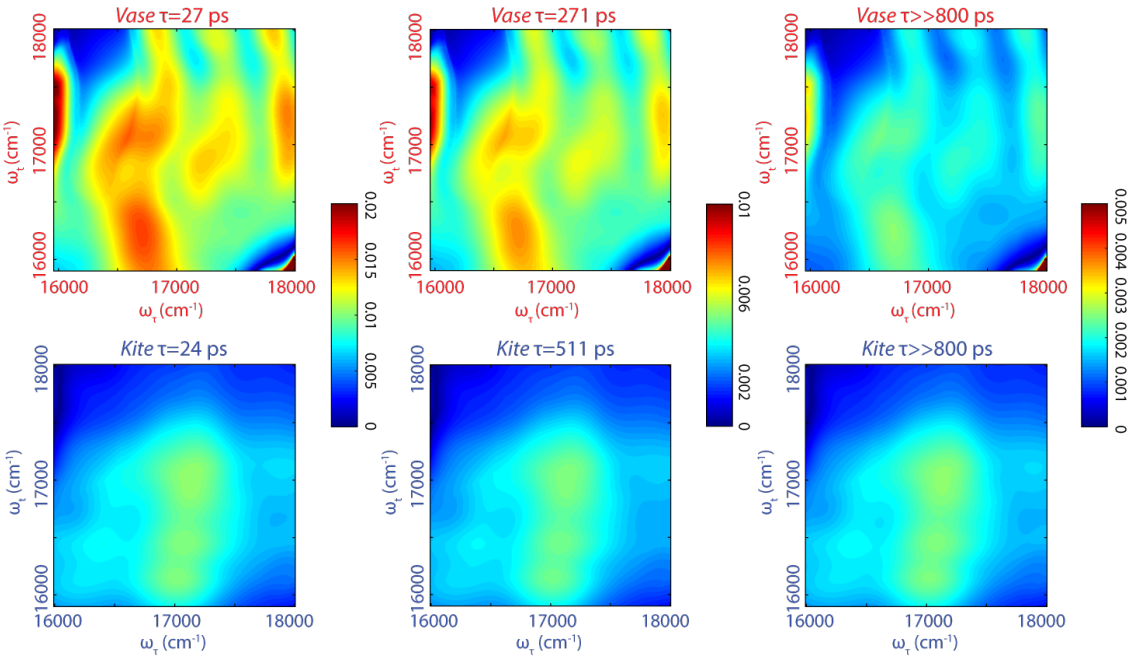

Figure 4.7: Absolute value of 95% confidence bounds for fitting maps presented in Figure 4.8.. Generated by multiplying one side of the symmetrical 95% confidence range of the relevant fit parameter (absolute value) with the starting real value signal as is done in Figure 4.8.

ation does not compete kinetically with energy transfer or fluorescence due to the multi-well potential energy surface of the excited donor [34].

While the lifetimes of this nonradiative relaxation pathway are very similar for both conformations, the corresponding lineshapes in the 2D lifetime map notably differ. In the *kite* spectrum (lower left plot, grey, in Figure 4.8), the signal is primarily due to one homogeneously broadened feature at 17000 cm^{-1}. The antidiagonal FWHM of this feature corresponds to a homogeneous process with a dephasing lifetime of 48 fs, coincident with the timescale of relaxation within the electronic excited state as seen via Stokes shift in femtosecond resolved 2DES (Figure 4.5). The *vase* spectrum (upper left plot in Figure 4.8) shows a similar feature near the diagonal as well as a below diagonal feature. The presence of this off diagonal feature suggests significant perturbation of the excited state potential energy surface due to the proximity of the acceptor.

The middle (orange) column in Figure 4.8 represents the strength of signal corresponding to a several hundred ps decay time. This decay lifetime is not observed in fluorescence lifetime

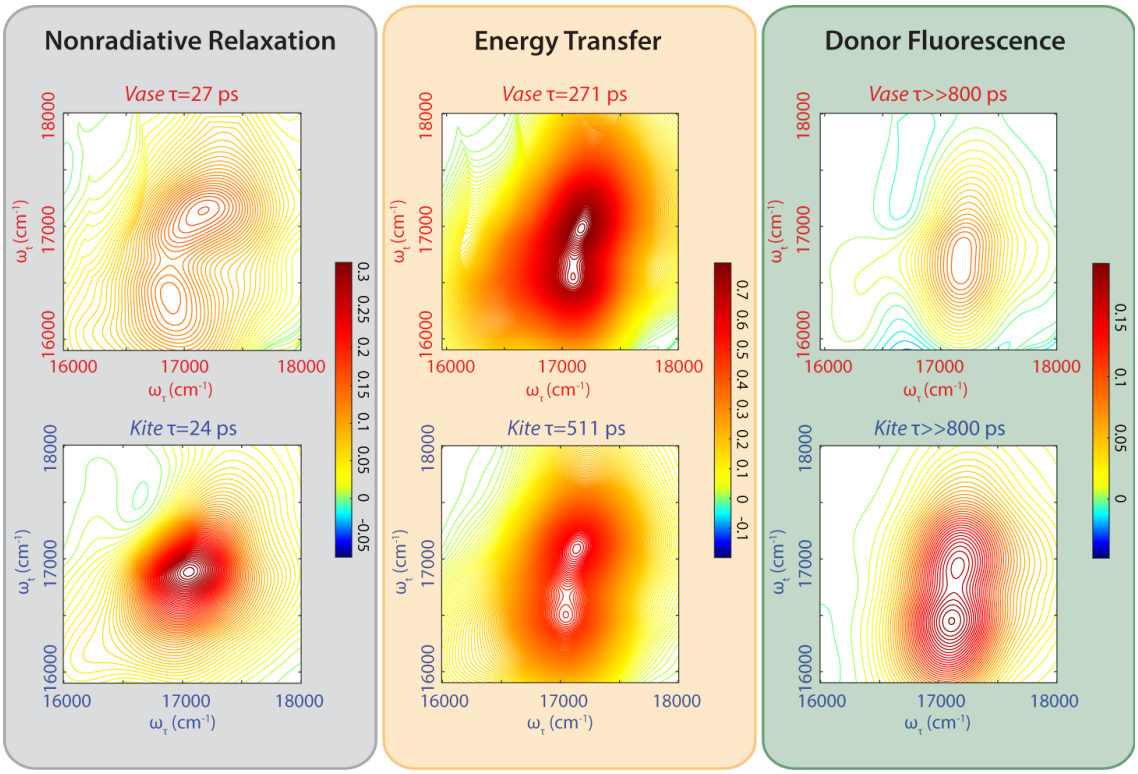

Figure 4.8: Lifetime maps reveal different energy transfer dynamics. Maps demonstrate relative distribution and strength (as indicated by colorbar) of features decaying at the labeled rate, and sum of all maps for a given conformation equals the normalized real-valued 2D spectra at T=5 ps. The grey, yellow, and green columns correspond to nonradiative relaxation, energy transfer (FRET), and donor fluorescence processes respectively.

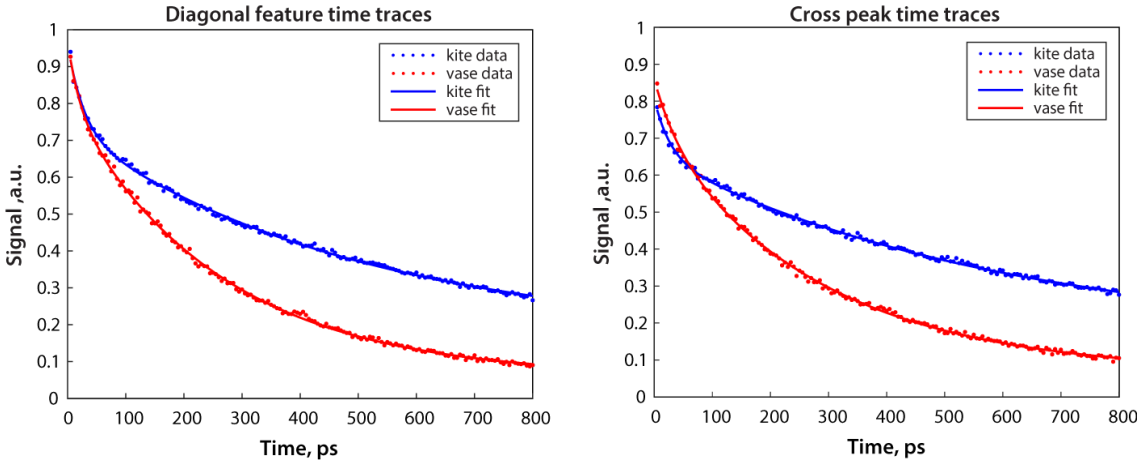

Figure 4.9: Representative time traces from the diagonal at 17100 cm^{-1} and at the cross peak at 17100 cm^{-1} and 16400 cm^{-1}. Fit parameters are listed in table 4.3.

diagnonal	A_1	τ_1 (ps)	A_2	τ_2 (ps)	A_3
RT	0.166 ± 0.017	20.2 ± 3.8	0.746 ± 0.007	260.9 ± 6.5	0.059 ± 0.005
-80°C	0.229 ± 0.012	26.8 ± 2.8	0.568 ± 0.009	496.2 ± 28.6	0.165 ± 0.014
crosspeak	A_1	τ_1 (ps)	A_2	τ_2 (ps)	A_3
RT	0.135 ± 0.033	39.5 ± 17.8	0.659 ± 0.027	286.0 ± 25.0	0.065 ± 0.013
cold	0.153 ± 0.023	27.2 ± 8.0	0.501 ± 0.028	598.0 ± 93.5	0.152 ± 0.038

Table 4.3: Fit parameters with 95% confidence intervals for time traces shown in Figure 4.9.

measurements of the donor solution. We assign this signal to be energy transfer between donor and acceptor (FRET). The energy of the diagonal feature matches with GSB from the donor, while the energy of the below-diagonal feature matches SE from the Stokes shifted excited donor as well as the absorption of the acceptor. Both features decay due to FRET transfer to the acceptor. Because Stokes shift in the donor is finished within 100 fs, all signal at the diagonal observed on this timescale is due to GSB of the donor, meaning that only the loss of donor excitation is observed. The below-diagonal features may contain signal from the acceptor and have longer lifetimes than features on the diagonal (Table 4.3 and Figure 4.9). Hence, the diagonal feature is used for donor lifetime measurements. This FRET transfer pathway contributes to the majority of the signal, particularly in the *vase* conformation where the chromophores are close. This observation is consistent with the higher expected transfer efficiency in the *vase* conformation relative to that of the *kite*.

The right (green) column shows the portion of the 2D signal that does not decay on the timescale of 800 ps. We assign this signal to residual donor fluorescence based on the measured fluorescence lifetime of the donor (2-3 ns, Figure 4.10). The double peak lineshape of this signal can be described by a combination of GSB at the diagonal (corresponding to the original absorption) and SE at the crosspeak (corresponding to Stokes shifted emission). Simulated spectra generated from the absorption and fluorescence of the donor alone (Figure 4.11) qualitatively match the lineshape of this long-lived signal for both conformations, further supporting our assignment.

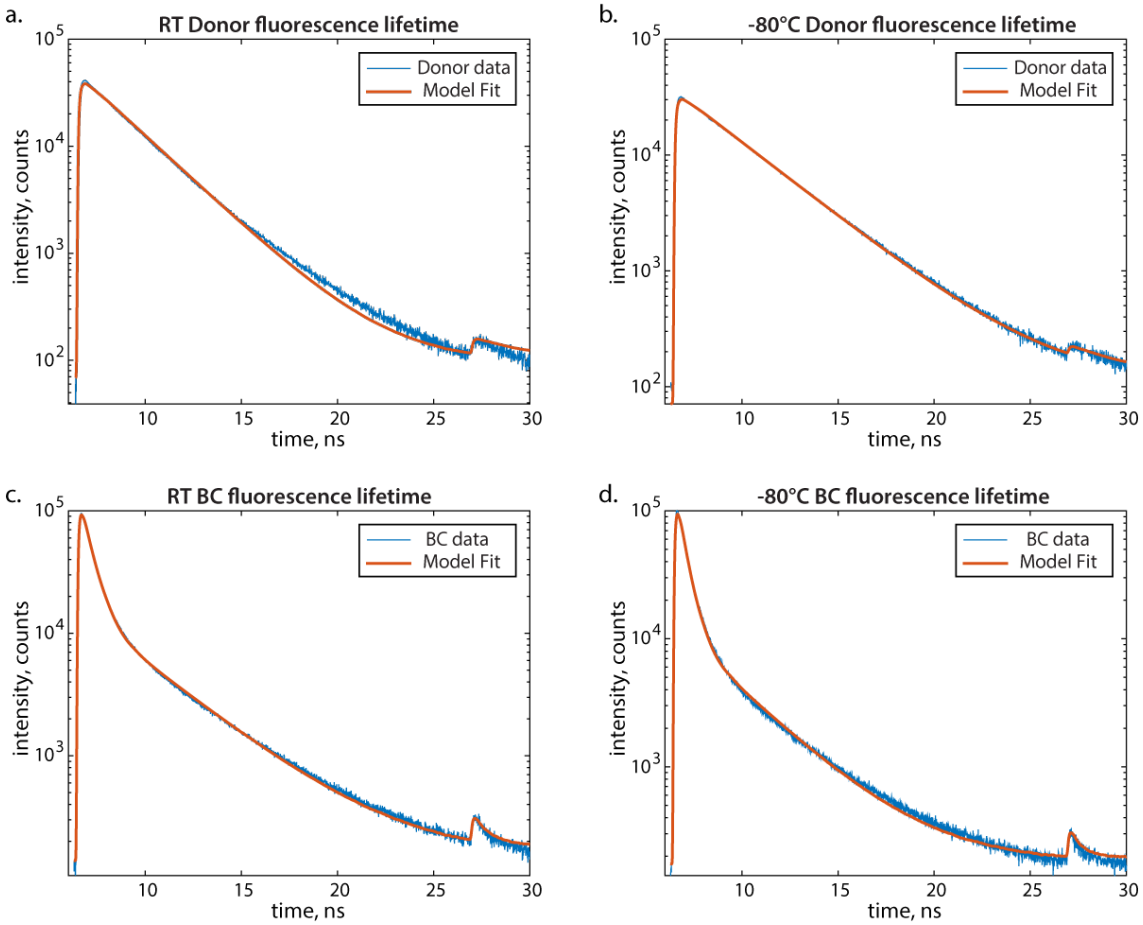

Figure 4.10: Fluorescence lifetimes measured by TCSPC. The measured data (in blue) are fitted to exponential decays convoluted with a measured instrument response function (in red) using software provided with the instrument. The jump at 27 ns is due to a small bleed through in the pulse picker used to control excitation pulse timing. The fluorescence lifetimes were measured on a ChronosBH lifetime fluorometer (ISS, Inc.) using Time-Correlated Single Photon Counting (TCSPC) methods. The fluorometer contained Becker-Hickl SPC-130 detection electronics and an HPM-100-40 Hybrid PMT detector. Tunable picosecond pulsed excitation at 560nm was provided by a Fianium SC400-2 supercontinuum laser source with integrated pulse picker and AOTF. Emission wavelengths were selected with bandpass filters (Chroma HQ615/85nm). The Instrument Response Function (IRF) was measured to be approximately 120 ps FWHM in a 1% scattering solution of Ludox LS colloidal silica. Multi-component exponential decay lifetimes were fit via a forward convolution method in the Vinci control and analysis software.

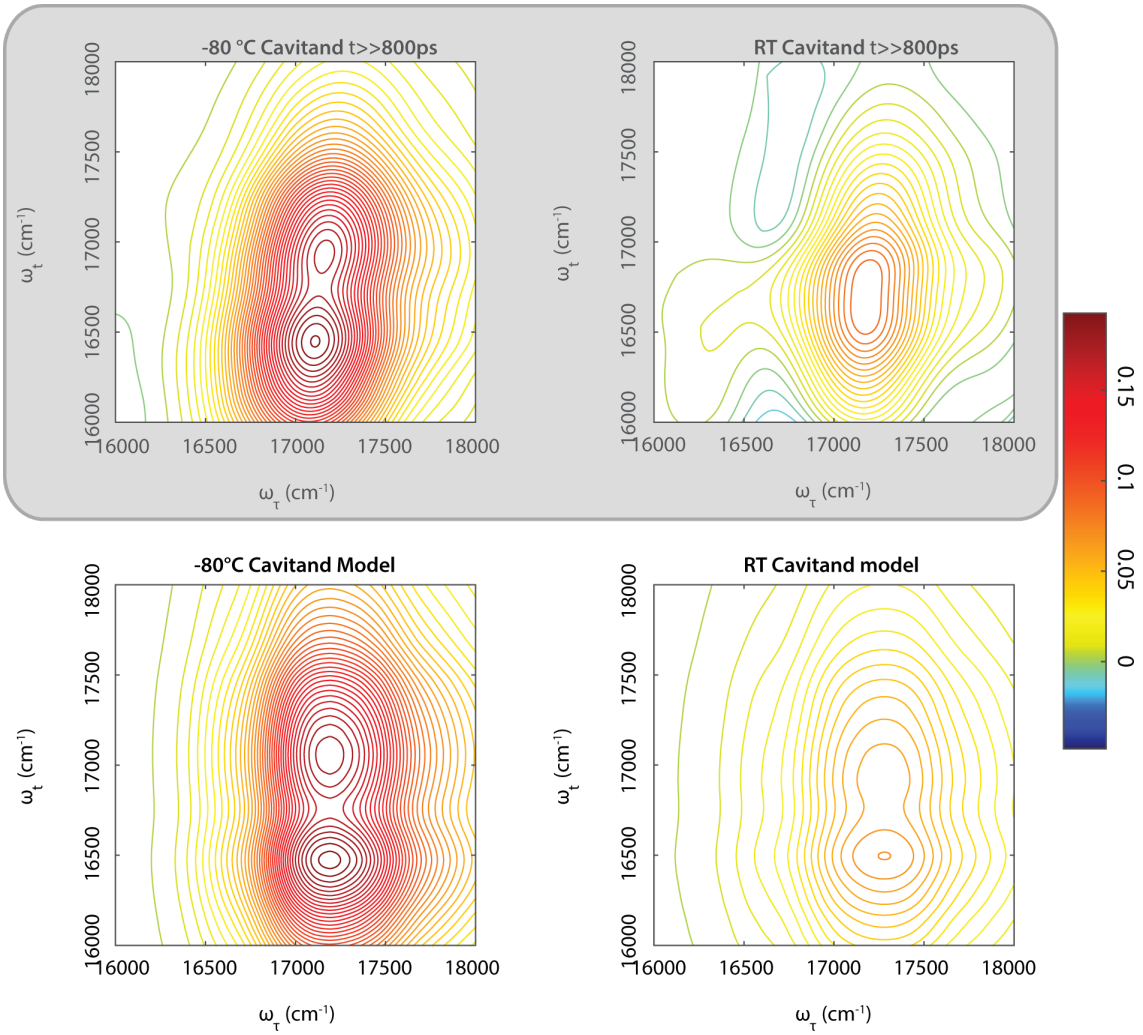

Figure 4.11: Comparison between residual fluorescence features in Figure 4.10 with simulated spectra of donor. Top row shows long time lifetime maps for both *kite* (-80°C) and *vase* (RT) configurations. Bottom row shows simulated spectra made from a convolution of the donor absorption with the sum of the donor absorption and fluorescence. Simulated spectra were also convoluted (twice in ω_{tau} and once in ω_t) with a measured laser spectrum to produce the expected 2D signal.

4.5 Energy diagram interpretation of the dynamics of the BODIPY-cavitand dimer

A summary of the dynamics observed in the BODIPY-cavitand dimer is given in Figure 4.12. Absorption in the donor from ground state D_0 to initial excited state D' rapidly leads to vibrational relaxation (Stokes shift) within the first 100 fs. This rapid relaxation to the multi-welled excited state manifold, shown as D'', affects the relative ratios of three following pathways. Nonradiative relaxation (shown in grey in Figure 4.8) reduces the total excited state population by 20-30% over the next few tens of picoseconds, thereby limiting the maximum efficiencies available to other pathways. This relaxation is caused by molecular rearrangement and does not compete kinetically with the other relaxation pathways. All remaining excitations relax via the electronic transition dipole, either as FRET or fluorescence. Chromophores in appropriate orientations decay via Föster transfer (orange in Figure 4.8). However, some chromophores have transition dipoles in orientations that prevent transfer, keeping them from decaying on the timescale of this experiment and instead relaxing via fluorescence (green in Figure 4.8). With a rate of a few hundred ps, FRET is the dominant dipole-driven relaxation pathway for the donor, which excites the acceptor as the donor returns to the ground state. The acceptor then quickly relaxes out of our laser bandwidth, and is not observed. Conformational change between *vase* and *kite* affects not only the transfer rate, but also the ratio of chromophores blocked from transfer and the contribution of nonradiative relaxation.

The multi-exponential nature of donor relaxation indicates that the branching ratios are determined by factors other than their relative rates, because processes that compete kinetically from the same state would lead to a single exponential as seen in equations 4.2 and 4.3. Fluorescence shown by the third lifetime (constant in the timescale of this experiment) is prevented from transfer to the acceptor, possibly by some incompatible configuration of transition dipoles. By comparison, the lifetime associated with energy transfer (orange in

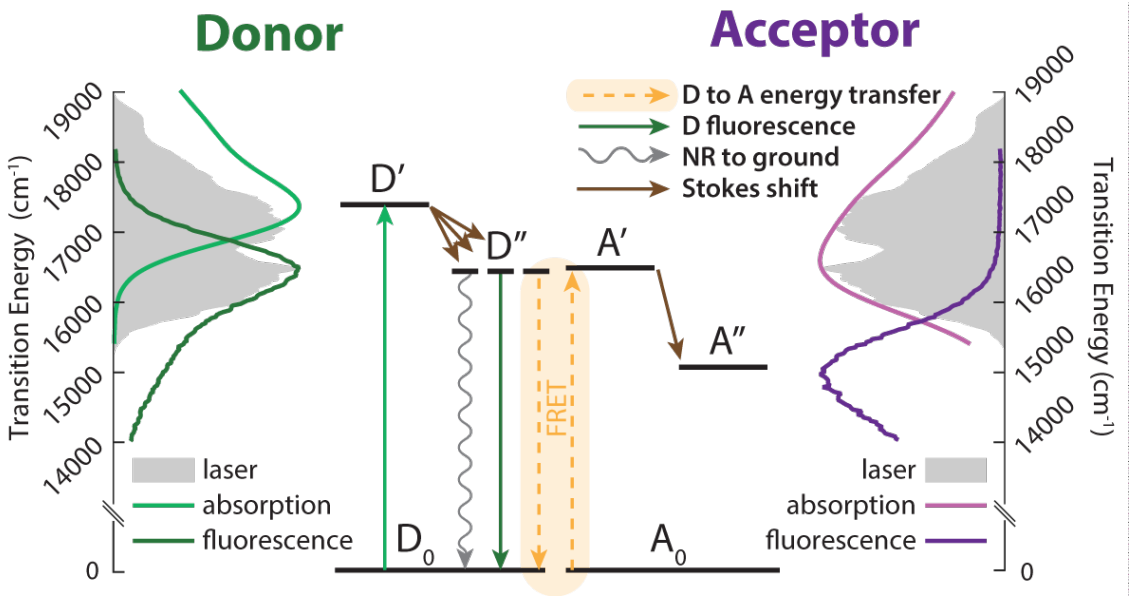

Figure 4.12: Energy diagram interpretation of the observed dynamics. Initial excitation to D′ (light green) quickly Stokes shifts to multiple wells in the vibrationally relaxed state D″. Excited donors then relax nonradiatively (grey), fluoresce (dark green), or transfer to the acceptor via FRET (orange) as seen in Figure 4.8. Side panels show donor (green) and acceptor (purple) absorption and emission spectra (light and dark lines) overlaid with the laser spectrum (solid grey).

Figure 4.8) actually corresponds to the decay of states able to transfer, and has contributions both from transfer and fluorescence. By assuming that the decay of these states is determined by the relative rates of transfer and fluorescence as in most FRET experiments [20, 29], we can approximate the transfer rate based on the following equation:

$$k_{2D} = k_{tr} + k_D \tag{4.5}$$

where k_{tr} is the transfer rate we calculate, k_{2D} is the observed decay rate, and k_D is the fluorescence decay rate of the unperturbed donor [48]. This is equivalent to equation 4.3, where $k_D = k_{D,f} + k_{D,nr}$ and is measured independently in solution via time-correlated single photon counting (TCSPC). As before, any rate k is defined as the inverse of the respective lifetime τ. Using this approach, we estimate the transfer lifetimes to be 303 ± 10ps for *vase* and 602 ± 58ps for *kite*.

Following the standard assumption that the only control of FRET efficiency is the relative rate of donor decay with and without an acceptor, one can calculate a transfer efficiency using equation 4.1, where τ_{DA} is the decay lifetime of the donor in the BODIPY-cavitand dimer, measured by 2DES, and τ_D is the fluorescence decay lifetime of the donor in solution, measured via TCSPC. Using this method, we calculate a transfer efficiency of 92.1 ± 1.3% transfer for *vase* and 78.0 ± 2.9% for *kite*. Calculations using τ_{DA} measured with TCSPC agree with this value for *kite*, but predict only 87.5% transfer for *vase*, likely due to interference from the ∼ 120 ps instrument response, as listed in Table 4.4. These calculations assume that the only relevant dynamics are transfer and fluorescence, but the nonradiative relaxation processes have a significant effect, as shown by the nonradiative relaxation signals shown in Figure 4.8 (grey), where nonradiative contributions increase by 38% from *vase* to *kite*. Taking this increase into account, we obtain FRET efficiencies of 68.7 ± 1.1% for *vase* and 44.3 ± 1.8% for *kite*, a significant reduction in overall values and a more than 70% increased change between conformations when compared to the values measured from rates alone.

	Temperature	τ_1 (ps)	A_2	E(%)
kite BODIPY-cavitand	-80°C	411 ± 1	3090 ± 4	87.5 ± 0.1
vase BODIPY-cavitand	RT	497 ± 1	3560 ± 4	78.0 ± 0.1
Donor	-80°C	3300 ± 1	-	-
Donor	RT	2600 ± 1	-	-

Table 4.4: Fluorescence lifetimes and FRET efficiencies measured by TCSPC.

4.6 Conclusions

When nonradiative processes affecting the same populations as FRET change with donor-acceptor distance, FRET measurements that fail to take these processes into account can be misleading. By separating features in both frequency and time with 2DES, we directly observe changes in nonradiative relaxation in a BODIPY-cavitand dimer. The dimer changes conformation with temperature, controlling the donor-acceptor distance and affecting the vi-

brational bath that interacts with the chromophores. To understand the nonradiative relaxation and FRET dynamics in this dimer, we used 2DES to deconvolute overlapping spectral features corresponding to nonradiative relaxation, FRET, and residual donor fluorescence, and used this to calculate efficiencies that differ significantly from those determined from lifetime measurements. In systems where nonradiative pathways affect the same population that transfers through FRET, understanding how these pathways change with variations in donor and acceptor environments is vital for the accurate determination of transfer efficiency. This understanding will allow for improved FRET efficiency measurements in the complex environments inherent to biological systems and advanced materials.

REFERENCES

[1] Modern quantum chemistry; istanbul lectures., 1965.

[2] Robert M Clegg. Fluorescence resonance energy transfer. *Current Opinion in Biotechnology*, 6(1):103–110, 1995.

[3] Paul R. Selvin. The renaissance of fluorescence resonance energy transfer. *Nat Struct Mol Biol*, 7(9):730–734, 09 2000.

[4] P. G. Wu and L. Brand. Resonance energy transfer: Methods and applications. *Analytical Biochemistry*, 218(1):1–13, 1994.

[5] L Stryer and R P Haugland. Energy transfer: a spectroscopic ruler. *Proceedings of the National Academy of Sciences*, 58(2):719–726, 08 1967.

[6] Cristobal G. dos Remedios and Pierre D. J. Moens. Fluorescence resonance energy transfer spectroscopy is a reliable "ruler" for measuring structural changes in proteins. *Journal of Structural Biology*, 115(2):175–185, 1995.

[7] Richard N. Day, Ammasi Periasamy, and Fred Schaufele. Fluorescence resonance energy transfer microscopy of localized protein interactions in the living cell nucleus. *Methods*, 25(1):4–18, 2001.

[8] Ben N. G. Giepmans, Stephen R. Adams, Mark H. Ellisman, and Roger Y. Tsien. The fluorescent toolbox for assessing protein location and function. *Science*, 312(5771):217, 04 2006.

[9] Marc Tramier, Isabelle Gautier, Tristan Piolot, Sylvie Ravalet, Klaus Kemnitz, Jacques Coppey, Christiane Durieux, Vincent Mignotte, and Maïté Coppey-Moisan. Picosecond-hetero-fret microscopy to probe protein-protein interactions in live cells. *Biophysical Journal*, 83(6):3570–3577, 12 2002.

[10] Steven S. Vogel, Christopher Thaler, and Srinagesh V. Koushik. Fanciful fret. *Science's STKE*, 2006(331):re2, 04 2006.

[11] Vladimir V Didenko. Dna probes using fluorescence resonance energy transfer (fret): Designs and applications. *BioTechniques*, 31(5):1106–1121, 11 2001.

[12] Chun-Yang Zhang, Hsin-Chih Yeh, Marcos T. Kuroki, and Tza-Huei Wang. Single-quantum-dot-based dna nanosensor. *Nat Mater*, 4(11):826–831, 11 2005.

[13] Sohila Zadran, Steve Standley, Kaylee Wong, Erick Otiniano, Arash Amighi, and Michel Baudry. Fluorescence resonance energy transfer (fret)-based biosensors: visualizing cellular dynamics and bioenergetics. *Applied Microbiology and Biotechnology*, 96(4):895–902, 2012.

[14] A Hillisch, M Lorenz, and S Diekmann. Recent advances in fret: distance determination in protein-dna complexes. *Current opinion in structural biology*, 11(2):201–207, 2001.

[15] Philippe I. H. Bastiaens and Anthony Squire. Fluorescence lifetime imaging microscopy: spatial resolution of biochemical processes in the cell. *Trends in Cell Biology*, 9(2):48–52, 2 1999.

[16] Rajesh Babu Sekar and Ammasi Periasamy. Fluorescence resonance energy transfer (fret) microscopy imaging of live cell protein localizations. *The Journal of Cell Biology*, 160(5):629, 03 2003.

[17] Kevin Truong and Mitsuhiko Ikura. The use of fret imaging microscopy to detect protein–protein interactions and protein conformational changes in vivo. *Current Opinion in Structural Biology*, 11(5):573–578, 9 2001.

[18] Horst Wallrabe and Ammasi Periasamy. Imaging protein molecules using fret and flim microscopy. *Current Opinion in Biotechnology*, 16(1):19–27, 2 2005.

[19] W. BECKER. Fluorescence lifetime imaging –techniques and applications. *Journal of Microscopy*, 247(2):119–136, 2012.

[20] Elizabeth A Jares-Erijman and Thomas M Jovin. Fret imaging. *Nat Biotech*, 21(11):1387–1395, 11 2003.

[21] Elizabeth A Jares-Erijman and Thomas M Jovin. Imaging molecular interactions in living cells by fret microscopy. *Current Opinion in Chemical Biology*, 10(5):409–416, 10 2006.

[22] David W. Piston and Gert-Jan Kremers. Fluorescent protein fret: the good, the bad and the ugly. *Trends in Biochemical Sciences*, 32(9):407–414, 9 2007.

[23] A. Paul Alivisatos, Weiwei Gu, and Carolyn Larabell. Quantum dots as cellular probes. *Annual Review of Biomedical Engineering*, 7(1):55–76, 2016/11/15 2005.

[24] Xiaoqin Chi, Dengtong Huang, Zhenghuan Zhao, Zijian Zhou, Zhenyu Yin, and Jinhao Gao. Nanoprobes for in vitro diagnostics of cancer and infectious diseases. *Biomaterials*, 33(1):189–206, 1 2012.

[25] Aaron R. Clapp, Igor L. Medintz, and Hedi Mattoussi. Förster resonance energy transfer investigations using quantum-dot fluorophores. *ChemPhysChem*, 7(1):47–57, 2006.

[26] Philip D. Howes, Rona Chandrawati, and Molly M. Stevens. Colloidal nanoparticles as advanced biological sensors. *Science*, 346(6205), 10 2014.

[27] Kim E. Sapsford, Lorenzo Berti, and Igor L. Medintz. Materials for fluorescence resonance energy transfer analysis: Beyond traditional donor–acceptor combinations. *Angewandte Chemie International Edition*, 45(28):4562–4589, 2006.

[28] Lin Yuan, Weiying Lin, Kaibo Zheng, and Sasa Zhu. Fret-based small-molecule fluorescent probes: Rational design and bioimaging applications. *Accounts of Chemical Research*, 46(7):1462–1473, 07 2013.

[29] Claude Berney and Gaudenz Danuser. Fret or no fret: A quantitative comparison. *Biophysical Journal*, 84(6):3992–4010, 6 2003.

[30] Ulai Noomnarm and Robert M. Clegg. Fluorescence lifetimes: fundamentals and interpretations. *Photosynthesis Research*, 101(2):181–194, 2009.

[31] Igor Pochorovski, Benjamin Breiten, W. Bernd Schweizer, and François Diederich. Fret studies on a series of bodipy-dye-labeled switchable resorcin[4]arene cavitands. *Chemistry –A European Journal*, 16(42):12590–12602, 2010.

[32] Igor Pochorovski and François Diederich. Fluorophore-functionalized and top-covered resorcin[4]arene cavitands. *Israel Journal of Chemistry*, 52(1-2):20–29, 2012.

[33] Igor Pochorovski, Tim Knehans, Daniel Nettels, Astrid M. Müller, W. Bernd Schweizer, Amedeo Caflisch, Benjamin Schuler, and François Diederich. Experimental and computational study of bodipy dye-labeled cavitand dynamics. *Journal of the American Chemical Society*, 136(6):2441–2449, 02 2014.

[34] Feirong Li, Sung Ik Yang, Yangzhen Ciringh, Jyoti Seth, Charles H. Martin, Deepak L. Singh, Dongho Kim, Robert R. Birge, David F. Bocian, Dewey Holten, and Jonathan S. Lindsey. Design, synthesis, and photodynamics of light-harvesting arrays comprised of a porphyrin and one, two, or eight boron-dipyrrin accessory pigments. *Journal of the American Chemical Society*, 120(39):10001–10017, 10 1998.

[35] Hooi Ling Kee, Christine Kirmaier, Lianhe Yu, Patchanita Thamyongkit, W. Justin Youngblood, Matthew E. Calder, Lavoisier Ramos, Bruce C. Noll, David F. Bocian, W. Robert Scheidt, Robert R. Birge, Jonathan S. Lindsey, and Dewey Holten. Structural control of the photodynamics of borondipyrrin complexes. *The Journal of Physical Chemistry B*, 109(43):20433–20443, 11 2005.

[36] L. Wang, I. S. Tamgho, L. A. Crandall, J. J. Rack, and C. J. Ziegler. Ultrafast dynamics of a new class of highly fluorescent boron difluoride dyes. *Physical Chemistry Chemical Physics*, 17(4):2349–2351, 2015.

[37] Gabriela S. Schlau-Cohen, Akihito Ishizaki, and Graham R. Fleming. Two-dimensional electronic spectroscopy and photosynthesis: Fundamentals and applications to photosynthetic light-harvesting. *Chemical Physics*, 386(1–3):1–22, 7 2011.

[38] Peter D. Dahlberg, Andrew F. Fidler, Justin R. Caram, Phillip D. Long, and Gregory S. Engel. Energy transfer observed in live cells using two-dimensional electronic spectroscopy. *The Journal of Physical Chemistry Letters*, 4(21):3636–3640, 11 2013.

[39] Elisabetta Collini, Cathy Y. Wong, Krystyna E. Wilk, Paul M. G. Curmi, Paul Brumer, and Gregory D. Scholes. Coherently wired light-harvesting in photosynthetic marine algae at ambient temperature. *Nature*, 463(7281):644–647, 02 2010.

[40] Dugan Hayes, Graham B. Griffin, and Gregory S. Engel. Engineering coherence among excited states in synthetic heterodimer systems. *Science*, 340(6139):1431, 06 2013.

[41] Artem A. Bakulin, Sarah E. Morgan, Tom B. Kehoe, Mark W. B. Wilson, Alex W. Chin, Donatas Zigmantas, Dassia Egorova, and Akshay Rao. Real-time observation of multiexcitonic states in ultrafast singlet fission using coherent 2d electronic spectroscopy. *Nat Chem*, 8(1):16–23, 01 2016.

[42] Chanelle C. Jumper, Jessica M. Anna, Anna Stradomska, Juleon Schins, Mykhaylo Myahkostupov, Valentina Prusakova, Daniel G. Oblinsky, Felix N. Castellano, Jasper Knoester, and Gregory D. Scholes. Intramolecular radiationless transitions dominate exciton relaxation dynamics. *Chemical Physics Letters*, 599:23–33, 4 2014.

[43] Michael J. Frisch, G. W. Trucks, H. Bernhard Schlegel, Gustavo E. Scuseria, Michael A. Robb, James R. Cheeseman, Giovanni Scalmani, Vincenzo Barone, Benedetta Mennucci, G. A. Petersson, H. Nakatsuji, M. Caricato, Xiaosong Li, H. P. Hratchian,

Artur F. Izmaylov, Julien Bloino, G. Zheng, J. L. Sonnenberg, M. Hada, M. Ehara, K. Toyota, R. Fukuda, J. Hasegawa, M. Ishida, T. Nakajima, Y. Honda, O. Kitao, H. Nakai, T. Vreven, J. A. Montgomery Jr., J. E. Peralta, François Ogliaro, Michael J. Bearpark, Jochen Heyd, E. N. Brothers, K. N. Kudin, V. N. Staroverov, Rika Kobayashi, J. Normand, Krishnan Raghavachari, Alistair P. Rendell, J. C. Burant, S. S. Iyengar, Jacopo Tomasi, M. Cossi, N. Rega, N. J. Millam, M. Klene, J. E. Knox, J. B. Cross, V. Bakken, C. Adamo, J. Jaramillo, R. Gomperts, R. E. Stratmann, O. Yazyev, A. J. Austin, R. Cammi, C. Pomelli, J. W. Ochterski, R. L. Martin, K. Morokuma, V. G. Zakrzewski, G. A. Voth, P. Salvador, J. J. Dannenberg, S. Dapprich, A. D. Daniels, Ödön Farkas, J. B. Foresman, J. V. Ortiz, J. Cioslowski, and Douglas J. Fox. Gaussian 09, 2009.

[44] Michael J. S. Dewar, Eve G. Zoebisch, Eamonn F. Healy, and James J. P. Stewart. Development and use of quantum mechanical molecular models. 76. am1: a new general purpose quantum mechanical molecular model. *Journal of the American Chemical Society*, 107(13):3902–3909, 06 1985.

[45] Vladimir A. Azov, Bernhard Jaun, and François Diederich. Nmr investigations into the vase-kite conformational switching of resorcin[4]arene cavitands. *Helvetica Chimica Acta*, 87(2):449–462, 2004.

[46] Minhaeng Cho. Coherent two-dimensional optical spectroscopy. *Chemical Reviews*, 108(4):1331–1418, 04 2008.

[47] Igor Stiopkin, Tobias Brixner, Mino Yang, and Graham R. Fleming. Heterogeneous exciton dynamics revealed by two-dimensional optical spectroscopy. *The Journal of Physical Chemistry B*, 110(40):20032–20037, 10 2006.

[48] Abraham Nitzan. *Chemical dynamics in condensed phases relaxation, transfer and reactions in condensed molecular systems*. Oxford University Press, Oxford ; New York,

2006.

[49] P. Hamm and M.T. Zanni. *Concepts and methods of 2D infrared spectroscopy.* Cambridge University Pres, Cambridge ; New York, 2011.

CHAPTER 5
EXCITATIONS PARTITION INTO TWO DISTINCT POPULATIONS IN BULK PEROVSKITES DUE TO POLARON FORMATION

Methylammonium cations have been hypothesized to solvate electrons within the perovskite, enhancing carrier lifetimes. However, it is difficult to test this hypothesis with thin films or crystal surfaces, in which the carrier dynamics is obscured by grain boundaries and surface defects. Here, we examine this hypothesis by performing transient absorption spectroscopy in a transmissive geometry on perovskite single-domain single crystals. We observe two distinct sets of carrier populations that coexist at the same radiation fluence but display different rate laws; one relaxes through second-order recombination, the other through third-order recombination. Using *ab initio* simulations, we find this observation is best explained by coexistence of free carriers and localized carriers due to polaron formation. Our calculations suggest that polarons will form in both $CH_3NH_3PbBr_3$ and $CH_3NH_3PbI_3$, but are more pronounced in $CH_3NH_3PbBr_3$. Single-crystal $CH_3NH_3PbBr_3$ could be the key to understanding the impact of polarons on the transport and optical properties.

5.1 Importance of probing carrier dynamics in perovskite single-domain single crystals

Organolead halide perovskites as both light absorbers and solar cell transport layers [1–4], have achieved certified power conversion efficiencies up to 21% [4]. Perovskite thin films and nanocrystals have also been used in light emitting devices, including low threshold optically pumped lasers [5–8] and bright photodiodes [9]. The extraordinary potential of perovskites for optoelectronic applications has driven the broad scientific community to understand their material and electronic properties. Optical spectroscopic studies such as photoluminescence

lifetime and transient absorption spectroscopy have been performed on perovskite thin films, revealing photogeneration of free charge carriers [10, 11], bimolecular charge recombination dynamics [6, 12], band filling behavior [12], and long carrier diffusion lengths [13, 14].

Recently, polaron formation is believed to play a crucial role in the optoelectronic properties of organic-inorganic lead halides [15–23]. The lattice distortions of polarons may prevent carrier recombination and extend carrier lifetime by screening the interaction between electrons and holes, minimizing their overlap and further localizing them to different portions of the lattice. The polaron hypothesis could potentially explain multiple important material properties such as long diffusion lengths and low mobilities, which are characteristic of organic-inorganic lead halides. However, nonintrinsic factors associated with thin films, such as grain boundaries and surface defects, can significantly affect the carrier dynamics and may obscure the discovery of polaron formation. For example, large densities of trap states were found at surface defects and grain boundaries [24, 25], causing carrier loss due to nonradiative recombination [26]. Exciton and carrier dynamics are also sensitive to the inherent polycrystallinity of thin films [27]. Perovskite single-domain single crystals can provide pristine systems independent of these nonintrinsic factors. Compared to the reported trap densities of 10^{16} - 10^{17} cm^{-3} exhibited in thin films [5], substantially lower trap densities of 10^{9} - 10^{10} cm^{-3} are observed in single crystals [28]. Recent breakthroughs in solution processes for single crystal growth also permit millimeter-sized single-domain single crystals that are large enough for optical measurements [28, 29].

In this work, we examine the polaron formation hypothesis by performing transient absorption spectroscopy on perovskite single-domain single crystals in a transmissive geometry. Compared to transient reflectance spectroscopy, transient absorption signal in a transmissive geometry is sensitive to the bulk rather than the crystal surfaces. The crystal surfaces are usually viewed as extended defect states and considered to be different from the bulk phase of the crystal [27]. Through a series of transient absorption experiments on CH3NH3PbBr3 single-domain single crystals with varied radiation fluences, we simultaneously observe evi-

dence for two different sets of photogenerated populations with second-order recombination and third-order recombination dynamics. Signatures of the two sets of populations are spectrally separated and simultaneously observed at the same radiation fluence. Our ab initio calculations suggest that these two sets of populations can be attributed to free carriers coexisting with localized carriers arising from polaron formation.

5.2 Single-domain single crystal preparation

Transient absorption measurements on perovskite single crystals are complicated by the thickness of large single crystals with a high absorption cross-section [30, 31] and by scattering. We developed a method of thin crystal preparation by polishing one dimension of millimeter-sized single crystals to ca. 70-90 μm. After polishing, these single crystals are thin enough in one dimension to transmit detectable probe light while still large relative to the beam size in the other two dimensions, enabling transient absorption measurements [32].

5.2.1 Synthesis of CH_3NH_3Br

Methylammonium bromide was synthesized by the reaction between 40 wt.% methylamine (CH_3NH_2) in methanol (TCI America) and 48 wt.% hydrobromic acid (HBr) in water (Sigma-Aldrich). An equimolar amount of HBr was added dropwise to the CH_3NH_2 solution under ice bath and stirred for 2 h. The volatiles were removed on a rotovap. The resulting solid was further recrystallized in ethanol to yield snow-white CH_3NH_3Br crystals. CH_3NH_3B crystals were stored under dynamic vacuum to remove residual ethanol.

5.2.2 Growth of $CH_3NH_3PbBr_3$ single crystals

Equimolar CH_3NH_3Br and $PbBr_2$ (1 M) were dissolved in N,N-dimethylformamide (DMF). The mixture was filtered with Teflon syringe filters (0.2 μm pore size, Fisher Scientific). Single crystals of $CH_3NH_3PbBr_3$ were grown through co-evaporation of the filtered DMF

solution with diethyl ether (1/50, v/v) in air.

5.2.3 Crystal polishing

The single crystals were mounted on one-inch glass slide using low melting point resin. The mounted crystals were polished with 600, 1200, and 1500-grit sandpapers stepwise to ca. 70 μm thickness. The crystal surfaces were further smoothed with polished finish pad (McMaster Part No. 4611A109). The polished crystals were then transferred to clean glass slides and mounted with optically clear double-sided tape. The prepared crystals were stored under vacuum for further use.

5.3 Single-domain single crystal characterization

5.3.1 Linear absorption and optical microscopy

The linear absorption spectrum of the crystal with onset at 553 nm (2.24 eV) is shown in Figure 5.1.a. The inset in Figure 5.1.a is an optical micrograph of a polished crystal mounted by optically clear double-sided tape on a one-inch glass slide. No grain boundaries were observed in the micrograph, indicating that the sample was indeed a single crystal composed of a single domain.

The single crystallinity was confirmed by single-crystal X-ray diffraction and supported by polarized optical microscopy. The birefringence of crystals can be used to detect crystallinity. For a single crystal with a single domain, all crystal lattices are oriented in the same way. Therefore, the whole crystal will exhibit the same change of brightness in a polarized optical microscopy measurement. For polycrystals, crystal lattices are oriented differently in different domains. Hence, different domains will exhibit different response to polarized light showing brightness contrast in polarized micrographs. For crystals with *Pm-3m* space group, the predicted single crystal shape is not square planar. We present polarized optical micrographs on a polished single crystal (Figure 5.2.a,b) and a large square planar crystal

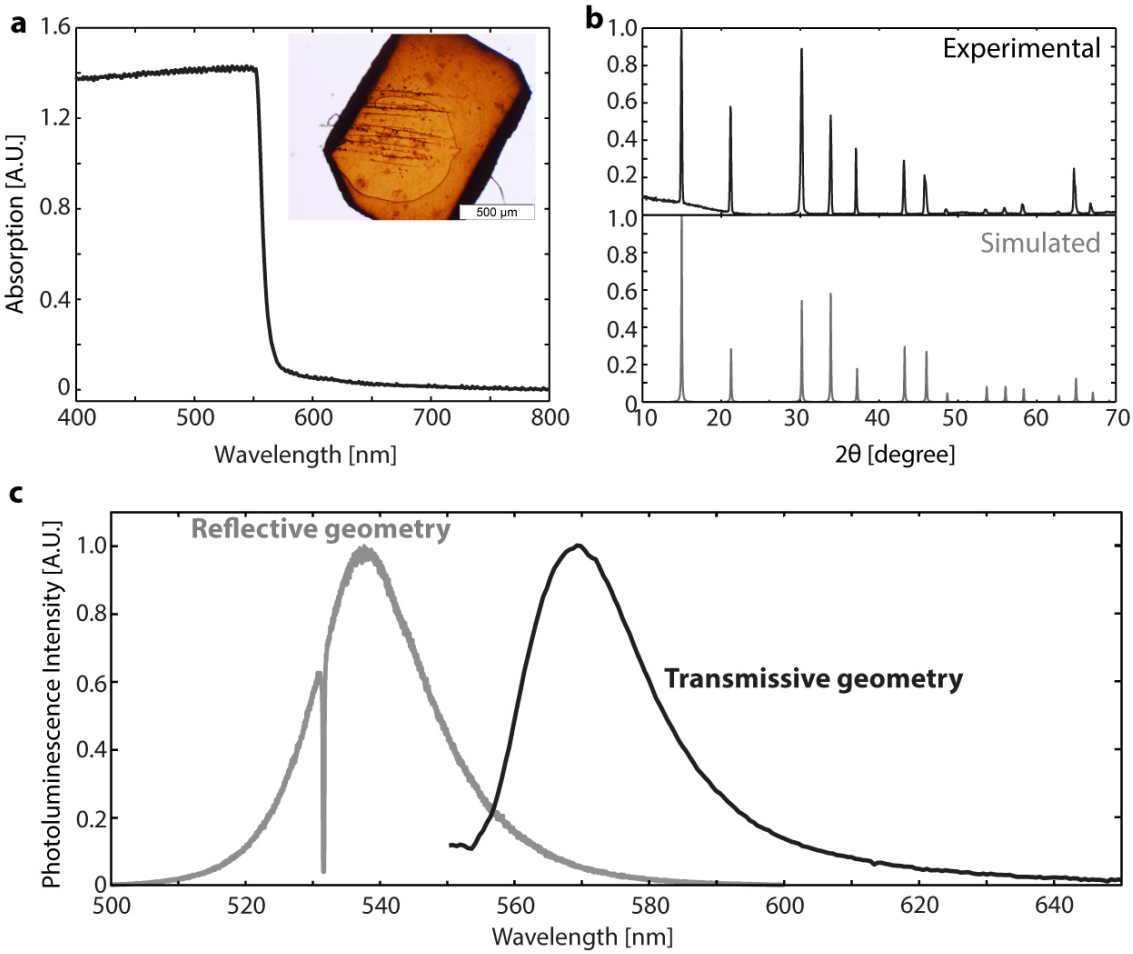

Figure 5.1: Characterization of $CH_3NH_3PbBr_3$ single crystals. (a) Linear absorption spectrum of $CH_3NH_3PbBr_3$ single-domain single crystal. Inset: Micrograph of a polished single-domain single crystal with 500 μm scale bar. (b) Upper: Experimental powder XRD pattern of the ground powder of several crystals. Lower: Simulated powder XRD pattern based on single crystal XRD measurement (attached in the Supplementary Materials). (c) Photoluminescence spectra of perovskite single-domain single crystal measured in a reflective geometry with 532 nm excitation (gray) and in a transmissive geometry with 535 nm excitation (black). The spectral dip at 532 nm in the reflective photoluminescence data is caused by a 532 nm notch filter.

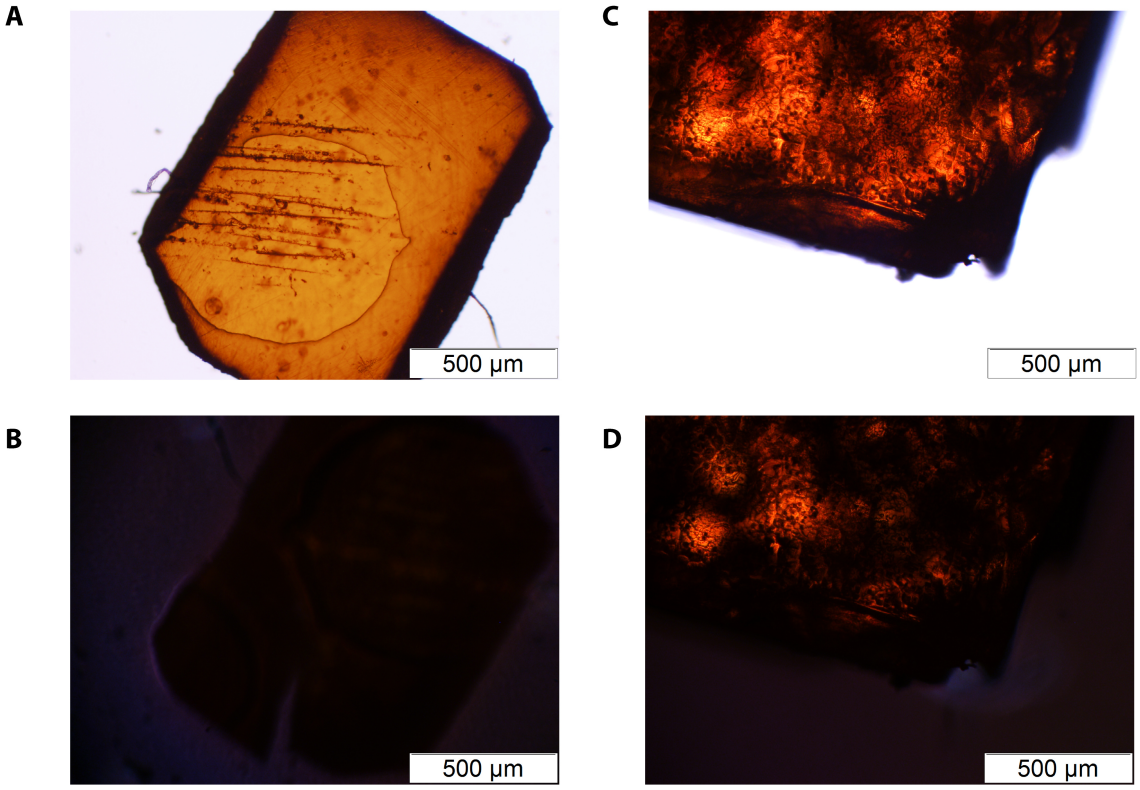

Figure 5.2: Polarized optical microscopy reveals crystallinity of perovskite crystals. (a) Micrograph of a polished single crystal. Scratches on the surface of the crystal are due to polishing with sand papers. The circular edge in the micrograph is the contact edge between the crystal and double-sided tape. Microscopy data was taken after all transient absorption data. (b) Cross-polarized micrograph of the same single crystal in a. The crack evident in b was caused by handling before polarized optical microscopy measurement but after all transient absorption measurements. (c) Micrograph of a large polycrystalline square planar perovskite sample for comparison (sample not used for spectroscopy). (d) Cross polarized micrograph of the same sample in c.

for comparison (Figure 5.2.c,d). Our observations prove that the polished crystal is indeed a single crystal with a single domain. The large square planar crystal is polycrystalline in nature.

Crystal thickness was measured using a Leica SP5 Tandem Scanner Spectral two-photon confocal microscope (Leica Microsystems, Inc., Buffalo Grove, IL) using backscattered 633 nm light. Figure 5.3 shows a vertical slice of a measured crystal with 77 μm thickness.

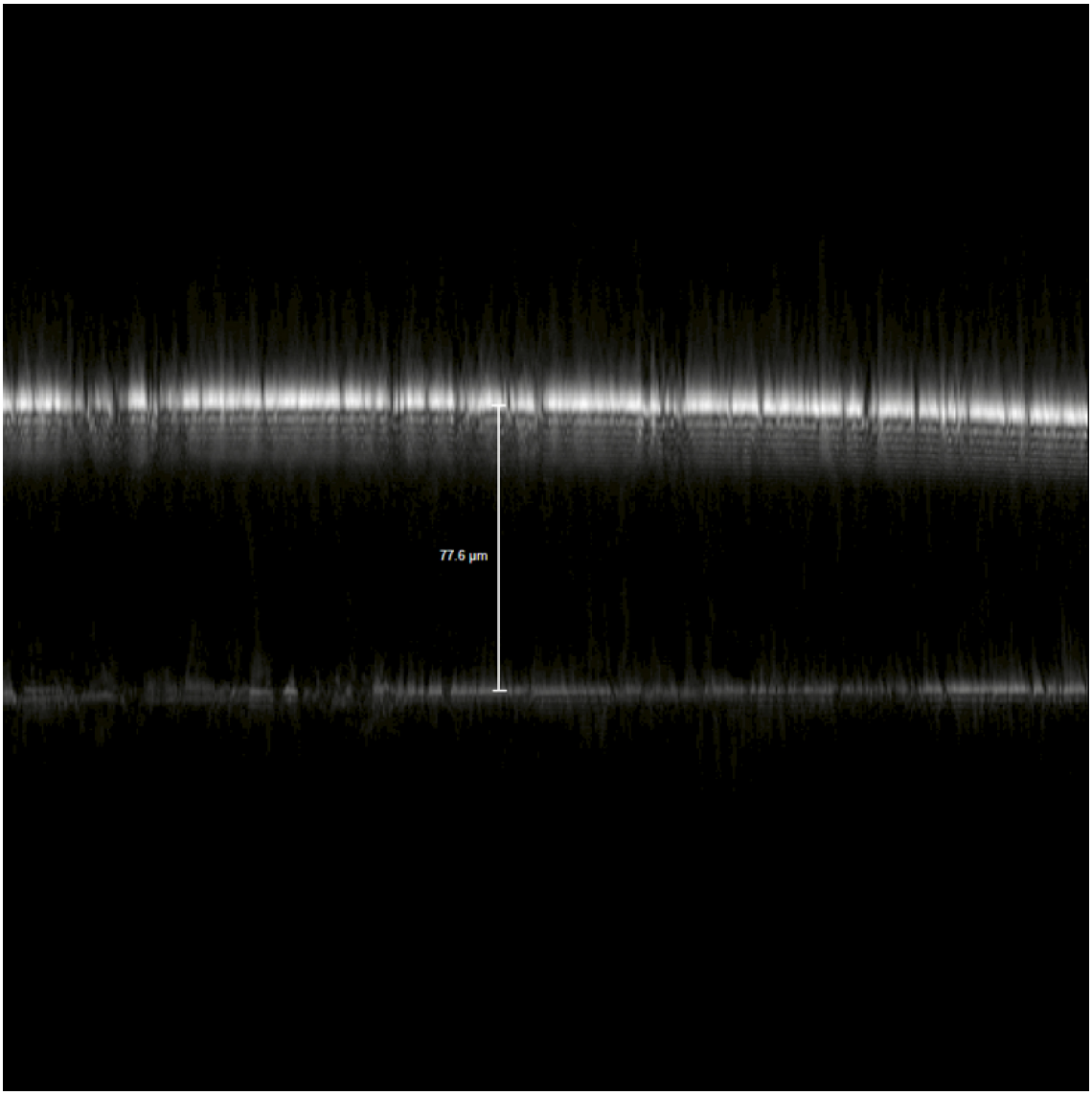

Figure 5.3: Confocal backscatter microscopy of the crystal surfaces shows 77 μm crystal thickness after polishing.

5.3.2 X-ray diffraction measurements

Single crystal X-ray diffraction (XRD) revealed *Pm-3m* space group, and powder XRD pattern confirmed cubic structure and phase purity (Figure 5.1.b).Powder X-ray diffraction data were measured at 293 K on a Bruker D8 Discover GADDS using a Cu-α source (40 kV, 40 mA) with a Vantec-2000 two-dimensional detector.

For the single crystal X-ray diffraction measurement, a very small crystal ($\approx$0.04 x 0.05 x 0.05 mm^3) was chosen in order to minimize absorption effects. The crystal was mounted on a Dual-Thickness MicroMounttm with 20 μm sample aperture with Fluorolube^{TM} oil. The diffraction data were measured at 293 K on a Bruker D8 VENTURE with PHOTON 100 CMOS detector system equipped with a Mo-target X-ray tube (λ = 0.71073 $\mathring{A}$). Data were collected using ω scans to survey a hemisphere of reciprocal space. Data reduction and integration were performed with the Bruker APEX3 software package. Data were scaled and corrected for absorption effects using the multi-scan procedure as implemented in SADABS [33]. The structure was refined by a full-matrix least-squares procedure using SHELX14 refinement program. Crystallographic data and details of the data collection and structure refinement are listed in Table 5.1. The precession images generated from a full data set of up to 0.7 $\mathring{A}$ resolution for the $CH_3NH_3PbBr_3$ crystal also confirm the single crystallinity of the sample, as shown in Fig 5.4 and 5.5.

Empirical formula	$CNPbBr_3$
Formula weight	472.94
Temperature/K	293(2)
Crystal system	cubic
Space group	*Pm-3m*
a/Å	5.9139(2)
b/Å	5.9139(2)
c/Å	5.9139(2)
$\alpha/^\circ$	90
$\beta/^\circ$	90
$\gamma/^\circ$	90
Volume/$\mathring{A}^3$	206.83(2)
Z	1
ρ_{calc} g/cm^3	3.797
μ/mm^{-1}	34.777
F(000)	200.0
Crystal size/mm^3	0.05 x 0.05 x 0.04
Radiation	MoKα (λ = 0.71073)
2Θ range for data collection/$^\circ$	6.89 to 67.284
Index ranges	-9 $\leq$ h $\leq$ 9, -9 $\leq$ k $\leq$ 9, -9 $\leq$ l $\leq$ 9
Reflections collected	6871
Independent reflections	116 [R_{int} = 0.0271]
Data/restraints/parameters	116/0/10
Goodness-of-fit on F^2	1.066
Final R indices [I$\geq$2σ (I)]	R_1 = 0.0140, wR_2 = 0.0339
Final R indices [all data]	R1 = 0.0140, wR2 = 0.0339
Largest diff. peak/hole / e $\mathring{A}^{-3}$	0.54/-0.72
$R_{int} = \sum \mid F_o^2 - <F_o^2> \mid / \sum \mid F_o^2 \mid$	
$R_1 = \sum \mid \mid F_o \mid - \mid F_c \mid \mid / \sum \mid F_o \mid$	
$wR_2 = [\sum [w(F_o^2 - F_c^2)^2] / \sum [w(F_o^2)^2]]^{1/2}$	
Goodness-of-fit = $[\sum [w(F_o^2 - F_c^2)^2] / (n-p)^{1/2}$	
n: number of independent reflections; p: number of refined parameters	

Table 5.1: Single crystal XRD data and structure refinement for $CH_3NH_3PbBr_3$.

5.3.3 Photoluminescence measurements

The photoluminescence spectra of the single-domain single crystal measured in a reflective geometry as well as in a transmissive geometry are shown in Figure 5.1.c. The difference between the two photoluminescence spectra suggests that signal of the single crystal is sensitive to the detection direction. Therefore, in addition to previous studies, transient absorption

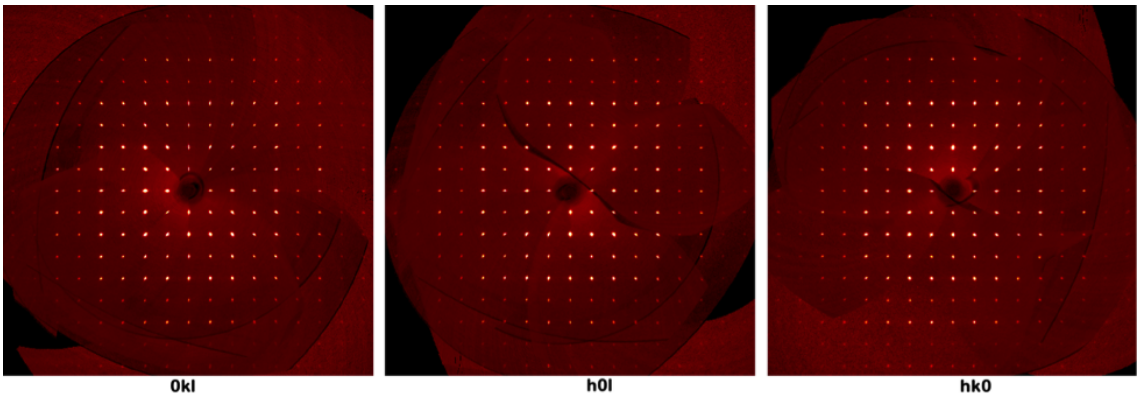

Figure 5.4: Reciprocal space slices for $CH_3NH_3PbBr_3$ single crystal reveal cubic symmetry and no detectable satellites. Left: 0kl slice. Middle: h0l slice. Right: hk0 slice.

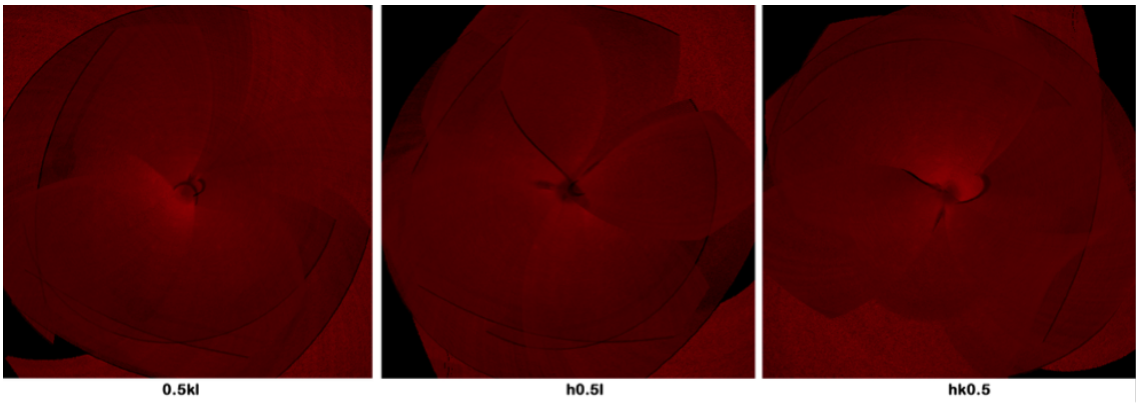

Figure 5.5: Reciprocal space slices for $CH_3NH_3PbBr_3$ crystal show no contamination from other phases/domains between hkl planes. Left: 0.5kl slice. Middle: h0.5l slice. Right: hk0.5 slice.

measurements on these crystals in a transmissive geometry are necessary.The photoluminescence spectrum of the perovskite single-domain single crystal in a reflective geometry was measured by Horiba LabRamHR Evolution confocal Raman microscope with a 532 nm laser source and an Andor back-illuminated EMCCD detector. The spectrum shows anti-Stokes photoluminescence at wavelengths shorter than 532 nm consistent with thermal population of phonon states. The photoluminescence spectrum of the perovskite single-domain single crystal in a transmissive geometry was measured by the transient absorption setup with pump beam only and recorded with a line scan camera (Teledyne Dalsa Spyder3 1k).

5.3.4 Photodamage examination

Photodamage examination was performed by exciting the perovskite single-domain single crystal with the highest radiation fluence that our laser can reach (14.1 mJ/cm^2) at 535 nm and by acquiring the photoluminescence spectrum over a period of 10 min twice. The photoluminescence intensities for the two runs (Figure 5.6) remain unchanged, indicating that the perovskite single-domain single crystal did not experience photodamage under this radiation fluence.

5.4 Transient absorption spectroscopy on $CH_3NH_3PbBr_3$ single-domain single crystal

Transient absorption spectroscopy was performed on a home-built apparatus described in Chapter 2 Section 2.1.1. The spot sizes used in the flux measurements were determined via placing a webcam at the sample position followed by measuring the full width at half maximum of the pump and probe beams. The instrumental response limit was measured by calculating the rise time of the signal trace at 560 nm (Figure 5.7). Based on the 0.6 ns rise time, we estimate the instrument response FWHM as 1.2 ns.

Transient absorption spectra of the single crystals were obtained with a narrowband pump

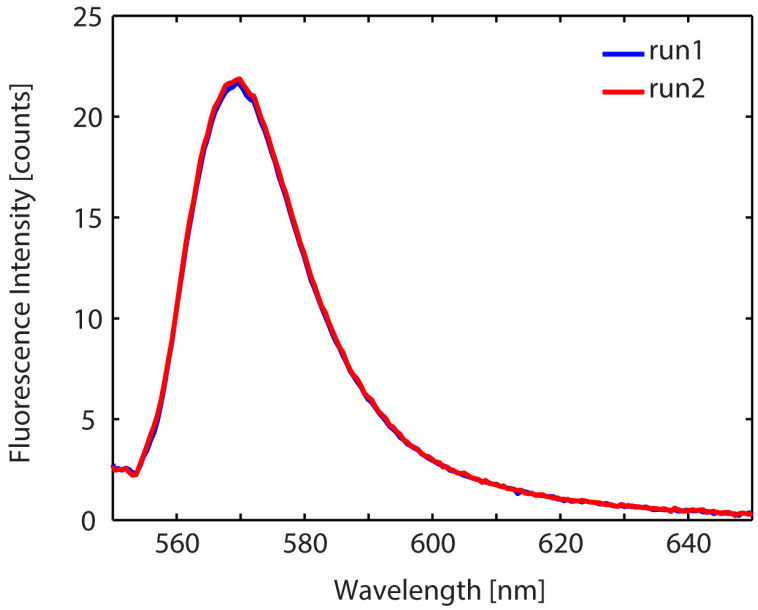

Figure 5.6: Fluorescence intensities of two runs at radiation fluence of 14.1 mJ/cm^2 remain unchanged, indicating no photodamage of the perovskite single-domain single crystal.

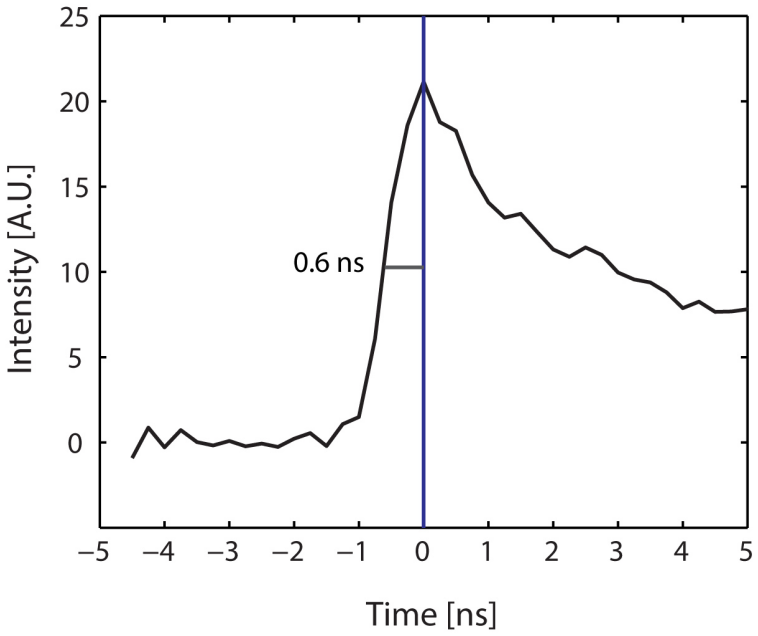

Figure 5.7: The instrumental response function of the transient absorption apparatus is shown to be 1.2 ns by measuring the rise time of signal trace at 560 nm.

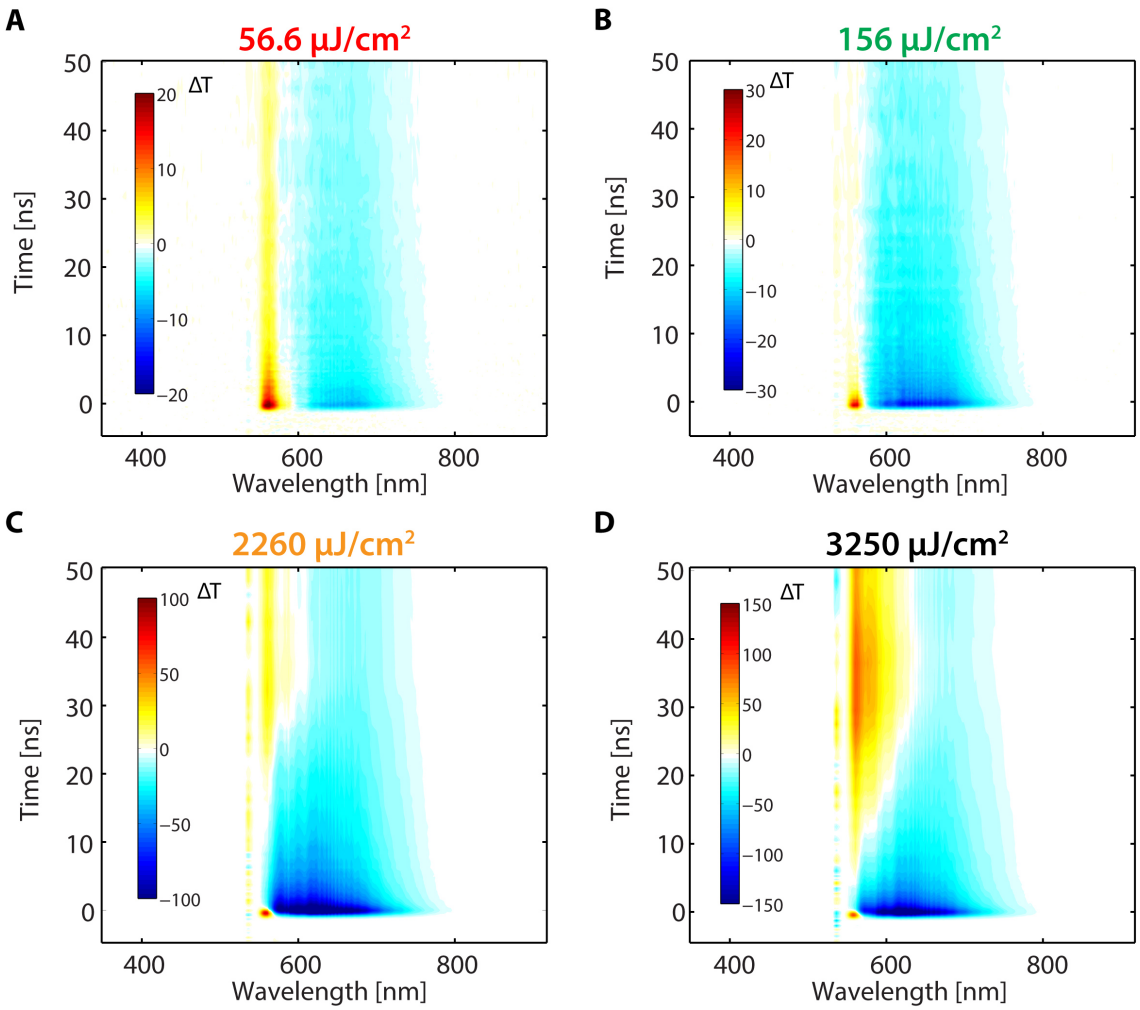

Figure 5.8: Transient absorption spectra of mm-sized $CH_3NH_3PbBr_3$ single-domain single crystal at varied radiation fluences show power-dependent dynamics. (a) 56.6 μJ/cm^2. (b) 156 μJ/cm^2. (c) 2260 μJ/cm^2. (d) 3250 μJ/cm^2.

laser centered at 540 nm and a broadband probe with spectrum ranging from 450 nm to 800 nm. The response of single crystals to radiation fluence was measured at pump fluences from 18.4 μJ/cm^2 to 3250 μJ/cm^2 while the probe fluence was kept constant at 20.4 μJ/cm^2. Representative transient absorption spectra with negative time background subtraction at different radiation fluences are shown separately in Figure 5.8. Spectra without background subtraction can be found in Figure 5.9.

At low radiation fluences (Figure 5.8.a,b), two features are present in the pump probe spectra: a positive stimulated emission feature and a broad negative excited state absorption

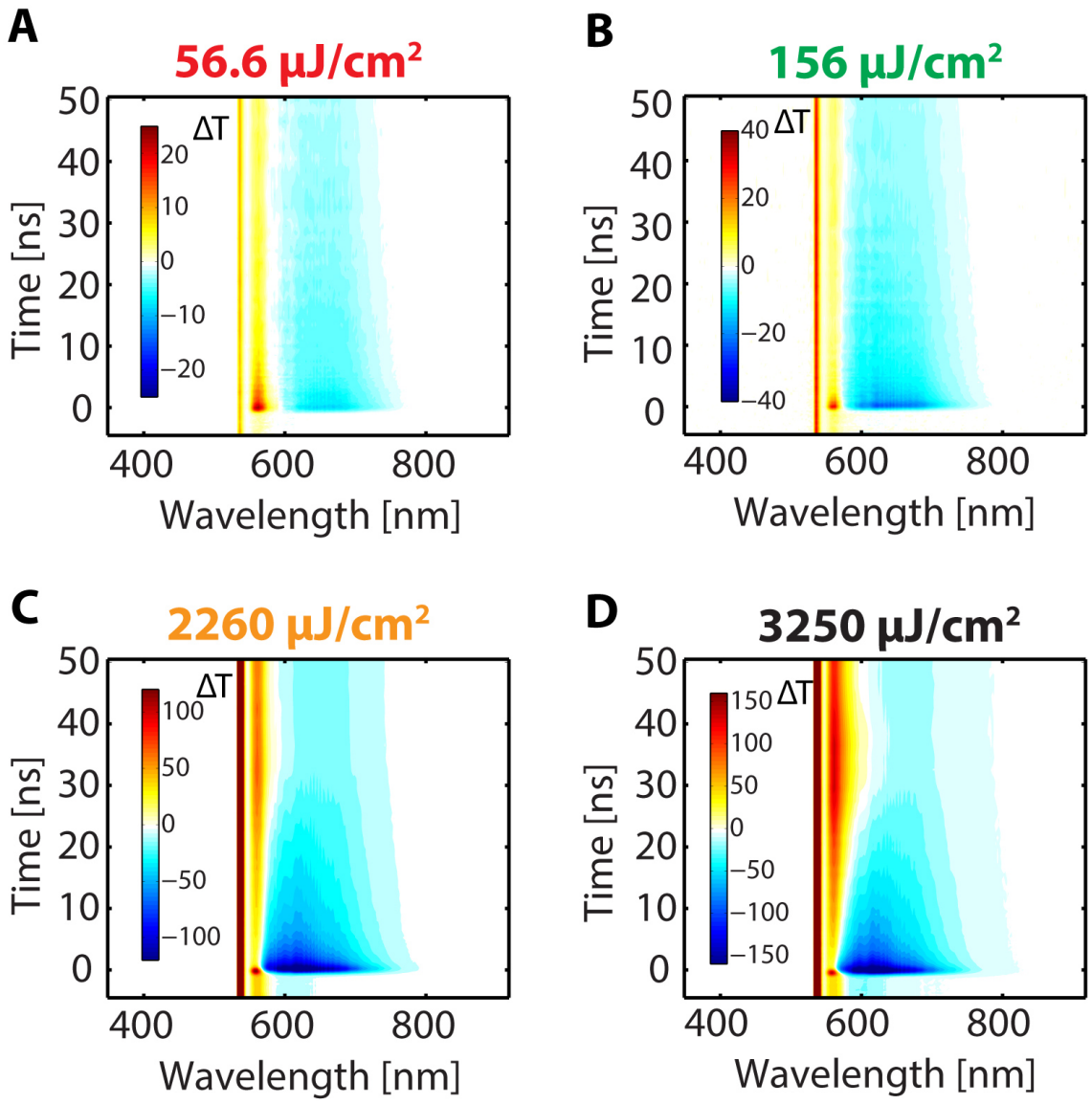

Figure 5.9: Transient absorption spectra without negative time subtraction. (a) 56.6 μJ/cm^2. (b) 156 μJ/cm^2. (c) 2260 μJ/cm^2. (d) 3,250 μJ/cm^2.

feature below band gap. The spectral positions of these features differ from the transient reflectance measurements by Yang and coworkers [16]. In their transient reflectance experiment, the positive signal was centered at 2.3 eV (540 nm, above bandgap), consistent with the peak position of our reflective geometry photoluminescence measurement, and was assigned as a result of surface recombination. However, in our transient absorption measurements on perovskite single crystals, the positive feature emerges below bandgap and matches with the transmissive geometry photoluminescence measurement. These differences suggest that the observed features in transient absorption measurements originate from the bulk states of perovskite single crystals. As radiation fluence increases, both features decay faster, yet with different rate laws. Multiple recombination mechanisms likely exist in perovskite crystals and provide different decay channels for photogenerated species with different dynamics. In general, the decay dynamics of any given carrier population can be analyzed by a rate equation [34, 35] as shown in Equation 5.1.

$$\frac{dn}{dt} = -k_1 n - k_2 n^2 - k_3 n^3 \tag{5.1}$$

The rate constant k_1 represents first-order single-particle dynamics due to either exciton recombination [36] or removal of charge carriers to form trap states. k_2 describes second-order (two particle) decay that could be attributed to electron-hole recombination. k_3 is the rate constant of a third-order process due to three-particle Auger recombination. Although it is common for the rate law to change as the laser fluence increases (e.g. higher order recombination mechanisms become more prevalent at higher fluence), a single population cannot show two different rate laws with the same radiation fluence.

Quantification of purely second-order dynamics in transient absorption spectroscopy can be obtained by solving the rate equation without first-order and third-order terms followed by converting excitation density n to transient absorption signal. As a result, ΔT^{-1} should be proportional to time delay for second-order recombination. Similarly, for decay dynamics dominated by third-order recombination, ΔT^{-2} should be linearly dependent on delay times.

Normalized time traces for the positive feature extracted at 560 nm and for the negative feature extracted at 700 nm are shown in Figure 5.10.a,d. Averaged unnormalized time traces for the positive feature extracted at 560 nm and for the negative feature extracted at 700 nm are shown in Figure 5.11 and Figure 5.12, respectively .Both features exhibit radiation fluence-dependent decay behavior, indicating that the decay is not dominated by first-order kinetics. Moreover, the positive feature exhibits a different decay timescale from the negative feature within a single transient absorption measurement, as shown in Figure 5.13, suggesting that the kinetics of these two features are dominated by different mechanisms. We therefore fit the decay traces at 560 nm and 700 nm to second-order and third-order dynamics separately, with representative fitting results at a single radiation fluence of 156 μJ/cm^2 shown in Figure 5.10.b,c,e,f. The fitting results for 560 nm traces and 700 nm traces at varied radiation fluences are summarized in Figure 5.14 with the results at each radiation fluence shown in Figure 5.15 - Figure 5.20 separately for clarity. A weighted linear curve fitting was performed on the kinetics of the averaged traces. R^2 values were calculated based on weighted fitting results. For the 560 nm feature, because this feature decays quickly and falls within our instrumental response limit at high radiation power, only traces at low radiation powers were fit. The decay of the 700 nm feature exhibits third-order kinetics consistently from low to high radiation fluences. This agreement among different fluences suggests that although thermal effects associated with relaxation of high concentration of carriers may play a role under high radiation fluence, such effects are negligible in the short time dynamics of perovskite single crystals.

At high radiation fluences, the 560 nm positive feature decays too quickly and falls within our instrumental response limit (1.2 ns, Figure 5.7). Hence, only 560 nm timetraces acquired at low fluence were fit. The fitting results show excellent agreement with second-order instead of third-order dynamics, as shown in Figure 5.10.b,c and Figure 5.14 and Figure 5.16. In contrast, the broad 700 nm negative feature unambiguously follows third-order kinetics due to Auger recombination, as shown in Figure 5.10.e,f. This third-order decay kinetics of the

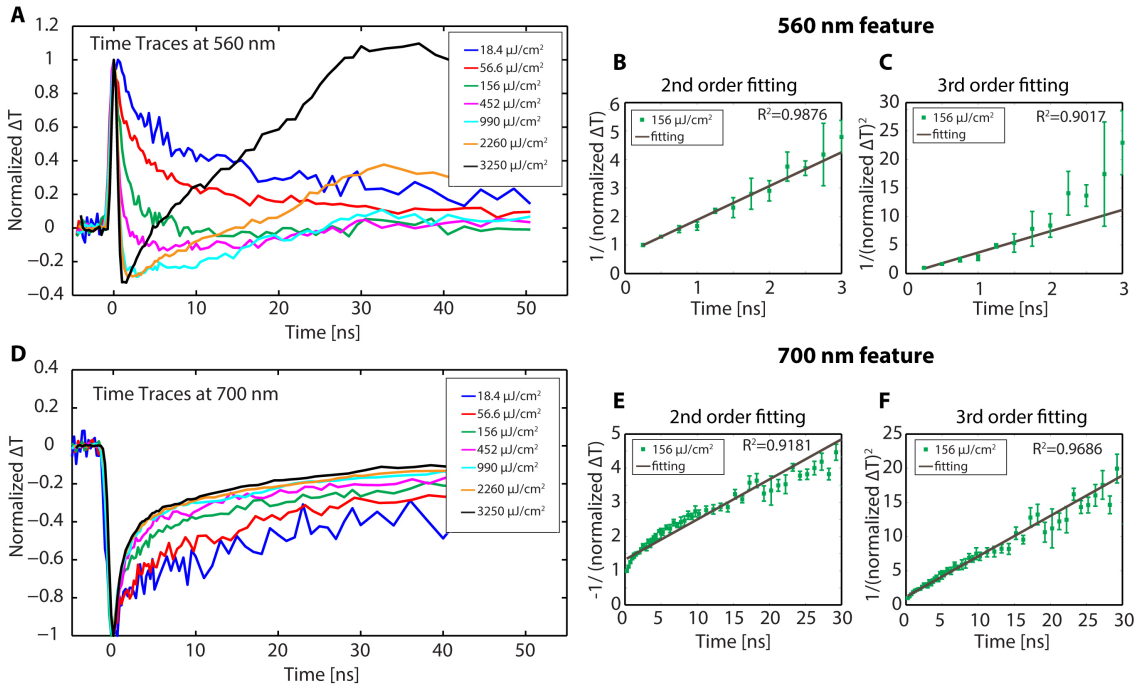

Figure 5.10: Radiation fluence-dependent transient absorption kinetics following different orders suggests two distinct photogenerated populations upon initial excitation. (a) Traces normalized at 0 ns recorded at 560 nm for different excitation intensities. (b) Second-order kinetics fitting result of the 156 μJ/cm^2 trace (green in a). (c) Third-order kinetics fitting result of 156 μJ/cm^2 trace in a. (d) Normalized traces recorded at 700 nm for different excitation intensities. (e) Second-order kinetics fitting result of the 156 μJ/cm^2 trace (green in d). (f) Third-order kinetics fitting result of the 156 μJ/cm^2 trace in d.

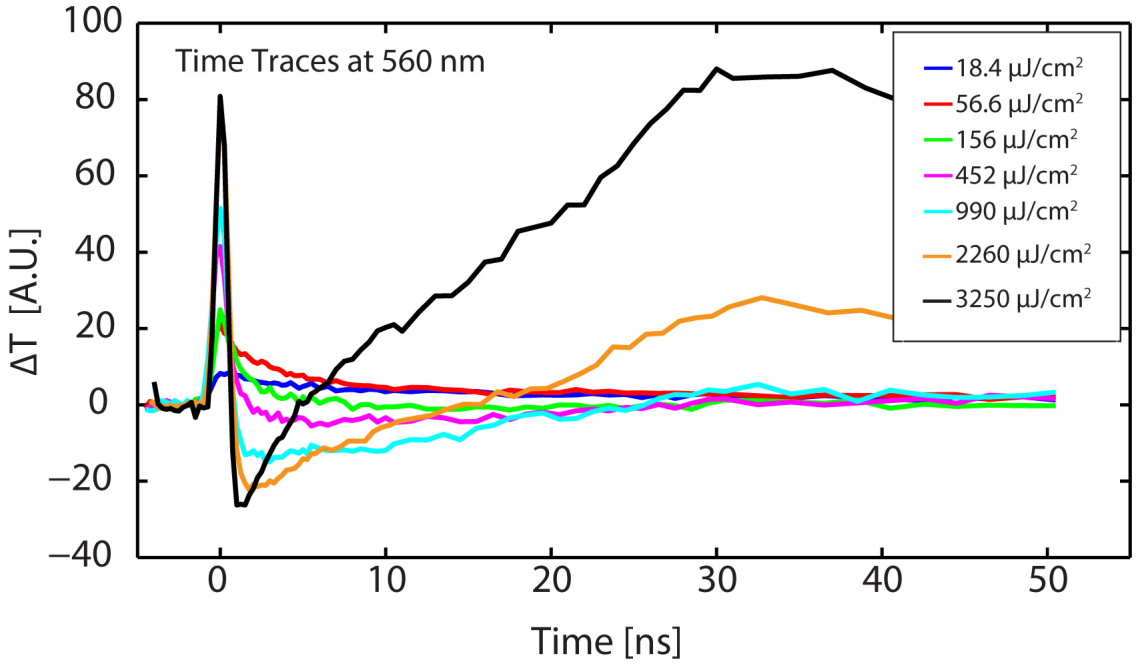

Figure 5.11: Unnormalized traces recorded at 560 nm for different radiation fluences.

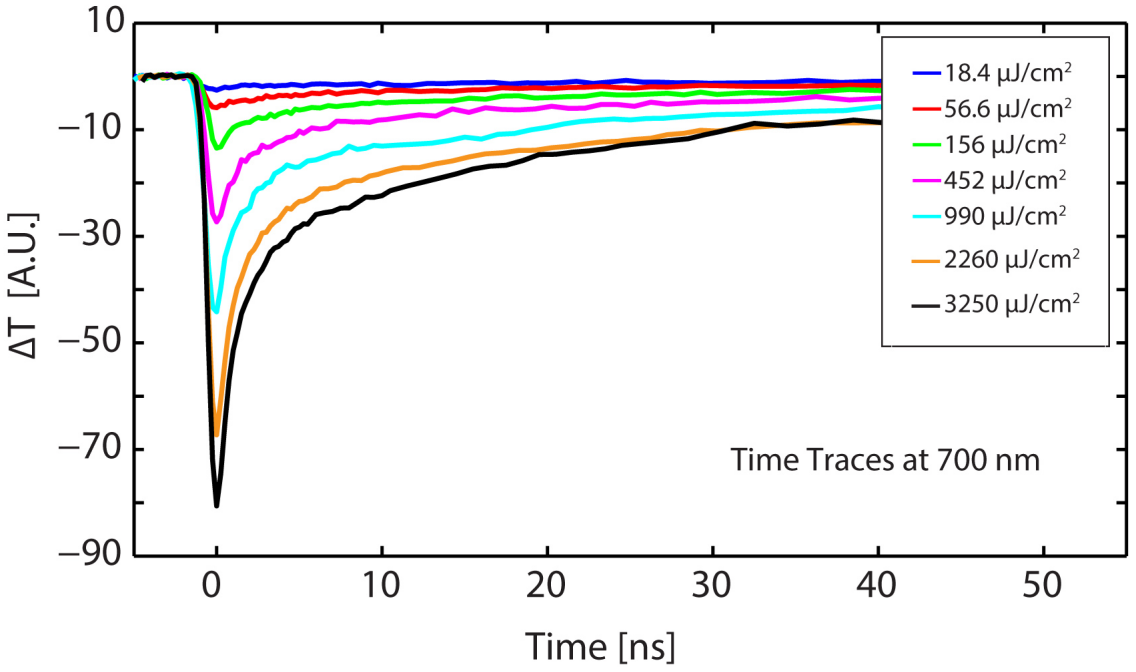

Figure 5.12: Unnormalized traces recorded at 700 nm for different radiation fluences.

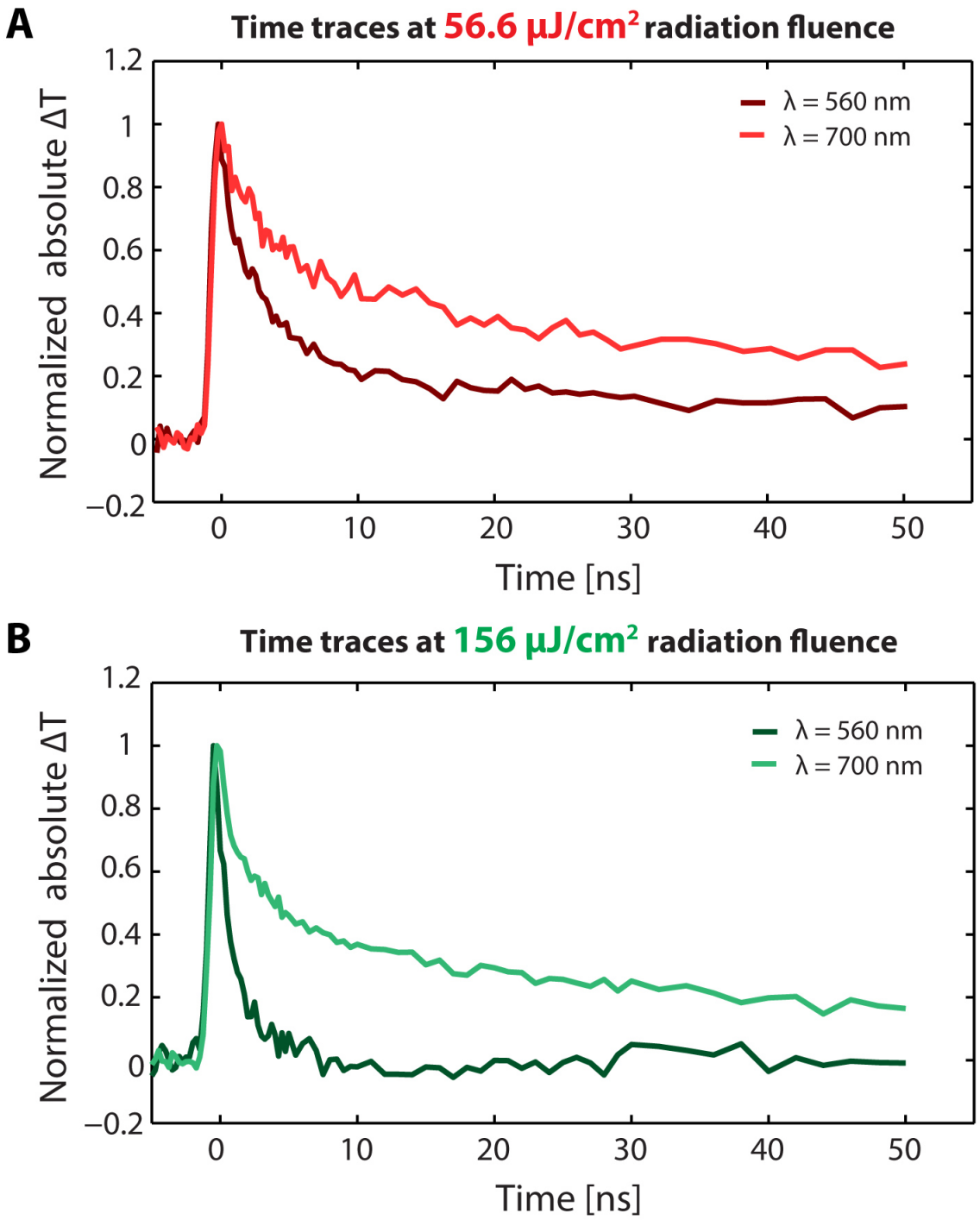

Figure 5.13: The different decay timescales of the traces at 560 nm and 700 nm indicate different decay mechanisms for these two features. (a) 56.6 μJ/cm^2. (b) 156 μJ/cm^2.

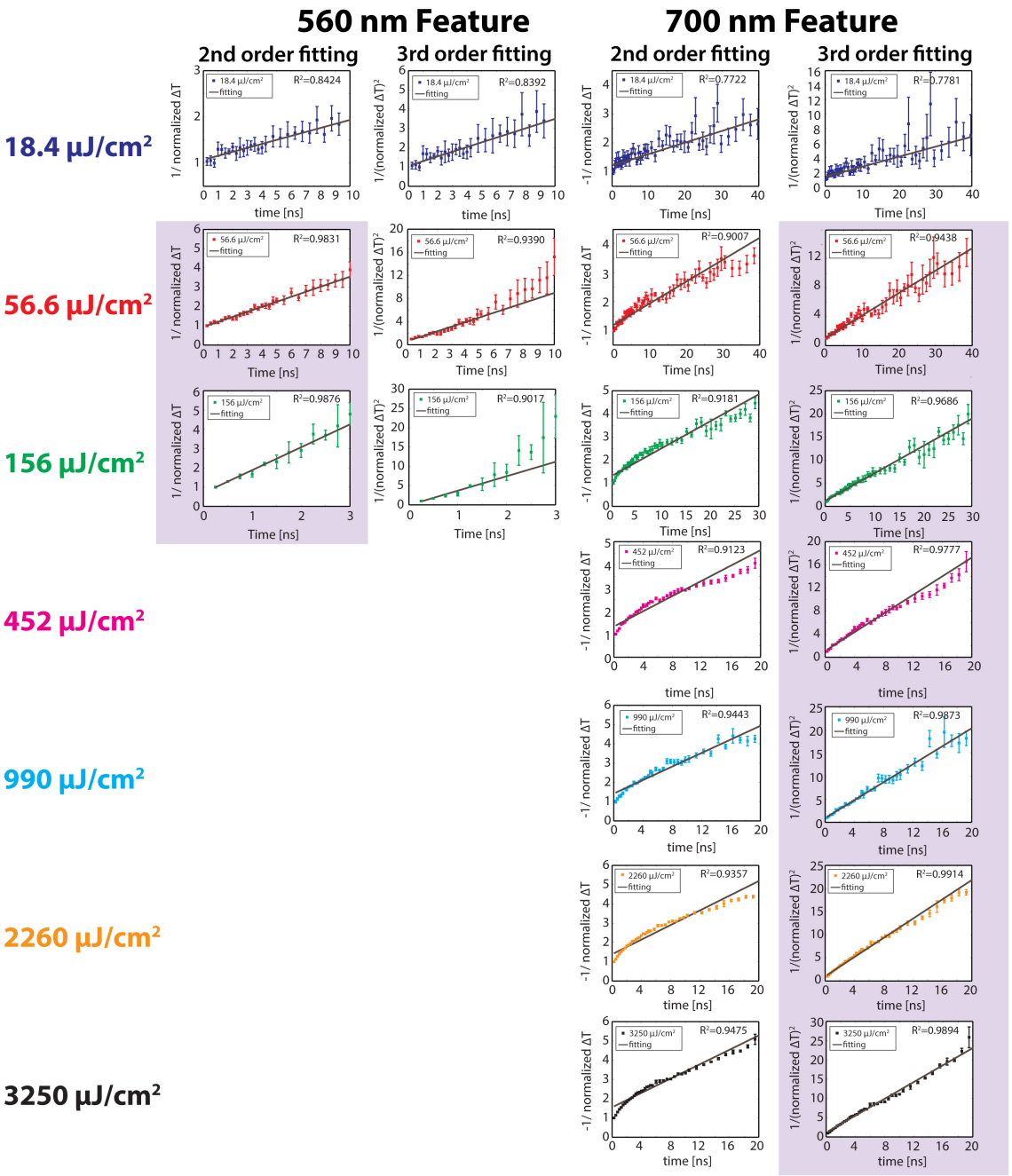

Figure 5.14: Summarized kinetics fitting results of the timetraces recorded at 560 and 700 nm at varied radiation fluences show two distinct carrier populations. Best fits are highlighted with the purple background.

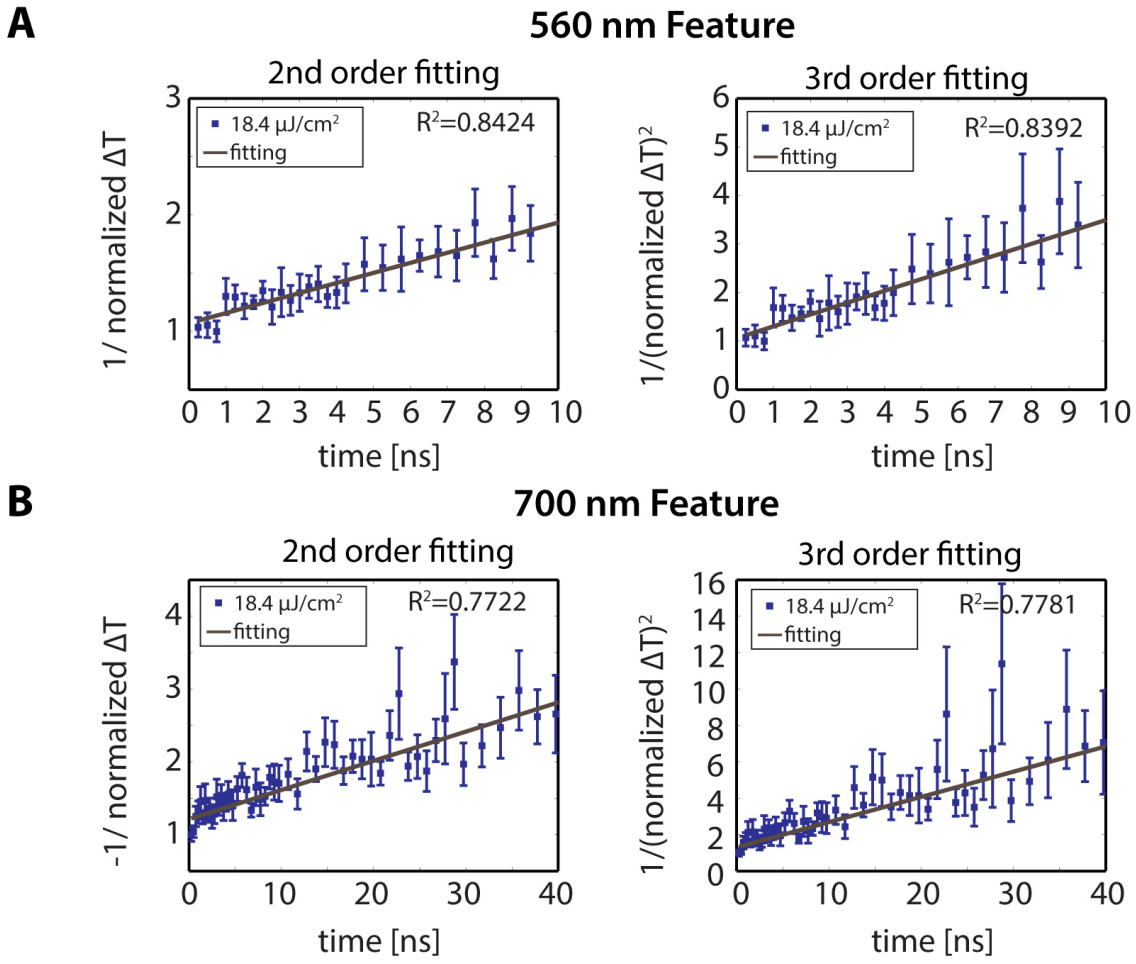

Figure 5.15: Kinetics fitting results of the traces at radiation fluence of 18.4 μJ/cm^2 recorded at (a) 560 nm; (b) 700 nm.

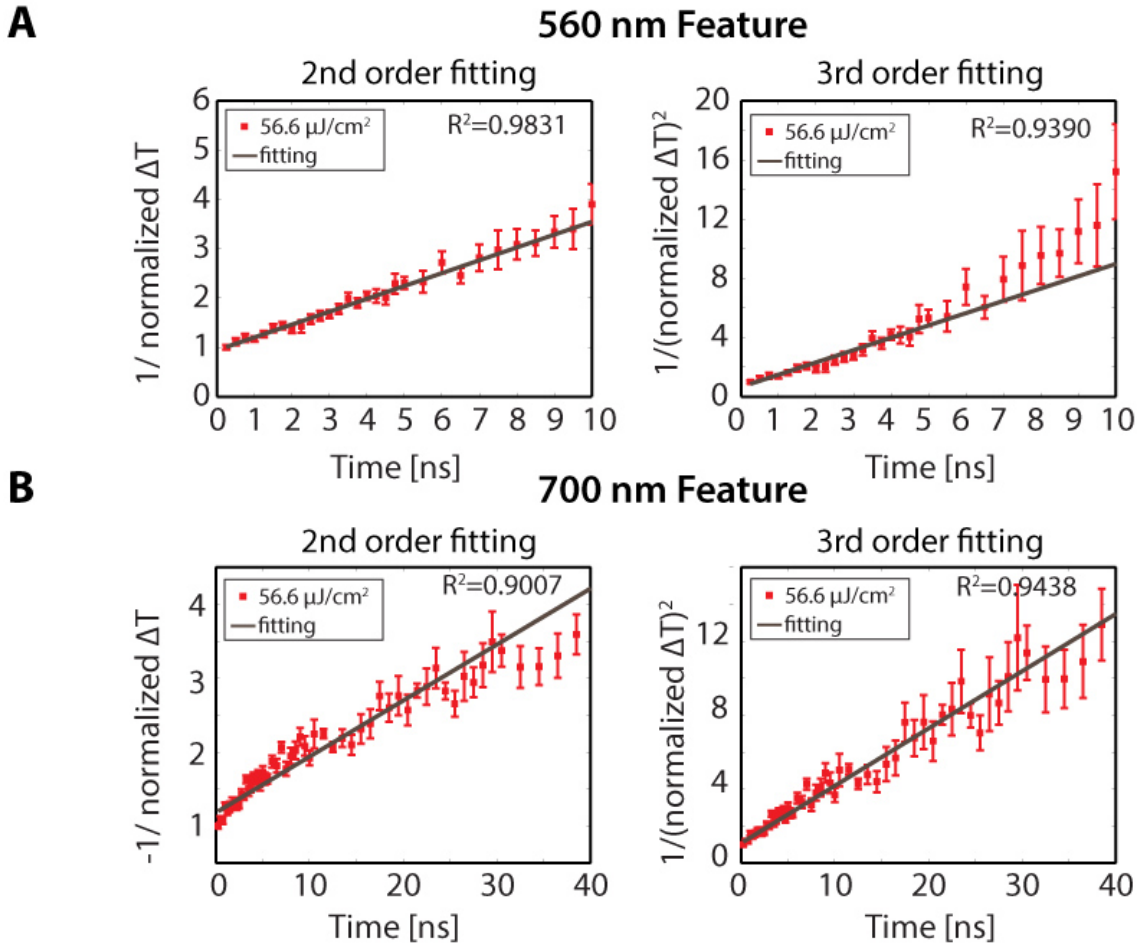

Figure 5.16: Kinetics fitting results of the traces at radiation fluence of 56.6 μJ/cm^2 recorded at (a) 560 nm; (b) 700 nm.

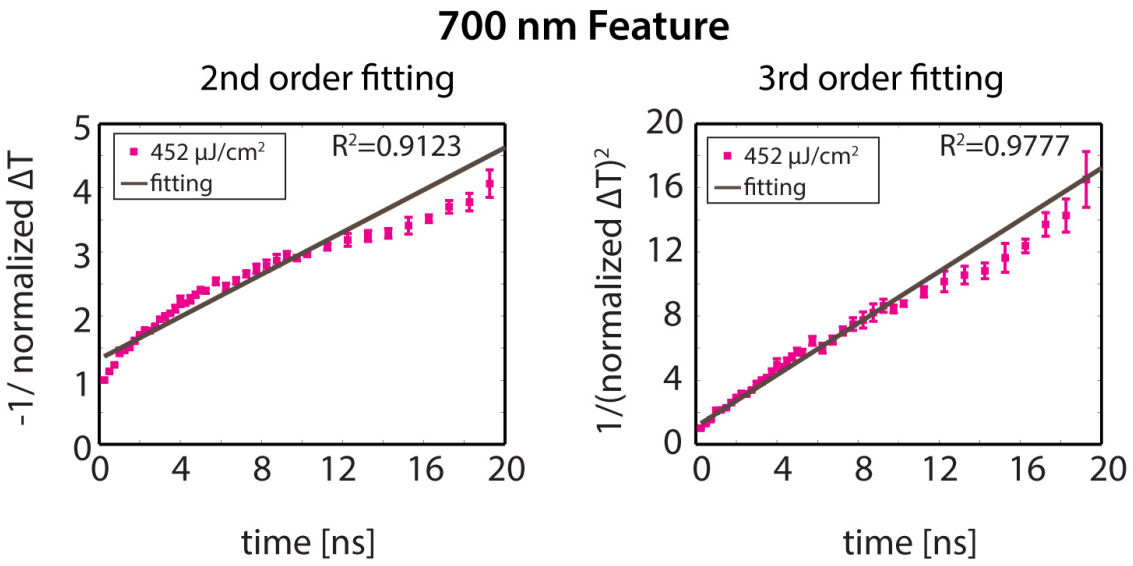

Figure 5.17: Kinetics fitting results of the traces at radiation fluence of 452 μJ/cm^2 recorded at (a) 560 nm; (b) 700 nm.

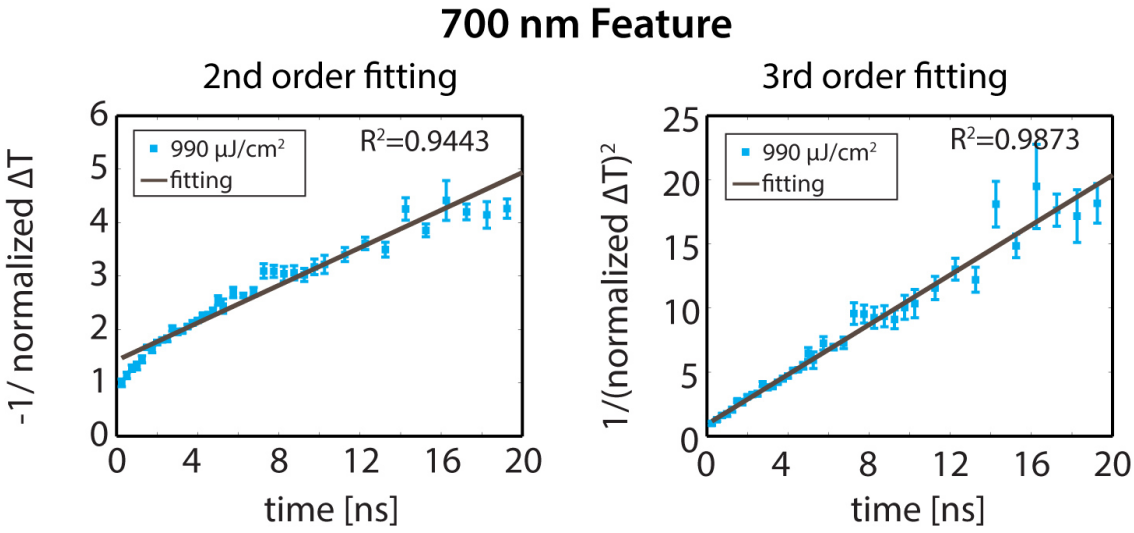

Figure 5.18: Kinetics fitting results of the traces at radiation fluence of 990 μJ/cm^2 recorded at (a) 560 nm; (b) 700 nm.

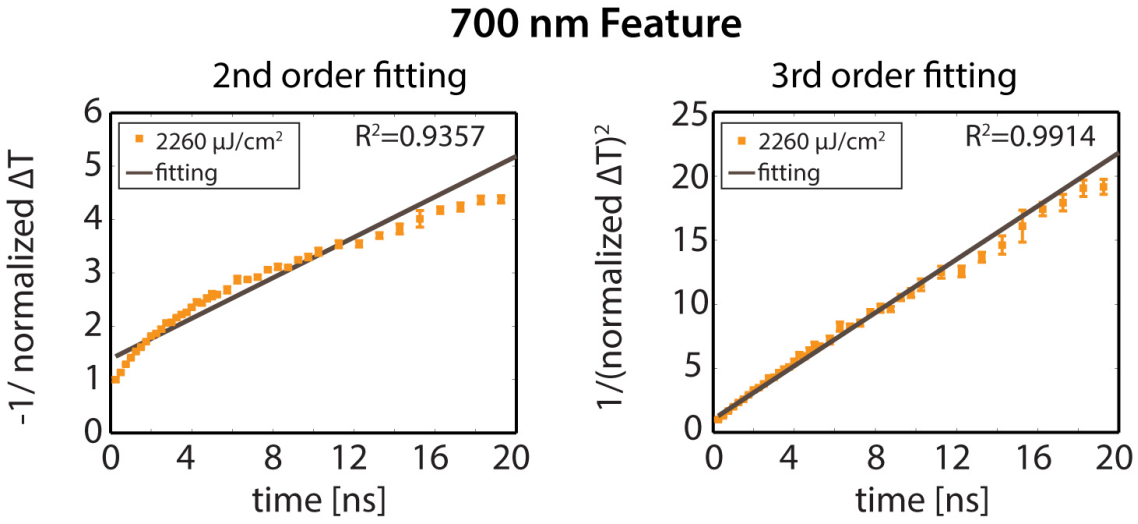

Figure 5.19: Kinetics fitting results of the traces at radiation fluence of 2260 μJ/cm^2 recorded at (a) 560 nm; (b) 700 nm.

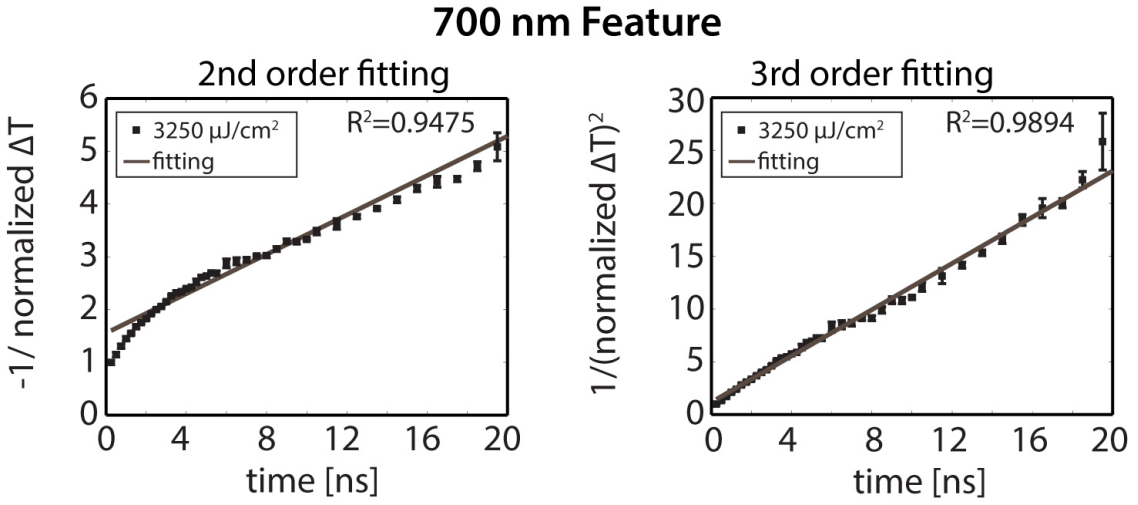

Figure 5.20: Kinetics fitting results of the traces at radiation fluence of 3250 μJ/cm^2 recorded at (a) 560 nm; (b) 700 nm.

negative feature is consistent from low to high radiation fluences (Figure 5.14 - Figure 5.20). During a three-body Auger process, two carriers lose energy nonradiatively while a third carrier gains energy through this process resulting in a hot carrier. The timescale for Auger recombination varies from tens of nanoseconds to a few nanoseconds as radiation fluence increases.

The distinct rate laws and timescales associated with these two spectral features (Figure 5.13 and Figure 5.14) indicate two distinct sets of carrier populations following different decay pathways in perovskite single crystals. One decays via second-order recombination while the other one decays via third-order Auger recombination. At high radiation fluences, we observe a third feature, broad and positive, emerging at later time delays (Figure 5.8.c,d and black and yellow traces in Figure 5.10.a). The unusual dynamic behavior suggests that this feature is not a direct result of initial laser excitation. Initial photogenerated populations, contributing to either second-order or third-order recombination, decay within only a few nanoseconds. Therefore, we exclude these initial photogenerated populations as the direct source of this unexpected new feature. Relaxation of hot carriers after Auger recombination and the concomitant thermal effect may account for this feature.

The carrier dynamics we observed in perovskite single-domain single crystals differs from that observed in thin films. Although the positive stimulated emission feature corresponding to photoluminescence exists in both thin films and single crystals, the dynamics of the negative excited state feature below the bandgap differs substantially. In the transient absorption spectroscopy studies of $CH_3NH_3PbBr_3$ thin films by Yang and coworkers [37] as well as Grancini and coworkers [27], they observed a negative ESA feature that completely decays by 1 ps. However, we observe an ESA feature lasting for tens of nanoseconds that decouples from the stimulated emission and undergoes third-order Auger recombination. We believe that this observation difference is due to the nonintrinsic factors associated with perovskite thin films, such as defects and grain boundaries, which may affect the inherent photophysical dynamics of these materials.

5.5 Conclusions

Our work shows that single-domain single crystals exhibit different dynamics from those reported in thin films [12–14, 27]. Auger recombination was considered to be a negligible effect in thin films [12]. However, in our measurement of bulk behavior of perovskite single crystals, Auger recombination contributes significantly to the overall transient absorption signal at all measured radiation fluences. Our theoretical calculations in Appendix A have suggested that the two distinct sets of photogenerated populations observed in the TA measurements are due to polaron formation rather than local spin polarization. Based on the difference between our observations from $CH_3NH_3PbBr_3$ single-domain single crystals and those from perovskite thin films, we believe that, the high crystallinity of single-domain single crystals may facilitate the polaron formation, which gives rise to the decoupled decay dynamics we observed in the TA measurements.

APPENDIX A

THEORETICAL CALCULATIONS ON PEROVSKITE BULK SINGLE CRYSTALS

A.1 Theoretical calculations on possible hypotheses for the observed two sets of carrier populations

The observations of two distinct sets of photogenerated populations that undergo second-order decay and third-order Auger recombination separately are consistent across all perovskite $CH_3NH_3PbBr_3$ single-domain single crystals we tested. One hypothesis for these two distinct sets of carrier populations is that they are carriers with different spin textures in spin split-off bands. Strong spin-orbit coupling in perovskites will induce local spin polarization such as Rashba and Dresselhaus effects [38]. The local spin polarization has been predicted not only in non-centrosymmetric systems but also in inversion-symmetric bulk crystals with symmetry breaking at individual sites [39]. We have calculated the relaxation lifetimes of charge carriers with different spin textures near the band edge (details shown in section A.2). These lifetimes are found to be on the order of femtoseconds (Figure A.2), much shorter than the time scales of our measurements. Hence, the different spin texture hypothesis is not likely to be the explanation for our observations.

The other hypothesis is that polaron formation may localize carriers giving rise to the second population. The polaron formation in organic-inorganic lead halide perovskites has been proposed by several papers [15, 17–23, 40]. The dipole moments of nearest neighbor $CH_3NH_3^+$ may orient toward a single Pb^{2+}, reducing the electrostatic potential energy of electrons around the Pb^{2+} and favoring the formation of a small polaron. The polaron formation will lead to localization of carriers, dramatically reducing the overlap between electron and hole wavefunctions. Hence, the recombination will be slowed by polaron formation [40] and decoupled from the recombination dynamics of the free carriers.

To test this hypothesis, we have estimated the polaron stabilization energy in cubic 3x3x3 and 4x4x4 supercells representing crystalline $CH_3NH_3PbBr_3$and $CH_3NH_3PbI_3$. We considered over 100 different $CH_3NH_3^+$ orientations to reduce the statistical errors. Two types of geometries were created. The first one contains $CH_3NH_3^+$ oriented in random directions, which we call the random (R) geometry. The second type of configurations, which we call the polaron (P) geometry, is based on the R geometry, but with the eight nearest neighbor $CH_3NH_3^+$ pointing toward a single Pb^{2+} at the center of the supercell(Figure A.1).

The electron polaron binding energy is given by Equation A.1

$$E_b = E_P^{q=-1} - E_R^{q=-1} \tag{A.1}$$

where E_P^q is the total energy of the system with net charge q (negative one in this case) in the P configuration, and E_R^q is the total energy of the system with net charge q in the R configuration. We estimated the polaron binding energy by using single particle energies of the neutral free carrier and polaron structures (Equation A.2):

$$E_b \approx \varepsilon_P^{q=0} - \varepsilon_R^{q=0} + \Delta V \tag{A.2}$$

where $\varepsilon_P^{q=0}$ is the Kohn-Sham energy of the lowest unoccupied molecular orbital (LUMO) of the system with a net neutral charge in the P configuration, $\varepsilon_R^{q=0}$ is the Kohn-Sham energy of the conduction band minimum of the system with a net neutral charge in the R configuration, and ΔV is the potential alignment term. We will refer to Equation A.2 as the polaron stabilization energy, which is an approximation to E_b defined in Equation A.1. We note that the use of Equation A.2 requires a common reference potential be obtained to compare single particle energies (ΔV) but it avoids the technical difficulties associated with computing energy differences of charged bulk systems. In Equation A.2 only energies of neutral configurations are required; hence the evaluation of the potential alignment term (ΔV) can be performed by simply computing the planar average potential far from the

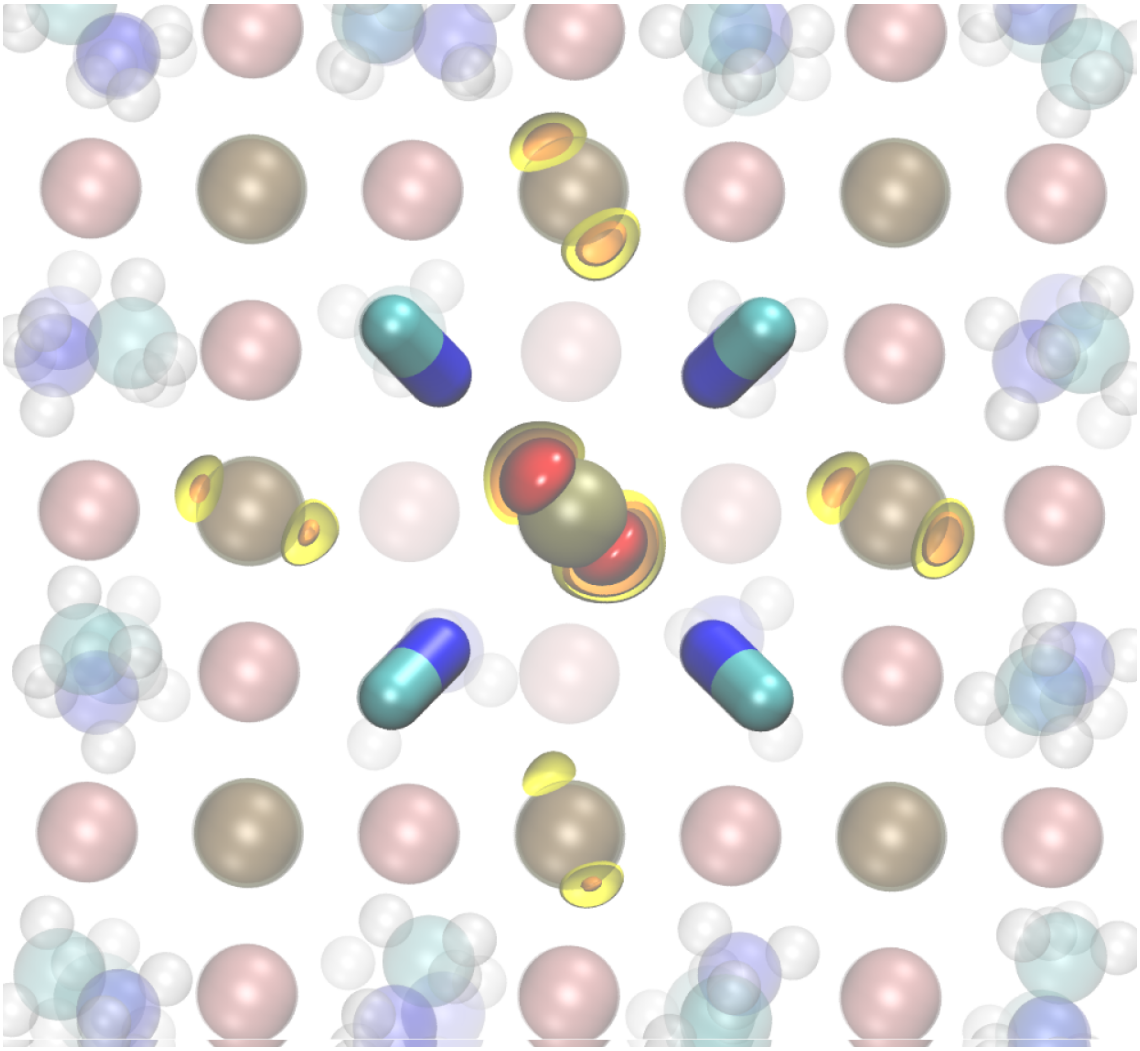

Figure A.1: Illustrative electron polaron geometries considered in the calculations. The red isosurface represents the square modulus of the single particle wavefunction of the conduction band minimum. White, tan, cyan, blue, and pink spheres represent H, Pb, C, N, and Br atoms, respectively. Hydrogen atoms on the nearest $CH_3NH_3^+$ from the polaron site have been removed from the Figure for clarity.

polaron site in the supercell.

We found that orienting nearest neighbor $CH_3NH_3^+$ toward a single Pb^{2+} is sufficient to localize a state below the conduction band minimum (Figure A.4), even when using a semi-local functional such as PBE [41]. Our estimate of the polaron stabilization energy with the largest models (4x4x4 supercell) at the PBE level of theory is 147 meV with a 95% confidence interval (118-169 meV). In addition, we calculated the total stabilization energy (electron and hole) of several configurations of 4x4x4 $CH_3NH_3PbI_3$ and obtained an average stabilization energy of 70 meV (above kT at room temperature, 26 meV), which is in agreement with Neukirch and coworkers [21]. The stabilization energies indicate that electron polarons could form in both $CH_3NH_3PbBr_3$ and $CH_3NH_3PbI_3$ perovskites, but are more pronounced in $CH_3NH_3PbBr_3$. Our current calculations, however, do not support the formation of hole polarons (detailed discussion shown in section A.2).

The $CH_3NH_3^+$ near the Pb^{2+} create an electrostatic potential that is attractive for the electrons but repulsive for the holes. The electron and hole wavefunctions are then separated spatially due to the electrostatic potential created by the $CH_3NH_3^+$, demonstrated by the computed spherical average of electron and hole wavefunctions in the polaron configuration shown in Figure A.3. As a consequence, their overlap is decreased and so is the rate of recombination. In addition, the presence of electron polaronic configurations favors the stabilization of excitons, consistent with previous observations of excitons (could be polaron-exciton in nature [23]) in perovskite bulk crystals [16, 42]. The formation of small electron polarons increases the effective mass of the electrons and therefore the exciton binding energy, as can be seen by considering a simple hydrogenic model: assuming Rydberg atomic units the exciton binding energy is:

$$E_x = \frac{E_{Ry}}{\varepsilon^2}\mu \tag{A.3}$$

where E_{Ry}=13.6 eV, ε is the static dielectric constant, and μ is the reduced effective mass given by $\frac{m_h m_e}{m_h+m_e}$. The reduced mass will be enhanced by the electron polaron effective

mass making the formation of excitons more likely in spatial regions where electron polarons form.

We expect that the formation of electron polaron occur in specific locations within the $CH_3NH_3PbBr_3$ perovskite lattice, depending on the local orientation of the $CH_3NH_3^+$. Free carriers and electron polarons are likely to be spatially separated in different domains formed by the collective orientation of $CH_3NH_3^+$ ions [43]. Polaron lattice distortions will be energetically less favorable than free carriers in regions where $CH_3NH_3^+$ have preferential orientations, e.g. in ferroelectric domains.

The differences between the polaron stabilization energy of $CH_3NH_3PbBr_3$ and $CH_3NH_3PbI_3$ can be explained by the differences in the optical dielectric constant. The long-range Coulomb-like potential well created by the displacements of ions around an isolated point charge is given by:

$$V(r) = -(\frac{1}{\varepsilon_{opt}} - \frac{1}{\varepsilon_{opt} + \varepsilon_o})\frac{e^2}{|r|} \tag{A.4}$$

where ε_{opt} is the optical dielectric constant (from the electrons) and ε_o is the ionic portion of the dielectric constant. In our model ε_o is the same for the two systems but the optical dielectric constant of $CH_3NH_3PbBr_3$ is smaller than $CH_3NH_3PbI_3$, hence, the potential created by the displacement of the $CH_3NH_3^+$ to localize the polaron will be greater in magnitude in $CH_3NH_3PbBr_3$.

Although we considered $CH_3NH_3PbBr_3$ and $CH_3NH_3PbI_3$, there is evidence in literature that the formation of polarons could be enhanced in mixed $CH_3NH_3PbI_{3-x}Cl_x$ perovskites. Recently, He and Galli found that the presence of chloride in mixed halide $CH_3NH_3PbI_{3-x}Cl_x$ perovskite can displace $CH_3NH_3^+$ cations and reduce the high frequency dielectric constant [44]. This observation suggests that Cl-doped $CH_3NH_3PbI_3$ single crystals may encourage polaron formation and could be a good system to employ the effects of polaron formation in solar-cell device applications.

A.2 Computational details

All density functional theory calculations were performed using the Quantum-ESPRESSO software package. We used a plane wave basis set with a wave function energy cutoff of 80 Ry. We used SG15 Optimized Norm-Conserving Vanderbilt (ONCV) pseudopotentials [45] and the generalized gradient approximation with the PBE exchange-correlation functional [41]. Supercell calculations were performed at the gamma point of the Brillouin zone.

The $CH_3NH_3PbBr_3$ cubic structure (*Pm-3m*) is stable at room temperature with a lattice constant of a = 5.91$\mathring{A}$ (Table 5.1). Even though our simulations are performed at 0 K, we used the experimental cubic structure with a lattice constant of 5.91 $\mathring{A}$ and 6.276 $\mathring{A}$ for the $CH_3NH_3PbBr_3$ and $CH_3NH_3PbI_3$ structures, respectively. $CH_3NH_3^+$ configurations were generated using random orientations and then used to point eight nearest neighbor $CH_3NH_3^+$ toward a single Pb^{2+}. Geometries with permanent dipole moments were included in the results.

A.2.1 Relaxation lifetimes of carriers with different spin textures

We explored the possibility of different spin textures giving rise to two distinct populations. We computed the relaxation time of excited carriers given by Equation A.5:

$$\tau_k = (2\Sigma_k(\omega, T))^{-1} \tag{A.5}$$

Where $\Sigma_k(\omega$,T) is the imaginary part of the electron self-energy given by equation (8) of Ref [46] We computed the electron self-energy using Wannier interpolation with the EPW code [46]. We used a 14 x 14 x 14 fine k grid centered at the Gamma point, a 6 x 6 x 6 coarse k grid, 500 random q points and a 2 x 2 x 2 coarse q-point grid. The calculations were performed assuming a temperature of 300 K with a Gaussian broadening of 1 meV. We found the relaxation lifetimes of charge carriers with different spin textures near the band edges to be of the order of femtoseconds (Figure A.2), much shorter than the time scales of

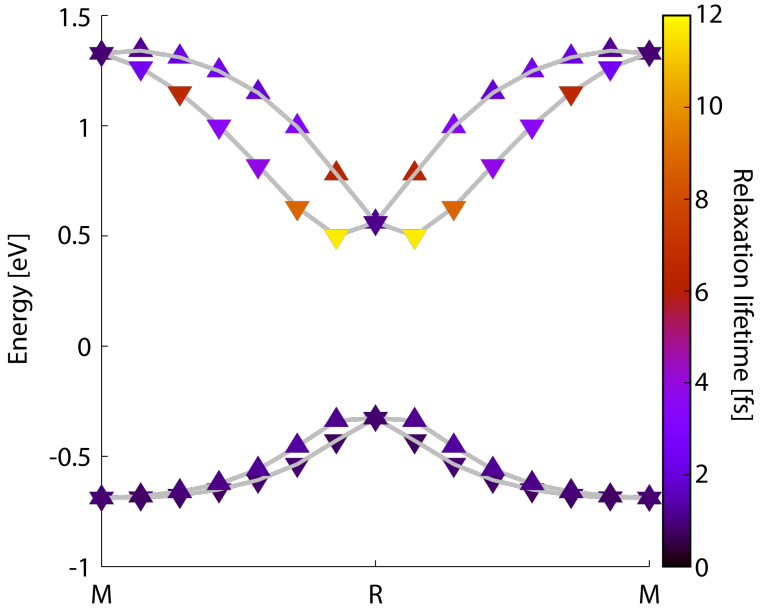

Figure A.2: Relaxation lifetimes of carriers with different spin textures for a single cross section around the M point in the BZ of $CH_3NH_3PbBr_3$.

our measurements. Hence the different spin texture hypothesis was discarded.

A.2.2 Wavefunction localization

As mentioned in section A.1, we verified that the electron wavefunction obtained for the polaron geometry was localized. In Figure A.3, we present the spherical average of the electron and hole wavefunctions for the polaron geometry. We found that the electron wavefunction was localized by the surrounding $CH_3NH_3^+$ while the hole remained delocalized. We also repeated this analysis with an additional electron added to the system and found the systems exhibited a localized electron wavefunction upon charging. Our current calculations, however, do not support the formation of hole polarons. or at least we did not find them to be stable when considering the same lattice distortions as those considered for electron polarons. We also oriented the $CH_3NH_3^+$ toward a single Br^- site and again did not find hole localization. The hole wavefunctions remain delocalized throughout the system except near the site where the $CH_3NH_3^+$ were reoriented toward the Pb^{2+}, as shown in Figure A.3. This result appears to be physically sensible although further investigations with hybrid

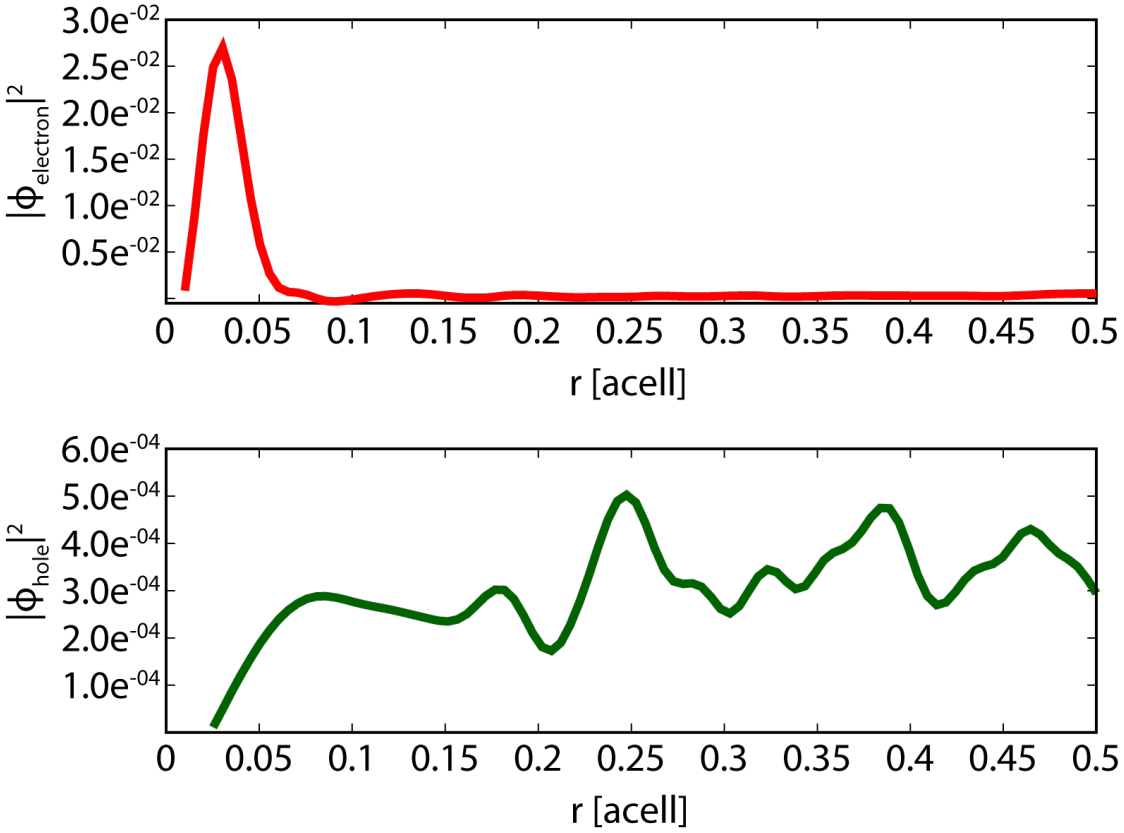

Figure A.3: Spherical averages of electron wavefunction (CBM, upper panel) and hole wavefunction (VBM, lower panel), centered at a Pb^{2+} with nearest neighbor $CH_3NH_3^+$ pointed toward the center Pb^{2+} in the polaron geometry.

functionals would be necessary to draw definitive conclusions. It is not unconceivable that using hybrid functionals one could find stable hole polarons.

A.2.3 Single particle energies

We verified that the conduction band minimum (CBM) is responsible for the reduction in the electronic gap in the polaronic configuration by aligning the average electrostatic potentials of the neutral polaronic and free charge configurations far from the Pb^{2+} where the nearest neighbor $CH_3NH_3^+$ were reoriented. Figure A.4 is a plot of the single particle energies for both the 3 x 3 x 3 and 4 x 4 x 4 supercells in the polaron and free charge configurations. Similar to the work of Neukirch and coworkers [21], we expect the use of

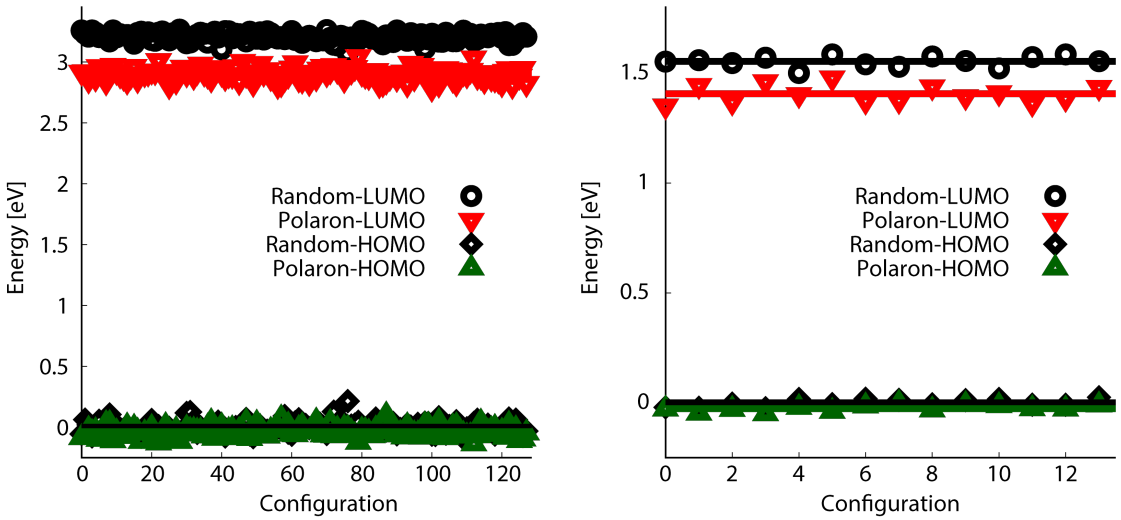

Figure A.4: Aligned VBM and CBM energies of random/polaron geometries of a 3 x 3 x 3 (left, calculated with SOC) and 4 x 4 x 4 (right, calculated without SOC) $CH_3NH_3PbBr_3$ supercells.

single particle energies of the neutral bulk structures to underestimate the polaron binding energy one would obtain by total energy differences of fully relaxed charged isolated clusters. Most of our calculations were carried out without spin-orbit coupling but we performed one calculation for a single 3 x 3 x 3 geometry and found the polaron stabilization energy to be even larger than the one obtained without SOC. We expect the stabilization energy to be underestimated by the PBE approximation; the use of hybrids with a judicious choice of the fraction of exact exchange [47–49]will most likely further localize the conduction band minimum (CBM) electronic wavefunction.

A.2.4 Band alignment

HOMO/LUMO energy eigenvalues of polaron and random geometries were aligned by computing the average over all planar averages along one direction of the potential far from the polaron site. The average difference in the planar average potential for the polaron and random $CH_3NH_3^+$ configurations in a $CH_3NH_3^+$ supercell is plotted in Figure A.5.

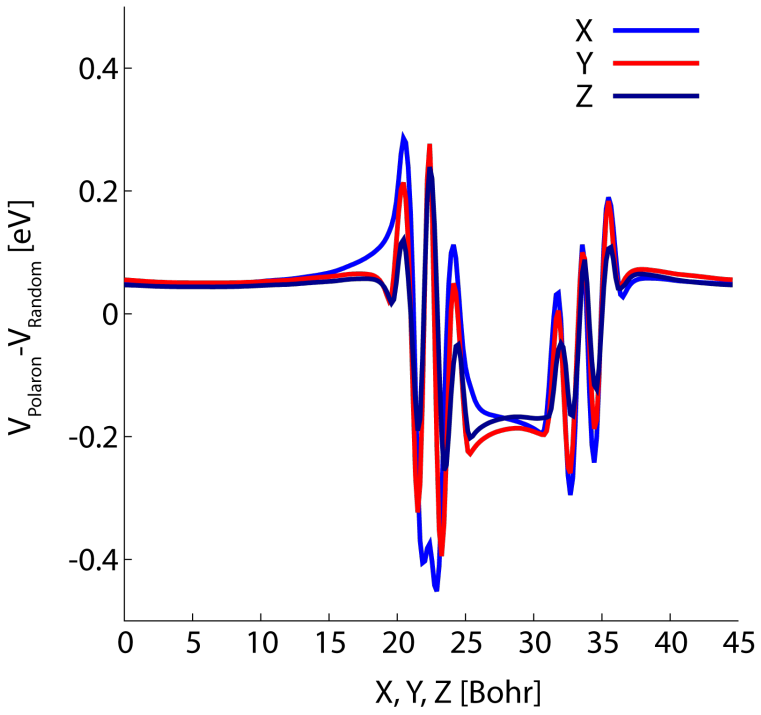

Figure A.5: Difference in the planar average potential along the x, y and z directions for the polaron and random $CH_3NH_3^+$ configurations in a 4 x 4 x 4 supercell.

REFERENCES

[1] Woon Seok Yang, Jun Hong Noh, Nam Joong Jeon, Young Chan Kim, Seungchan Ryu, Jangwon Seo, and Sang Il Seok. High-performance photovoltaic perovskite layers fabricated through intramolecular exchange. *Science*, 348(6240):1234, 06 2015.

[2] Huanping Zhou, Qi Chen, Gang Li, Song Luo, Tze-bing Song, Hsin-Sheng Duan, Ziruo Hong, Jingbi You, Yongsheng Liu, and Yang Yang. Interface engineering of highly efficient perovskite solar cells. *Science*, 345(6196):542, 07 2014.

[3] Wanyi Nie, Hsinhan Tsai, Reza Asadpour, Jean-Christophe Blancon, Amanda J. Neukirch, Gautam Gupta, Jared J. Crochet, Manish Chhowalla, Sergei Tretiak, Muhammad A. Alam, Hsing-Lin Wang, and Aditya D. Mohite. High-efficiency solution-processed perovskite solar cells with millimeter-scale grains. *Science*, 347(6221):522, 01 2015.

[4] Dongqin Bi, Chenyi Yi, Jingshan Luo, Jean-David Décoppet, Fei Zhang, Shaik Mohammed Zakeeruddin, Xiong Li, Anders Hagfeldt, and Michael Grätzel. Polymer-templated nucleation and crystal growth of perovskite films for solar cells with efficiency greater than 21%. *Nature Energy*, 1:16142 EP –, 2016.

[5] Guichuan Xing, Nripan Mathews, Swee Sien Lim, Natalia Yantara, Xinfeng Liu, Dharani Sabba, Michael Grätzel, Subodh Mhaisalkar, and Tze Chien Sum. Low-temperature solution-processed wavelength-tunable perovskites for lasing. *Nat Mater*, 13(5):476–480, 05 2014.

[6] Felix Deschler, Michael Price, Sandeep Pathak, Lina E. Klintberg, David-Dominik Jarausch, Ruben Higler, Sven Hüttner, Tomas Leijtens, Samuel D. Stranks, Henry J. Snaith, Mete Atatüre, Richard T. Phillips, and Richard H. Friend. High photoluminescence efficiency and optically pumped lasing in solution-processed mixed halide

perovskite semiconductors. *The Journal of Physical Chemistry Letters*, 5(8):1421–1426, 04 2014.

[7] Brandon R. Sutherland, Sjoerd Hoogland, Michael M. Adachi, Chris T. O. Wong, and Edward H. Sargent. Conformal organohalide perovskites enable lasing on spherical resonators. *ACS Nano*, 8(10):10947–10952, 10 2014.

[8] Haiming Zhu, Yongping Fu, Fei Meng, Xiaoxi Wu, Zizhou Gong, Qi Ding, Martin V. Gustafsson, M. Tuan Trinh, Song Jin, and X-Y. Zhu. Lead halide perovskite nanowire lasers with low lasing thresholds and high quality factors. *Nat Mater*, 14(6):636–642, 06 2015.

[9] Zhi-Kuang Tan, Reza Saberi Moghaddam, May Ling Lai, Pablo Docampo, Ruben Higler, Felix Deschler, Michael Price, Aditya Sadhanala, Luis M. Pazos, Dan Credgington, Fabian Hanusch, Thomas Bein, Henry J. Snaith, and Richard H. Friend. Bright light-emitting diodes based on organometal halide perovskite. *Nat Nano*, 9(9):687–692, 09 2014.

[10] Arianna Marchioro, Joel Teuscher, Dennis Friedrich, Marinus Kunst, Roel van de Krol, Thomas Moehl, Michael Gratzel, and Jacques-E. Moser. Unravelling the mechanism of photoinduced charge transfer processes in lead iodide perovskite solar cells. *Nat Photon*, 8(3):250–255, 03 2014.

[11] Carlito S. Ponseca, Tom J. Savenije, Mohamed Abdellah, Kaibo Zheng, Arkady Yartsev, Tobjörn Pascher, Tobias Harlang, Pavel Chabera, Tonu Pullerits, Andrey Stepanov, Jean-Pierre Wolf, and Villy Sundström. Organometal halide perovskite solar cell materials rationalized: Ultrafast charge generation, high and microsecond-long balanced mobilities, and slow recombination. *Journal of the American Chemical Society*, 136(14):5189–5192, 04 2014.

[12] Joseph S. Manser and Prashant V. Kamat. Band filling with free charge carriers in organometal halide perovskites. *Nat Photon*, 8(9):737–743, 09 2014.

[13] Guichuan Xing, Nripan Mathews, Shuangyong Sun, Swee Sien Lim, Yeng Ming Lam, Michael Grätzel, Subodh Mhaisalkar, and Tze Chien Sum. Long-range balanced electron- and hole-transport lengths in organic-inorganic $CH_3NH_3PbI_3$. *Science*, 342(6156):344, 10 2013.

[14] Samuel D. Stranks, Giles E. Eperon, Giulia Grancini, Christopher Menelaou, Marcelo J. P. Alcocer, Tomas Leijtens, Laura M. Herz, Annamaria Petrozza, and Henry J. Snaith. Electron-hole diffusion lengths exceeding 1 micrometer in an organometal trihalide perovskite absorber. *Science*, 342(6156):341, 10 2013.

[15] Jue Gong, Mengjin Yang, Xiangchao Ma, Richard D. Schaller, Gang Liu, Lingping Kong, Ye Yang, Matthew C. Beard, Michael Lesslie, Ying Dai, Baibiao Huang, Kai Zhu, and Tao Xu. Electron–rotor interaction in organic–inorganic lead iodide perovskites discovered by isotope effects. *The Journal of Physical Chemistry Letters*, 7(15):2879–2887, 08 2016.

[16] Ye Yang, Yong Yan, Mengjin Yang, Sukgeun Choi, Kai Zhu, Joseph M. Luther, and Matthew C. Beard. Low surface recombination velocity in solution-grown $CH_3NH_3PbBr_3$ perovskite single crystal. *Nature Communications*, 6:7961 EP –, 08 2015.

[17] Artem A. Bakulin, Oleg Selig, Huib J. Bakker, Yves L. A. Rezus, Christian Müller, Tobias Glaser, Robert Lovrincic, Zhenhua Sun, Zhuoying Chen, Aron Walsh, Jarvist M. Frost, and Thomas L. C. Jansen. Real-time observation of organic cation reorientation in methylammonium lead iodide perovskites. *The Journal of Physical Chemistry Letters*, 6(18):3663–3669, 09 2015.

[18] E. Menéndez-Proupin, P. Palacios, P. Wahnón, and J. C. Conesa. Self-consistent relativistic band structure of the $CH_3NH_3PbI_3$ perovskite. *Physical Review B*, 90(4):045207–, 07 2014.

[19] Jarvist M. Frost and Aron Walsh. What is moving in hybrid halide perovskite solar cells? *Accounts of Chemical Research*, 49(3):528–535, 03 2016.

[20] Emilio J. Juarez-Perez, Rafael S. Sanchez, Laura Badia, Germá Garcia-Belmonte, Yong Soo Kang, Ivan Mora-Sero, and Juan Bisquert. Photoinduced giant dielectric constant in lead halide perovskite solar cells. *The Journal of Physical Chemistry Letters*, 5(13):2390–2394, 07 2014.

[21] Amanda J. Neukirch, Wanyi Nie, Jean-Christophe Blancon, Kannatassen Appavoo, Hsinhan Tsai, Matthew Y. Sfeir, Claudine Katan, Laurent Pedesseau, Jacky Even, Jared J. Crochet, Gautam Gupta, Aditya D. Mohite, and Sergei Tretiak. Polaron stabilization by cooperative lattice distortion and cation rotations in hybrid perovskite materials. *Nano Letters*, 16(6):3809–3816, 06 2016.

[22] Haiming Zhu, Kiyoshi Miyata, Yongping Fu, Jue Wang, Prakriti P. Joshi, Daniel Niesner, Kristopher W. Williams, Song Jin, and X. Y. Zhu. Screening in crystalline liquids protects energetic carriers in hybrid perovskites. *Science*, 353(6306):1409, 09 2016.

[23] Arman Mahboubi Soufiani, Fuzhi Huang, Peter Reece, Rui Sheng, Anita Ho-Baillie, and Martin A. Green. Polaronic exciton binding energy in iodide and bromide organic-inorganic lead halide perovskites. *Applied Physics Letters*, 107(23):231902, 2015.

[24] Nakita K. Noel, Antonio Abate, Samuel D. Stranks, Elizabeth S. Parrott, Victor M. Burlakov, Alain Goriely, and Henry J. Snaith. Enhanced photoluminescence and solar cell performance via lewis base passivation of organic–inorganic lead halide perovskites. *ACS Nano*, 8(10):9815–9821, 10 2014.

[25] Ilya A. Shkrob and Timothy W. Marin. Charge trapping in photovoltaically active perovskites and related halogenoplumbate compounds. *The Journal of Physical Chemistry Letters*, 5(7):1066–1071, 04 2014.

[26] Dane W. de Quilettes, Sarah M. Vorpahl, Samuel D. Stranks, Hirokazu Nagaoka, Giles E. Eperon, Mark E. Ziffer, Henry J. Snaith, and David S. Ginger. Impact of microstructure on local carrier lifetime in perovskite solar cells. *Science*, 348(6235):683, 05 2015.

[27] Giulia Grancini, Ajay Ram Srimath Kandada, Jarvist M. Frost, Alex J. Barker, Michele De Bastiani, Marina Gandini, Sergio Marras, Guglielmo Lanzani, Aron Walsh, and Annamaria Petrozza. Role of microstructure in the electron–hole interaction of hybrid lead halide perovskites. *Nat Photon*, 9(10):695–701, 10 2015.

[28] Dong Shi, Valerio Adinolfi, Riccardo Comin, Mingjian Yuan, Erkki Alarousu, Andrei Buin, Yin Chen, Sjoerd Hoogland, Alexander Rothenberger, Khabiboulakh Katsiev, Yaroslav Losovyj, Xin Zhang, Peter A. Dowben, Omar F. Mohammed, Edward H. Sargent, and Osman M. Bakr. Low trap-state density and long carrier diffusion in organolead trihalide perovskite single crystals. *Science*, 347(6221):519, 01 2015.

[29] Makhsud I. Saidaminov, Ahmed L. Abdelhady, Banavoth Murali, Erkki Alarousu, Victor M. Burlakov, Wei Peng, Ibrahim Dursun, Lingfei Wang, Yao He, Giacomo Maculan, Alain Goriely, Tom Wu, Omar F. Mohammed, and Osman M. Bakr. High-quality bulk hybrid perovskite single crystals within minutes by inverse temperature crystallization. *Nature Communications*, 6:7586 EP –, 07 2015.

[30] Martin A. Green, Anita Ho-Baillie, and Henry J. Snaith. The emergence of perovskite solar cells. *Nat Photon*, 8(7):506–514, 07 2014.

[31] Kenichiro Tanaka, Takayuki Takahashi, Takuma Ban, Takashi Kondo, Kazuhito Uchida, and Noboru Miura. Comparative study on the excitons in lead-halide-based perovskite-

type crystals ch3nh3pbbr3 ch3nh3pbi3. *Solid State Communications*, 127(9–10):619–623, 9 2003.

[32] Edoardo Mosconi, Anna Amat, Md. K. Nazeeruddin, Michael Grätzel, and Filippo De Angelis. First-principles modeling of mixed halide organometal perovskites for photovoltaic applications. *The Journal of Physical Chemistry C*, 117(27):13902–13913, 07 2013.

[33] George Sheldrick. Crystal structure refinement with shelxl. *Acta Crystallographica Section C*, 71(1):3–8, 01 2015.

[34] Rebecca L. Milot, Giles E. Eperon, Henry J. Snaith, Michael B. Johnston, and Laura M. Herz. Temperature-dependent charge-carrier dynamics in $CH_3NH_3PbI_3$ perovskite thin films. *Advanced Functional Materials*, 25(39):6218–6227, 2015.

[35] Chan La-o vorakiat, Teddy Salim, Jeannette Kadro, Mai-Thu Khuc, Reinhard Haselsberger, Liang Cheng, Huanxin Xia, Gagik G. Gurzadyan, Haibin Su, Yeng Ming Lam, Rudolph A. Marcus, Maria-Elisabeth Michel-Beyerle, and Elbert E. M. Chia. Elucidating the role of disorder and free-carrier recombination kinetics in $CH_3NH_3PbI_3$ perovskite films. *Nature Communications*, 6:7903 EP –, 07 2015.

[36] Excitonic processes in solids, 1986.

[37] Ye Yang, Mengjin Yang, Zhen Li, Ryan Crisp, Kai Zhu, and Matthew C. Beard. Comparison of recombination dynamics in ch3nh3pbbr3 and ch3nh3pbi3 perovskite films: Influence of exciton binding energy. *The Journal of Physical Chemistry Letters*, 6(23):4688–4692, 12 2015.

[38] Mikaël Kepenekian, Roberto Robles, Claudine Katan, Daniel Sapori, Laurent Pedesseau, and Jacky Even. Rashba and dresselhaus effects in hybrid organic–inorganic perovskites: From basics to devices. *ACS Nano*, 9(12):11557–11567, 12 2015.

[39] Xiuwen Zhang, Qihang Liu, Jun-Wei Luo, Arthur J. Freeman, and Alex Zunger. Hidden spin polarization in inversion-symmetric bulk crystals. *Nat Phys*, 10(5):387–393, 05 2014.

[40] X. Y. Zhu and V. Podzorov. Charge carriers in hybrid organic–inorganic lead halide perovskites might be protected as large polarons. *The Journal of Physical Chemistry Letters*, 6(23):4758–4761, 12 2015.

[41] John P. Perdew, Kieron Burke, and Matthias Ernzerhof. Generalized gradient approximation made simple. *Physical Review Letters*, 77(18):3865–3868, 10 1996.

[42] Qingfeng Dong, Yanjun Fang, Yuchuan Shao, Padhraic Mulligan, Jie Qiu, Lei Cao, and Jinsong Huang. Electron-hole diffusion lengths >175 m in solution-grown $CH_3NH_3PbI_3$ single crystals. *Science*, 347(6225):967, 02 2015.

[43] Aurelien M. A. Leguy, Jarvist Moore Frost, Andrew P. McMahon, Victoria Garcia Sakai, W. Kockelmann, ChunHung Law, Xiaoe Li, Fabrizia Foglia, Aron Walsh, Brian C. O'Regan, Jenny Nelson, João T. Cabral, and Piers R. F. Barnes. The dynamics of methylammonium ions in hybrid organic–inorganic perovskite solar cells. *Nature Communications*, 6:7124, 05 2015.

[44] Yuping He and Giulia Galli. Instability and efficiency of mixed halide perovskites ch3nh3ai3–xclx (a = pb and sn): A first-principles, computational study. *Chemistry of Materials*, 29(2):682–689, 01 2017.

[45] Martin Schlipf and François Gygi. Optimization algorithm for the generation of oncv pseudopotentials. *Computer Physics Communications*, 196:36–44, 11 2015.

[46] Poncé S.; Margine E. R.; Verdi C. V.; Giustino F. Electron-phonon coupling, transport and superconducting properties using maximally localized wannier functions. *arXiv:1604.03525*, 2016.

[47] Jonathan H. Skone, Marco Govoni, and Giulia Galli. Self-consistent hybrid functional for condensed systems. *Physical Review B*, 89(19):195112–, 05 2014.

[48] Jonathan H. Skone, Marco Govoni, and Giulia Galli. Nonempirical range-separated hybrid functionals for solids and molecules. *Physical Review B*, 93(23):235106–, 06 2016.

[49] Nicholas P. Brawand, Márton Vörös, Marco Govoni, and Giulia Galli. Generalization of dielectric-dependent hybrid functionals to finite systems. *Physical Review X*, 6(4):041002–, 10 2016.

CHAPTER 6

SCALABLE LIGAND-MEDIATED TRANSPORT SYNTHESIS OF ORGANIC-INORGANIC HYBRID PEROVSKITE NANOCRYSTALS WITH RESOLVED ELECTRONIC STRUCTURE AND ULTRAFAST DYNAMICS

Colloidal perovskite nanocrystals support bright, narrow photoluminescence tunable over the visible spectrum. However, bandgap tuning of these materials remains limited to laboratory-scale syntheses. In this chapter, we present polar-solvent-free ligand-mediated transport synthesis of high quality organic-inorganic perovskite nanocrystals under ambient conditions with photoluminescence quantum yields up to 97%. Our synthesis employs a ligand-mediated transport mechanism that circumvents the need for exquisite external control (*e.g.,* temperature control, inert-gas protection, dropwise addition of reagents) required by other methods due to extremely fast reaction kinetics. In the ligand-mediated transport mechanism, multiple equilibria cooperatively dictate reaction rates and enable precise control over NC size. These small nanocrystals exhibit high photoluminescence quantum yields due to quantum confinement. Nanosecond transient absorption spectroscopy experiments reveal a fluence-independent PL decay originating from exciton recombination. Two-dimensional electronic spectroscopy resolves multiple spectral features reflecting the electronic structure of the nanocrystals. The resolved features exhibit size-dependent spectral positions, further indicating the synthesized nanocrystals are quantum-confined.

The research described in this Chapter has been published in: L. Wang, N.E. Williams, E.W. Malachosky, J.P. Otto, D. Hayes, R.E. Wood, P. Guyot-Sionnest, and G.S. Engel. Scalable Ligand-Mediated Transport Synthesis of Organic-Inorganic Hybrid Perovskite Nanocrystals with Resolved Electronic Structure and Ultrafast Dynamics. *ACS Nano*, DOI: 10.1021/acsnano.6b07574.

6.1 Background information about perovskite nanocrystals

Organic-inorganic lead-halide perovskite materials have recently attracted extensive research attention due to their extraordinary photophysical properties and performance in optoelectronic applications. Previous studies have demonstrated that perovskite microcrystals and bulk single crystals exhibit characteristics including large absorption coefficients [1], small exciton binding energies [2], efficient photogeneration of free carriers [3, 4], high charge carrier mobility [5, 6], and bimolecular charge recombination dynamics [7, 8]. Solar cells using organolead halide perovskite thin films as their active layer have achieved certified power conversion efficiencies up to 23% [9–13]. Perovskites have also shown promise for applications in low-threshold optically-pumped lasers [14–16] and light-emitting diodes (LEDs) [17]. In perovskite microcrystals and bulk single crystals, excitons spontaneously dissociate into free carriers due to the weak binding energy, which is ideal for solar cell devices. However, nonradiative recombination of the carriers limits the light-emitting performance of perovskites [18]. Increasing the exciton binding energy through quantum confinement has recently been explored to overcome the relatively weak photoluminescence (PL) of perovskite microcrystals and bulk single crystals by fabricating nanostructured materials [19–23]. Perovskite nanocrystals (NCs), both organic-inorganic (typically incorporating methylammonium, MA^+) and purely inorganic (typically incorporating cesium ions), demonstrate high defect-tolerance, low density of detrimental mid-gap trap states, and high photoluminescence quantum yield (PLQY) at room temperature without additional surface passivation [19, 21, 24–26]. The narrow PL of these perovskite NCs is tunable over the entire visible range (from 410 to 700 nm) by adjusting the size and halide composition [20, 22, 27, 28], making these materials applicable to lasers [19, 28], optical sensing [29], and color-tuning displays [21].

Although perovskite NCs exhibit remarkable properties, bandgap tuning of these NCs is usually realized via composition tuning subsequent to synthesis of pure perovskite NCs by hot-injection [19, 30] or ligand-assisted reprecipitation (LARP) [18, 21, 24, 25, 31] methods.

These methods are not readily adaptable to industrial scale preparations.These syntheses demand delicate external control over reaction conditions due to the extremely fast kinetics of NC formation and require the usage of polar solvents (e.g. DMF), which are detrimental to the long-term colloidal stability and structural integrity of the NCs [26, 27, 32]. Moreover, mixed-halide or iodide-based perovskite NCs are synthesized either under inert atmosphere [21, 26] or via indirect postsynthetic anion exchange [20, 22]. The postsynthetic anion exchange requires pure pre-synthesized NCs [20, 22] (usually bromide based) and introduces an extra synthetic step.

Here, we present an atmospheric, room-temperature, ligand-mediated transport method in non-polar solvent to prepare perovskite NCs with bright and spectrally narrow emission. We focus on the synthesis of organic-inorganic perovskite NCs ($MAPbX_3$, X = Br, I, mixed halide). The ligand-mediated transport synthesis employs non-polar solvents (hexane or toluene) containing a trace capping ligand (octylamine, protonated by oleic acid), which are added to the mixed solid precursors (PbX_2 and MAX, X = Br, I, or mixed halide). Then, through vigorous stirring, the colloidal NCs are formed as the ligands solvate the lead salt and bring it into the solution phase. This strategy allows the direct synthesis of mixed-halide and iodide-based perovskite NCs without inert atmosphere protection and yields colloidal NC solutions at high concentrations. The resultant NCs demonstrate good colloidal stability even at high sample concentration, enabling spectroscopic investigations of their ultrafast dynamics by techniques including two-dimensional electronic spectroscopy (2DES), which requires 10^2 - 10^3 times more concentrated solutions (about 0.2 OD in a 200 μm path length) than fluorescence measurements. Our broadband femtosecond 2DES experiments on MAPbI3 NCs resolve multiple spectral features that shift with NC sizes reflecting the electronic structure of these NCs, as well as ultrafast dynamics (including relaxation and quantum-beating signals) after the initial excitation. Nanosecond transient absorption (TA) spectroscopy experiments reveal a PL decay that is independent of radiation fluence, indicating that the PL originates from exciton recombination.

6.2 Ligand-mediated transport mechanism of $MAPbX_3$ nanocrystal synthesis

Besides the practical advantages of performing NC synthesis at room temperature and under ambient conditions, our ligand-mediated transport strategy offers better NC size control compared to the hot-injection and LARP methods, due to slower nucleation and crystal growth. In our synthesis, multiple equilibria cooperatively control NC nucleation kinetics and growth rates, circumventing the high temperature kinetics of hot injection and the prompt solubility changes in LARP that result in rapid product formation [24, 25]. The reaction mechanism of ligand-mediated transport is illustrated in Figure 6.1, and compared with those of hot injection and LARP in the Figure 6.2. In our synthesis, the mechanism first involves the dissolution equilibria of the two precursors. Because non-polar solvents are used, these equilibria strongly favor the solid phases. Trace ligands in the non-polar solvents transport Pb into the solution phase (*Step 1*) through coordination, initiating nucleation and subsequent nanocrystal growth (*Step 2*). The formation of these NCs in return drives the dissolution equilibria to the solution phase, ensuring further NC growth. Because the same ligands cap the NCs as aid dissolution of the lead, the kinetics become, to some degree, self-limiting. Thus, the crystal growth can be finely controlled by reaction time and quenched by removing the solid precursors. These equilibria cooperatively dictate reaction rates and enable precise control over NC size, making the size distribution highly reproducible.

In addition to the benefits mentioned above, the ligand-mediated transport method improves colloidal stability by allowing unreacted solid precursors to be easily removed via filtration or centrifugation. Recent 2D-NMR studies have suggested that capping ligands dynamically stabilize perovskite NCs synthesized via hot injection or LARP, exhibiting fast exchange between bound and free states [33]. Thus, any unreacted MA^+ would replace the capping ligands, causing further, undesirable aggregation. In our ligand-mediated transport synthesis, removal of solid precursors and exclusive use of non-polar solvents significantly

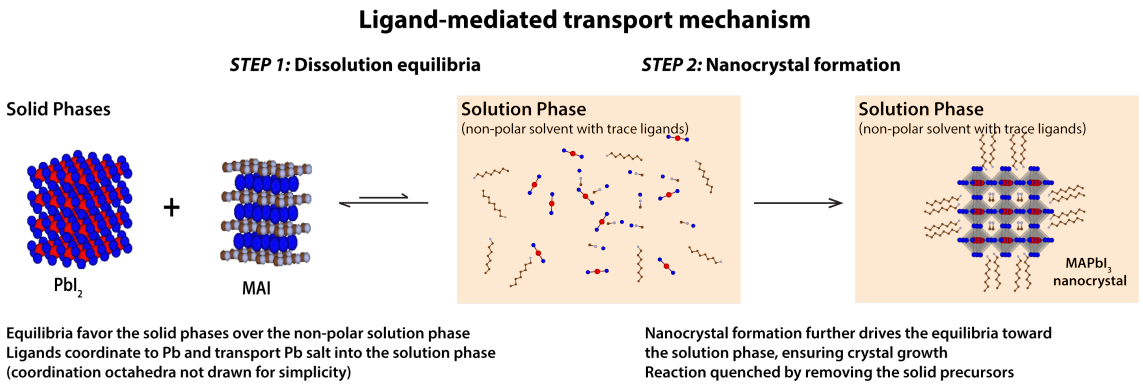

Figure 6.1: Illustrative reaction mechanism of the ligand-mediated transport strategy (using the synthesis of $MAPbI_3$ NCs as an example). Red, blue, brown, and white spheres represent Pb, I, C, and N atoms, respectively. The first mechanistic step (*Step 1*) involves the dissolution equilibria of the two precursors (PbI_2 and MAI) between the solid and solution phases. The equilibria strongly favor the solid phases over the non-polar solution phase. However, the trace ligands help dissolve the PbI_2 by coordinating to the Pb center and transport the Pb salt into solution phase to initiate the reaction. (Coordination octahedra are not drawn in the figure for simplicity.) *Step 2* presents the nanocrystal formation from the dissolved precursors and ligands in the solution phase. The NC formation further drives the dissolution equilibria toward the solution phase, ensuring NC growth. The reactions can then be quenched by removal of the solid precursors via centrifugation or filtration.

suppress the presence of excess MA^+ in solution and therefore the replacement of capping ligands with MA^+ , hence enhancing the colloidal stability of the resulting NCs.

6.3 Synthetic details of $MAPbX_3$ nanocrystals

6.3.1 Synthesis of CH_3NH_3Br

Methylammonium bromide was synthesized by the reaction between 40 wt.% methylamine (CH_3NH_2) in methanol (TCI America) and 48 wt.% hydrobromic acid (HBr) in water (Sigma-Aldrich). An equimolar amount of HBr was added dropwise to the CH_3NH_2 solution under ice bath and stirred for 2 h. The solvent was removed on a rotovap. The resulting solid was further recrystallized in ethanol to yield snow-white CH_3NH_3Br crystals. CH_3NH_3Br crystals were dried under vacuum to remove residual ethanol.

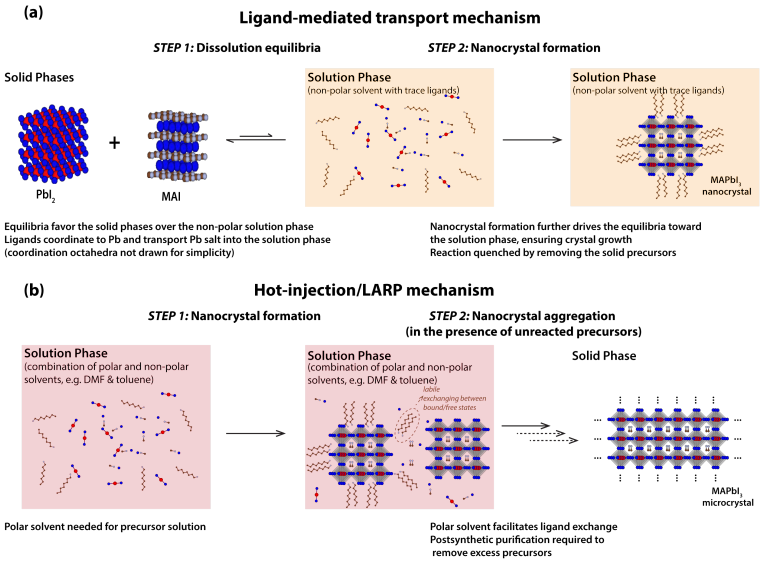

Figure 6.2: Comparison between reaction mechanisms of the solid-extraction strategy versus other strategies (using the synthesis of $MAPbI_3$ nanocrystals as an example). (a) Illustrative reaction mechanism of the solid-extraction strategy (same as shown in Figure 6.1). Red, blue, brown, and white spheres represent Pb, I, C, and N atoms, respectively. The first mechanistic step (*Step 1*) involves the dissolution equilibria of the two precursors (PbI_2 and MAI) between the solid and solution phases. The equilibria strongly favor the solid phases over the non-polar solution phase. However, the trace ligands help dissolve the PbI_2 by coordinating to the Pb center and transport the Pb salt into the solution phase to initiate the reaction. (Coordination octahedra are not drawn in the figure for simplicity.) *Step 2* presents the nanocrystal formation from the dissolved precursors and ligands in the solution phase. The NC formation further drives the dissolution equilibria toward the solution phase, ensuring NC growth. The reactions can then be quenched by removal of the solid precursors via centrifugation or filtration. (b) Illustrative reaction mechanism of the other strategies (hot-injection and LARP). *Step 1*: In hot-injection or LARP method, precursors are usually prepared in polar solvents (such as DMF) and the reaction starts in the solution phase (combination of both polar and non-polar solvents). Size control is more difficult in these methods due to the extremely fast reaction dynamics; in LARP, crystal growth is driven by the prompt solubility change induced by solvent mixing, while in hot injection, the formation rate is determined by the underlying ionic metathesis reaction at high temperature. *Step 2*: In the presence of unreacted precursors in the solution, the nanocrystals will slowly aggregate to form microcrystals and eventually precipitate from the solution phase. For colloidal perovskite nanocrystals, the capping ligands exchange between bound and free states on the nanocrystal surfaces, dynamically stabilizing the nanocrystals. The remaining MA^+, if any, will replace the capping ligand and cause nanocrystal aggregation. Polar solvents will quickly desorb the capping ligands and further facilitate the exchange reaction. Hence, postsynthetic purification removing excess precursors is required to improve colloidal stability.

6.3.2 Synthesis of CH_3NH_3I

Methylammonium iodide was synthesized by the reaction between 40 wt.% methylamine (CH_3NH_2) in methanol (TCI America) and 57 wt.% hydriodic acid (HI) in water (Sigma-Aldrich). An equimolar amount of HI was added dropwise to the CH_3NH_2 solution under ice bath and stirred for 2 h. The solvent was removed on a rotovap. The resulting solid was further recrystallized in ethanol to yield snow-white CH_3NH_3I crystals. CH_3NH_3I crystals were dried under vacuum to remove residual ethanol.

6.3.3 Synthesis of $MAPbBr_3$ nanocrystals

17.9 mg (0.16 mmol) CH_3NH_3Br and 73.4 mg (0.20 mmol) $PbBr_2$ (98%, Sigma-Aldrich) were added into a 4 mL scintillation vial. 1 mL toluene, 20 μL octylamine (99%, Sigma-Aldrich), and 40 μL oleic acid (technical grade, 90%, Sigma-Aldrich) were added to the solid precursors. The resulting mixture was stirred vigorously under ambient conditions for 1 h, followed by centrifugation for 5 min at 6000 rpm to remove the remaining solid precursors. A solution of $MAPbBr_3$ nanocrystals with an average size of 3.0 nm (PLQY 92%) was obtained. Similarly, the same amount of solid precursors in 1 mL toluene with 5 μL octylamine and 10μL oleic acid reacting for 3 h at ambient condition yielded $MAPbBr_3$ nanocrystals with an average size of 5.0 nm (PLQY 70%).The as-synthesized nanocrystal solutions were stored at room temperature without further purification.

6.3.4 Synthesis of $MAPb(I/Br)_3$ nanocrystals

17.9 mg (0.16 mmol) CH_3NH_3Br, 36.7 mg (0.10 mmol) $PbBr_2$, and 46.0 mg (0.10 mmol) PbI_2 (99%, Sigma-Aldrich) were added into a 4 mL scintillation vial. 1 mL solvent (1:1 v/v toluene/hexane), 20 μL octylamine, and 40 μL oleic acid were added to the solid precursors. The resulting mixture was stirred vigorously under ambient conditions for 45 min, followed by centrifugation for 5 min at 6000 rpm to remove the remaining solid precursors. A solution

of $MAPb(Br/I)_3$ nanocrystals with an average size of 3.6 nm (PL centered at 550 nm with FWHM of 29 nm) was obtained. Similarly, 17.9 mg (0.16 mmol) CH_3NH_3Brand 92.0 mg (0.20 mmol) PbI_2 in 1 mL solvent (1:1 v/v toluene/hexane), 20 μL octylamine, and 40 μL oleic acid reacting for 45 min at ambient condition yielded $MAPb(Br/I)_3$ with an average size of 2.6 nm (PL centered at 580 nm with FWHM of 28 min). The as-synthesized nanocrystal solutions were stored at room temperature without further purification. The presence of both Br and I in the mixed-halide perovskite nanocrystals has been confirmed by energy-dispersive X-ray spectroscopy (EDX) (Figure 6.3). The nanocrystals with PL centered at 580 nm contain significantly higher composition of I compared to the nanocrystals with PL centered at 550 nm.

6.3.5 Synthesis of $MAPbI_3$ nanocrystals

19.0 mg (0.12 mmol) CH_3NH_3I and 69.0 mg (0.15 mmol) PbI_2 were added into a 4 mL scintillation vial. 1 mL hexane, 20 μL octylamine, and 40 μL oleic acid were added to the solid precursors. The resulting mixture was stirred vigorously under ambient conditions for 1 h, followed by centrifugation for 5 min at 6000 rpm to remove the remaining solid precursors. A solution of $MAPbI_3$ nanocrystals with an average size of 2.6 nm (PLQY 97%) was obtained. Similarly, 25.4 mg (0.16 mmol) CH_3NH_3I and 92.0 mg (0.20 mmol) PbI_2 in 1 mL hexane, 20 μL octylamine, and 40 μL oleic acid reacting for 3 h at ambient condition yielded $MAPbI_3$ with an average size of 5.0 nm (PLQY 52%). The as-synthesized nanocrystal solutions were stored at room temperature without further purification.

6.4 Characterization of $MAPbX_3$ nanocrystals

6.4.1 Linear absoprtion and photoluminescence measurements

The linear absorption and PL spectra of ligand-mediated transport synthesized NCs are shown in Figure 6.4.a. These NCs exhibit spectrally narrow (FWHM of 12 - 50 nm) and

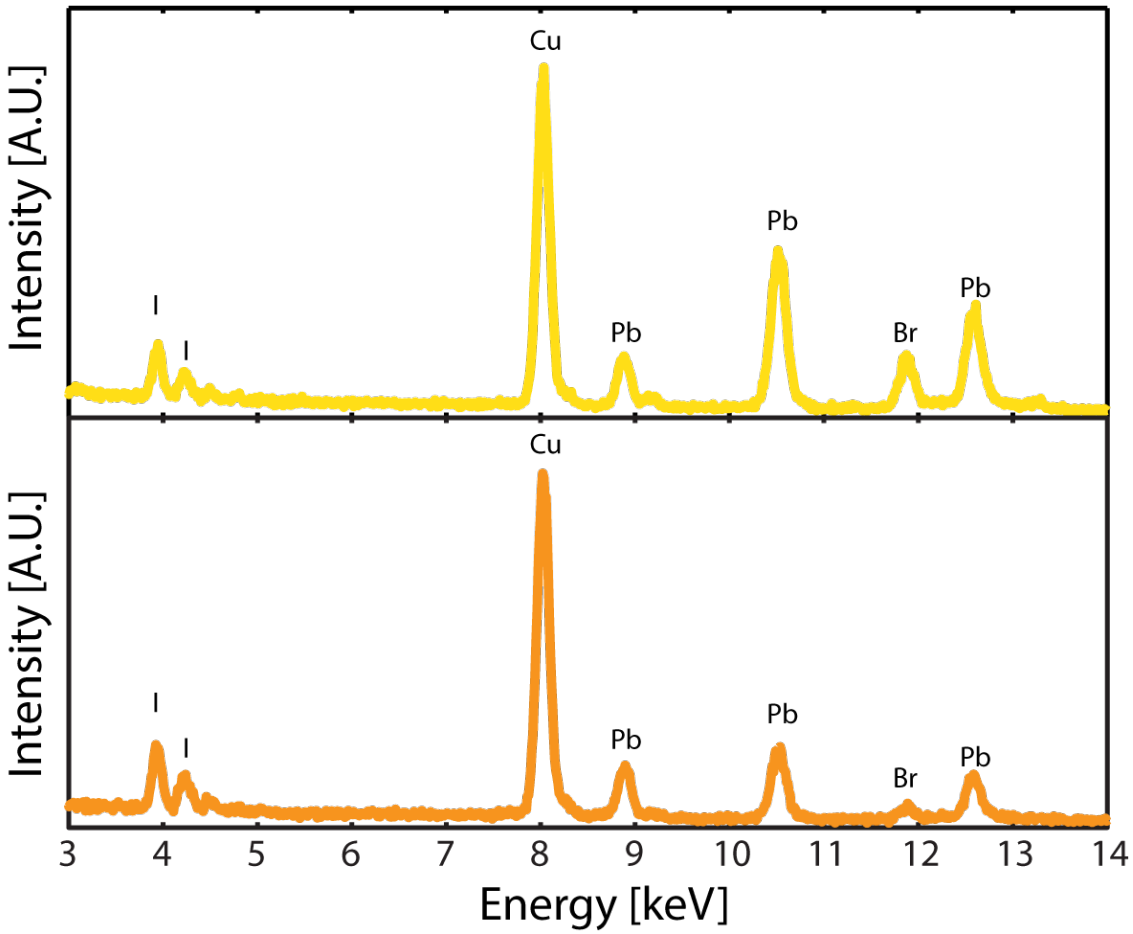

Figure 6.3: EDX spectra of $MAPb(Br/I)_3$ nanocrystals. Upper: Mixed-halide nanocrystals with PL centered at 550 nm. Lower: Mixed-halide nanocrystals with PL centered at 580 nm.

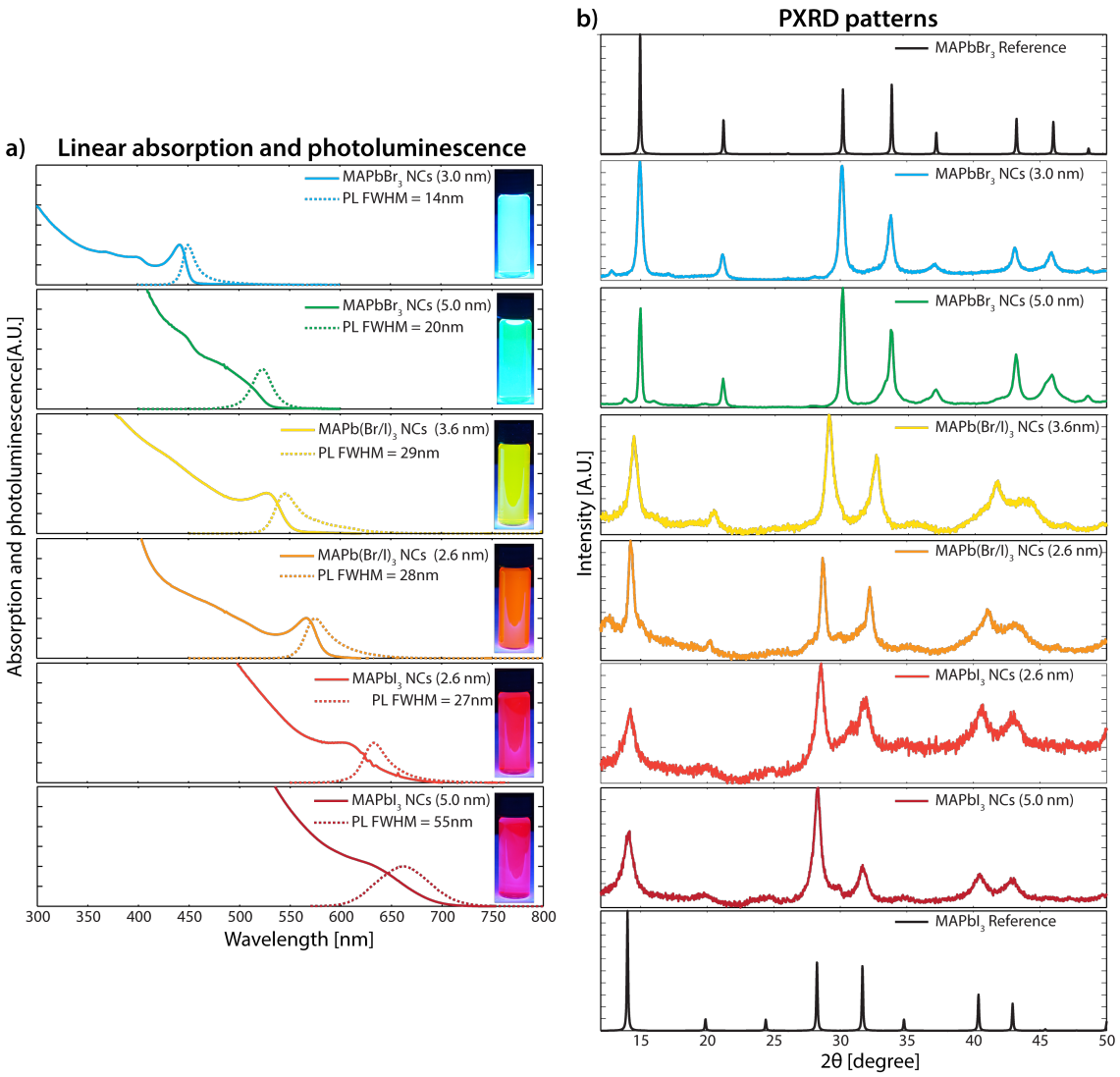

Figure 6.4: Characterization of the as-synthesized organic-inorganic perovskite NCs. (a) Linear absorption and photoluminescence spectra. (b) PXRD patterns. The top and bottom panels are reference patterns simulated from the single-crystal structure of $MAPbBr_3$ and $MAPbI_3$, respectively.

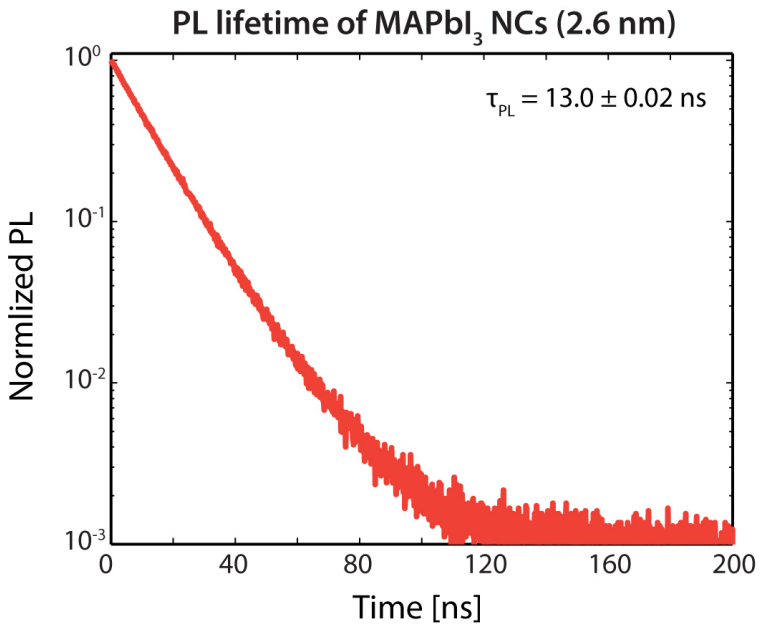

Figure 6.5: TCSPC measurement of $CH_3NH_3PbI_3$nanocrystals (2.6 nm) yield a PL lifetime of 13 ns.

remarkably bright (QY up to 97% measured with an integrating sphere) PL with tunability over the entire visible spectrum. We attribute the bright PL to increased exciton binding resulting from quantum confinement.

The steady-state PL spectra of the perovskite nanocrystals were measured by a Horiba Fluorolog-3 spectrofluorometer. The PLQYs were measured by the same spectro-fluorometer with a calibrated integrating sphere (Quanta-phi, Horiba). The PL lifetimes were measured by a time-correlated single photon counting (TCSPC) fluorescence lifetime spectrometer (ISS chronosBH), with the PL lifetime measurement of $MAPbI_3$ NCs (2.6 nm) shown in Fig. 6.5.

6.4.2 Powder X-ray diffraction (PXRD) measurements

Powder X-ray diffraction data were measured at 293 K on a Bruker D8 Discover GADDS using a Cu-α source (40 kV, 40 mA) with a Vantec-2000 two-dimensional detector. The as-synthesized perovskite nanocrystals (with no postsynthetic purification) were drop-casted on glassed slides and subjected to PXRD measurements.

The powder X-ray diffraction (PXRD) patterns demonstrate the high crystallinity and

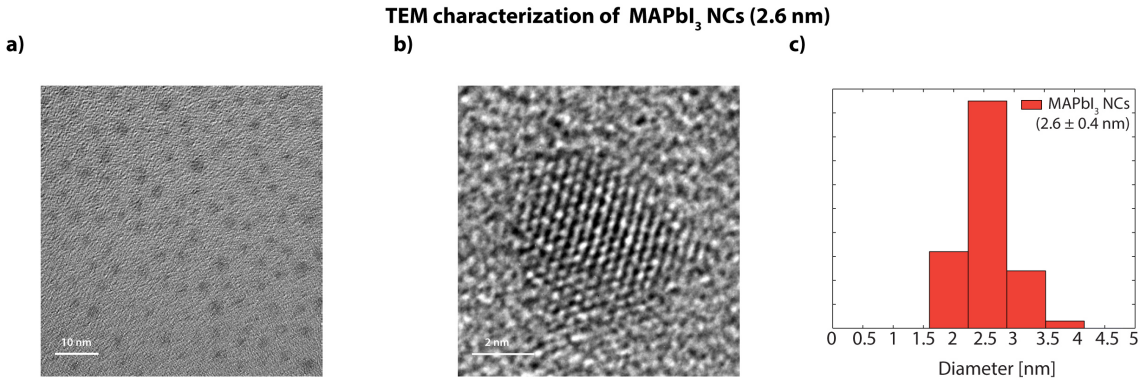

Figure 6.6: TEM characterization on $MAPbI_3$ NCs (average size 2.6 nm). (a) TEM image of the $MAPbI_3$ NCs. (b) Magnified TEM image confirms crystallinity of these NCs. (c) Size distribution of the $MAPbI_3$ NCs shows an average size of 2.6 nm.

phase purity of these NCs (Figure 6.4.b). The PXRD pattern of the $MAPbBr_3$ NCs matches their reference pattern (top panel in Figure 6.4.b), which is simulated from the bulk, cubic single-crystal structure at room temperature (a = 5.9334(5) Å, space group *Pm-3m*). The PXRD pattern of $MAPbI_3$ matches their simulated spectra (bottom panel in Figure 6.4.b) as well, but the simulated pattern is obtained from the bulk, pseudo-cubic single-crystal structure at high temperature (400 K, a = 6.3115(2) Å, c = 6.3161(2) Å, space group *P4mm*), as opposed to the room-temperature tetragonal phase (a = 8.8922(1) Å, c = 12.635(3) Å, space group *I4/m*). As shown in Figure 6.4, the PXRD pattern shifts continuously and deviates incrementally from the cubic phase toward the pseudo-cubic phase with the composition change from Br^- to I^-, due to the larger radius of I^- versus Br^-.

6.4.3 Transmission electron microscopy of $MAPbX_3$ nanocrystals

The size distributions of these NCs were characterized by high-resolution TEM. TEM images were obtained by a FEI Tecnai F30 transmission electron microscope operating at 300 kV. The as-synthesized nanocrystals were further diluted in hexane. A few drops of the resulting solution were drop-casted onto a Formvar-coated lacy carbon grid, and further dried in air for the measurements.

Figure 6.6.a shows the TEM images of $MAPbI_3$ nanocrystals with PL centered at 635 nm

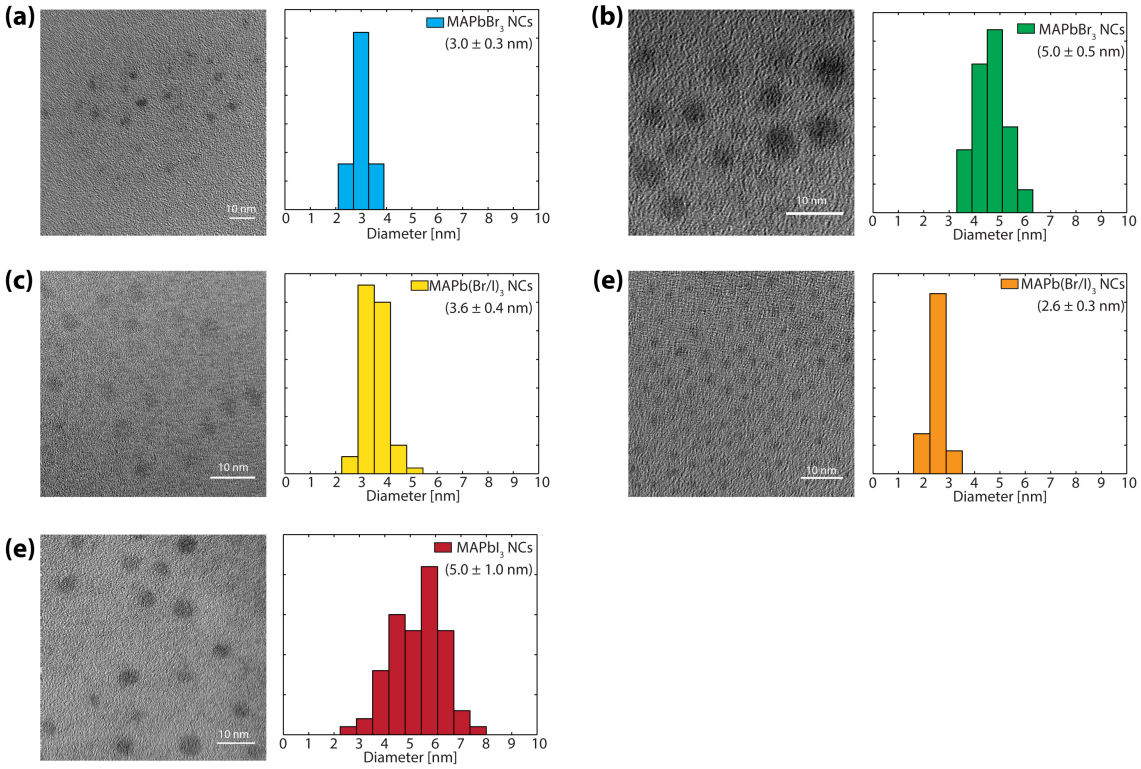

Figure 6.7: TEM images and size distributions of the as-synthesized perovskite nanocrystals. Color-coding is consistent with the color-coding used in the linear absorption and PL spectra (as shown in Figure 6.4).

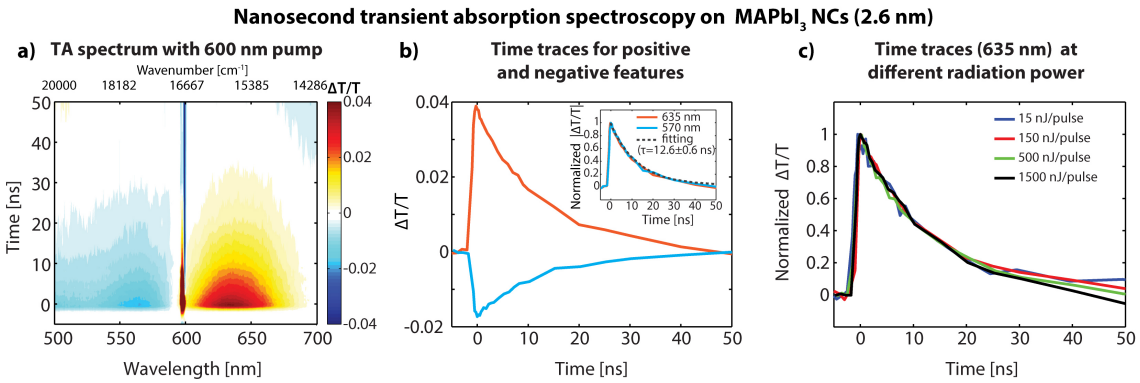

Figure 6.8: Nanosecond TA spectroscopy on $MAPbI_3$ NCs (average size 2.6 nm). (a) TA spectrum of $MAPbI_3$ (2.6 nm). (b) Time traces extracted from the negative feature (570 nm) and the positive feature (635 nm). Absolute-valued normalized traces are shown in the inset and demonstrate the same decay dynamics for both features. (c) Normalized time traces of the positive feature under varied radiation fluences reveal power-independent decay dynamics.

and an average size of 2.6 ± 0.4 nm. The magnified TEM image demonstrates well-defined lattice patterns, and further confirms the high crystallinity of these samples. The images and size distributions of other perovskite NCs are attached in Figure 6.7.

6.5 Nanosecond transient absorption spectroscopy on $MAPbI_3$ nanocrystals

We investigated the photophysical dynamics of our perovskite NCs using nanosecond TA and broadband femtosecond 2DES. Transient absorption spectroscopy was performed on a home-built apparatus with a narrowband pump (Ekspla Pl2210 Nd:YAG and OPO with a pulse duration of 50 ps, centered at 600 nm) and a broadband super continuum fiber laser probe (Leukos STM with a pulse duration of 700 ps, 500 - 700 nm). Time delays were achieved using a delay generator (SRS DG535) externally synchronized to a 1 kHz master clock from the pump laser. The signal was spectrally resolved via a spectrometer (Acton Research Corporation Spectra Pro 2150i) and recorded with a line scan camera (Teledyne Dalsa Spyder3 1k) at 1 kHz.

Nanosecond TA results from the $MAPbI_3$ NCs (2.6 nm) are shown in Figure 6.8. Two

features are observed in the TA spectrum (Figure 6.8.a, plotted in transmitted light ΔT): a negative feature due to excited-state absorption and a positive feature corresponding to stimulated emission from the PL state. The time traces of these features (extracted at 570 nm and 635 nm, respectively) show exactly the same decay dynamics (Figure 6.8.b), suggesting that both features arise from the same PL state. Single exponential fitting of the decay shows a lifetime of 12.6 ± 0.6 ns, consistent with the PL lifetime obtained from time-correlated single photon counting (TCSPC) measurement (Figure 6.5). The decay of the PL state exhibits no radiation fluence dependence (Figure 6.8.c), indicating that the PL is due to the radiative recombination of excitons. In contrast, the dim PL of the bulk perovskites is power-dependent and caused by charge-carrier recombination [8]. The calculated Bohr radius for an exciton in $MAPbI_3$ is 2.8 nm (5.6 nm in diameter) [34], larger than the size of measured $MAPbI_3$ NCs. Therefore, the observed radiation fluence-independent PL (excitonic in nature) is most likely due to the increased binding energy generated by quantum confinement of the exciton within the NC.

6.6 Femtosecond two-dimensional electronic spectroscopy on $MAPbI_3$ nanocrystals

The nanosecond TA measurements can only capture the dynamics of the PL state. Better temporal resolution is required to investigate other phenomena after initial photoexcitation. We therefore performed femtosecond 2DES measurements on these NCs. 2DES can be viewed as simultaneously performing multiple spectrally-resolved TA measurements with different excitation wavelengths in a single experiment. Displaying signals as two-dimensional frequency-frequency correlation maps as a function of time delay (T), 2DES can reveal couplings between different electronic states, ultrafast coherent dynamics as well as detailed energy transfer pathways.

In a 2D spectrum, the horizontal axis (excitation frequency) indicates the energy ab-

sorbed by the sample, while the vertical axis (detection frequency) indicates the energy emitted (or absorbed) by the sample after a certain waiting time (T). The two-dimensional representation permits improved resolution of the underlying electronic structure. For example, ground-state bleach signals will usually stay stationary, while the stimulated-emission features will shift downward and appear as lower-diagonal crosspeaks as energy transfer occurs. This separation resolves different features that would otherwise overlap spectrally in the TA measurements.

2D electronic spectra were measured with a home-built phase-stabilized four-wave described in Chapter 2 Section 2.1.3. The output from a regenerative amplifier was then directed to a tube filled with argon gas (length: 2 m, pressure: 15 psi) to generate broadband white light. A cold mirror was used to filter the white light, yielding a spectrum with FWHM from 550 nm to 680 nm. Multiphoton intrapulse interference phase scan method (MIIPS) and a spatial light modulator (Biophotonic Solutions) were used to compress the pulses to 12 fs at the sample position. Three ultrashort laser pulses interacted with the sample and generated a third-order signal in the phase-matched direction. The signal was heterodyne-detected with a local oscillator pulse and recorded on a CCD (Andor Newton) thermoelectrically cooled to -50 °C. The time delay between the first two pulses is coherence time (τ). The time delay between pulse 2 and pulse 3 is referred as waiting time (T), similar to the time delay in a typical TA measurement. The time delay between pulse 3 and the third-order signal is rephasing time (t). Fourier transforms over both coherence time (τ) and rephasing time (t) domains yield two-dimensional electronic spectra in the frequency-frequency domain. In the 2DES measurements on $MAPbI_3$ nanocrystals, the coherence time was scanned from -90 to 90 fs with a step-size of 1.5 fs. Two sets of waiting time were scanned to capture the ultrafast dynamics, one from -20 to 1000 fs with a step size of 10 fs and the other from -20 to 200 fs with a step size of 2 fs. All 2DES measurements were conducted at room temperature. The perovskite NCs are measured with a concentration about 0.2 OD in 200 μm path length and are stable for at least about two weeks experimental time under

illumination.

The 2D spectra at T=1000 fs of $MAPbI_3$ NCs with average sizes of 2.6 and 5.0 nm are shown respectively in Fig 6.9. Three resolved spectral features are observed in the 2D spectra of $MAPbI_3$ NCs with both sizes. The spectral position of the lowest energy feature within each spectrum is consistent with the corresponding PL state. Horizontal slices from each 2D spectrum are shown in Fig. 6.9.b. The excitation energies of these spectral features shifts with NC size, indicating that the probed NCs are quantum-confined and these three spectral features reflect the inherent electronic structures of the NCs instead of vibronic progressions [35].

We have shown a series of 2D spectra of $MAPbI_3$ NCs (2.6 nm) at different waiting times (10, 30, 50, 100, 500 and 1000 fs, respectively), the time traces extracted from three lower diagonal crosspeaks exhibiting sub-50 fs relaxation dynamics, and quantum-beating signals observed from the upper diagonal excited state absorption features in Fig. 6.10.

At T = 10 fs, the elongated lineshapes of the main diagonal features show that the system maintains memory of its initial excitation frequency on the timescale of the pulse duration (12 fs). Such elongated lineshapes at early waiting times may arise from probing a system that has either a complex electronic structure or an inhomogeneous distribution. To differentiate and determine the origin of the features, we examine the longer waiting time spectra. As the waiting time evolves, the elongated feature evolves into three features (marked as labels 1-3 in Fig. 6.10). The spectral position of feature 3 is consistent with the PL state. The stimulated emission of features 1 and 2 clearly moves down as energy is transferred, resulting in three crosspeaks (1-2, 1-3, and 2-3) on the 2D spectra. After T = 100 fs, the 2D spectra remain almost unchanged. The growth of the lower diagonal crosspeaks indicates clearly that these features all exist on the same NC. Thus, this crosspeak pattern demonstrates that all the features shown on the main diagonal of the 2D spectrum at T = 10 fs are due to the electronic structure of the NCs rather than an inhomogeneous distribution.

These resolved features demonstrate NC size-dependent spectral shift, indicating that the

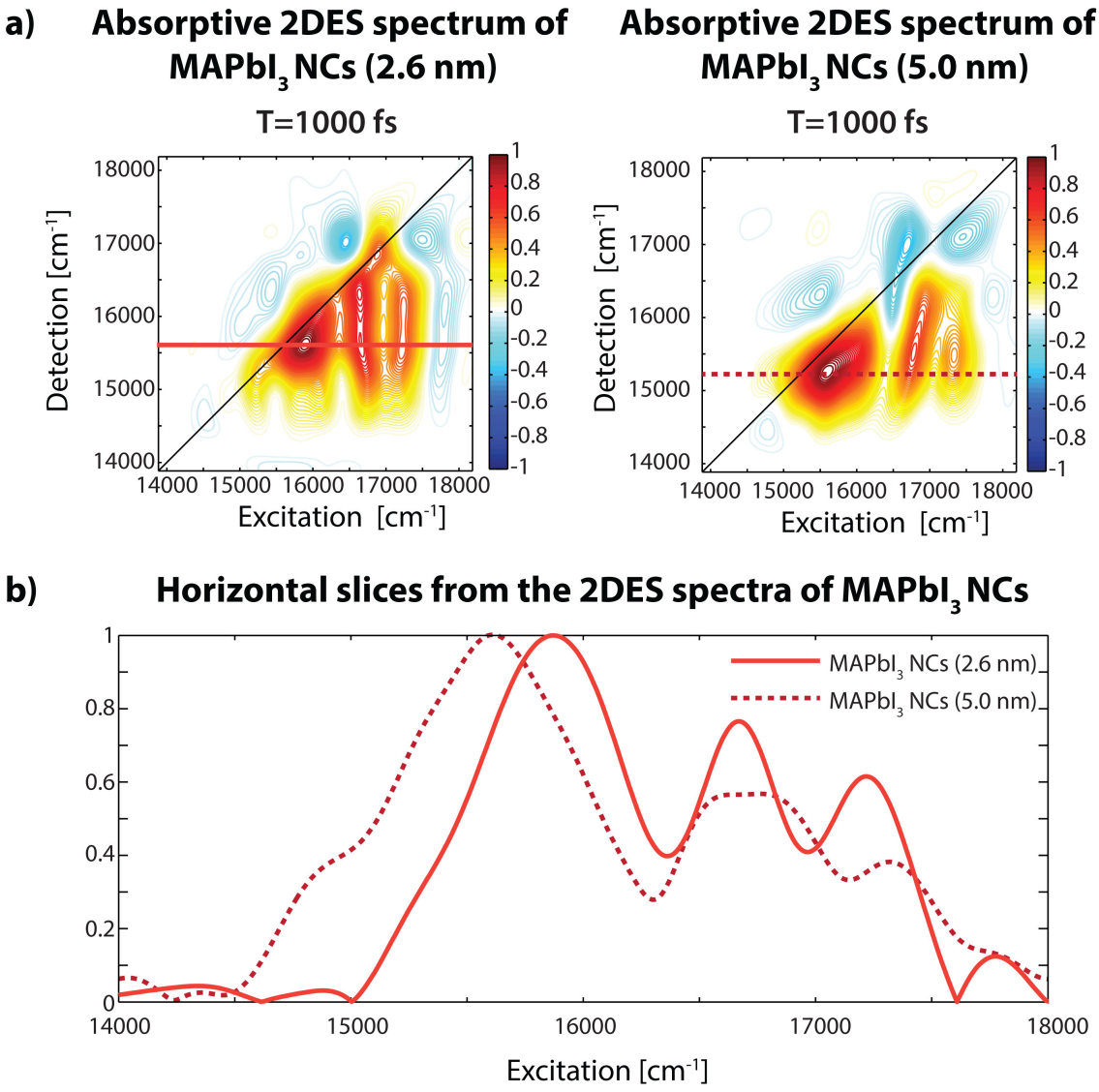

Figure 6.9: 2DES spectra of $MAPbI_3$ NCs with different sizes demonstrate electronic nature of the probed states. (a) Left: Absorptive 2DES spectrum of $MAPbI_3$ NCs (2.6 nm) at T = 1000 fs. Right: Absorptive 2DES spectrum of $MAPbI_3$ NCs (5.0 nm) at T = 1000 fs. (b) Horizontal slices from the 2DES spectra of $MAPbI_3$ NCs shown in panel (a). Both slices show three spectral features. The spacing between these spectral features shift with NC sizes, indicating that the probed NCs are quantum-confined and the three spectral features reflect the electronic structure of the NCs.

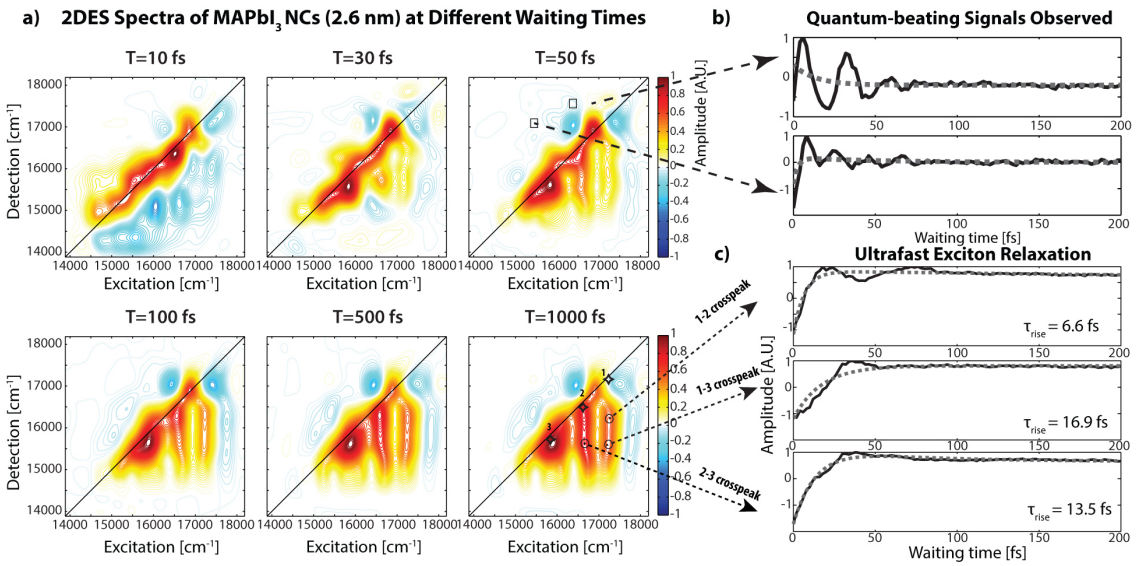

Figure 6.10: Femtosecond 2D electronic spectroscopy on $MAPbI_3$ NCs (2.6 nm). (a) 2D spectra of $MAPbI_3$ at different waiting times. (b) Upper diagonal crosspeaks show quantum-beating signals. (c) Lower diagonal crosspeaks reveal sub-50 fs relaxation.

NCs are quantum-confined and the spectral features reflect the inherent electronic structure of the NCs. However, due to the lack of the electronic structure calculations on the $MAPbI_3$ NCs, it is challenging to assign these observed spectral features to certain electronic states or transitions.

Time traces from the three lower diagonal cross peaks are shown in Fig. 6.10.c. The growth of these crosspeak indicates ultrafast energy transfer dynamics. Exponential fits of the time traces from the three crosspeaks yield relaxation time constants on the order of ten femtoseconds.

Time traces from the upper diagonal regions exhibit quantum-beating signals. These oscillatory signals extracted from different spectral regions of the 2D spectrum also yield different beating frequencies. These oscillatory signals completely dephase after 100 fs and show up predominantly in the upper diagonal spectral region rather than the lower diagonal crosspeaks. At the lower right half of the 2DES spectrum, the coherent dynamics overlaps with population relaxation (incoherent dynamics). The coherences, if originating from the excited states, may be smeared/diminished by the ultrafast energy transfer and limited by

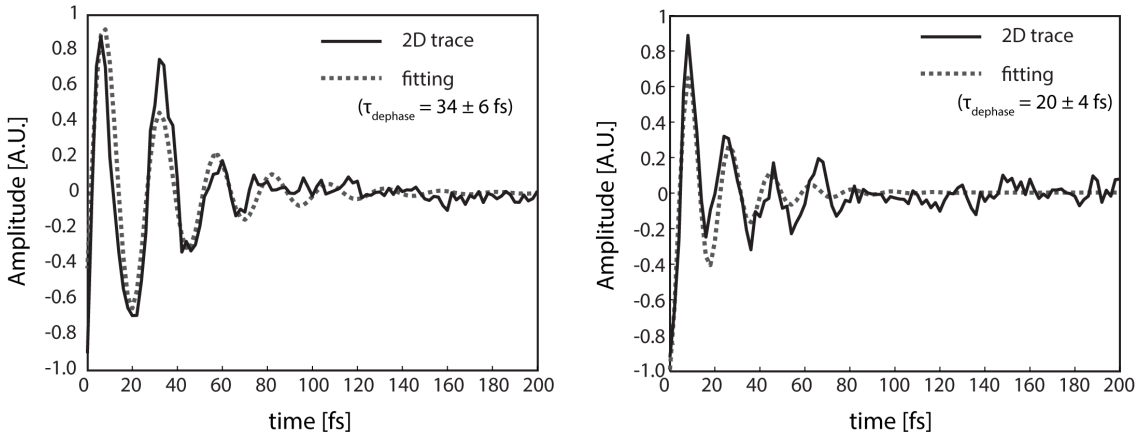

Figure 6.11: Dephasing times fit to observed oscillatory signals shown in Figure 6.8. The signals were fit to an exponential decay envelope and a single sinusoidal oscillation with arbitrary phase.

the excited state lifetimes. This overlap effect might explain why the quantum-beating signals are not significant in the lower diagonal features.

Due to the ultrafast dephasing of the observed coherences, as shown in Fig 6.11, the ultrafast energy transfer process and spectral overlap at room temperature, it is impossible to definitively assign the exact nature of these coherences (purely electronic or vibronic) with our current experiment. Further work will be required to provide full assignments. We believe that the analysis on the exact physical origin of the observed quantum-beating signals requires further investigation such as low temperature resolved 2DES, in which spectral features could be better resolved and coherences should last longer. The low temperature resolved 2DES could provide a detailed beating map analysis on the prolonged coherences and dissecting signals from electronic coupling and vibronic coupling. Polarization studies may also be useful to fully assign these features.

6.7 Conclusions

We have developed a ligand-mediated transport synthesis of quantum-confined organic-inorganic perovskite ($MAPbX_3$) NCs that operates under ambient conditions. Due to its robust reaction conditions and convenient external controls, this ligand-mediated trans-

port method moves this material closer to industrial realization. The dissolution equilibria involved in the reaction allow precise control of size and composition, yielding quantum-confined NCs with high PLQY. Nanosecond TA spectra reveal an excitonic PL decay that is independent of radiation fluence, indicating direct radiative excitonic recombination. Femtosecond 2DES spectra resolve spectral features that shift with NC size reflecting the inherent electronic structure of the NCs. These observations confirm that our NCs are quantum-confined. Additionally, we observe sub-50 fs excitonic relaxation and quantum-beating signals that dephase with lifetimes of about 40 fs. Further investigation is required to assign these ultrafast dynamics and to understand the mechanisms of relaxation to the PL state. Of particular interest would be whether energy relaxes to the PL state through a coherent or incoherent mechanism.

REFERENCES

[1] Martin A. Green, Anita Ho-Baillie, and Henry J. Snaith. The emergence of perovskite solar cells. *Nat Photon*, 8(7):506–514, 07 2014.

[2] Valerio D'Innocenzo, Giulia Grancini, Marcelo J. P. Alcocer, Ajay Ram Srimath Kandada, Samuel D. Stranks, Michael M. Lee, Guglielmo Lanzani, Henry J. Snaith, and Annamaria Petrozza. Excitons versus free charges in organo-lead tri-halide perovskites. *Nature Communications*, 5:3586 EP –, 04 2014.

[3] Arianna Marchioro, Joel Teuscher, Dennis Friedrich, Marinus Kunst, Roel van de Krol, Thomas Moehl, Michael Gratzel, and Jacques-E. Moser. Unravelling the mechanism of photoinduced charge transfer processes in lead iodide perovskite solar cells. *Nat Photon*, 8(3):250–255, 03 2014.

[4] Carlito S. Ponseca, Tom J. Savenije, Mohamed Abdellah, Kaibo Zheng, Arkady Yartsev, Tobjörn Pascher, Tobias Harlang, Pavel Chabera, Tonu Pullerits, Andrey Stepanov, Jean-Pierre Wolf, and Villy Sundström. Organometal halide perovskite solar cell materials rationalized: Ultrafast charge generation, high and microsecond-long balanced mobilities, and slow recombination. *Journal of the American Chemical Society*, 136(14):5189–5192, 04 2014.

[5] Guichuan Xing, Nripan Mathews, Shuangyong Sun, Swee Sien Lim, Yeng Ming Lam, Michael Grätzel, Subodh Mhaisalkar, and Tze Chien Sum. Long-range balanced electron- and hole-transport lengths in organic-inorganic $CH_3NH_3PbI_3$. *Science*, 342(6156):344, 10 2013.

[6] Samuel D. Stranks, Giles E. Eperon, Giulia Grancini, Christopher Menelaou, Marcelo J. P. Alcocer, Tomas Leijtens, Laura M. Herz, Annamaria Petrozza, and Henry J. Snaith. Electron-hole diffusion lengths exceeding 1 micrometer in an organometal trihalide perovskite absorber. *Science*, 342(6156):341, 10 2013.

[7] Felix Deschler, Michael Price, Sandeep Pathak, Lina E. Klintberg, David-Dominik Jarausch, Ruben Higler, Sven Hüttner, Tomas Leijtens, Samuel D. Stranks, Henry J. Snaith, Mete Atatüre, Richard T. Phillips, and Richard H. Friend. High photoluminescence efficiency and optically pumped lasing in solution-processed mixed halide perovskite semiconductors. *The Journal of Physical Chemistry Letters*, 5(8):1421–1426, 04 2014.

[8] Joseph S. Manser and Prashant V. Kamat. Band filling with free charge carriers in organometal halide perovskites. *Nat Photon*, 8(9):737–743, 09 2014.

[9] Huanping Zhou, Qi Chen, Gang Li, Song Luo, Tze-bing Song, Hsin-Sheng Duan, Ziruo Hong, Jingbi You, Yongsheng Liu, and Yang Yang. Interface engineering of highly efficient perovskite solar cells. *Science*, 345(6196):542, 07 2014.

[10] Woon Seok Yang, Jun Hong Noh, Nam Joong Jeon, Young Chan Kim, Seungchan Ryu, Jangwon Seo, and Sang Il Seok. High-performance photovoltaic perovskite layers fabricated through intramolecular exchange. *Science*, 348(6240):1234, 06 2015.

[11] Wanyi Nie, Hsinhan Tsai, Reza Asadpour, Jean-Christophe Blancon, Amanda J. Neukirch, Gautam Gupta, Jared J. Crochet, Manish Chhowalla, Sergei Tretiak, Muhammad A. Alam, Hsing-Lin Wang, and Aditya D. Mohite. High-efficiency solution-processed perovskite solar cells with millimeter-scale grains. *Science*, 347(6221):522, 01 2015.

[12] Bo Chen, Yang Bai, Zhengshan Yu, Tao Li, Xiaopeng Zheng, Qingfeng Dong, Liang Shen, Mathieu Boccard, Alexei Gruverman, Zachary Holman, and Jinsong Huang. Efficient semitransparent perovskite solar cells for 23.0%-efficiency perovskite/silicon four-terminal tandem cells. *Advanced Energy Materials*, 6(19):n/a–n/a, 2016.

[13] Dongqin Bi, Chenyi Yi, Jingshan Luo, Jean-David Décoppet, Fei Zhang, Shaik Mohammed Zakeeruddin, Xiong Li, Anders Hagfeldt, and Michael Grätzel. Polymer-

templated nucleation and crystal growth of perovskite films for solar cells with efficiency greater than 21%. *Nature Energy*, 1:16142 EP –, 09 2016.

[14] Guichuan Xing, Nripan Mathews, Swee Sien Lim, Natalia Yantara, Xinfeng Liu, Dharani Sabba, Michael Grätzel, Subodh Mhaisalkar, and Tze Chien Sum. Low-temperature solution-processed wavelength-tunable perovskites for lasing. *Nat Mater*, 13(5):476–480, 05 2014.

[15] Haiming Zhu, Yongping Fu, Fei Meng, Xiaoxi Wu, Zizhou Gong, Qi Ding, Martin V. Gustafsson, M. Tuan Trinh, Song Jin, and X-Y. Zhu. Lead halide perovskite nanowire lasers with low lasing thresholds and high quality factors. *Nat Mater*, 14(6):636–642, 06 2015.

[16] Brandon R. Sutherland, Sjoerd Hoogland, Michael M. Adachi, Chris T. O. Wong, and Edward H. Sargent. Conformal organohalide perovskites enable lasing on spherical resonators. *ACS Nano*, 8(10):10947–10952, 10 2014.

[17] Zhi-Kuang Tan, Reza Saberi Moghaddam, May Ling Lai, Pablo Docampo, Ruben Higler, Felix Deschler, Michael Price, Aditya Sadhanala, Luis M. Pazos, Dan Credgington, Fabian Hanusch, Thomas Bein, Henry J. Snaith, and Richard H. Friend. Bright light-emitting diodes based on organometal halide perovskite. *Nat Nano*, 9(9):687–692, 09 2014.

[18] Jun Xing, Fei Yan, Yawen Zhao, Shi Chen, Huakang Yu, Qing Zhang, Rongguang Zeng, Hilmi Volkan Demir, Xiaowei Sun, Alfred Huan, and Qihua Xiong. High-efficiency light-emitting diodes of organometal halide perovskite amorphous nanoparticles. *ACS Nano*, 10(7):6623–6630, 07 2016.

[19] Sergii Yakunin, Loredana Protesescu, Franziska Krieg, Maryna I. Bodnarchuk, Georgian Nedelcu, Markus Humer, Gabriele De Luca, Manfred Fiebig, Wolfgang Heiss, and Maksym V. Kovalenko. Low-threshold amplified spontaneous emission and lasing

from colloidal nanocrystals of caesium lead halide perovskites. *Nature Communications*, 6:8056 EP –, 08 2015.

[20] Georgian Nedelcu, Loredana Protesescu, Sergii Yakunin, Maryna I. Bodnarchuk, Matthias J. Grotevent, and Maksym V. Kovalenko. Fast anion-exchange in highly luminescent nanocrystals of cesium lead halide perovskites (Cs_3PbX_3, X = Cl, Br, I). *Nano Letters*, 15(8):5635–5640, 08 2015.

[21] Feng Zhang, Haizheng Zhong, Cheng Chen, Xian-gang Wu, Xiangmin Hu, Hailong Huang, Junbo Han, Bingsuo Zou, and Yuping Dong. Brightly luminescent and color-tunable colloidal $CH_3NH_3PbX_3$ (X = Br, I, Cl) quantum dots: Potential alternatives for display technology. *ACS Nano*, 9(4):4533–4542, 04 2015.

[22] Dong Myung Jang, Kidong Park, Duk Hwan Kim, Jeunghee Park, Fazel Shojaei, Hong Seok Kang, Jae-Pyung Ahn, Jong Woon Lee, and Jae Kyu Song. Reversible halide exchange reaction of organometal trihalide perovskite colloidal nanocrystals for full-range band gap tuning. *Nano Letters*, 15(8):5191–5199, 08 2015.

[23] Dandan Zhang, Samuel W. Eaton, Yi Yu, Letian Dou, and Peidong Yang. Solution-phase synthesis of cesium lead halide perovskite nanowires. *Journal of the American Chemical Society*, 137(29):9230–9233, 07 2015.

[24] Shibin Sun, Dan Yuan, Yuan Xu, Aifei Wang, and Zhengtao Deng. Ligand-mediated synthesis of shape-controlled cesium lead halide perovskite nanocrystals via reprecipitation process at room temperature. *ACS Nano*, 10(3):3648–3657, 03 2016.

[25] Hailong Huang, Fangchao Zhao, Lige Liu, Feng Zhang, Xian-gang Wu, Lijie Shi, Bingsuo Zou, Qibing Pei, and Haizheng Zhong. Emulsion synthesis of size-tunable ch3nh3pbbr3 quantum dots: An alternative route toward efficient light-emitting diodes. *ACS Applied Materials & Interfaces*, 7(51):28128–28133, 12 2015.

[26] Yehonadav Bekenstein, Brent A. Koscher, Samuel W. Eaton, Peidong Yang, and A. Paul Alivisatos. Highly luminescent colloidal nanoplates of perovskite cesium lead halide and their oriented assemblies. *Journal of the American Chemical Society*, 137(51):16008–16011, 12 2015.

[27] Ioannis Lignos, Stavros Stavrakis, Georgian Nedelcu, Loredana Protesescu, Andrew J. deMello, and Maksym V. Kovalenko. Synthesis of cesium lead halide perovskite nanocrystals in a droplet-based microfluidic platform: Fast parametric space mapping. *Nano Letters*, 16(3):1869–1877, 03 2016.

[28] Yanqing Xu, Qi Chen, Chunfeng Zhang, Rui Wang, Hua Wu, Xiaoyu Zhang, Guichuan Xing, William W. Yu, Xiaoyong Wang, Yu Zhang, and Min Xiao. Two-photon-pumped perovskite semiconductor nanocrystal lasers. *Journal of the American Chemical Society*, 138(11):3761–3768, 03 2016.

[29] Fengrui Hu, Huichao Zhang, Chun Sun, Chunyang Yin, Bihu Lv, Chunfeng Zhang, William W. Yu, Xiaoyong Wang, Yu Zhang, and Min Xiao. Superior optical properties of perovskite nanocrystals as single photon emitters. *ACS Nano*, 9(12):12410–12416, 12 2015.

[30] Luciana C. Schmidt, Antonio Pertegás, Soranyel González-Carrero, Olga Malinkiewicz, Said Agouram, Guillermo Mínguez Espallargas, Henk J. Bolink, Raquel E. Galian, and Julia Pérez-Prieto. Nontemplate synthesis of ch3nh3pbbr3 perovskite nanoparticles. *Journal of the American Chemical Society*, 136(3):850–853, 01 2014.

[31] Shouqiang Huang, Zhichun Li, Long Kong, Nanwen Zhu, Aidang Shan, and Liang Li. Enhancing the stability of $CH_3NH_3PbBr_3$ quantum dots by embedding in silica spheres derived from tetramethyl orthosilicate in "waterless" toluene. *Journal of the American Chemical Society*, 138(18):5749–5752, 05 2016.

[32] Younghoon Kim, Emre Yassitepe, Oleksandr Voznyy, Riccardo Comin, Grant Walters, Xiwen Gong, Pongsakorn Kanjanaboos, Ana F. Nogueira, and Edward H. Sargent. Efficient luminescence from perovskite quantum dot solids. *ACS Applied Materials & Interfaces*, 7(45):25007–25013, 11 2015.

[33] Jonathan De Roo, Maria Ibáñez, Pieter Geiregat, Georgian Nedelcu, Willem Walravens, Jorick Maes, Jose C. Martins, Isabel Van Driessche, Maksym V. Kovalenko, and Zeger Hens. Highly dynamic ligand binding and light absorption coefficient of cesium lead bromide perovskite nanocrystals. *ACS Nano*, 10(2):2071–2081, 02 2016.

[34] Kenichiro Tanaka, Takayuki Takahashi, Takuma Ban, Takashi Kondo, Kazuhito Uchida, and Noboru Miura. Comparative study on the excitons in lead-halide-based perovskite-type crystals ch3nh3pbbr3 ch3nh3pbi3. *Solid State Communications*, 127(9–10):619–623, 9 2003.

[35] Alexei Halpin, JohnsonPhilip J. M., Roel Tempelaar, R. Scott Murphy, Jasper Knoester, JansenThomas L. C., and MillerR. J. Dwayne. Two-dimensional spectroscopy of a molecular dimer unveils the effects of vibronic coupling on exciton coherences. *Nat Chem*, 6(3):196–201, 03 2014.

CHAPTER 7

FUTURE DIRECTIONS

The singly linked fluorescein heterodimers and the SWNT packing strategy described in Chapter 3 have provided a straightforward and synthetically manipulable platform to control the vibronic coherences in synthetic multichromophoric systems. However, there is still much to be done to understand the role of vibronic coherences in the energy transfer mechanism in depth and further employ the coherent mechanism in the application of artificial systems, such as organic photovoltaics. In the first half of this chapter, I will discuss some new synthetic systems that could be interesting and fruitful to test the coherent energy transfer mechanisms in artificial systems via two-dimensional electronics spectroscopy. In Chapter 5, we demonstrate polaron formation in organic-inorganic perovskite bulk single crystals by nanosecond transient absorption spectroscopy. In Chapter 6 , we present the development of ligand-mediated transport synthesis of organic-inorganic hybrid perovskite nanocrystals and their ultrafast dynamics probed by femtosecond two-dimensional electronic spectroscopy at room temperature. However, the photophysical properties of perovskite materials, as both bulk and nanocrystal forms, are not yet fully explored and deserve further investigations. In the second half of this chapter, I will talk about future directions on the perovskite materials that can take advantage of our broadband femtosecond 2DES to contribute to the understanding of inherent photophysical properties of these materials.

7.1 Future directions for coherent dynamics studies on synthetic small molecules

The series of singly inked fluorescein heterodimers described in Chapter 3 were designed to test the synthetic requirements for vibronic coherences and control the presence of vibronic coherences via packing the dimer on SWNT surfaces. To explore the design principles of vibronic coherence, we intentionally create the heterodimers with weak electronic coupling

between the two constituent monomeric units. That is, we wanted to measure the effects of orientation and shared environment on the dynamics of an excited state resonant with another excited state plus a vibration. To observe the effects, we specifically worked in the weak coupling regime where energy transfer is rather slow compared to dephasing. However, to test the role of vibronic coherences on the excited state energy transfer processes, one should instead optimize energy transfer by creating stronger coupling between constituent monomers so that more energy transfer occurs before the vibronic coherences dephase.

7.1.1 Rigid fluorescein heterodimers with shorter linker

One way to introduce stronger coupling between the two constituent monomers is to shorten the linkage due to the R^{-6} distance dependence of the dipole-dipole coupling. A proposed synthetic route for creating double-linked fluorescein heterodimer with shorter linkers is shown in Figure 7.1.The first step in this synthetic route is the S_N2 allylation reaction of fluorescein monomers with substituted groups (X=H, Me, Cl). These different substituted groups are used to tune the electronic transition energies of these monomers. For halide groups, Cl can be used because it is relatively inert for the Heck coupling reactions in the later synthetic steps. However, Br and I are not ideal groups for tuning the energy levels due to their relatively high reactivity.

Installing Br and I on fluorescein monomers needs careful thoughts to avoid side reactions or difficulties in the purification of final products. For this S_N2 allylation reaction, the desired product is the fluorescein diallyl ether, which is a minor product of the allylation reaction. Large-scale synthesis is required for this step because the yield of fluorescein diallyl ether is usually less than 10%. The major product (fluorescein allyl ether allyl ester) and the minor product (fluorescein diallyl ester) can be easily separated via recrystallization. Recrystallization of the crude reaction mixture in ethyl acetate yields pure fluorescein allyl ether allyl ester. Evaporation of the remaining solution followed by recrystallization in methanol yields pure fluorescein diallyl ether as a pale yellow solid. The above-mentioned

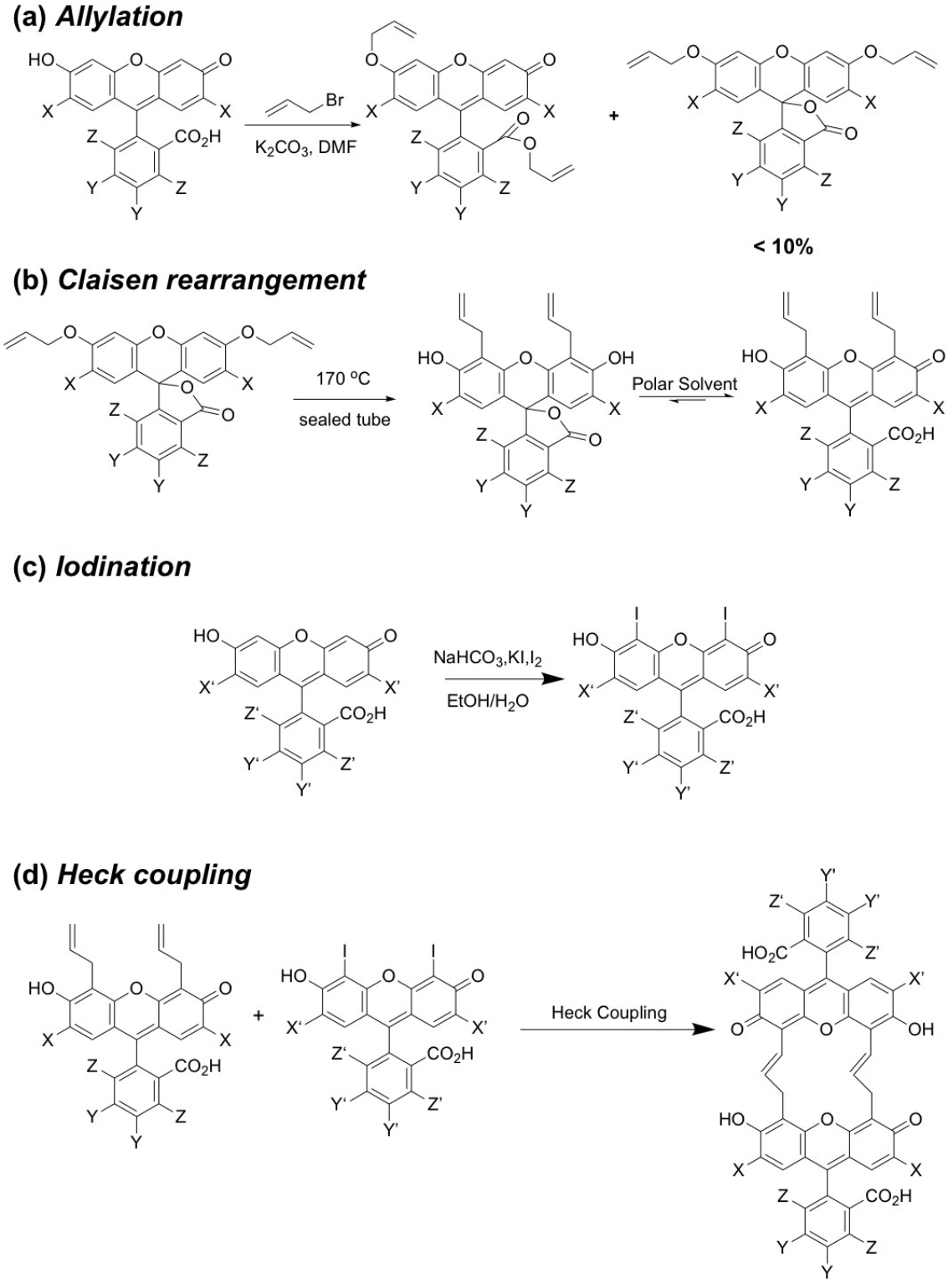

Figure 7.1: Synthetic scheme for doubly linked fluorescein heterodimer with shorter linkages.

separation protocol has been carefully tested and the ^{1}H NMR spectrum of 2',7'-dichlorofluorescein diallyl ether in $CDCl_3$ is shown in Figure 7.2.

The second step in the synthetic scheme is a Claisen rearrangement reaction to install both allyl groups on the 4',5'-positions of the xanthene ring. This reaction has to be conducted in the sealed tube with inert gas protection at 170 °C to avoid polymerization of the fluorescein diallyl ether induced by O_2. This dual Claisen rearrangement reaction will take longer time (>24 h) to completion compared to a single Claisen rearrangement. The 4',5'-diallyl fluorescein monomer can be further purified by chromatography. The ^{1}H NMR spectrum of 2',7'-dichloro-4',5'-diallyl fluorescein in CD_3OD is also attached in Figure 7.3 to prove the feasibility of this dual Claisen rearrangement reaction shown in Figure 7.1.

The third step is to prepare diiodo-substituted fluorescein for the final Heck coupling reaction. The two iodo groups should be installed on the 4',5'-positions of the xanthene ring to guarantee the favorable geometry for the Heck coupling. Meanwhile, for the choice of fluoresceins in this step, the 2',7'-positions of the xanthene ring should be protected by other groups such as Me and Cl to inhibit iodination on these sites.

The final step is the Heck coupling reaction between 4',5'-diallylfluorescein and 4',5'-diiodofluorescein. This reaction needs to be conducted in the sealed tube in the presence of Pd catalyst under basic conditions and inert gas protection. Note that the carboxylic acid groups of the two monomers need to be accounted when molecular ratio of the added base is calculated. An alternative way to deal with the carboxylic acid groups is ester protection by $-CH_2Ph$ or Et groups. Ester protection will ease the purification procedure by increasing the solubility of the final product in normal organic solvents such as chloroform and ethanol, but will also introduce additional steps in the synthesis. Hydrogenation of this rigid dimer may be necessary to remove the Z,E isomerism introduced by the C=C double bonds on the linkages. If one chose to use CH_2Ph as the protected group for the carboxylic acid in the Heck coupling reaction, the CH_2Ph protecting group could be removed simultaneously in the hydrogenation reaction catalyzed by Pd/C with H_2.

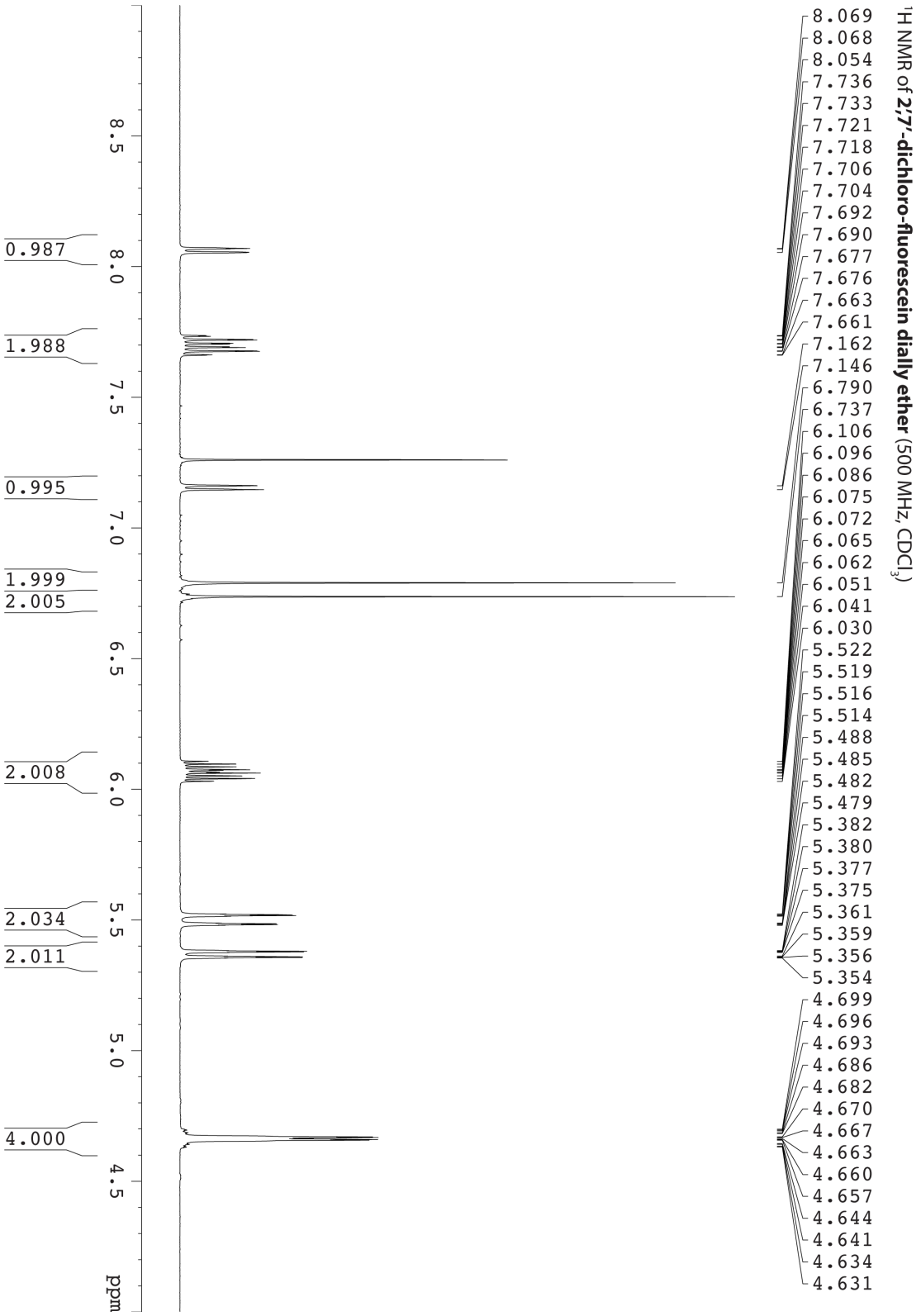

Figure 7.2: ^{1}H NMR spectrum of 2',7'-dichloro-fluorescein diallyl ether in $CDCl_3$.

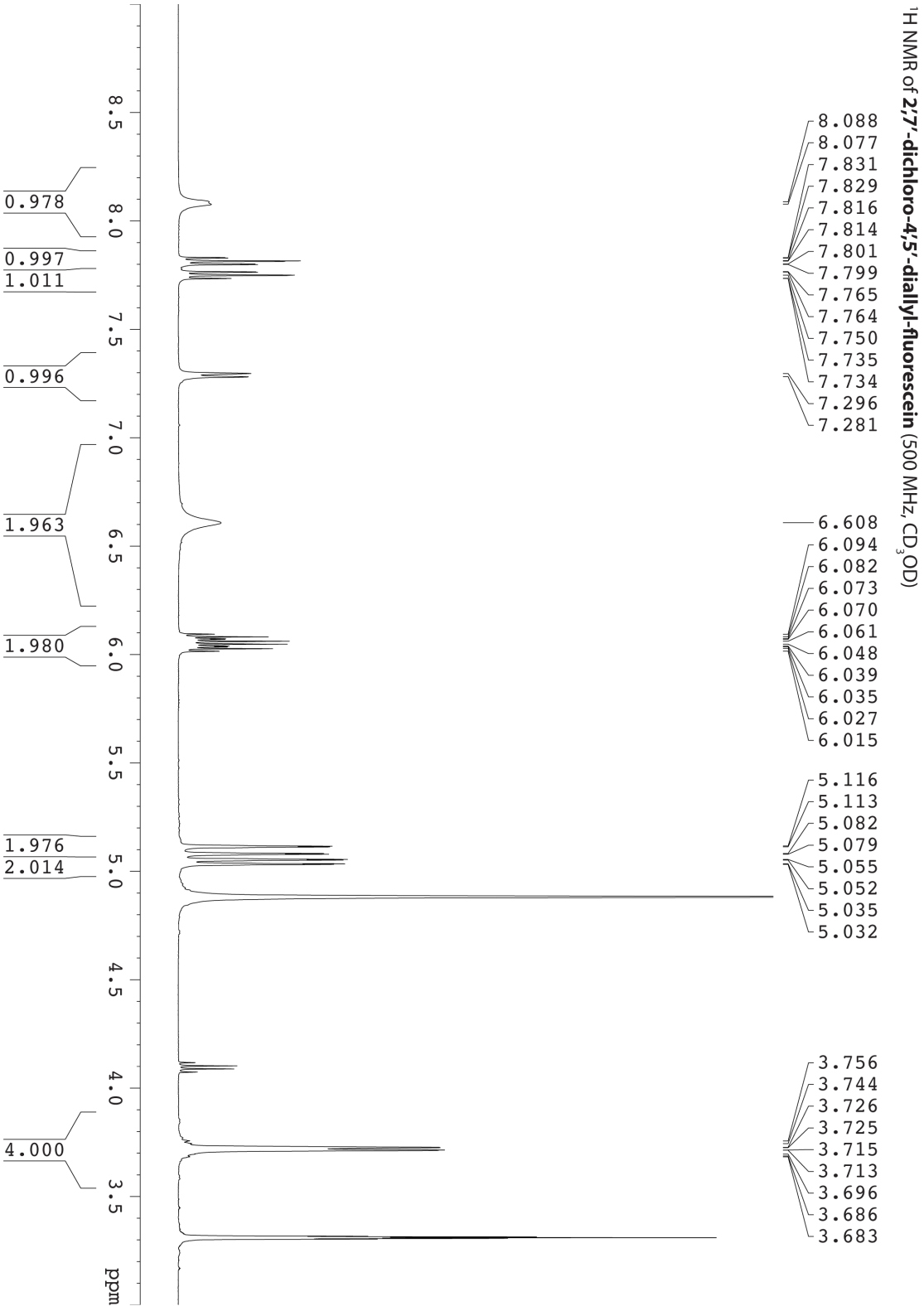

Figure 7.3: ^{1}H NMR spectrum of 2',7'-dichloro-4',5'-diallyl fluorescein in CD_3OD.

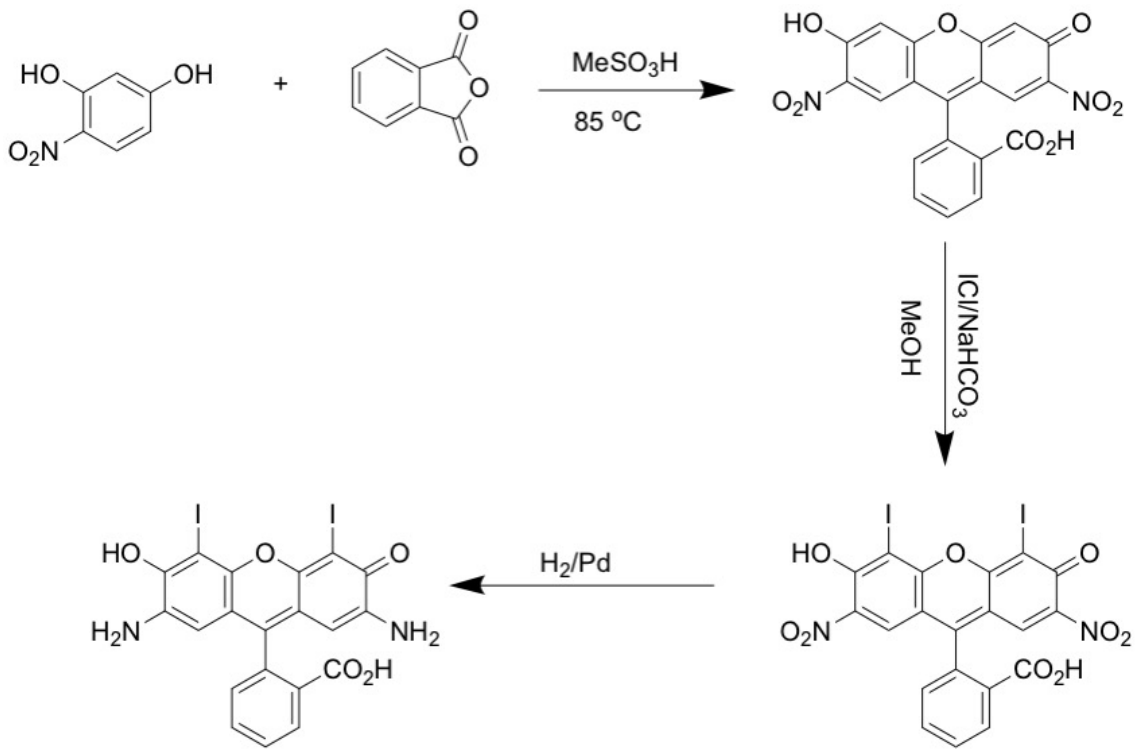

Figure 7.4: Synthesis of 4',5'-diiodo-2',7'-diaminofluorescein.

7.1.2 Synthetic heterotrimers

To test the role of coherence on the transport process to other constituent monomers, multi-chormophoric systems other than the dimer systems are required. A feasible model of artificial multi-chromophoric system is synthetic fluorescein heterotrimers. The energy difference can be varied by choices of different substituent groups. Halide substituent groups can vary the electronic transitions by several nanometers, enough for disentangling the electronic transition from certain vibrational modes but insufficient to create an energy trap within the molecule. If one desires an energy trap within the molecule to study the effect of coherent energy transport, the easiest way to create such a trap is to use 4',5'-diiodo-2',7'-dinitrofluorescein as one of the constituent monomers. The nitro groups stay inert in the Heck coupling but can be reduced to diaminofluorescein by H_2 and Pd/C, as shown in Figure 7.4, in which the amino groups redshift the linear absorption spectrum by tens of nanometers.

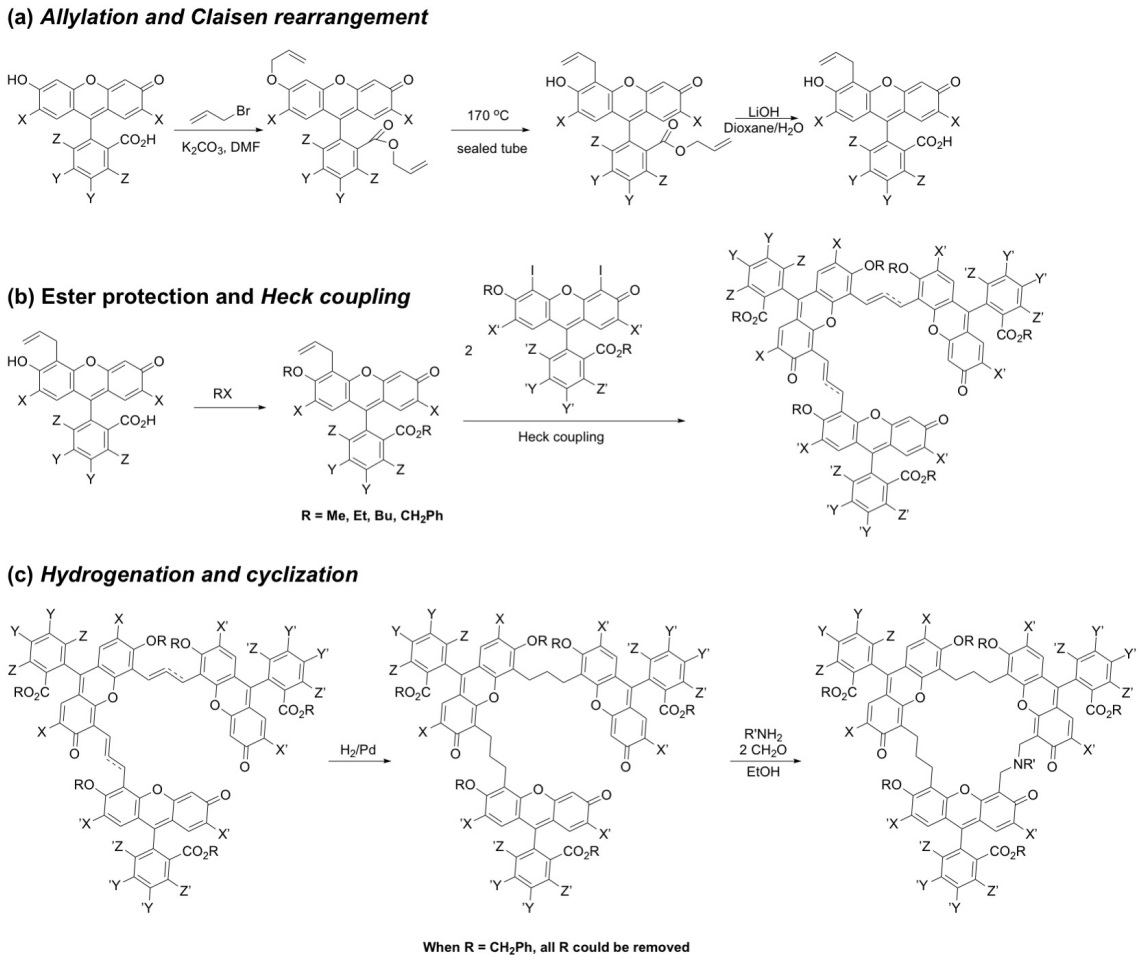

Figure 7.5: Synthetic scheme for fluorescein isosceles trimers.

The synthetic scheme for isosceles fluorescein heterotrimers is shown in Figure 7.5. The first few steps are allylation and Claisen rearrangements, similar to the procedures described in Chapter 3. Ester protection is crucial for the synthesis of fluorescein heterotrimers. Without the ester protection groups, as more constituent monomers attached to the molecule, the solubility of the molecule decreases severely in the solution, posing difficulties to further reaction and purification. Heck coupling between 2 equiv of monoallyl fluorescein and 1 equiv of 4',5'-diiodofluorescein yields an open isosceles fluorescein heterotrimer. Hydrogenation is required before cyclization to ensure the favorable geometry. A cyclic isosceles heterotrimer can be obtained by cyclization via Mannich reaction.

The synthetic scheme for fluorescein full heterotrimer is shown in Figure 7.6. The first few

steps are the same as those of singly-linked fluorescein heterodimer we described in Chapter 3. Heck coupling between the singly linked fluorescein heterodimer with 4',5'-diiodofluorescein yield a full heterotrimer. The reaction yield of the last step may be low, but the solubility difference among the monomer, dimer and trimer should be significant, which is convenient for further purification via chromatography.

The syntheses of fluorescein heterotrimers might be difficult to realize. In my opinion, the schemes I listed in this chapter are the most practical routes within the Engel Group. One could also attempt to collaborate with expert synthetic chemists from other groups to design other non-fluorescein based heterotrimers. Despite the difficulty associated with the syntheses, I believe that probing the effects of coherent energy transfer in an artificial multi-chromophoric system serve as both an interesting and an important aspect of our research, which we can apply the lessons learned from the photosynthetic pigment-protein complexes to other fields and exploit the importance/benefice of these coherences in future device applications.

7.2 Future directions for the studies of ultrafast dynamics of perovskite materials

Perovskites, as an extremely promising class of materials in optoelectronic devices, have attracted extensive research attention to their extraordinary photophysical properties. Bulk organic-inorganic hybrid perovskites as light absorber in solar cell devices have demonstrated power conversion efficiency up to 23% [1], while perovskite nanocrystals exhibit bright and narrow photoluminescence with quantum yield up to 97%, suitable for LED applications. In Chapter 5 and Chapter 6, we present some interesting observations on the ultrafast dynamics of both bulk single crystals and nanocrystals of organic-inorganic hybrid perovskite. However, more investigations are still needed to fully understand the photophysical properties of perovskite materials. In this section, I will discuss some future directions on perovskite

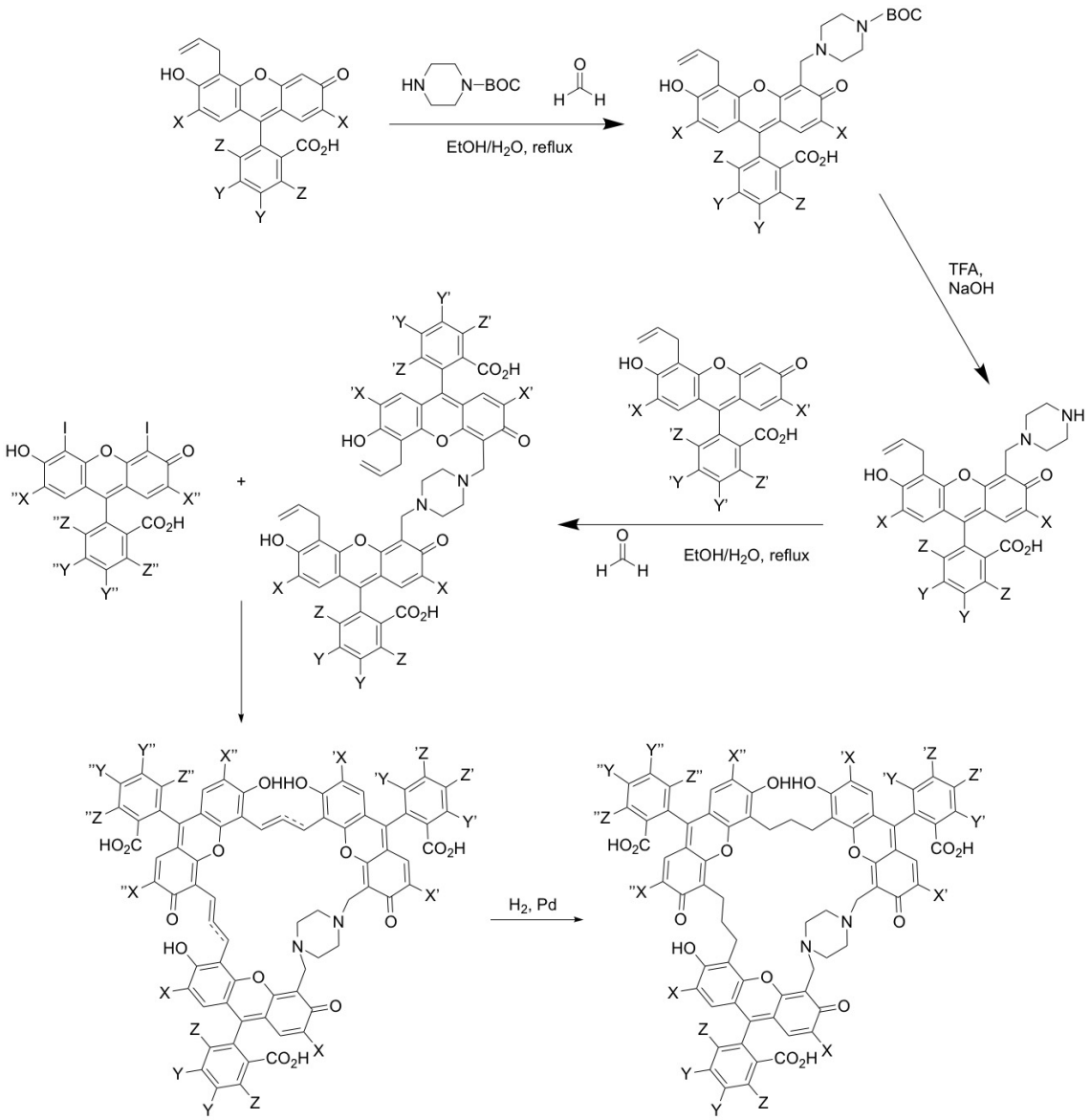

Figure 7.6: Synthetic scheme for fluorescein full heterotrimers.

materials that are feasible in Engel Lab.

7.2.1 Colloidal perovskite nanocrystals

In Chapter 6, we demonstrate ligand-mediated transport synthesis of organic-inorganic hybrid perovskite nanocrystals with octylamine protonated by oleic acid as capping ligands. It has been reported that capping ligands can affect the shape of perovskite nanomaterials to afford nanocrystals (quantum dots), nanocubes, nanorods and nanoplatelets [2]. One can employ the ligand-mediated transport syntheses with other capping ligands, such as dodecylamine protonated by hexanoic acid, oleic acid or acetate acid. A comparison of the electronic structure and ultrafast dynamics among perovskite nanomaterials with different shapes would be important to understand the quantum confinement effects on these materials. In the previous chapters, we focuse on organic-inorganic perovskites (methylammounium based). One can also study the ultrafast dynamics of purely-inorganic perovskite nanocrystals (Cesium based) and compare the results with organic-inorganic perovskites. The role of methylammounium cations (associated with permanent dipoles) in the perovskite nanocrystals could be an interesting future project because we know that the methylammounium cations can reorient to induce polaron formations in perovskite bulk crystals while cesium cations cannot [3].

The colloidal stability of perovskite nanocrystals might be a concern for our ultrafast spectroscopy due to their sensitivity to humidity, which is caused by the ionic nature of the crystal lattice. Recent studies have shown that heavily branched ligands can improve the colloidal stability of these nanocrystals against polar solvents [4]. One can also incorporate our ligand-mediated transport synthesis with branched ligands to further improve the stability of the nanocrystals. This approach would significantly ease the time limit on the 2DES measurements posed by sample stability, avoiding the scenarios that one must synthesize the nanocrystals and troubleshoot the laser at the same time.

In Chapter 6, we have reported the femtosecond 2D spectra of $CH_3NH_3PbI_3$ nanocrys-

tals at room temperature. These 2D spectra present some interesting observations, but are insufficient to definitely assign the microscopic mechanisms of the observed coherences or to assign specific transition/electronic states to the observed spectral features due to the extremely fast (sub-50fs) dynamics at room temperature. To unambiguously assign the origin of the observed coherences (electronic *vs* vibronic), low-temperature 2DES would be necessary to prolong the coherences and further resolve these spectral features. Unfortunately, the common solvents for perovskite nanocrystals, such as hexane and toluene, are not good candidates for glass formation at low temperature. Identifying a solvent that can form nice glass at low temperature and afford perovskite nanocrystals at high concentration for 2DES measurement might be a major challenge for this project.

Additionally, the choice of temperature and radiation power requires careful thoughts for future 2DES measurements on perovskite nanocrystals. These nanocrystals will experience phase transitions from cubic/pseudocubic phase (at room temperature) to tetragonal phase to orthorhombic upon lowering the temperature [5, 6]. High radiation fluence may generate multi-exciton effects and thus affect the lineshapes of the spectrum and the corresponding dynamics [7]. A radiation-fluence dependent 2DES study on these nanocrystals at either room temperature or low temperature is necessary to definitively assign the observed spectral features to certain transitions/electronic states. The pulse power I used for $CH_3NH_3PbI_3$ nanocrystals is 10 nJ/pulse with spectrum from 550 - 680 nm (FWHM). This power is within the low to moderate range for typical nanocrystals 2DES measurements but might still be at risk of multi-exciton generation due to the enormous cross section of perovskite nanocrystal [8, 9]. However, the signal intensity recorded on the CCD camera is only about 2000 counts. Therefore, improving the signal-to-noise ratio in the Redfield lab would be a prerequisite to obtain publication-quality 2DES data with extremely low radiation fluence.

7.2.2 Perovskite thin films

Perovskite materials are usually applied in the optoelectronic devices as thin films, not in colloidal solutions. Therefore, the studies of ultrafast dynamics of perovskite thin films are more important because these materials may exhibit different photophysical properties as compared to those in colloidal solutions. Two types of perovskite thin films can be considered as possible subjects of study in Engel Group.

The first type is perovskite thin film of microcrystals. $CH_3NH_3PbBr_3$ and $CH_3NH_3PbI_3$ microcrystals thin films can be obtained by spin-coating precursor solutions (lead halide and methylammounium halide, typically in DMF) of varied concentration, affording average grains of sub-μm to 10 μm [10]. The bandgap of Br-based perovskite thin films are typically around 530 nm, not easily accessible with our femtosecond lasers. Whereas the bandgap of I-based perovskite thin films are typically around 710 - 720 nm, suitable for our laser bandwidth, but more care must be taken due to their sensitivity to humidity. Heterogeneity of perovskite microcrystal thin films is an important factor for the 2DES measurement. As mentioned before, the average grain size could range from sub-μm to10 μm. The beam size of focus at sample position is usually 70-100 μm. Hence, the probing area of the thin films is extremely sensitive because it can either provide result of a single grain or "ensemble" results from several grains with different sizes, depending on the morphology of thin films. It has been reported that the size and morphology of the microcrystals can significant affect the corresponding ultrafast dynamics of the charge carriers [10]. Hence, conventional 2DES on perovskite microcrystal thin films might be complicated by the heterogeneity and the morphology of the films. However, due to the same fact, perovskite microcrystal thin films could be perfect candidates for the Optical Resonance Imaging apparatus in Engel Group [11], which can spatially resolve the morphology and temporarily resolve the ultrafast dynamics of the perovskite thin films simultaneously.

The second type is perovskite thin film of nanocrystals, which is a suitable candidate for conventional ultrafast 2DES due to its relatively homogeneous morphology. Perovskite

nanocrystal thin films can be obtained by spin-coating a solution of pre-synthesized nanocrystals on to a glass substrate. Ultrafast 2DES on thin films of $CH_3NH_3PbI_3$ nanocrystals, at both room temperature or low temperature, is readily accessible with the current laser bandwidth in the Redfield Lab and is a project worth pursuing. Another interesting project is the ultrafast dynamics of mixed-halide perovskite nanocrystal thin films. The photoluminescence quantum yields of colloidal mixed-halide perovskite nanocrystals are much weaker compared to purely Br- or I-based nanocrystals, probably due to trap states associated with composition mismatch. But the PL of mixed-halide perovskite nanocrystal is tunable across a significant portion of the visible spectrum (540 to 630 nm). Hence, understanding the electronic structure/trap states associated with these nanocrystals would be important for future materials design and applications of these materials in light-emitting devices.

The anion exchange property of the perovskite nanocrystals may also enable real-time observation of chemical reactions probed by ultrafast dynamics. Real-time observation of chemical reactions has been proposed during the last several years in the Engel group, yet finding a suitable system/reaction is challenging. We have attempted to conduct this type of studies on the synthesis of PbS magic-size clusters, however, the concentration of colloidal product is too low to generate any observable signals. Perovskite nanocrystals can undergo anion exchange reaction both in solution and as thin films [12–14]. $CH_3NH_3PbI_3$ nanocrystal thin films can be produced with sufficient optical density to generate 2DES signals. Hence, the real-time observation on the chemical dynamics can be realized by conducting 2DES measurements with GRAPS apparatus on a thin films of $CH_3NH_3PbI_3$ nanocrystals while pumping solutions (containing Br anions) through the film to initiate the anion exchange reaction. The reaction time can be adjusted by the concentration of Br anions in solution to match with the experimental time required by 2DES.

7.2.3 Perovskite bulk single crystals

In Chapter 5 we performed nanosecond transient absorption spectroscopy on $CH_3NH_3PbBr_3$ bulk single crystals and attributed the two observed decoupled populations to the coexistence of free and localized carrier due to polaron formation. We have suggested that doping $CH_3NH_3PbI_3$ bulk single crystals with Cl may improve the polaron formation effect because the chloride can displace $CH_3NH_3^+$ cations and reduce the high frequency dielectric constant [15]. Therefore, future studies on the doped perovskite bulk crystals would be interesting. It is possible to synthesize doped perovskite bulk single crystals via the anti-solvent method reported by Shi *et al* [16] with varied ratio of different halide precursors. I have successfully synthesized $CH_3NH_3PbBr_3$ single crystals doped with I before. The doped crystals are darker in color as compared to pure $CH_3NH_3PbBr_3$ single crystals, but the crystal lattice parameters remain the same probed by X-ray diffraction. Hence, more sophisticated experimental design on the doped-perovskite crystallization is required and the elemental analysis on these doped crystals is necessary for characterization. Ultrafast dynamics of these perovskite bulk crystals may suffer from the scattering caused by the crystal lattice, but still remains as an interesting project for further studies.

REFERENCES

[1] Bo Chen, Yang Bai, Zhengshan Yu, Tao Li, Xiaopeng Zheng, Qingfeng Dong, Liang Shen, Mathieu Boccard, Alexei Gruverman, Zachary Holman, and Jinsong Huang. Efficient semitransparent perovskite solar cells for 23.0%-efficiency perovskite/silicon four-terminal tandem cells. *Advanced Energy Materials*, 6(19), 2016.

[2] Shibin Sun, Dan Yuan, Yuan Xu, Aifei Wang, and Zhengtao Deng. Ligand-mediated synthesis of shape-controlled cesium lead halide perovskite nanocrystals via reprecipitation process at room temperature. *ACS Nano*, 10(3):3648–3657, 03 2016.

[3] Haiming Zhu, Kiyoshi Miyata, Yongping Fu, Jue Wang, Prakriti P. Joshi, Daniel Niesner, Kristopher W. Williams, Song Jin, and X. Y. Zhu. Screening in crystalline liquids protects energetic carriers in hybrid perovskites. *Science*, 353(6306):1409, 09 2016.

[4] Binbin Luo, Ying-Chih Pu, Sarah A. Lindley, Yi Yang, Liqiang Lu, Yat Li, Xueming Li, and Jin Z. Zhang. Organolead halide perovskite nanocrystals: Branched capping ligands control crystal size and stability. *Angewandte Chemie*, 128(31):9010–9014, 2016.

[5] He Wang, Luisa Whittaker-Brooks, and Graham R. Fleming. Exciton and free charge dynamics of methylammonium lead iodide perovskites are different in the tetragonal and orthorhombic phases. *The Journal of Physical Chemistry C*, 119(34):19590–19595, 08 2015.

[6] Rebecca L. Milot, Giles E. Eperon, Henry J. Snaith, Michael B. Johnston, and Laura M. Herz. Temperature-dependent charge-carrier dynamics in $CH_3NH_3PbI_3$ perovskite thin films. *Advanced Functional Materials*, 25(39):6218–6227, 2015.

[7] Elad Harel, Sara M. Rupich, Richard D. Schaller, Dmitri V. Talapin, and Gregory S. Engel. Measurement of electronic splitting in pbs quantum dots by two-dimensional nonlinear spectroscopy. *Physical Review B*, 86(7):075412–, 08 2012.

[8] Yanqing Xu, Qi Chen, Chunfeng Zhang, Rui Wang, Hua Wu, Xiaoyu Zhang, Guichuan Xing, William W. Yu, Xiaoyong Wang, Yu Zhang, and Min Xiao. Two-photon-pumped perovskite semiconductor nanocrystal lasers. *Journal of the American Chemical Society*, 138(11):3761–3768, 03 2016.

[9] Fengrui Hu, Huichao Zhang, Chun Sun, Chunyang Yin, Bihu Lv, Chunfeng Zhang, William W. Yu, Xiaoyong Wang, Yu Zhang, and Min Xiao. Superior optical properties of perovskite nanocrystals as single photon emitters. *ACS Nano*, 9(12):12410–12416, 12 2015.

[10] Giulia Grancini, Ajay Ram Srimath Kandada, Jarvist M. Frost, Alex J. Barker, Michele De Bastiani, Marina Gandini, Sergio Marras, Guglielmo Lanzani, Aron Walsh, and Annamaria Petrozza. Role of microstructure in the electron–hole interaction of hybrid lead halide perovskites. *Nat Photon*, 9(10):695–701, 10 2015.

[11] Marco A. Allodi, Peter D. Dahlberg, Richard J. Mazuski, Hunter C. Davis, John P. Otto, and Gregory S. Engel. Optical resonance imaging: An optical analog to mri with subdiffraction-limited capabilities. *ACS Photonics*, 3(12):2445–2452, 12 2016.

[12] Georgian Nedelcu, Loredana Protesescu, Sergii Yakunin, Maryna I. Bodnarchuk, Matthias J. Grotevent, and Maksym V. Kovalenko. Fast anion-exchange in highly luminescent nanocrystals of cesium lead halide perovskites (Cs_3PbX_3, X = Cl, Br, I). *Nano Letters*, 15(8):5635–5640, 08 2015.

[13] Dong Myung Jang, Kidong Park, Duk Hwan Kim, Jeunghee Park, Fazel Shojaei, Hong Seok Kang, Jae-Pyung Ahn, Jong Woon Lee, and Jae Kyu Song. Reversible halide exchange reaction of organometal trihalide perovskite colloidal nanocrystals for full-range band gap tuning. *Nano Letters*, 15(8):5191–5199, 08 2015.

[14] Quinten A. Akkerman, Valerio D'Innocenzo, Sara Accornero, Alice Scarpellini, Annamaria Petrozza, Mirko Prato, and Liberato Manna. Tuning the optical properties of

cesium lead halide perovskite nanocrystals by anion exchange reactions. *Journal of the American Chemical Society*, 137(32):10276–10281, 08 2015.

[15] Yuping He and Giulia Galli. Instability and efficiency of mixed halide perovskites $CH_3NH_3PbAI_3$–xClx (A = Pb and Sn): A first-principles, computational study. *Chemistry of Materials*, 29(2):682–689, 01 2017.

[16] Dong Shi, Valerio Adinolfi, Riccardo Comin, Mingjian Yuan, Erkki Alarousu, Andrei Buin, Yin Chen, Sjoerd Hoogland, Alexander Rothenberger, Khabiboulakh Katsiev, Yaroslav Losovyj, Xin Zhang, Peter A. Dowben, Omar F. Mohammed, Edward H. Sargent, and Osman M. Bakr. Low trap-state density and long carrier diffusion in organolead trihalide perovskite single crystals. *Science*, 347(6221):519, 01 2015.

CHAPTER 8

CONCLUSIONS

Photosynthesis can harvest solar energy with remarkable quantum efficiencies. Since the observation of long-lived quantum-beating signals in photosynthetic complexes with two-dimensional electronic spectroscopy from 2007, much effort has been devoted to investigate numbers of questions on these quantum-beating signals. These quantum-beating signals were originally attributed to purely electronic coherences between different excited states. The prolonged electronic coherences suggest that energy may migrate in a wave-like manner in the photosynthetic complexes which accounts for the near perfect transfer efficiencies. However, there is a huge debate over the microscopic origin of the observed beating signals due to the existence of multiple vibrational modes in these photosynthetic complexes and the coincident of a vibrational mode near the electronic energy gap.

One important question is the nature of these beating signals. Do they arise from purely vibrational coherences, purely electronic coherences between different excited states, or coherences with vibronic character that arise from the non-adiabatic coupling between the excited-state surfaces of the two chromophores? Purely vibrational coherences on the electronic ground state cannot impact the energy transfer while electronic and vibronic coherences can. Unambiguous assignment of these observed beating signals is required before claiming their biological significance. If these coherences are indeed electronic or vibronic in nature, can they be reproduced in artificial systems? If so, what are the requirements for molecular design?

In Chapter 3, I have endeavored to answer the aforementioned questions. The signal observed in two-dimensional electronic spectroscopy is the summed signal from all accessible pathways. Systems that can dissect contributions from vibrational, electronic and vibronic pathways would be ideal to unveil the microscopic origins and design principles of these coherences. In photosynthetic complexes, protein provides two coupled functionalities: finely tuned excitation energy gaps of the individual chromophores and rigid structural support

that holds chromophores in fixed spatial relationships. Therefore, photosynthetic systems is not an ideal system for such studies due to the difficulty on tuning the electronic energy gap away from vibrational modes without losing structural integrity.

I have designed and synthesized a series of synthetic fluorescein heterodimers instead to differentiate coherences with different origins. The rich chemical variability in these synthetic systems provide facile tunability of the electronic energy gap to match or deviate from certain vibrational modes. These heterodimers are structurally flexible in solution with a single linkage between the two constituent monomers that allows one monomer to rotate freely relative to the other. But these heterodimers can experience fixed spatial relationship between chromophores when packed on single-walled carbon nanotube surfaces, in crude analogy to the protein environment in photosynthetic systems. With this molecular design, I can dissect contributions of different coherences and test the impact of energy gap and rigid structural support on coherences separately. By employing two-dimensional electronic spectroscopy along with these synthetic controls, I demonstrate that the presence of vibronic coherence can be controlled in artificial systems. The two prerequisites to generate vibronic coherence in artificial systems are as follows: a resonant vibrational mode with the electronic energy gap, and limiting the relative orientation of the chromophores. Our observation will be informative for further investigations on coherent energy transport and biomimetic artificial materials that could exploit coherent transport in photovoltaics.

In Chapter 4, I have presented the two-dimensional electronic spectra of a cavitand molecular switch with a pair of functionalized BODIPY dyes attached on the opposite walls of the backbone. This cavitand switch failed to meet the design principle of vibronic coherence but is particularly useful for understanding the impact of nonradiative transition on the overall Föster energy transfer efficiency, which is often neglected in typical steady-state and time-resolved fluorescence measurements. Switching from *vase* to *kite* conformation increases the donor-acceptor distance from 0.5 to 3 nm and affects FRET efficiency. By disentangling different dynamics based on lifetimes in 2D spectra, I separate three processes associated with

the donor of the cavitand: nonradiative relaxation, energy transfer (FRET), and residual fluorescence. The 2D spectra for the *vase* and *kite* conformations demonstrate a 70% greater change in FRET efficiency with donor-acceptor distance than that determined by standard lifetime-based measurements. These observations suggest that nonradiative processes are sensitive to the local chemical environment and must be taken into account when highly accurate measurements of FRET efficiency are desired.

The studies in Chapter 3 and Chapter 4 are motivated by the efficient light-harvesting processes in photosynthesis. Understanding the ultrafast dynamics and the energy transfer mechanisms of these molecular systems are important for future biomimetic materials design and their device applications. Solar energy can also be harvested by photovoltaics, although usually with lower quantum efficiency compared to photosynthesis. Therefore, investigations on the photophysical dynamics of functional materials used in the active layers of photovoltaic devices will be crucial for understanding device performance.

The remarkable power conversion efficiencies demonstrated by photovoltaic devices using perovskites (microcrystals thin films and bulk single crystals) as light absorbs have raised broad scientific interests to these fascinating materials. What are the photogenerated species in these materials? Are they excitons, free charge carriers, or polarons? How would these photogenerated species impact the device performance?

In Chapter 5, I have sought to clarify some aspects of the fundamental photophysical properties of perovskite bulk crystals. Previous research efforts were devoted to perovskite thin films, in which nonintrinsic factors such as grain sizes and grain boundaries may obscure the inherent photophysical dynamics of perovskite materials. I have performed the first nanosecond transient absorption spectroscopy in a transmissive geometry on perovskite single crystals. These single crystals are polished to ca. 70 μm thickness, ensuring detectable probe light through the crystals. Compared to transient reflectance spectroscopy, transient absorption signal in a transmissive geometry is sensitive to the bulk rather than crystal surfaces. Through transient absorption experiments on perovskite crystals with varied radi-

ation fluences, I observe the coexistence of two different sets of photogenerated populations in bulk perovskites. One decays through second-order recombination while the other decays through third-order recombination dynamics, differing from the observed carrier dynamics in perovskite thin films. By performing *ab initio* calculations on perovskites, we find this observation is best explained by the coexistence of localized carriers and free carriers in bulk perovskites. Methylammonium cations can solvate electrons within perovskite, resulting in polaron formation at specific locations within perovskite lattice. Polaron formation will lead to localization of carriers and dramatically reduce the overlap between the electron and hole wavefunctions. Hence, the recombination will be retarded by polaron formation and decoupled from the recombination dynamics of free carriers. Our calculations of perovskite polaron stabilization energy on both $CH_3NH_3PbBr_3$ and $CH_3NH_3PbI_3$ suggest that polarons will form in both perovskites but are more pronounced in $CH_3NH_3PbBr_3$. Our observation of perovskite bulk carrier dynamics is an important step toward understanding the impact of polarons on the transport and optical properties of perovskite.

While the spontaneous dissociation of exciton into carriers in perovskite bulk crystals and microcrystals may be ideal for photovoltaics, the nonradiative recombination of these carriers constrains their light-emitting performance. Nanostructured perovskites, which can increase the exciton binding energy through quantum confinement and overcome the relatively weak photoluminescence of bulk perovskite, have then attracted extensive research attentions. Perovskite nanocrystals exhibit remarkably bright and spectrally narrow photoluminescence tunable across the entire visible range, inspiring investigations on their photophysical properties. Important questions raised on perovskite nanocrystals include: Is the enhancement of PL QY due to quantum confinement in the NCs? Will excitations stay as excitons or separate immediately into carriers in perovskite nanocrystals? What are the electronic structures of these perovskite nanocrystals? Is it possible to generate these quantum-confined nanocrystals in large scale under convenient reaction conditions for future industrial applications?

In Chapter 6, I have answered some of the aforementioned questions by probing the ultra-

fast dynamics of perovskite nanocrystals. Previous syntheses on perovskite nanocrystals via ligand-assisted reprecipitation (LARP) and hot-injection methods require exquisite experimental control, which constrains their scalability. The extremely fast nucleation dynamics in LARP and hot-injection method also pose difficulty on precise size control and postsynthetic purification. I have therefore developed a scalable ligand-mediated transport synthesis of organic-inorganic perovskite nanocrystals. This synthesis operates at ambient conditions and provides high quality (PL QY up to 97%) organic-inorganic hybrid perovskite nanocrystals for 2DES measurements. The ligand-mediated transport synthesis employs a different reaction mechanism from previous methods, circumventing the need for exquisite external control (*e.g.* temperature control, inert-gas protection, dropwise addition of reagents). In the ligand-mediated transport mechanism, multiple equilibria cooperatively dictate reaction rates and enable precise control over NC size. Nanosecond transient absorption spectroscopy on these perovskite nanocrystals reveals radiation fluence-independent PL decay, suggesting that excitons are the primary photogenerated species and the bright photoluminescence is due to quantum confinement of excitonic within these NCs. Femtosecond 2DES spectra of these NCs resolve spectral features that shift with NC size, reflecting the inherent electronic structure of these NCs. The ultrafast dynamics of these NCs, including sub-50 fs excitonic relaxation and quantum-beating signals that dephase with lifetimes of about 40 fs, are also observed. The existence of quantum-beating signals in these perovskite NCs is an interesting observation, resembling the photosynthetic systems that also exhibit these quantum-beating signals and near unity transfer quantum yields. Although it is difficult to assign the microscopic origin of these quantum-beating signals in perovskite NCs due to their ultrafast dephasing at room temperature, our observation will certainly inspire future investigation on the nature of these beating signals and their impact on energy transport. Of particular interest will be whether the energy relaxes to PL state in a coherent or incoherent manner and whether the observed coherences can help avoid 'trapping' in the local minima and explain the high PLQYs in perovskite NCs. The knowledge we obtained is an important

step toward depicting the electronic structure of the NCs and the energy transfer mechanism within a NC.

In summary, we have investigated ultrafast dynamics of functional light-harvesting materials related to photosynthesis and photovoltaics. The molecular designs we have provided and the photophysical properties of various materials we observed would inspire future design of artificial light-harvesting materials in device applications.